National Library
of Canada

Bibliothèque nationale
du Canada

Canadian Theses Service

Service des thèses canadiennes

Ottawa, Canada
K1A 0N4

NOTICE

The quality of this microform is heavily dependent upon the quality of the original thesis submitted for microfilming. Every effort has been made to ensure the highest quality of reproduction possible.

If pages are missing, contact the university which granted the degree.

Some pages may have indistinct print especially if the original pages were typed with a poor typewriter ribbon or if the university sent us an inferior photocopy.

Reproduction in full or in part of this microform is governed by the Canadian Copyright Act, R.S.C. 1970, c. C-30, and subsequent amendments.

AVIS

La qualité de cette microforme dépend grandement de la qualité de la thèse soumise au microfilmage. Nous avons tout fait pour assurer une qualité supérieure de reproduction.

S'il manque des pages, veuillez communiquer avec l'université qui a conféré le grade.

La qualité d'impression de certaines pages peut laisser à désirer, surtout si les pages originales ont été dactylographiées à l'aide d'un ruban usé ou si l'université nous a fait parvenir une photocopie de qualité inférieure.

La reproduction, même partielle, de cette microforme est soumise à la Loi canadienne sur le droit d'auteur, SRC 1970, c. C-30, et ses amendements subséquents.

NL-339 (r. 88/04) c

Canada

UNIVERSITY OF ALBERTA

ANALYSIS OF PROGRESSIVE FAILURE OF CARSINGTON DAM

by

CHEN ZHONGHUA

A THESIS

SUBMITTED TO THE FACULTY OF GRADUATE STUDIES AND RESEARCH
IN PARTIAL FULFILMENT OF THE REQUIREMENTS FOR THE DEGREE
OF DOCTOR OF PHILOSOPHY

DEPARTMENT OF CIVIL ENGINEERING

EDMONTON, ALBERTA
SPRING 1990

National Library of Canada
Canadian Theses Service

Ottawa, Canada
K1A 0N4

Bibliothèque nationale du Canada
Service des thèses canadiennes

NOTICE

The quality of this microform is heavily dependent upon the quality of the original thesis submitted for microfilming. Every effort has been made to ensure the highest quality of reproduction possible.

If pages are missing, contact the university which granted the degree.

Some pages may have indistinct print especially if the original pages were typed with a poor typewriter ribbon or if the university sent us an inferior photocopy.

Reproduction in full or in part of this microform is governed by the Canadian Copyright Act, R.S.C. 1970, c. C-30, and subsequent amendments.

AVIS

La qualité de cette microforme dépend grandement de la qualité de la thèse soumise au microfilmage. Nous avons tout fait pour assurer une qualité supérieure de reproduction.

S'il manque des pages, veuillez communiquer avec l'université qui a conféré le grade.

La qualité d'impression de certaines pages peut laisser à désirer, surtout si les pages originales ont été dactylographiées à l'aide d'un ruban usé ou si l'université nous a fait parvenir une photocopie de qualité inférieure.

La reproduction, même partielle, de cette microforme est soumise à la Loi canadienne sur le droit d'auteur, SRC 1970, c. C-30, et ses amendements subséquents.

ISBN 0-315-60327-5

NL-339 (r. 88/04) c

Canada

micro

UNIVERSITY OF ALBERTA

RELEASE FORM

NAME OF AUTHOR CHEN ZHONGHUA

TITLE OF THESIS ANALYSIS OF PROGRESSIVE FAILURE OF CARSINGTON DAM

DEGREE FOR WHICH THESIS WAS PRESENTED DOCTOR OF PHILOSOPHY

YEAR THIS DEGREE GRANTED SPRING 1990

Permission is hereby granted to THE UNIVERSITY OF ALBERTA LIBRARY to reproduce single copies of this thesis and to lend or sell such copies for private, scholarly or scientific research purposes only.

The author reserves other publication rights, and neither the thesis nor extensive extracts from it may be printed or otherwise reproduced without the author's written permission.

(SIGNED) Chen Zhonghua

PERMANENT ADDRESS:

P. O. Box 366,
Beijing,
P. R. C.

DATED Jan. 25th 1990

THE UNIVERSITY OF ALBERTA

FACULTY OF GRADUATE STUDIES AND RESEARCH

The undersigned certify that they have read, and recommend to the Faculty of Graduate Studies and Research, for acceptance, a thesis entitled ANALYSIS OF PROGRESSIVE FAILURE OF CARSINGTON DAM submitted by CHEN ZHONGHUA in partial fulfilment of the requirements for the degree of DOCTOR OF PHILOSOPHY.

N.R. Morgenstern ....
Supervisor

Dave Chan ....Dave Chan....................
J. Colbourne ....J R Colbourne....................
A. Elwi ....
Z. Eisenstein ....

K.Y. Lo ....
External Examiner

Date....January 15, 1990................

To my beloved mother Liangju Zhu

ABSTRACT

The thesis deals mainly with a systematic and methodological research into the application of nonlinear finite element methods to analyses of progressive failure due to strain softening. As a case history, the Carsington Dam failure is back-analysed. As far as the theoretical background is concerned, the theory of plasticity for small strain and deformation is adopted. The research has touched almost all the main topics from theory to practice. The main purpose is to enhance the applicability of finite element analyses to complicated engineering problems. Emphases are placed on practical applications.

The incremental theory for strain softening materials is re-examined and strengthened. Within the framework of the existing theories, no violation of the loading criteria is the sufficient and necessary conditon for the true solution. For unstable softening, absurd solutions will be obtained by neglecting dynamic terms in statics. Such solutions violate the loading criteria. An extended Coulomb damping model is developed to better our understanding of finite element solution behavior. Although no incremental solution can be obtained for unstable softening, brittle models can be used to obtain acceptable solutions for engineering judgement. Theoretical eigenvalue analyses are presented. The obtained analytical expressions provide guides for correct use of material paramters, reveal the capacity of the adopted formulation to capture localized deformations and help explain solution behavior. Limitations of the adopted theories are also discussed.

The Carsington dam failure is back-analysed. New techniques are developed to locate the incipient slip surface in treating the results. The results are satisfactory and promising. This reveals the effectiveness of finite element methods in analysing the failure mechanism of complex engineering structures. However, accurate prediction of deformation needs further development of field investigation and laboratory test techniques. The definition of factor of safety is also discussed when strain softening is involved.

Studies on mesh design and iteration methods are also presented to guarantee reliable solutions. Most conclusions are problem dependent. However, the case history of the Carsington Dam failure is quite complicated. Therefore, conclusions from this case may be of general interest and helpful to similar engineering problems.

ACKNOWLEDGEMENTS

The author would like to express his gratitude to Dr. N. R. Morgenstern for his continuous and patient guidance in completing this thesis. His orientation, ideas and discussions throughout the research are very much appreciated.

The first three years of graduate study would not have been possible without the finacial support of the Institute of Water Conservancy and Hydro-electric Power, Beijing, China, nor would the completion of the thesis have been possible without the support of the Department of Civil Engineering, the University of Alberta. To the above sponsors the author is very much indebted.

The author would also like to express his thanks to Dr. D. H. K. Chan for his valuable suggestions and for his kind help in using and modifying the program SAGE which is the main tool in completing the numerical work.

The author is also grateful to professor Vaughan and Imperial College and to the Severn Trent Water Authority for providing material concerning the extensive work on the Carsington Dam failure. Without their generosity, this research would not have been possible.

Thanks are given to Dr. De Alancar for his permission to use the revised version of SAGE, in which, incremental pore pressure loads and cracking models are incorporated.

The author also wishes to thank his sister Li, brother Ming, his son Niuniu and all his other family members for

their encouragement and support for his study abroad. The love of the author's father Yusong and his spirit in pursuing knowledge have always been a source of strength during the research. Special thanks are given to his wife Xinsheng for her great understanding and endurance and for her typing the thesis.

Finally, the author wishes to dedicate this thesis to his beloved mother Liang Ju Zhu who died on 1st July 1986, but whose hope and wish have stimulated the author to overcome many obstacles in completing his graduate study.

Table of Contents

Chapter Page

1. INTRODUCTION 1

1.1 The Problem of Progressive Failure 1

1.2 Problems in Using Finite Element Analyses 5

1.3 Purpose of the Research and Scope of Each Chapter 7

2. FINITE ELEMENT FORMULATATION AND SOLUTION FOR STRAIN SOFTENING MATERIALS 12

2.1 General Formulation and Material Models 12

2.1.1 General formulation 12

2.1.2 Material models 20

2.1.3 Discussion of cracking models 25

2.2 Implications from Eigenvalue Analyses 29

2.2.1 General remarks 29

2.2.2 Correct use of material parameters 32

2.2.3 The weak direction 33

2.2.4 Capture of localized deformation 37

2.3 Study on Solution Behavior 39

2.3.1 Introduction 39

2.3.2 Mechanical model for diagonalized equilibrium equations 42

2.3.3 Solution behavior of the mechanical model .46

2.3.4 Solution behavior of the global equilibrium equations 54

2.4 Summary 60

3. ITERATION TECHNIQUES AND MESH DESIGN 63

3.1 Iteration Techniques for Material Nonlinearity ..64

3.1.1 Selection of iteration methods 64

3.1.2 Evaluation of effectiveness and efficiency 68

3.1.3 Improvement of iteration methods and result analyses 71

3.1.4 Conclusions on the iteration techniques ...86

3.2 Mesh Study 91

3.2.1 Basic requirements for mesh design 91

3.2.2 Objectives and methods of mesh study 94

3.2.3 Comparison of the results from different meshes 96

3.2.4 Conclusions and recommendations for mesh design 117

4. THE CARSINGTON DAM FAILURE 119

4.1 Introduction of the Carsington Dam Failure 119

4.1.1 Geology and construction 119

4.1.2 Properties of materials 126

4.1.2.1 Foundation 126

4.1.2.2 Yellow Clay 126

4.1.2.3 Core material 131

4.1.2.4 Zone I fill 134

4.1.2.5 Zone II fill 136

4.1.3 Pore pressure and deformation observation 138

4.1.4 Description of failure 142

4.2 Summary of Previous Reserach 151

4.2.1 Main conclusions 151

4.2.2 Brief comments on the previous work 154

4.2.3 Recommendations for further nonlinear analyses 160

5. DEFINING THE CARSINGTON DAM FAILURE FOR FINITE ELEMENT ANALYSES 162

5.1 Summary of Preliminary Numerical Studies 163
    5.1.1 Trial limit equilibrium analyses 163
    5.1.2 Trial finite element analyses 165
5.2 Defining the Boundary Problem for Back-analyses 178
    5.2.1 Feasibility of formulating the problem in plasticity 178
    5.2.2 Evaluating the pore pressure distribution 180
    5.2.3 Selecting suitable material models 186
    5.2.4 Determining material parameters 188
        5.2.4.1 Unit weight and strength parameter 188
        5.2.4.2 Poisson's ratio 189
        5.2.4.3 Elastic modulus 191
        5.2.4.4 Strain softening rate 193
6. ANALYSES OF THE CARSINGTON DAM FAILURE 198
6.1 Introduction 198
6.2 Techniques for Result Treatment 199
    6.2.1 Creating section 200
    6.2.2 Interpolation techniques 201
    6.2.3 Description of instantaneous movement 203
    6.2.4 Locating the critical slip surface 206
6.3 Results and Discussions 208
    6.3.1 The critical dam height 208
    6.3.2 Comparison of typical deformation and stress quantities 212
    6.3.3 The critical slip surface and failure mechanism 219
    6.3.4 Discussion of factors of safety 237
6.4 Parametric study 243

7. CONCLUSIONS 248

7.1 Conclusions 248

7.2 Recommendations 253

BIBLIOGRAPHY 256

A. APPENDIX - THE MOHR-COULOMB MODEL WITH HYPERBOLIC STRAIN SOFTENING 261

B. APPENDIX - ANALYTICAL EIGENVALUE ANALYSES 267

B.1 Eigenvalue Study on Elastic Constitutive Relationship 267

B.2 Eigenvalue Study on Perfect Elastoplastic Relationship 270

B.3 Eigenvalue Study on Elastoplastic Model with Strain Softening 273

B.4 The Impact of Strain Softening on the Global Stiffness Matrix 282

C. APPENDIX - SOLUTION OF THE ELASTICALLY CONNECTED COULOMB DAMPING MODEL 285

D. APPENDIX - APPLICATION OF BRITTLE MODELS TO UNSTABLE SOFTENING 295

E. APPENDIX - INCREMENTAL THEORIES CONCERNING MATERIAL STABILITY 302

E.1 Basic Assumptions 302

E.2 Quasi-static State 304

E.3 The Loading Criteria 307

E.4 The Principle of Potential Energy and the Uniqueness of Solution 311

F. APPENDIX - THE AITKEN ACCELERATION METHOD AND SPARSE QUASI-NEWTON LS & LDU UPDATES 317

F.1 The Newton-Raphson Iteration Method 317

F.2 The Aitken Acceleration Method 319

F.3 Sparse Quasi-Newton LS & LDU Updates 320

F.3.1 General update formulation 320

F.3.2 The DM method 323

F.3.3 The TZ method 325

G. APPENDIX - LIMIT EQUILIBRIUM ANALYSES 331

List of Tables

Table Page

2.1 Loading Criteria 17

3.1 Performance of the selected methods, elastoplastic materials under associated flow law 81

3.2 Performance of the selected methods, elastoplastic materials under the non-associated flow law 82

3.3 Performance of the selected iteration method for complex problems 83

3.4 Influence of the magnitude of load increments 85

3.5 Influnce of the convergence tolerance 87

3.6 Examples of the best iteration method in certain situations 88

3.7 Table 3.6 - continued 89

3.8 General performances of the selected iteration methods 92

3.9 Main features of the meshes 98

3.10 Comparison of main results of meshes with different density 99

3.11 Comparison of main results of different foundations 113

4.1 Materials at the dam site 124

4.2 Index properties 127

4.3 Reduction of factors of safety due to different factors 153

4.4 Factors of safety at different sections 154

5.1 Influence of some material parameters 163

5.2 Comparison of material models 167

5.3 Comparison of material parameters 169

5.4 Selected material models 187

5.5 Unit weight 189

Table Page

5.6 Strength parameters C' & Ø' 189

6.1 Factor of safety - effective stress analyses 238

6.2 Factor of safety - total stress analyses(a) 241

6.3 Factor of safety - total stress analyses(b) 241

C.1 Complete solution of displacements 289

C.2 Complete solution of node forces 290

C.3 Solution behavior 291

C.4 The first dynamic response of Coulomb damping model 294

G.1 Comparison between different methods 331

G.2 Influence of unit weight of Zone II 334

G.3 Influence of ϕ' in the Yellow Clay 334

G.4 Influence of average C_u 335

G.5 Operational undrained shear strengths 336

G.6 Comparison of different peak strengths 337

G.7 Factor of safety at EL. 198.0m 338

G.8 Upper and lower bounds of factors of safety 339

List of Figures

Figure Page

2.1 Loading criteria 18

2.2 Cracking model and corner problem 21

2.3 Orthogonally anisotropic model 23

2.4 Weak direction 34

2.5 Extended elastically connected Coulomb damping model 44

2.6 Solution of stable strain softening 47

2.7 Critical minus stiffness contribution 49

2.8 Comparison of frictional work 50

2.9 Dynamic paths of unstable softening 52

2.10 Brittle models for unstable softening 53

2.11 Unstable nonlinear softening 55

2.12 Solution behavior at each degree of freedom 57

3.1 Average computing time of Newton-Raphson iteration 70

3.2 Construction of an embankment 72

3.3 Convergence behavior of the modified N-R method (A) 74

3.4 Convergence behavior of the modified N-R method (B) 75

3.5 Convergence behavior of the TZ method 76

3.6 Convergence behavior of the DM method 77

3.7 Convergence behavior of the Aitken method 78

3.8 Comparison of different meshes 97

3.9 Mesh study - comparison of the maximum displacement 100

3.10 Mesh study - comparison of toe movements 102

3.11 Mesh study - comparison of horizontal displacements 103

Figure Page

3.12 Mesh study - comparison of vertical displacements 104

3.13 Mesh study - comparison of vertical strains 105

3.14 Mesh study - comparison of vertical stresses 107

3.15 Mesh study - very dense mesh - displacement vector increments 108

3.16 Mesh study - dense mesh - displacement vector increments 109

3.17 Mesh study - coarse mesh - displacement vector increments 110

3.18 Dense mesh with foundation simulated by an elastic layer 112

3.19 Study of meshes for foundation - comparison of the maximum displacement 114

3.20 Study of meshes for foundation - comparison of horizontal displacements 115

3.21 Study of meshes for foundation - comparison of vertical displacements 116

4.1 Plan of the Carsington scheme 120

4.2 Longitudinal profile of the Carsington Dam 121

4.3 Typical cross-section of the Carsington Dam 122

4.4 Peak shear strength 129

4.5 Post-peak behavior of intact Yellow Clay 130

4.6 Strength along solifluction shears and slip surfaces 132

4.7 Stress-displacement curves for the Yellow Clay 133

4.8 Post peak behavior of the core 135

4.9 Shear box drained test curves for Zone II fill 137

Figure Page

4.10 Piezometric readings prior to failure 139

4.11 Relation between fill height and piezometric height 140

4.12 Horizontal movement of the upstream face vs. time 143

4.13 Observed vertical strains and estimated horizontal displacements 144

4.14 Plan of the dam during failure 146

4.15 Sudden reduction of pore pressures after failure 148

4.16 Investigative section at CH 725 149

4.17 Investigative section at CH 825 150

4.18 Definition of safety factor 158

5.1 Geometry and mesh for CH 725 in the REPORT 166

5.2 Results in REPORT - displacement vector increments 172

5.3 Trial F.E.A.- vertical stress contour 174

5.4 Trial F.E.A.- peg movements 176

5.5 Trial F.E.A.- vertical strains in the core 177

5.6 Piezometric observation in Zone I fill 182

5.7 Typical piezometric line for the core and boot 185

5.8 Strain softening at point B in the Yellow Clay 196

5.9 Assumed post-peak strain softening rate for the Yellow Clay 197

6.1 Kinematically possible slip surface 204

6.2 Illustration of yield ratio along a slip surface 207

6.3 Finite element mesh for CH 725 209

Figure Page

6.4 Comparison of results of peg movements 210

6.5 Determination of the critical dam height 211

6.6 Results of total vertical stresses 213

6.7 Results of vertical displacements 215

6.8 Results of horizontal displacements 216

6.9 Comparison of results with observed data 218

6.10 Incremental displacement vectors - effective stress analyses 220

6.11 Determination of the critical slip surface - effective stress analyses 221

6.12 Illustration of stable deformation 223

6.13 Movement paths in successive loading steps 225

6.14 Yield status(a) along the critical slip - effective stress analysis 226

6.15 Yield status(b) along the critical slip surface - effective stress analysis 227

6.16 Comparison of the critical slip surfaces 229

6.17 Yield status along the observed slip surface - effective stress analysis 231

6.18 Incremental displacement vectors - total stress analyses 232

6.19 Determination of the critical slip surface - total stress analyses 234

6.20 Yield status along the observed slip surface - total stress analysis 235

6.21 Yield status along the critical slip surface - total stress analysis 236

6.22 The assumed pore pressure distribution along the observed slip surface 240

A.1 Hyperbolic strain softening model 262

B.1 Illustration of weak directions 281

Figure Page

C.1 One dimensional strain softening or hardening 288

D.1 Possible errors in using brittle models 298

D.2 Programming flow chart for unstable strain softening 301

E.1 Criteria for permissible solutions 309

E.2 The maxiumum potential energy 312

E.3 Strain softening in a body 314

G.1 Limit equilibrium analyses by Sarmar's method 332

1. INTRODUCTION

The thesis deals mainly with a systematic study of the application of nonlinear finite element methods to the analysis of progressive failure due to strain softening. As a case history, the Carsington Dam failure is back-analyzed. Practical applications of the results of the research are emphasized.

1.1 The Problem of Progressive Failure

Progressive failure is concerned with the failure of strain softening materials, in which localized failure due to non-uniform strains eventually leads to an unstable failure mechanism of a structure.

Strain softening behavior can be found in many rock, soil and concrete materials. Physically it may be caused by

1. dilation, e.g. in the dense sand;
2. unfavorable particle orientation, e.g. in a weak layer or by concentrated straining which starts from defects of materials;
3. bond break-down of rock bridge.

However, softening behavior may not be related to any of the above inherent physical reasons. For example, when a soil tested under the undrained condition, the strength after peak may decrease due to pore pressure effects, i.e. the decrease of effective stresses due to the increase of the pore pressures makes the undrained strength reduce to a lower shear stress level after peak.

The problem of progressive failure is of general significance, since strain softening behavior can be found in many engineering problems. Whenever strain softening is involved, solutions of bearing capacity, excavation, dam construction and stability of natural slopes, etc. depend on our understanding of this topic.

The sudden failure of the Carsington Dam, an earth-rockfill dam in England, in 1984, has attracted wide attention. The observation during failure and intensive field investigation and laboratory tests after failure have indicated that this was a typical progressive failure problem due to strain softening. Since abundant observed data are available, the case history is valuable for a methodological study of the application of finite element analyses.

Only a brief literature review is given below. More detailed discussion of progressive failure was presented by Chan (1986). Skempton (1964) pointed out the importance of non-uniform mobilization of shear strength along slip surfaces and raised the concept of residual factor to describe the reduction of strength due to strain softening. Bjerrum (1967) outlined the basic mechanism of progressive failure due to softening. He listed three conditions:

1. non-homogeneous strain development with localized straining sufficient to strain the soil beyond the failure;
2. distinct strain softening behavior characterized by

rapid decrease in strength after peak;

3. shear stresses have reached the peak along a continuous slip surface.

Time effects are not a necessary condition for progressive failure. This distinguishes progressive failure defined above from the delayed failure, in which pore pressure redistribution or bond degradation with time may cause failure. No doubt, time effects can create favorable conditions for progressive failure. However, as observed in the field and shown by back-analyses, the case history of sudden failure of the Carsington Dam was promoted mainly by strain softening. The research concentrates on this aspect and no time effects are considered.

Bishop (1967) raised the concept of brittleness index to measure the amount of strain softening and recognized the importance of localized deformations or shear bands caused by strain softening during the developement of progressive failure. Morgenstern and Tchalenko (1967) observed real shear bands by means of microscopic techniques.

Theoretical studies, limit equilibrium methods and finite element methods have all been applied to further an understanding of progressive failure and shear band.

Palmer and Rice (1973) used the concept of J-integral and stress intensity factor to formulate a criterion for shear band propagation in a one dimensional case. Theoretical work can help explain the initiation and propagation of progressive failure, but cannot be used directly for real complex situations.

By assuming that strength decrease to the residual immediately after peak, limit equilibrium methods were used to analyse progressive failure (Law and lumb, 1978). Obviously, the so-determined limit load or factor of safety may be too conservative and the slip surface must be assumed before analyses. The method cannot reflect the true strength reduction between the peak and residual, since it neglects non-uniform straining.

Finite element analyses can follow the developement of a non-homogeneous strain field and have been proved to be the most effective means for complex engineering problems. Hyperbolic elastic models (Lo,1972) were used to simulate bifurcation in the shear band and pseudo-elastic models (Gates, 1972) were also used. The elastic bifurcation models may not be appropiate for many real problems, since structures often behave elastoplastically. In his Ph.D. thesis, Chan (1986) studied the possibility of simulating localized deformations by using elastoplastic models and reported on the effectiveness of finite element analyses in tackling real engineering problems. His research revealed promising directions. The Carsington Dam was also analysed by using elastoplastic models (Babtie and Skempton, 1985). Only total stress analyses were carried out and the results merit re-evaluating. By experience, the finite element analysis based on the theory of plasticity can find wide applications in practice. It has been chosen as the main tool in this research.

1.2 Problems in Using Finite Element Analyses

The proper application of finite element analyses to a complicated engineering problem includes:

1. to define the problem within the scope of appropriate theories in solid machanics;
2. to choose suitable material models and reliable material parameters in describing material behavior;
3. to design a mesh with suitable density in order to guarantee accuracy and limit computation costs;
4. to use sufficiently small load increments, effective iteration methods and suitable convergence criteria to simulate nonlinear stress and strain paths both in view of the required accuracy and in view of the available computation budget;
5. to check the reliability of the results by parametric studies since the input information, especially that related to deformation, is not reliable enough in most cases;
6. to interpret the results correctly for practical use.

It is easy to understand that any mistake or carelessness in the above complicated procedures may lead to serious difficulties in computation, wrong solution or misuse of results. Experience needs to be accumulated to work out quidelines.

When the constitutive relationship including the strain softening is adopted, two important problems merit attention. The first one is related to the fundamental theory. Due to violation of Drucker's material stability postulates, negative diagonal elements in the global stiffness matrix may be encountered, which may lead to a totally absurd solution. For example, if a strain softening curve of a sample test is simulated with finite element methods, it is well known that the correct answer for the post-peak behavior can be obtained only from displacement controlled boundary conditions. If external loads are further applied in the softening direction, numerical solutions can still be obtained but they are totally absurd. Unlike simple examples, absurd solutions may be very difficult to find for a complicated problem involving complex loading and unloading strain-stress paths. Therefore, a study of the solution behavior is of great importance. Both theory and practical methods to cope with such complex situations have not been well studied up to now.

The second problem is related to practical use. In designing embankments or dams or studying the stability of a slope, engineers need a conventional factor of safety, which is obtained from limit equilibrium analyses. With strain softening involved, the choice of correct strength parameters needs the strain distribution along the slip surface, which can be provided by the finite element analyses. However, experience is limited in determining and using the so-determined factor of safety.

In short, no guidlines are availble for solving such a complex engineering problem. There is a long way to go before engineers can comfortably use finite element analyses in design with confidence. Therefore, a systematic and methodological study from theory to practice is undoubtedly necessary.

At present, nonlinear finite element analyses are expensive and time-consuming. Besides, field investigation and laboratory tests generally cannot provide sufficient and reliable information for accurate prediction of deformations. These two reasons also limit the application of finite element analyses. However, with the advance of science and technology, the future of finite element methods is promising.

1.3 Purpose of the Research and Scope of Each Chapter

The main purpose of this thesis is to enhance the applicability of finite element analyses to progressive failure due to strain softening in complex engineering problems.

In order to achieve this goal, attempts have been made to complete the fundamental theories concerning the theoretical eigenvalue analyses of elastoplastic constitutive relationships and to study the solution behavior involving negative stiffness. For practical use, experience has been gained with mesh design, selection of iteration methods and choice of convergence criteria. Examples have been presented to give a detailed description of how to define the problem by appropriate finite element formulations and how to choose suitable material models and evaluate the reliability of material parameters. New techniques for treatment of results have been developed to interpret the failure mechanism and locate the slip surface. The failure of the Carsington Dam chosen as the case history for back-analysis is complex enough to make conclusions and gain experience of general significance.

The procedures for the application of nonlinear finite element analyses are complicated and there are flexible options in designing mesh, using formulations, choosing models and adopting iteration methods. Therefore, it is not practical in a simple thesis to work out general guidelines. The author hopes that the conclusions and experiences reported here will make successors less confused in following the complicated precedures and more confident in using the results.

The finite element program used for the analyses was the program "Stress Analysis in Geotechnical Engineering" (SAGE) developed by Chan (1986) and revised by De Alencar (1988). To cope with the task of the research, the program has been further modified by adding the selected iteration methods (Chapter 3), anisotropic models and different models for cracks (Chapter 2). Other auxiliary programs for treatment of input data and results have also been compiled to check the input data, renumber the mesh with an optimized stiffness matrix length and to help interpret the results by plotting.

The thesis is divided into seven chapters. Chapter 2 presents a general finite element formulation, describes main conclusions and implications of the theoretical eigenvalue analysis and discusses the solution behavior involving negative stiffness.

Theoretically speaking, the eigenvalue analysis and the study of solution behavior are indispensable parts for a complete theory of plasticity and its finite element formulation. In the research, both analytical eigenvalue analyses and theoretical study of solution behavior were carried out within the scope of the incremental theory and practical approaches were also suggested to guarantee a reasonable solution for any complex problem with negative stiffness inside the body.

In editing Chapter 2, effort was made to obtain clarity and conciseness. As a result, only the main conclusions are introduced. The derivation and theoretical discussion are given in appendices, although there are original ideas and newly-developed expressions. Firstly, this is because the derivation and expression of eigenvalues and eigenvectors are long and complicated. Secondly, no negative diagonal element is found in analysing the case history. Therefore, the importance of the study of solution behavior is mainly on the theoretical side. Generally speaking, a positive definite stiffness matrix can often be quaranteed in simulating the response of a real man-made structure from low loading level before failure, since the existence of the structure implies inherent material stability. However, this does not imply that the theoretical study is less important. At least, one should answer the question whether the solution is abnormal or not before one uses the the results in analysing progressive failure. In the future, when a badly-designed dam is checked, parametric studies are carried out or post-failure behavior is simulated, it is possible that indefinite global stiffness matrices may be encountered.

In Chapter 3, a mesh study and comparison of iteration methods are presented to ensure sufficiently accurate results and to limit the computation budget within an acceptable range.

The case history of the Carsington Dam failure is introduced in Chapter 4. The previous work on the case history is described in detail in a report " Carsington Dam - the Mechanism of Failure ", which is issued by the Severn Trent Water Authority (Babtie and Skempton, 1986). For brevity, we call this report as the " REPORT ", since its contents will be quoted frequently. Proprosals for further analyses are raised by summarizing and reviewing the previous work.

In Chapter 5, the Carsington Dam failure is defined for finite element analyses. Each link which might affect the reliability of the results is examined and discussed. The results from trial limit equilibrium and finite element analyses are also used to define the problem as clearly and reasonably as possible.

Chapter 6 presents the results and discussions from both total and effective stress analyses. New techniques are introduced to help determine the slip surface. The approaches to determine the factor of safety with strength reduction due to strain softening are also discussed.

Conclusions and recommendations for further research are listed in Chapter 7.

2. FINITE ELEMENT FORMULATATION AND SOLUTION FOR STRAIN SOFTENING MATERIALS

2.1 General Formulation and Material Models

2.1.1 General formulation

The finite element formulation for elastoplastic models including strain softening is based on the theory of plasticity. A good summary of this topic can be found in Chan (1986). However, the basic assumptions and equations will be reviewed below.

The basic equations in finite element analyses are the global equilibrium equations with the nodal displacements as unknown variables. In incremental form (Bathe, 1983), we have

$$[K]\{\Delta u\} = \{\Delta R\} , \qquad (2.1)$$

in which

$\{\Delta u\}$, is the incremental displacement vector;

$[K]$ is the global stiffness matrix, with

$$[K]=\int_v [B]^T[C^{EP}][B]dv , \qquad (2.2)$$

where

$[B]$ is the geometry matrix and $[C^{EP}]$ is the elastoplastic matrix. The integration is with respect to

the whole volume of the body under consideration;
$\{\Delta R\}$ is the incremental nodal force vector, and

$$\{\Delta R\} = \int_v [N]^T\{\gamma\}dv + \int_{St}[N]^T[N]\{P\}ds \ , \tag{2.3}$$

where

$[N]$ = interpolation function matrix,

$\{\gamma\}$ = body force vector,

$\{P\}$ = nodal surface traction vector,

s_t = surface subjected to external traction.

Although there is no special requirement for any correct constitutive relationship in using the equations, the existence of the minimum potential energy and uniqueness of the solution require material stability as the sufficient condition. By Drucker's definition (1956), the condition for stability in the large is

$$(\sigma_{ij}-\sigma_{ij}^{o})d\epsilon_{ij}^{P} > 0 \ , \tag{2.4}$$

and for stability in the small is

$$d\sigma_{ij}\ d\epsilon_{ij}^{P} \geq 0 \ , \tag{2.5}$$

where

σ_{ij} is the current state of stress,

σ_{ij}^{o} is the stress state on the yield surface,

$d\sigma_{ij}$ is the increment of stress,

and $d\epsilon_{ij}^{P}$ is the increment of plastic strain.

By introducing strain softening constitutive relationships into the analysis, inequality (2.4) may be violated and inequality (2.5) will definitely be violated. However, the above stability conditions are only sufficient conditions. Therefore, on the one hand we may still be able to obtain the true solution with strain softening involved, but, on the other hand, absurd solutions may also be found.

According to the theory of plasticity, the constitutive relationship can be derived with the following assumptions:

1. The total strain increment is divided into elastic and plastic strain increments, i.e.

$$\{d\epsilon\} = \{d\epsilon^{E}\} + \{d\epsilon^{P}\} \ . \tag{2.6}$$

2. The change in stress is due to change in elastic strain alone, i.e.

$$\{d\sigma\} = [C^{E}]\{d\epsilon^{E}\} \ , \tag{2.7}$$

where

$[c^{E}]$ is the elastic constitutive matrix.

By eqn. 2.6 and 2.7, the elastic and plastic stress increments are defined as

$$\{d\sigma^{E}\} = [C^{E}]\{d\epsilon\} \ , \tag{2.8}$$

$$\{d\sigma^P\} = \{d\sigma^E\} - \{d\sigma\} , \qquad (2.9)$$

3. There exists a plastic potential Q such that

$$\{d\epsilon^P\} = \lambda\{\frac{dQ}{d\sigma}\} , \qquad (2.10)$$

where

λ is positive for plastic deformations,

4. There exists a yield function F with the consistency condition:

$F(\sigma_{ij}, \epsilon^P_{ij}) > 0$ is not permissible,

$F(\sigma_{ij}, \epsilon^P_{ij}) = 0$ for yielding state,

$F(\sigma_{ij}, \epsilon^P_{ij}) < 0$ for elastic state. (2.11)

5. The incremental stress and strain path is defined by the loading criteria, which constitutes an essential part of the theory of plasticity as described below.

All the possible stress and strain paths can be classified from the present stress and strain state as elastic ($F<0$) and yielding ($F=0$). Then, for the yielding state, they can be further sub-classified as loading, neutral loading and unloading in the next incremental step. Physically, loading indicates that the plastic strain continues to increase in the yielding condition, neutral loading indicates that the plastic strain increment is zero but the yielding condition does not change, and unloading indicates that the stress state goes back to the elastic state. Note that the word "loading" is referred to plastic deformation, not to external loads. We use the expressions in the paper of Qu and Yin (1981) to define loading criteria. If the yield function are described in both stress and strain spaces (Fig. 2.1), i.e.

$$f(\{\epsilon\},\ \{\epsilon^P\}) = F[[C^E](\{\epsilon\}-\{\epsilon^P\}),\ \{\epsilon^P\}]\ , \tag{2.12}$$

in which, f is the yield function in the strain space. We choose

$$l_1 = <\frac{\partial f}{\partial \epsilon}>\{d\epsilon^E\} = <\frac{\partial F}{\partial \sigma}>\{d\sigma\}\ , \tag{2.13}$$

$$l_2 = <\frac{\partial f}{\partial \epsilon}>\{d\epsilon\} = <\frac{\partial F}{\partial \sigma}>\{d\sigma^E\}\ , \tag{2.14}$$

$$l_3 = <\frac{\partial f}{\partial \epsilon}>\{d\epsilon^P\} = <\frac{\partial F}{\partial \sigma}>\{d\sigma^P\} \tag{2.15}$$

as the standard. Equations 2.7 to 2.9 show that they are not independent and

$$l_2 = l_1 + l_3\ . \tag{2.16}$$

The criteria associated with l_1, l_2 and l_3 are listed in Table 2.1. The importance of the loading criteria lies not only in the correct choice of constitutive relationship but also in the determination of unstable softening (Section 2.3.4).

Table 2.1 Loading Criteria

	l_1			l_2	l_3
	Hardening	Perfect	Softening		
Loading	> 0	$= 0$	< 0	> 0	> 0
Neutral	$= 0$	$= 0$	$= 0$	$= 0$	$= 0$
Unloading	< 0	< 0	< 0	< 0	$= 0$

From Table 2.1, it can be seen that a rigorous classification can be given independently only by using l_2. For convenience l_1 and l_3 can also be used. Both l_1 and l_2 possess clear geometrical meaning in stress and strain spaces as shown in Fig. 2.1.

The reason why we list these criteria as basic assumptions is that, in establishing these criteria, besides other basic assumptions, the yield function is assumed to expand in the strain space whenever plastic strains are developing. We do not study the material behavior which violates this assumption.

Based on the above assumptions, we can obtain the elastoplastic constitutive relationship in matrix form as

$$[C^{EP}] = [C^{E}] - \frac{[C^{E}]\{\partial Q/\partial \sigma\}<\partial F/\partial \sigma>[C^{E}]}{<\partial F/\partial \sigma>[C^{E}]\{\partial Q/\partial \sigma\} - <\partial F/\partial \epsilon^{P}>\{\partial Q/\partial \sigma\}} . \qquad (2.17)$$

The first term of the denominator in the above equation reflects perfectly plastic deformation and the second term

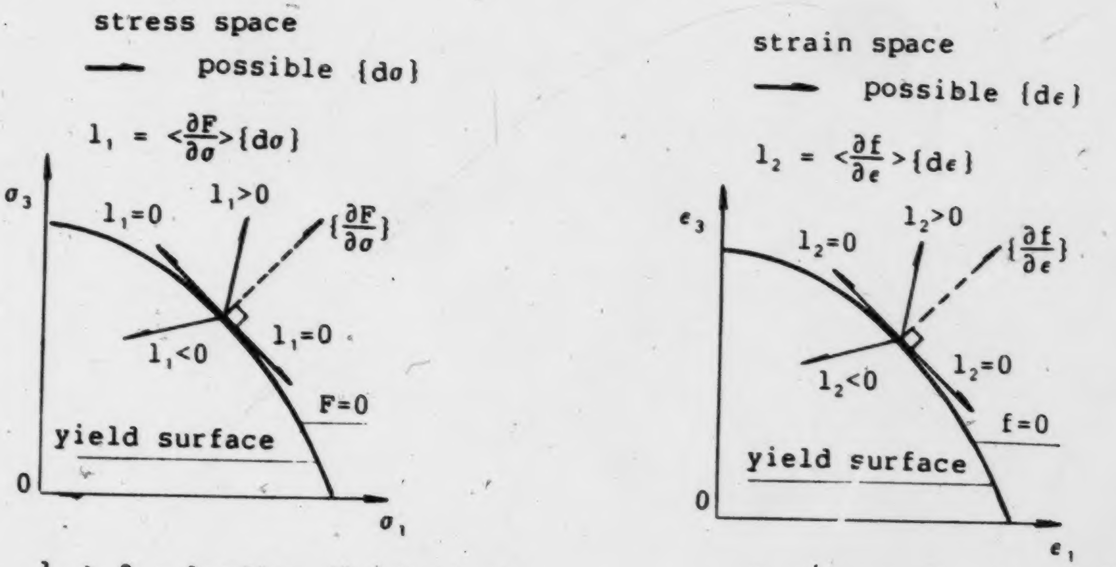
stress space
possible {dσ}
$1_1 = <\frac{\partial F}{\partial \sigma}>\{d\sigma\}$
σ3
1_1=0
1_1>0
$\{\frac{\partial F}{\partial \sigma}\}$
1_1<0
1_1=0
F=0
yield surface
0
σ1
strain space
possible {dε}
$1_2 = <\frac{\partial f}{\partial \epsilon}>\{d\epsilon\}$
ε3
1_2=0
1_2>0
$\{\frac{\partial f}{\partial \epsilon}\}$
1_2<0
1_2=0
f=0
yield surface
0
ε1

$1_1 > 0$: loading (hardening)
$1_1 = 0$: loading (perfect)
and neutral loading
$1_1 < 0$: loading (softening)
and unloading

$1_2 > 0$: loading
$1_2 = 0$: neutral loading

$1_2 < 0$: unloading

Figure 2.1: Loading criteria

reflects strain hardening (or softening) deformation. When the yield function is expressed in the conventional form:

$$F = F(\{\sigma\}, \{\epsilon^P\}, \kappa) , \tag{2.18}$$

the second term $<\frac{\partial F}{\partial \epsilon^P}> \{\frac{\partial Q}{\partial \sigma}\}$ becomes

$$<\frac{\partial F}{\partial \epsilon^P}> \{\frac{\partial Q}{\partial \sigma}\} = <\frac{\partial F}{\partial \epsilon^P}> \{\frac{\partial \epsilon^P}{\partial \sigma}\} + \frac{\partial F}{\partial \kappa}<\frac{\partial \kappa}{\partial \epsilon^P}>\{\frac{\partial Q}{\partial \sigma}\} , \tag{2.19}$$

where the first term represents kinematic hardening and the second term represents isotropic hardening.

If a singularity exists at the intersection of two or more different functions in the stress space, the direction of the plastic strain $\{\epsilon^P\}$ cannot be determined uniquely. This is called the corner problem (Christoffersen and Hutchinson 1979). One conventional approach is to assume that the plastic strain increment is the average of those from either side of a corner. In this research, for corners defined by two different yield criteria (F_1 and F_2) with two corresponding potential functions (Q_1 and Q_2), we use another conventional assumption that:

$$\{d\epsilon^P\} = [\{\frac{\partial Q_1}{\partial \sigma}\} \ \{\frac{\partial Q_2}{\partial \sigma}\}] <\lambda_1 \ \lambda_2>^T . \tag{2.20}$$

By experience, this assumption is convenient to use for the corner of the tension criterion and frictional yield criterion (e.g. the Mohr-Coulomb criterion). Its physical meaning is that the plastic strain incremental vector is the resultant of those defined by the two different potential functions, as shown in Fig. 2.2.

Now, we have an additional unknown number λ_2 in the assumption (eqn. 2.20) as compared with equation 2.10. However, we have an additional equation ($F_2=0$). The elastoplastic matrix can be obtained as

$$[C^{EP}] = [C^E] - [C^E][\{\frac{\partial Q_1}{\partial \sigma}\} \ \{\frac{\partial Q_2}{\partial \sigma}\} \ ][D]^{-1}[\{\frac{\partial F_1}{\partial \sigma}\} \ \{\frac{\partial F_2}{\partial \sigma}\} \ ]^T[C^E], \tag{2.21}$$

in which, -1 is for the inverse and

$$[D] = \Big[[\{\frac{\partial F_1}{\partial \sigma}\} \ \{\frac{\partial F_2}{\partial \sigma}\} \ ]^T[C^E][\{\frac{\partial Q_1}{\partial \sigma}\} \ \{\frac{\partial Q_2}{\partial \sigma}\} \ ] - [\{\frac{\partial F_1}{\partial \epsilon^p}\} \ \{\frac{\partial F_2}{\partial \epsilon^p}\} \ ]^T[\{\frac{\partial Q_1}{\partial \sigma}\} \ \{\frac{\partial Q_2}{\partial \sigma}\} \ ]\Big] \ . \tag{2.22}$$

It is easy to extend the above expression for the situations where three yield functions intersect with each other.

2.1.2 Material models

Failure in earth materials is due to shear but cracks may also form. In this research, the Mohr-Coulomb criterion with hyperbolic strain softening rate is used for effective stress analyses. The von-Mises criterion with hyperbolic strain softening is adopted for total stress analyses. Tension criteria with respect to principal stresses are also

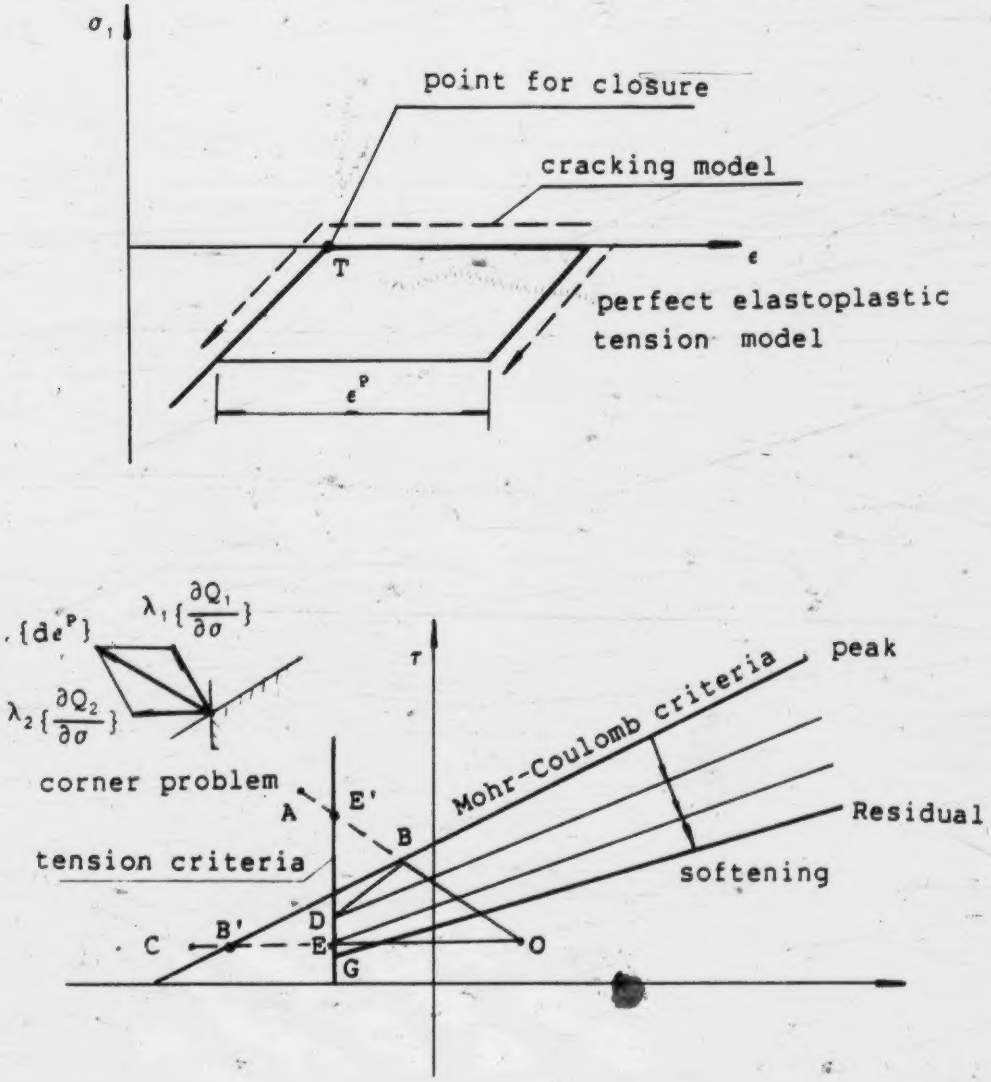
σ_1
point for closure
cracking model
T
ϵ
perfect elastoplastic tension model
ϵ^P
$\{d\epsilon^P\}$
$\lambda_1\{\frac{\partial Q_1}{\partial \sigma}\}$
$\lambda_2\{\frac{\partial Q_2}{\partial \sigma}\}$
τ
peak
Mohr-Coulomb criteria
corner problem
A
E'
B
Residual
tension criteria
softening
D
C
B'
E
O
G

Figure 2.2: Cracking model and corner problem

used to simulate cracking failure. The pore pressure distribution in effective analyses is taken from the observed data. The reason for the model selections and determination of material paremeters will be given in detail in Chapter 5 after introducing the Carsington Dam failure. Most of the specific expressions of the above models can be found in the theses of Chan (1986) and de Alancar (1988). In order to analyse the case history, supplementary work has been undertaken.

In introducing softening behavior into the Mohr-Coulomb model, similar hyperbolic functions to those adopted by Chan are used both for the friction angle ϕ and the cohesion C. The derivation is straightforward as given in Appendix A.

An orthogonally anisotropic model of the Mohr-Coulomb type as expressed in the local coordinate system r-s-t in Fig. 2.3 is useful to capture shear bands in materials with oriented weak directions and to investigate the influence of the horizontal deformation modulus in parametric studies. Its elastic behavior depends on five parameters E_1, E_2, ν_1, ν_2 and G_2 as marked in Fig. 2.3. Before peak, we have

$$<\sigma_r \ \sigma_s \ \sigma_t \ \tau_{st} \ \tau_{tr} \ \tau_{rs}>^T = [C^E]_{ani}<\epsilon_r \ \epsilon_s \ \epsilon_t \ \gamma_{st} \ \gamma_{tr} \ \gamma_{rs}>^T \ ,$$

and $[C^E]_{ani}$ takes the form:

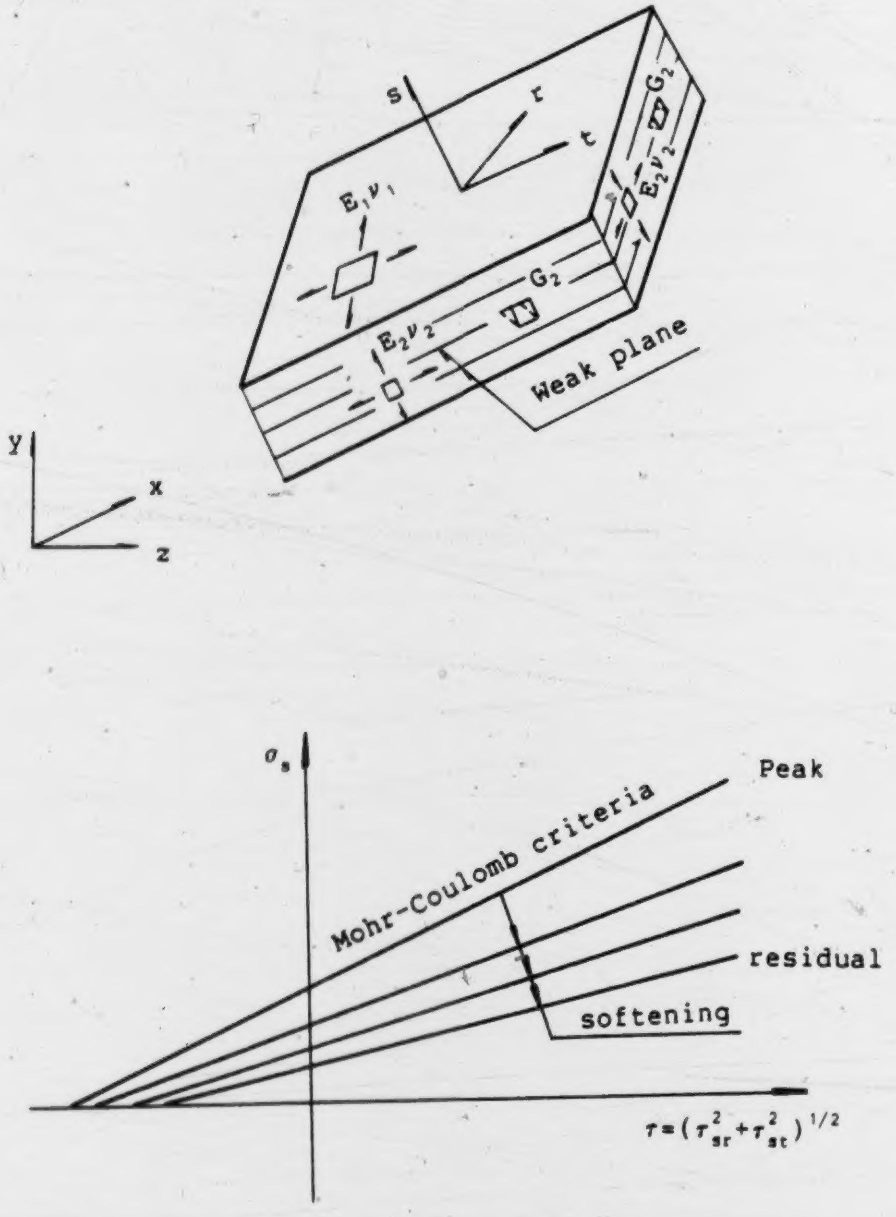
s
r
t
G_2
$E_2\nu_2$
$E_1\nu_1$
G_2
$E_2\nu_2$
Weak plane
y
x
z
σ_s
Peak
Mohr-Coulomb criteria
residual
softening
$\tau=(\tau_{sr}^2+\tau_{st}^2)^{1/2}$

Figure 2.3: Orthogonally anisotropic model

$$E_2/\beta \begin{bmatrix} n(1-n\nu_2^2) & n\nu_2(1+\nu_1) & n(\nu_1+n\nu_2) & 0 & 0 & 0 \\ & 1-\nu_1^2 & n\nu_2(1+\nu_1) & 0 & 0 & 0 \\ & & n(1-n\nu_2^2) & 0 & 0 & 0 \\ & & & m\beta & 0 & 0 \\ & & & & n\beta/2(1+\nu_1) & 0 \\ & & & & & m\beta \end{bmatrix}$$

in which

$\beta = (1+\nu_1)(1-\nu_1-2n\nu_2^2)$,

$n = E_1/E_2$,

$m = G_2/E_2$.

(2.23)

The yield and potential functions are

$$F = (\tau_{sr}^2+\tau_{st}^2)^{1/2} + \tan\phi\sigma_s - C \ , \tag{2.24}$$

$$Q = (\tau_{sr}^2+\tau_{st}^2)^{1/2} + \tan\psi\sigma_s - C \ , \tag{2.25}$$

with

$$\frac{\partial F}{\partial \sigma} = \left< 0,\ \tan\phi,\ 0,\ \frac{\tau_{st}}{(\tau_{sr}^2+\tau_{st}^2)^{1/2}},\ 0,\ \frac{\tau_{rs}}{(\tau_{rs}^2+\tau_{st}^2)^{1/2}} \right> \ , \tag{2.26}$$

$$\frac{\partial Q}{\partial \sigma} = \left< 0,\ \tan\psi,\ 0,\ \frac{\tau_{st}}{(\tau_{sr}^2+\tau_{st}^2)^{1/2}},\ 0,\ \frac{\tau_{rs}}{(\tau_{rs}^2+\tau_{st}^2)^{1/2}} \right> \ . \tag{2.27}$$

For strain softening, it can be derived that

$$\frac{\partial F}{\partial \bar{\epsilon}^p} = \frac{a_c c_p}{(a_c + b_c \bar{\epsilon}^p)^2} - \frac{\sec\phi^2 a_\phi \phi_p}{(a_\phi + b_\phi \bar{\epsilon}^p)^2} , \qquad (2.28)$$

where the notations can be found in eqn. A.10 and A.14, Appendix A.

$$\bar{Q} = \frac{\sqrt{2}}{\sqrt{3}}\left(\frac{\tau_{sr} + \tau_{st}}{\tau_{sr}^2 + \tau_{st}^2} + \frac{2}{3}\tan\phi^2 \right)^{1/2} . \qquad (2.29)$$

With the above expressions, the elastoplastic matrix can be calculated from the general equation 2.17. Note that transformation from the local to global coordinate system is needed for the elastoplastic matrix of anisotropic models.

Failure across the layer may occur and is treated by using the isotropic yield criteria. Along the weak layer, the strength is reduced due to pre-shears while no reduction of strength is considered across the weak plane. In calculations, the failure along the weak layer is checked first. If no failure occurs, isotropic yield is then checked across the layer.

2.1.3 Discussion of cracking models

The slow convergence speed is well known when the stress tranfer method (Zienkiwicz, 1968) is used to eliminate tensile stresses for no tension materials. In the thesis of De Alencar (1988), improved cracking models have been adopted. The cracking models were originally established for concrete materials in plane analyses (Chen and Suzuki, 1980). In fact, we can obtain the constitutive relation of the cracking model easily by using the general equations 2.17 and 2.21. For one crack ($F=Q=\sigma_1$), the constitutive relation after cracking is

$$\begin{bmatrix} d\sigma_1 \\ d\sigma_3 \end{bmatrix} = E/(1-\mu^2)\begin{bmatrix} 0 & 0 \\ 0 & 1 \end{bmatrix} \begin{bmatrix} d\epsilon_1 \\ d\epsilon_3 \end{bmatrix} \tag{2.30}$$

and for two cracks ($F_1=Q_1=\sigma_1$ and $F_2=Q_2=\sigma_2$),

$$\begin{bmatrix} d\sigma_1 \\ d\sigma_2 \end{bmatrix} = E/(1-\mu^2)\begin{bmatrix} 0 & 0 \\ 0 & 0 \end{bmatrix} \begin{bmatrix} d\epsilon_1 \\ d\epsilon_2 \end{bmatrix} \tag{2.31}$$

By using transformation, it is easy to obtain the formulations in which $<d\sigma_x \ d\sigma_y \ d\tau_{xy}>$ and $<d\epsilon_x \ d\epsilon_y \ d\gamma_{xy}>$ are used. Note that the above expressions are the same as those derived in De Alencar's or Chen's works.

Let us call the model derived from the general formulation as the perfect elastoplastic tension model. For this model, loading criteria still hold during unloading. Therefore, when the stress changes from tension to compression, restoration of the elastic modulus is assumed to be immediate, but the opening still exists because the plastic strain due to tension is not recoverable under the basic assumptions. The strain-stress path is shown in Fig. 2.2. The results confict with common sense, since the stiffness cannot resume its original value immediately if openings exist. The developers of the cracking model try to follow another strain-stress path (Fig. 2.2), and so use the criterion in the strain space to seek the point where a crack just closes. Before it closes, the elastoplastic relation still holds, and, after it closes, the original stiffness (or with a certain reduction) will be resumed. Theoretically speaking, this is more reasonable.

In practical use, it is often not easy to find the closing point. Due to the adoption of criteria defined in both stress and strain spaces, very complex iteration procedures are required. De Alencar (1988) gave a complete formulation for computer programming and discussed the iteration problems. In his opinion, the only way to solve the iteration problem is to use as small as possible an incremental load. However, small load increments may not work when the structure is near failure in a complex practical problem. If the materials are brittle, no matter how small the load increment is, excess stresses of finite magnitude will be released and the solution may oscillate between tension and compression. To seek the closing point requires modification of stiffness at every iteration. Any approximate solution will bring appreciable errors due to the large difference between the stiffness before and after closing. Solution by trial and error is often too expensive to be practical. But, such an unfavorable situation only appears when the structure is near failure. At lower loading stages, the cracking model is reasonable and efficient. It is suggested that the perfect elastoplastic tension model be used near failure for the whole incremental loading step, since it is reasonable to assume no healing of cracks at this stage. Obviously, it will be very efficient for iterations.

If one crack develops in an element, the material is, in fact, in a uniaxial loading condition in the direction parallel to the crack. Therefore, the shear strength is only provided by the cohesion. Unlike concrete, soils generally possess very small amounts of cohesion. Frictional yield criteria must be introduced, otherwise, unreasonable results are inevitable. If the Mohr-Coulomb criterion is adopted, the elastoplastic matrix can be derived from the general expressions (eqn. 2.21 and 2.22). For example without softening,

$$[C^{EP}] = [0] \ . \tag{2.32}$$

This implies that no more load can be supported by the soil, and reflects the true situation in a uniaxial loading condition.

Proper techniques should be used to force the stress state to satisfy the consistency condition of $F=0$, if the calculated stress level is outside both yield surfaces as shown in Fig. 2.2. Strictly speaking, both yield functions should be tried in determining the correct yielding point (B or E) intersected by the stress increment with one of the two yield functions. Otherwise, the wrong point (B' or E') will be obtained. The correct stress path for vector OA is OBD, for OC is OE (Fig. 2.2). After the correct point is found, integration techniques for the correct stress path can be found in the literature (e.g. Chan 1986). There is no need to repeat them.

Another simplified method to treat the corner problem is to force the stress state A (Fig. 2.2) to decrease to point G (the intersection of the tension failure surface with the residual Mohr-Coulomb yield surface), then release excess stresses and assume the elastoplastic matrix to be near zero. This method is not only efficient but also reasonable for soils. Mathematically, the error will not be large with a small value of cohesion, and the results will be on the safe side.

2.2 Implications from Eigenvalue Analyses

2.2.1 General remarks

The importance of the eigenvalue analysis on the constitutive relationship of materials has been raised with the development of the localized deformation theories, including the study of bifurcation and discontinuity relations in solid mechanics. In this research, the eigenvalue study will be carried out only on elastoplastic constitutive relationships. According to the localized deformation theories, the development of a shear band may be considered as an instability in the constitutive relationship of a material. A general review of the relevent basic theories was given by Chan(1986).

The instability of materials is defined by the non-positive definite constitutive relationship tensor. In matrix form, it is equivalent to the condition

$$<\Delta\epsilon>[C^{EP}]\{\Delta\epsilon\} \leq 0 \ , \tag{2.33}$$

for at least one non-zero strain tensor in the vector form $\{\Delta\epsilon\}$. In the incremental theory, the strain and stress follow a linear path in each incremental loading step, i.e.

$$\{\Delta\sigma\} = [C^{EP}]\{\Delta\epsilon\}.$$

Hence, the above condition is equivalent to the condition in terms of the perturbation energy in a unit volume, which is defined as

$$\frac{dW_{pert}}{dV} = <\Delta\sigma>\{\Delta\epsilon\} = <\Delta\epsilon>[C^{EP}]\{\Delta\epsilon\} \ . \tag{2.34}$$

The perturbation energy is a measure of stability of the materials under certain external disturbance conditions corresponding to the constitutive relationship $[C^{EP}]$.

The positive definite nature of the perturbation energy is well known for elastic and strain hardening materials. For perfect plasticity and strain softening, the specific perturbation energy will be zero or negative for at least one non-zero $\{\Delta\epsilon\}$, since $[C^{EP}]$ has zero (perfect elastoplastic) or negative eigenvalues (strain softening). The corresponding eigenvector defines a weak direction. For the strain along the weak direction, no external work will be needed (for zero eigenvalue) or even excess elastic energy will be released (for negative eigenvalue) under a disturbance. The latter case implies the possibility of progressive failure. In a quasi-static process, the load increment is arbitrarily small and applied extremely slowly. If the released energy due to failure cannot be consumed by the internal friction in an element itself, this element will be unstable and more elastic energy will be released due to softening. Further, if the excess energy cannot be dissipated or absorbed by surrounding materials, a series of unstable softening movements will be triggered and the movement will be spontaneously accelerated. When this process has developed in the macro dimension, progressive failure can be observed and may lead to the complete collapse of a structure. This may happen even if a disturbance is infinitesimal and acts only for an arbitrarily short time length. Therefore, the eigenvalue analysis is of great importance both to theoretical study and to practice.

Numerical tests have been carried out on this aspect (Chan, 1986). In this research, general analytical eigenvalue analyses will be presented with respect to elastoplastic constitutive relationships in terms of elastic parameters and gradients of yield and potential functions in the principal stress space. Derivations of analytical expressions of eigenvalues and eigenvectors are long and complicated as given in Appendix B. In this section, only the contributions to this research will be described.

2.2.2 Correct use of material parameters

Absurd solutions were obtained in parametric studies when anisotropic models were used in plane strain conditions to investigate the influence of the horizontal deformation modulus. Later, it was found that the elastic matrix was not positive definite due to an inappropriate use of the material parameters E_1, E_2, ν_1 and ν_2. As shown by inequality B.10 in Appendix B, the condition for three positive eigenvalues is:

$$1 - v_1 - 2\left(\frac{E_1}{E_2}\right)v_2^2 > 0$$

This condition is both sufficient and necessary for the positive definite nature of this anisotropic elastic constitutive relationship. If the above inequality takes the equal sign, the material becomes incompressible. In practice, the condition can help us to check the assumed Poisson's ratios in carrying out a parametric study or to check the correctness of the test data, especially for a higher modulus ratio E_1/E_2. For example, if $E_1/E_2=4$ and $\nu_1=0.30$, the maximum value of ν_2 for anisotropic deformation is about 0.295. Both of ν_1 and ν_2 are much less than 0.5.

Another example is the perfect elastoplastic constitutive relationship with a non-associated flow law. In this case, one eigenvalue should be zero and the other two should be positive. Equation B.19 shows that this requires the two gradients of the yield and potential functions make an acute angle in stress space. In this research, our assumption conforms with the requirement. In short, the analytical expressions can provide the criteria to check whether a model is correctly defined by the chosen parameters.

2.2.3 The weak direction

General analytical expressions for eigenvalues and eigenvectors defined in the principal stress space are presented in detail in Appendix B. The main conclusions are described below.

In the three dimensional stress space, among the three eigenvalues for the elastoplastic matrix, one is zero while the other two are different and positive. The three eigenvectors are orthogonal under the associated flow law as shown in Fig. 2.4. When the incremental strain is decomposed in these three directions, the component along the eigenvector for zero eigenvalue is just in the normal direction of the yield surface. According to the principle of normality, this component is the portion for plastic strain. The other two components represent elastic strains. With the eigenvalue being zero, the component of stress

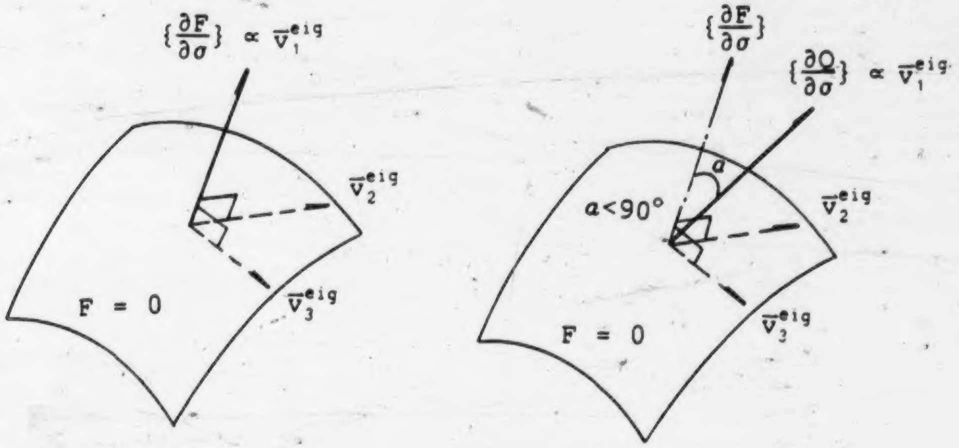
$\{\frac{\partial F}{\partial \sigma}\} \propto \overline{v}_1^{eig}$
$\overline{v}_2^{eig}$
$\overline{v}_3^{eig}$
F = 0
$\{\frac{\partial F}{\partial \sigma}\}$
$\{\frac{\partial Q}{\partial \sigma}\} \propto \overline{v}_1^{eig}$
α
$\alpha<90°$
$\overline{v}_2^{eig}$
$\overline{v}_3^{eig}$
F = 0

A. associated flow law perfect elastoplastic

B. non-associated flow law perfect elastoplastic

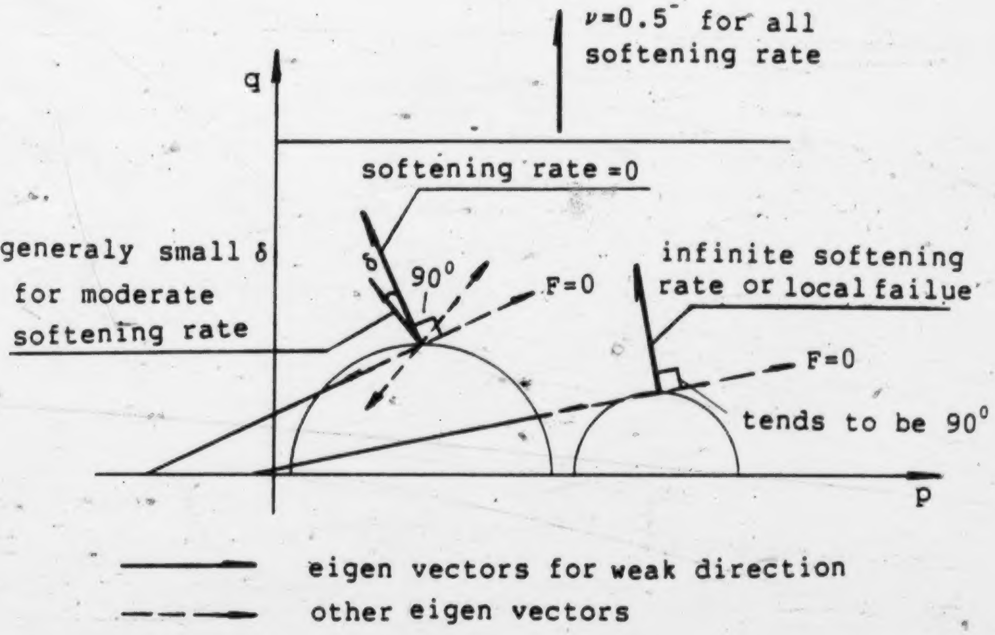
$\nu=0.5^-$ for all softening rate
q
softening rate =0
generaly small δ for moderate softening rate
δ
90^0
F=0
infinite softening rate or local failue
F=0
tends to be 90^0
p
eigen vectors for weak direction
other eigen vectors

C. strain softening

Figure 2.4: Weak direction

increment in the the normal direction will be zero, and the total stress increment will be along a certain direction on the yield surface to keep the consistency condition of F=0. Under the non-associated flow law, the weak direction may no longer be perpendicular to the other two (Fig. 2.4), since the elastoplastic matrix is generally not symmetric. However, the three eigenvectors are linearly independent. Taking them as base vectors, the physical explanation for the three components of the strain and stress increments are the same as before, only with the plastic strain increment along the gradient of the potential function.

Only two dimensional analytical ~~expres~~sions are derived for strain softening materials. In Appendix B, a method to illustrate the weak direction in the conventional p-q space is also given. Here, $p=\frac{1}{2}(\sigma_1+\sigma_3)$ and $q=\frac{1}{2}(\sigma_1-\sigma_3)$. Both theoretical examination and numerical tests have been carried out. For practical use, it seems more helpful to describe the general conclusions:

1. When the determinant of $[C^{EP}]$ in the equation 2.33 is negative in the two dimensional stress space, one eigenvalue is negative and the other one is positive (eqn. B.30, Appendix B). The weak direction is generally not normal to either the yield surface or the potential surface.
2. If ν tends to 0.5, by taking the limit in eqn. B.35d, we can see that the weak direction will tend to make an angle of 45° with the principal stress.

Therefore, if the soil is incompressible the weak direction is independent of softening rates.

3. No softening term will be involved in the analytical expressions if $\nu=0$ (eqn. B.35a to B.35f). Therefore, the smaller the value of ν is, the smaller is the influence of softening on the deviation of the weak direction from that of the perfectly plastic case.
4. It is easy to understand when the softening rate tends to zero, the weak direction tends to that of the corresponding perfect elastoplastic model. Note that this will also apply to the situation when plastic strains are highly developed to bring the strength down near to the residual with a very low softening rate.
5. With a moderate softening rate, numerical tests show that the deviation of the weak plane from that of the corresponding perfect elastoplastic model is not large. To measure the softening rate, we use the softening parameter h^p, which may be expressed as the ratio of the softening term to the perfect term in eqn. 2.17. For example, with a moderate softening rate $h^p<-0.5$, ν between 0.3 and 0.45, the friction angle being 30^0, the deviation of the weak direction is less than 4.15° away from conventional failure angle $(45^\circ - \frac{30^\circ}{2})$.
6. If the softening rate tends to become infinite, the material behavior is independent of the surrounding

support and the strength will immediately decrease to its residual value, and so the weak direction is defined by the corresponding perfect elastoplastic model with residual strengths. This also applies to the situation where the large localized deformation has indicated a local collapse due to unstable softening (Section 2.3.3).

The above conclusions are illustrated for the associated flow law in Fig. 2.4.

2.2.4 Capture of localized deformation

The theoretical eigenvalue analyses has shown that the weak direction is clearly defined by the eigenvector corresponding to the zero or minus eigenvalue. It is no doubt that there exist possibilities for elastoplastic models to capture localized deformation. The weak plane in failure due to cracks is too obvious for us to discuss. We only discuss the weak plane due to shear.

The development of strain softening depends on the surrounding support. If a weak layer exists in the structure, the initial formation of a shear band characterized by a high shear strain gradient can be easily captured.

In isotropic regions, the formation of shear bands may often develop in a smeared pattern in the beginning, except that highly concentrated strains develop under certain loading conditions or special boundary conditions, e.g. near a localized weak zone. This is reasonable since the isotropic assumption implies that the defects of the material are distributed at random, which restricts the localized deformation. In reality, localized deformations will finally develop along the most critical potential slip surface during failure. However, under the assumption of deformation continuity, the elastoplastic model is not capable of simulating further large deformation with macro separation and dislocation of materials.

Incremental strains are obtained by differentiating incremental displacements. Therefore, the impact of weak directions of strain increments should be involved in directions of incremental displacement vectors. In analysing the failure mechanism, the potential slip surface may be approximately integrated by taking directions of incremental displacement vectors as the tangent. This is because these vectors at failure present a picture of movements inside a body. Practical techniques and examples will be given in Chapter 6. Here, we want to point out that the so determined critical slip surface is generally approximate as compared with the observed one in real life. Such fully developed shear bands along the observed slip surface may not be simulated under our assumptions as mentioned before. Further deformations from an incipient failure involve changes of principal stress and srain directions, hence changes of weak directions and the location of the critical slip surface.

In short, although the possibility of capturing localized deformation is revealed by the eigenvalue analyses, the assumptions of continuity and small strain and deformation limit the present formulation to capture the fully developed shear band. At most, we can only locate the slip surface in the existing weak layers and the incipient slip surface in isotropic materials. From the engineering point of view, the prediction of the incipient slip surface may be sufficient for the stability analysis of a man-made structure.

2.3 Study on Solution Behavior

2.3.1 Introduction

The instability caused by unstable softening or cracking does not definitely imply the failure of a structure, especially a natural structure. From the engineering point of view, a cracked reinforced concrete slab may be safe or acceptable when it used in a grain container but may be unsafe or unacceptable in a liquid container. Hence, safety or acceptability is not defined by pure science, but by engineering judgement. In order to clarify the concepts, we use local collapse to indicate cracking or unstable softening and we use the adjectives such as abnormal and impermissible. For stable softening, we use their antonyms. All the above terms are used in the incremental sense in statics. For engineering judgement, we use reasonable, acceptable and safe or their antonyms.

Abnormal solutions may be obtained in finite element analyses due to unstable strain softening. However, engineering practice needs reasonable solutions at least due to the following reasons,

1. The failure mechanism cannot be analysed with abnormal solutions, e.g. in locating a slip surface.
2. If the degree of safety of a structure is acceptable, reasonable solutions are needed for further analyses, even if the solution becomes abnormal.
3. Finite element analyses will be used more and more widely in the future. In checking a new design or doing parametric studies, abnormal solutions may appear frequently.

Therefore, we have two tasks. One is to judge whether the solution is abnormal or not, while the other is to continue an analysis until unacceptable failure appears when abnormal solutions are found. The first task is of great importance, because the results cannot be used confidently without detecting abnormal solutions due to unstable softening.

For practical use, first we study the criteria to detect abnormal solutions, then, we study how to treat them. The solutions should be known at first, since there is no way to judge absurd solutions due to unstable softening before solving a complex problem.

The research starts from the study of an equivalent form of the global equilibrium equations. In the equivalent form, the global stiffness matrix is transformed into a diagonal matrix by taking the singular response (if it exists) as the limit of a non-singular response of the system, and so the response of each degree of freedom is uniquely defined by a generalized force.

The response of each degree of freedom can be simulated by an extended elastically connected Coulomb damping model. Both the static and dynamic characteristics of softening behavior as well as its relation with brittle models will be investigated in detail. And so, the criteria for both normal and abnormal solutions are presented.

Since the solution behavior for all degrees of freedom under the generalized force is mathematically the same, conclusions for the global system can be drawn.

The application of brittle models are described in order to obtain meaningful results for unstable softening. No unstable softening is detected before failure in our case history. The suggested method is described in Appendix D, since the applicability and validity of the method need to be proved by case histories.

The loading criteria, existence of the true solution and its uniqueness for strain softening in continuum mechanics are re-examined in Appendix E. The study reveals that violation of the loading criteria at any point inside a body will cause an absurd solution. In practice, we may suppose that there exists a true solution, then, we can use the principle of virtual work to formulate the governing equations. After solving by introducing the boundary conditions, we check the solution by the loading criteria. If the criteria are satisfied, the solution is correct. If not, it should be discarded.

2.3.2 Mechanical model for diagonalized equilibrium equations

According to the theory of linear algebra, if the global stiffness matrix is non-singular, by using elementary matrix transformations, the global equilibrium equations can be transformed into the form:

$$[K_{ii}]\{\Delta u\} = \{\Delta T^{g}\} \qquad (i = 1, n) \, , \tag{2.35}$$

in which $[K_{ii}]$ is a diagonal matrix with all its diagonal elements retaining their original value. $\{\Delta T^{g}\}$ is a generalized force vector under the same transformation.

In nonlinear finite element analyses, the matrix may become singular. In order to investigate solution behavior, we use the concept of the limit. The method is to assign an arbitrary small number to the diagonal element during the above linear transformation whenever it becomes zero. We name this arbitrary small number as $^{+}0^{-}$. The limit will be studied both with $K_{ii}\to 0^{+}$ and $K_{ii}\to 0^{-}$. Now, for any global stiffness matrix we can complete the above linear transformation. The range of K_{ii} is

$$-\infty < K_{ii} < {}^{-}0 \qquad \text{and} \qquad 0^{+} < K_{ii} < +\infty. \tag{2.36}$$

By introducing the limit analysis, the above range will cover all the possible values we may encounter in any stiffness matrix.

Now the equation at each degree of freedom becomes

$$K_{ii}\Delta u_i = \Delta T_i^g \ . \tag{2.37}$$

For a known solution,

$$\Delta T_i^g = \Delta T_i - \sum_{r=j}^{p} K_{ir}\Delta u_r \ , \tag{2.38}$$

in which K_{ir} is the stiffness coefficient at the related degrees of freedom as shown in Fig. 2.5.

It should be mentioned that the solution behavior along any direction from any node can be described in the same mathematical form of eqn. 2.37 and 2.38 by using coordinate transformation. Therefore, no generality will be lost in the further study. The meaning of the above equation is different from the equation derived directly from the unsolved global equilibrium equation. Here all the Δu_r are known. That is to say that we are studying the solution behavior of each degree of freedom with prescribed displacement boundary conditions.

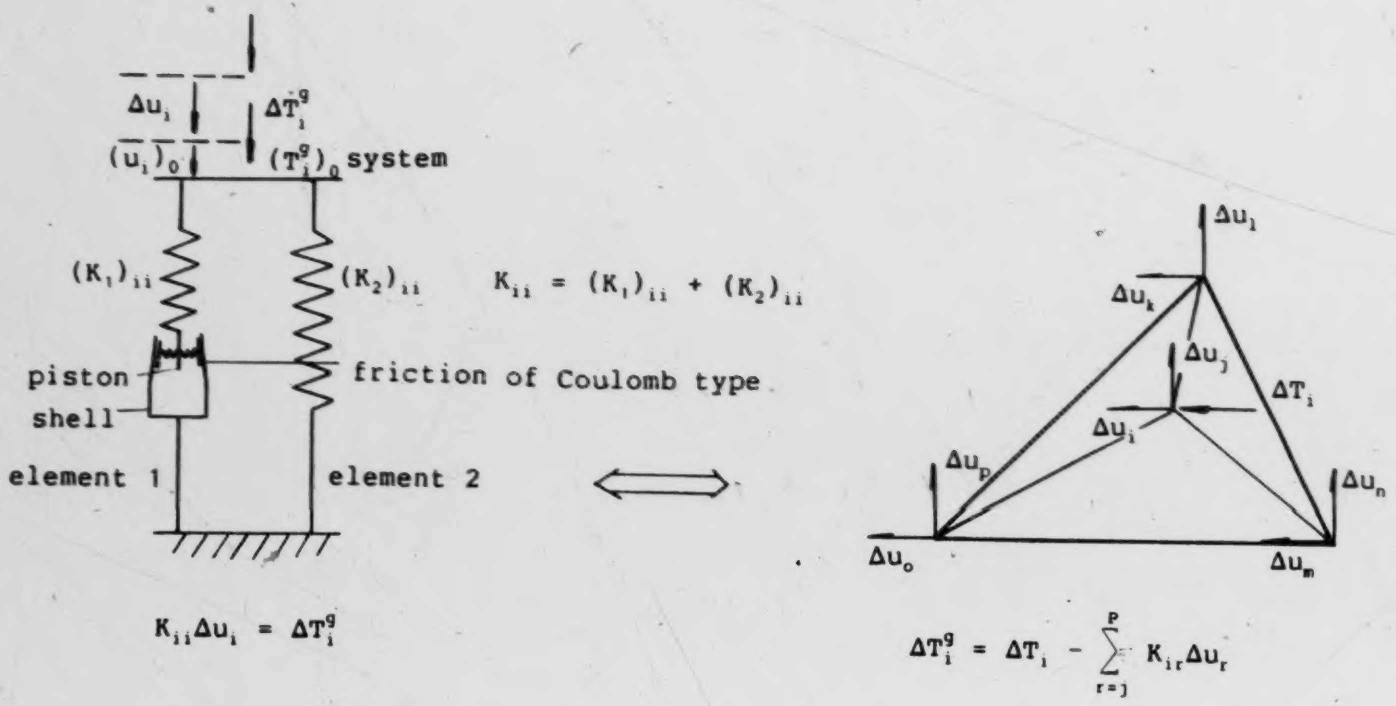
Δu_i
ΔT_i^g
$(u_i)_0$
$(T_i^g)_0$ system
$(K_1)_{ii}$
$(K_2)_{ii}$
piston
shell
friction of Coulomb type
element 1
element 2
Δu_l
Δu_k
Δu_j
ΔT_i
Δu_i
Δu_p
Δu_n
Δu_o
Δu_m

$$K_{ii} = (K_1)_{ii} + (K_2)_{ii}$$

$$K_{ii}\Delta u_i = \Delta T_i^g$$

$$\Delta T_i^g = \Delta T_i - \sum_{r=j}^{p} K_{ir}\Delta u_r$$

Figure 2.5: Extended elastically connected Coulomb damping model

The behavior with any degree of freedom may be considered as the joint response of negative and positive stiffness contributions (see detail in section B.4, Appendix B). For practical use, there is no need to study all the specific conditions which cause negative contributions to K_{ii} or even negative K_{ii}. We only need to know that there exists such a possibility and to know how to cope with it. Without negative contribution, the solution behavior is well known. We concentrate our study on the negative contribution.

As shown in Fig. 2.5, an extended elastically connected Coulomb damping model is used for this study. The difference between this model and that original one (Harris, 1976) lies in that the friction provided in the damping element will decrease as the relative movement increases between the piston and shell. Hence, negative stiffness will be contributed after failure. The elastic element is used to model the postive contribution. For the convenience, subscripts $_{ii}$ or $_{i}$ and superscript ^{g} in studying each degree of freedom are omitted, and subscripts $_{1}$ or $_{2}$ are used to indicate the damping and elastic elements.

Since the global stiffness matrix can be assumed as constant and it is independent of the past strain-stress history except the present strain-stress state and loading directions, the above model is a general model in the incremental sense, no matter how complex the material models or loading history might be. In checking an obtained solution, all the variables in the discussion below can be known (see Appendix C). For positive stiffness contribution, $K_2>0$, with unloading elastic stiffess k_2, and if $K_2=0$, no positive contribution exists (Fig. 2.6); for negative contribution, $K_1<0$ with unloading elastic stiffness k_1. Notice that k_1, k_2, K_1 and K_2 are constant in an incremental step.

Now, the basic equation is

$$\Delta T = K\Delta u = (K_1+K_2)\Delta u \ . \qquad (2.39)$$

2.3.3 Solution behavior of the mechanical model

A full study of the mechanical model has been carried out on both the static solution behavior of stable softening and the dynamic solution behavior of unstable softening. Since the basic equation 2.39 is very simple, it may be adequate to elucidate the conclusions by reference to figures. The corresponding expressions for the solution can be found in Appendix C.

If $K>0$, i.e. the positive contribution K_2 prevails over the negative contribution K_1, strength hardening behavior dominates. The external loads can be taken along the direction to promote further softening as shown in solution A in Fig. 2.6. If $K<0$, under stable displacement boundary conditions, ΔT will be in the unloading direction. The total external loads will be released, but Δu will still be advanced in the softening direction as shown for solution D

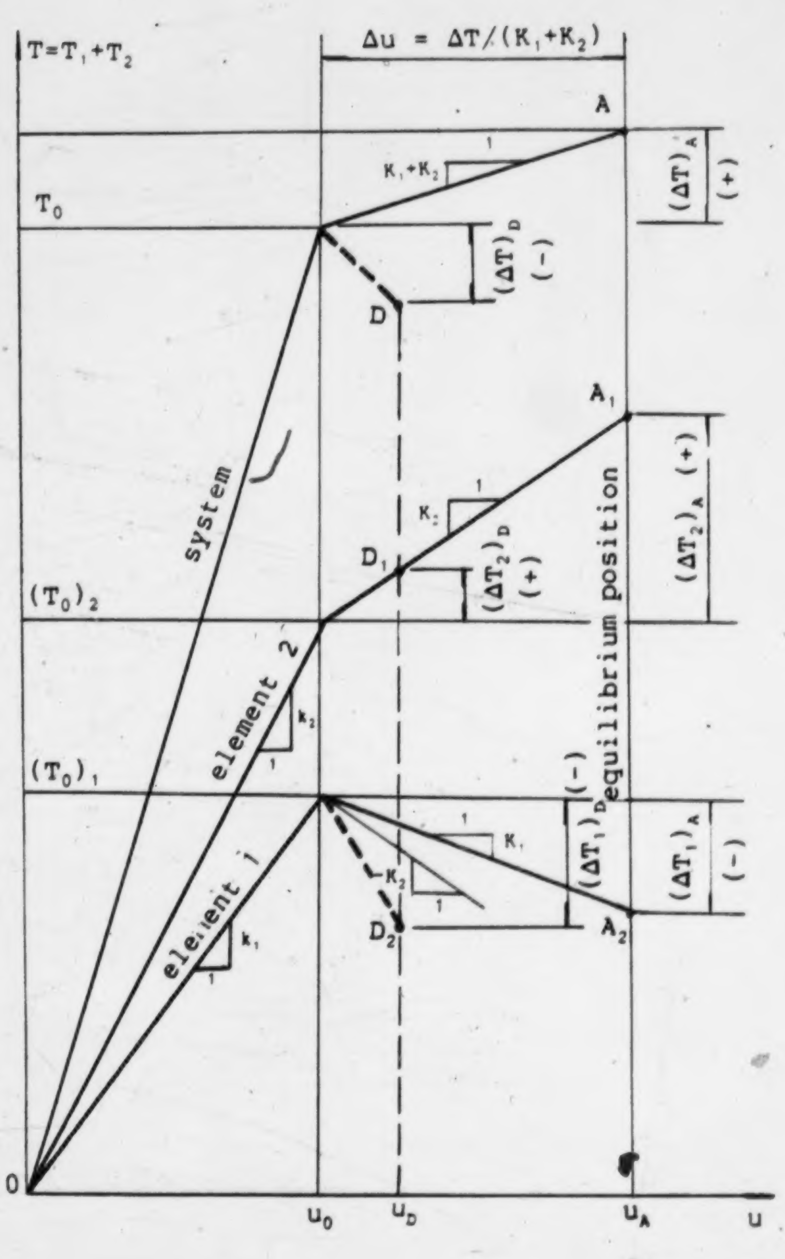
T=T$_1$+T$_2$
Δu = ΔT/(K$_1$+K$_2$)
A
1
K$_1$+K$_2$
(ΔT)$_A$ (+)
T$_0$
(ΔT)$_D$ (-)
D
A$_1$
system
1
K$_2$
(ΔT$_2$)$_A$ (+)
D$_1$
(ΔT$_2$)$_D$ (+)
equilibrium position
(T$_0$)$_2$
element 2
K$_2$
1
(T$_0$)$_1$
(ΔT$_1$)$_D$ (-)
1
K$_1$
(ΔT$_1$)$_A$ (-)
element 1
K$_2$
1
K$_1$
1
D$_2$
A$_2$
0
u$_0$
u$_D$
u$_A$
u

Figure 2.6: Solution of stable strain softening

in Fig. 2.6. Now, strain softening dominates. There exists a critical negative stiffness K_2 which makes $K_1+K_2=0$. At this critical negative stiffness (Fig. 2.7), the system behaves like a perfectly plastic model and the incremental displacement is infinite.

If $K<0$ but the external load is still applied along the further softening direction, the solution will be abnormal. The load in this direction may be caused by the release of excessive stresses after failure from the neighboring Gaussian integration points or by application of further loads. The reason why we call this solution abnormal is that the plastic work becomes negative due to the wrong direction of the incremental displacement Δu as shown in Fig. 2.8.

It is interesting to note that all the requirements for the true solution are satisfied by an abnormal solution except the loading criteria (see details in Appendix C). This is why the true solution can be obtained if the loading criteria are obeyed. The theoretical background is given in Appendix E.

In Appendix C, the loading criteria for a degree of freedom are explained in terms of the generalized forces. Because the generalized force are generally not recorded and the stiffness contribution is assembled from each Gaussian point, it is convenient to check the loading criteria in Table 2.1 at all Gaussian integration points for a stable solution.

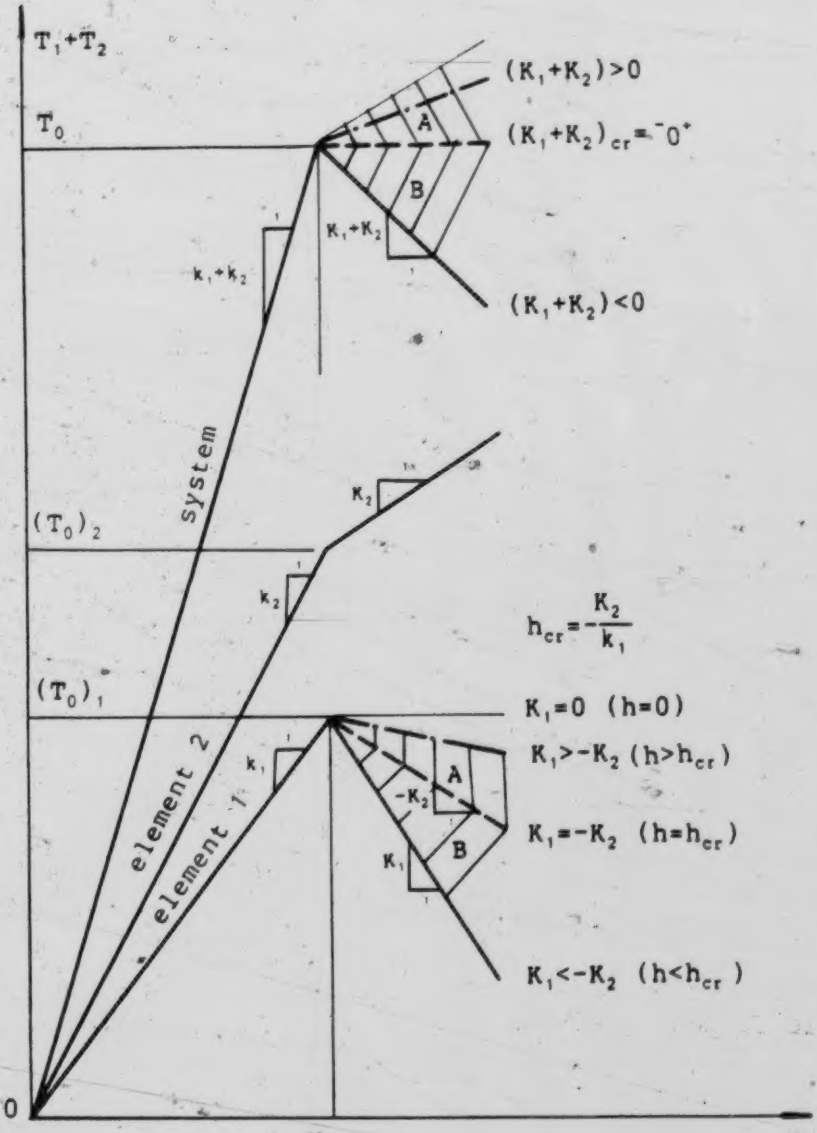
T_1+T_2
T_0
$(K_1+K_2)>0$
A
$(K_1+K_2)_{cr}=^-0^+$
B
K_1+K_2
k_1+k_2
1
$(K_1+K_2)<0$
system
$(T_0)_2$
K_2
k_2
$h_{cr}=-\frac{K_2}{k_1}$
$(T_0)_1$
$K_1=0$ (h=0)
$K_1>-K_2$ $(h>h_{cr})$
k_1
A
$-K_2$
$K_1=-K_2$ $(h=h_{cr})$
K_1
B
element 2
element 1
$K_1<-K_2$ $(h<h_{cr})$
0
u_0
u

Figure 2.7: Critical minus stiffness contribution

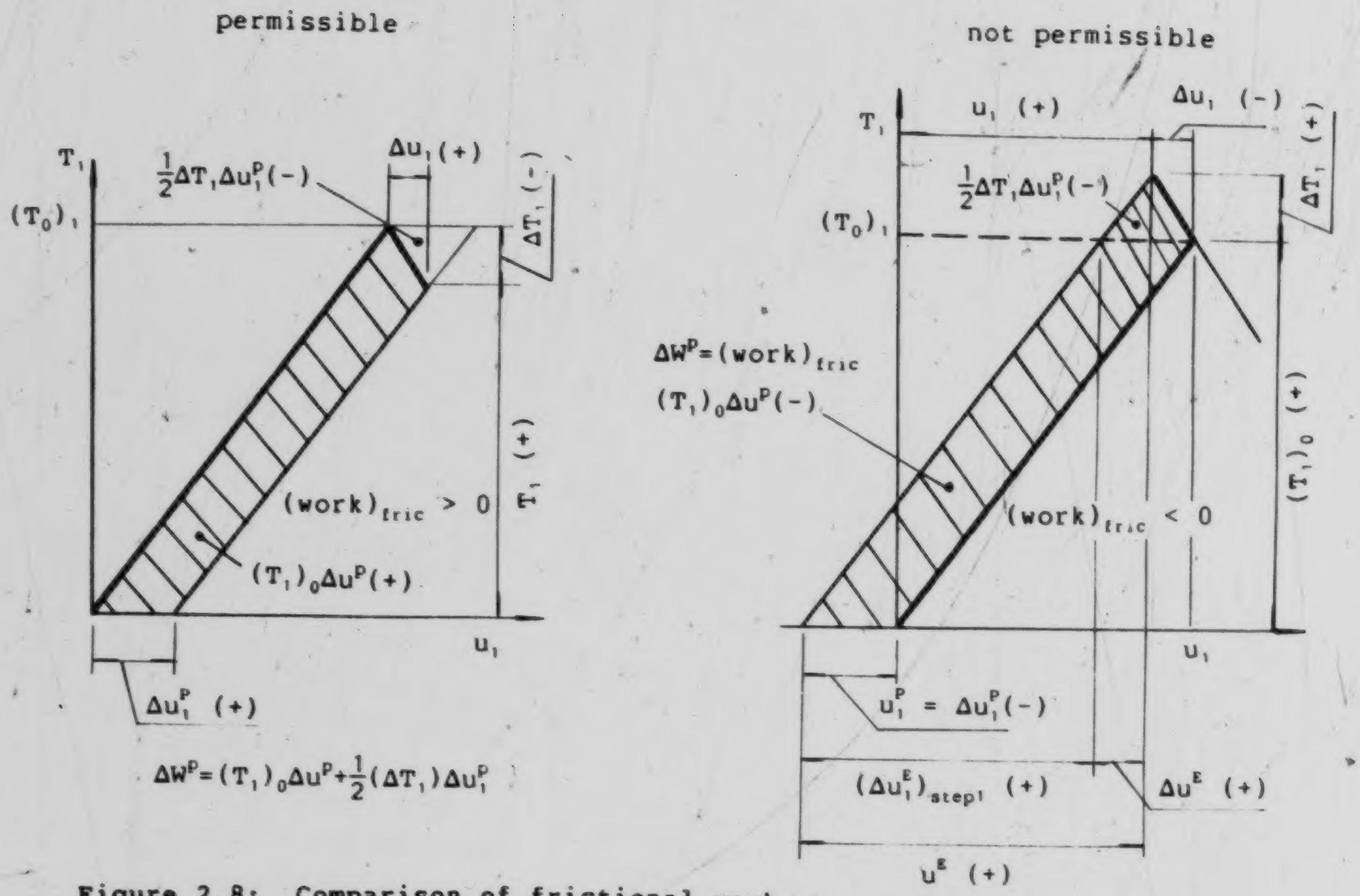

permissible

not permissible

T_1
$(T_0)_1$
$\frac{1}{2}\Delta T_1 \Delta u_1^P(-)$
$\Delta u_1(+)$
$\Delta T_1\ (-)$
$T_1\ (+)$
$(work)_{fric} > 0$
$(T_1)_0 \Delta u^P(+)$
u_1
$\Delta u_1^P\ (+)$
$\Delta W^P = (T_1)_0 \Delta u^P + \frac{1}{2}(\Delta T_1)\Delta u_1^P$
T_1
$u_1\ (+)$
$\Delta u_1\ (-)$
$\Delta T_1\ (+)$
$(T_0)_1$
$\frac{1}{2}\Delta T_1 \Delta u_1^P(-)$
$\Delta W^P = (work)_{fric}$
$(T_1)_0 \Delta u^P(-)$
$(work)_{fric} < 0$
$(T_1)_0\ (+)$
u_1
$u_1^P = \Delta u_1^P(-)$
$(\Delta u_1^E)_{step1}\ (+)$
$\Delta u^E\ (+)$
$u^E\ (+)$

Figure 2.8: Comparison of frictional work

In fact, abnormal solutions indicate unstable softening. A complete solution is a task of dynamics. As shown in Appendix C, by neglecting the inertial term in dynamic equations, abnormal solutions will be obtained in statics. We also call unstable softening local collapse in this research. Further understanding of this unstable process needs study by means of this simple system in dynamics. The solution are also presented in Appendix C.

The solution for linear unstable softening is illustrated by the dynamic strain-stress paths in Fig. 2.9. Note that we are only taking the response under the action of external forces in the further softening direction. Unlike abnormal solutions, the first response of Δu is in the same direction of ΔT. This conforms with the common sense. Certainly, after the first response, displacement cannot increase unlimitedly. In our simple linear model, the dynamic equation will change form until and only until the strength is lowered down to the residual with $K_1=0$ and $K=K_2>0$. Then, the motion is governed by the stable dynamic equation until the final equilibrium position is reached due to damping (Fig. 2.9)

Since static force equilibrium should be maintained when everything comes to rest, this position can be found by using the brittle model to replace the softening model (Fig. 2.10), if we assume the constitutive relationship is unchanged.

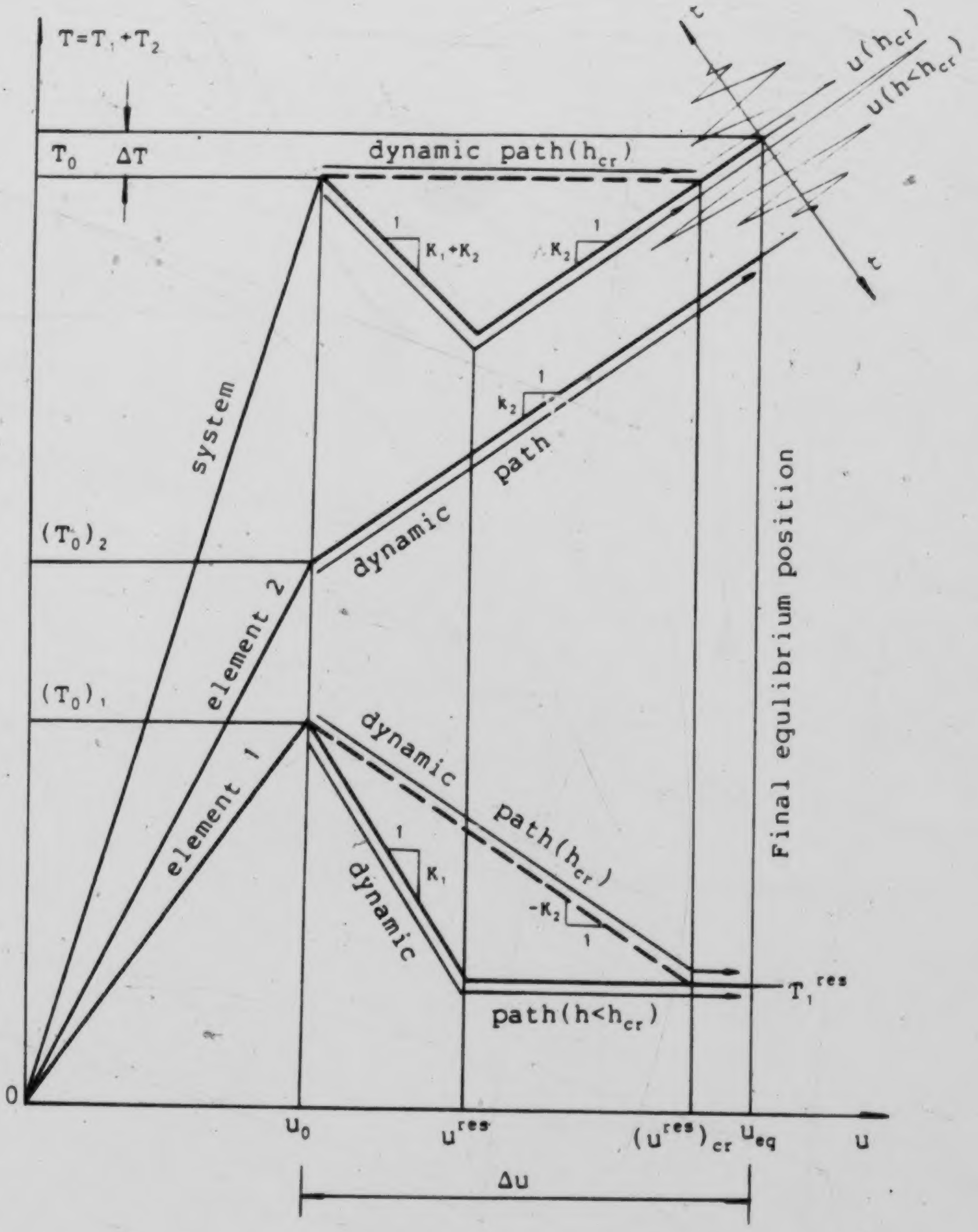
$T=T_1+T_2$
T_0
ΔT
dynamic path(h_{cr})
1
K_1+K_2
1
K_2
t
$u(h_{cr})$
$u(h<h_{cr})$
t
system
1
k_2
dynamic
path
$(T_0)_2$
element 2
$(T_0)_1$
element 1
dynamic
path(h_{cr})
1
K_1
dynamic
$-K_2$
1
T_1^{res}
path($h<h_{cr}$)
Final equlibrium position
0
u_0
u^{res}
$(u^{res})_{cr}$
u_{eq}
u
Δu

Figure 2.9: Dynamic paths of unstable softening

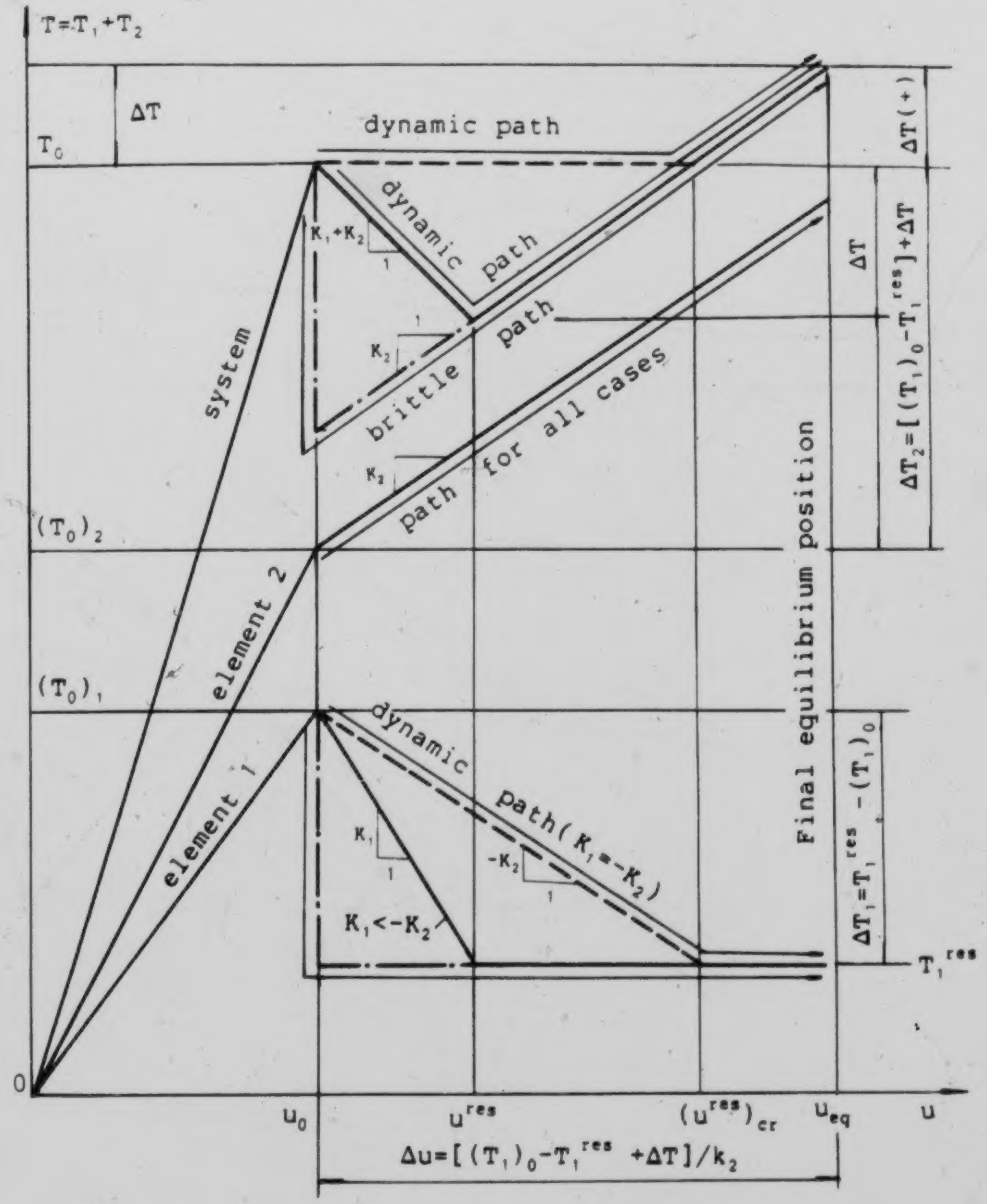
T=T₁+T₂
ΔT
T₀
dynamic path
dynamic path
K₁+K₂
1
system
brittle path
K₂
1
path for all cases
K₂
(T₀)₂
element 2
(T₀)₁
element 1
dynamic path(K₁=-K₂)
K₁
1
-K₂
1
K₁<-K₂
Final equilibrium position
ΔT(+)
ΔT
ΔT₂=[(T₁)₀-T₁^res]+ΔT
ΔT₁=T₁^res -(T₁)₀
T₁^res
0
u₀
u^res
(u^res)cr
u_eq
u
Δu=[(T₁)₀-T₁^res +ΔT]/k₂

Figure 2.10: Brittle models for unstable softening

From Fig. 2.10 we can see that,

1. the incremental displacement is finite no matter how small the increment force is.
2. as to the final equilibrium position, there is no difference between all the softening rates which make K_1+K_2 less zero.

Generally, the unstable softening process is nonlinear as shown in Fig. 2.11 in which point C with a tangential critical negative stiffness indicates the turning point for the change of governing dynamic equation into stable pseudo-harmonic type. Although iteration methods can be formulated to try the secant apparent softening stiffness K_a by assuming a residual strength (Fig. 2.11), it is often too expensive to be practical for complex problems. Methods to solve this problem are suggested in Appendix D.

2.3.4 Solution behavior of the global equilibrium equations

Based on the study of the linear model in the last section, let us investigate the true solution at each degree of freedom. If K_{ii} or $(K_1+K_2)_{ii}$ is greater than zero, or less than zero but without local collapse, the displacement solution at this degree of freedom can be exactly simulated by the simple model demonstrated in the previous section. The reason is that the incremental displacements will be infinitesimal if the incremental external forces are infinitesimal, and so the linear assumption is valid. Note that the above conclusion requires normal solutions at all

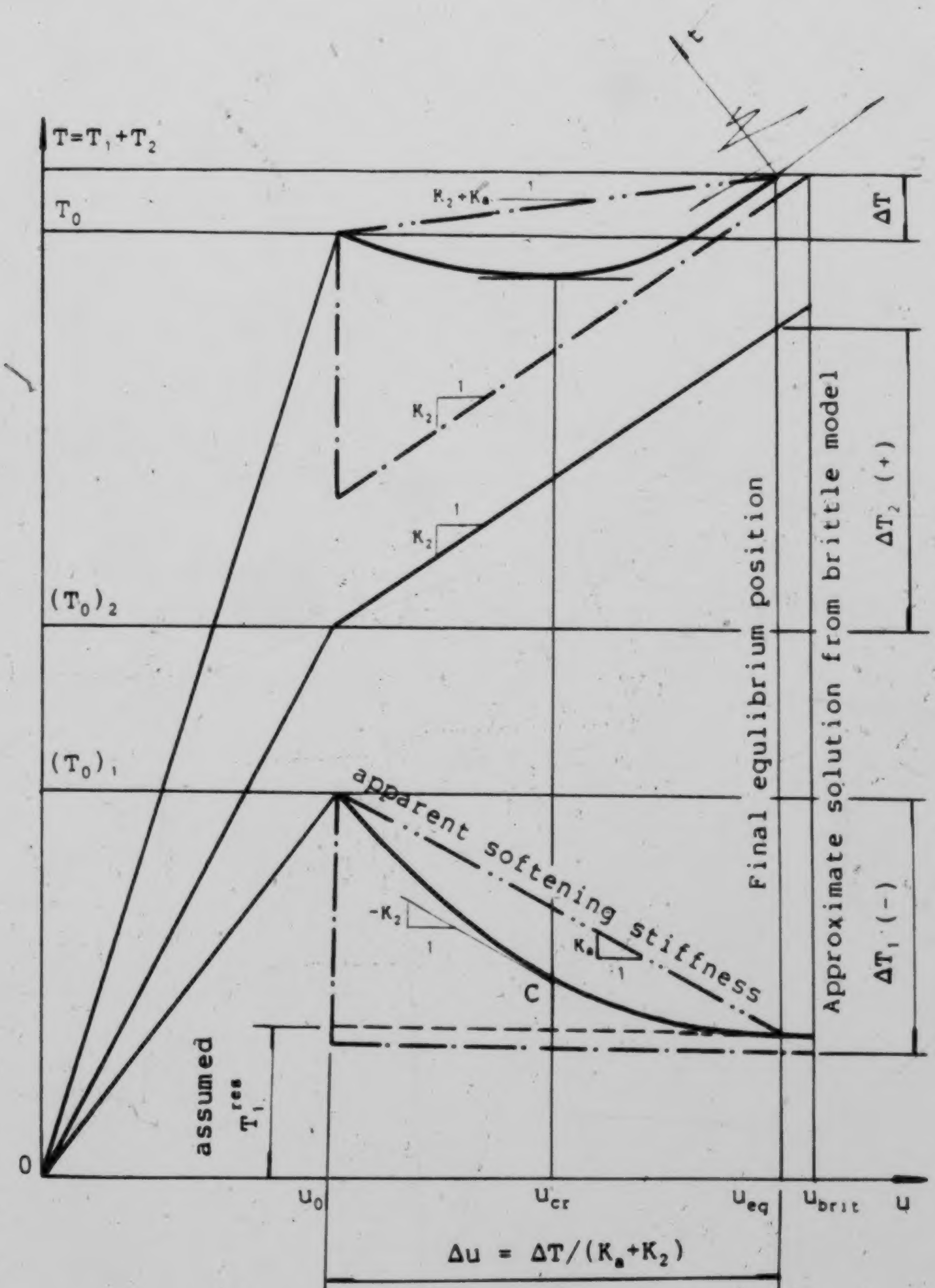
t
$T=T_1+T_2$
T_0
K_2+K_a
1
K_2
1
K_2
1
$(T_0)_2$
$(T_0)_1$
apparent softening stiffness
$-K_2$
1
K_a
1
C
assumed T_1^{res}
0
u_0
u_{cr}
u_{eq}
u_{brit}
u
$\Delta u = \Delta T/(K_a+K_2)$
Final equlibrium position
Approximate solution from brittle model
ΔT
ΔT_2 (+)
ΔT_1 (-)

Figure 2.11: Unstable nonlinear softening

the related degrees of freedom.

If local collapse takes place, K_{ii} cannot be treated as constant and $(K_1)_{ii}$ and $(K_2)_{ii}$ will be coupled, because finite or even infinite displacement solutions can be obtained no matter how small the incremental external force might be. The loading path of the incremental displacement and generalized external force will become much more complex than that illustated for the simple Coulomb damping model. However, we can still use the simple model to locate the loading path by changing stiffness coefficients K_1 and K_2. That is to say, the global stiffness matrix needs to be re-assembled whenever the constitutive relationship changes along the loading path.

As shown in Fig. 2.12, the true displacement solutions at any degree of freedom can be classified into three groups. In Fig. 2.12, the three groups are marked with A or D, B and C, subscripts 1 and 2 are for the damping and elastic elements , K_1 and K_2 changes as local collapses take place and K_{cr} is for the critical stiffiness which varies as K_2 changes. If elastic models and softening rates are nonlinear, the straight line segments will be curved, but this does not affect the discussion.

Group A and D represents the stable solution Δu_A ($K_{ii}>0$) and Δu_D ($K_{ii}<0$). When K_{ii} tends to zero or generalized force tends to infinity, the displacement will tend to infinity, which is acceptable for engineering judgement. The criterion for permissible Δu_D is that ΔT_i^g should take the opposite

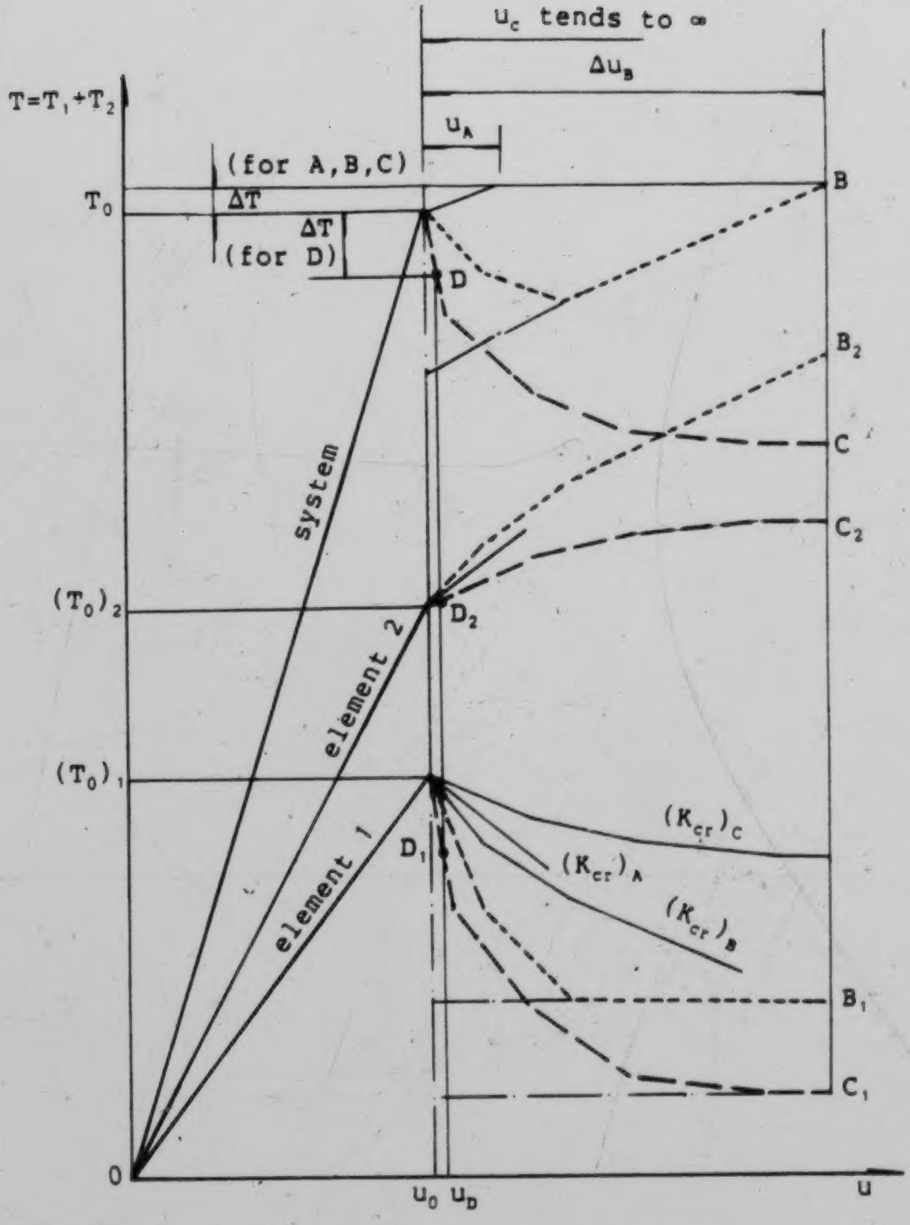
u_c tends to ∞
Δu_B
$T=T_1+T_2$
u_A
(for A,B,C)
T_0
ΔT
ΔT
(for D)
B
D
B_2
C
system
C_2
$(T_0)_2$
D_2
element 2
$(T_0)_1$
$(K_{cr})_C$
D_1
$(K_{cr})_A$
element 1
$(K_{cr})_B$
B_1
C_1
0
u_0 u_D
u

Figure 2.12: Solution behavior at each degree of freedom

sign to that of the total generalized force at the end of the last incremental step, while Δu_D should take the same sign. Certainly, zero Δu_D is also permissible. The compliance of the loading criteria is guaranteed by the normal solutions of all the related degrees of freedom.

Group B represents constrained local collapse. The dynamic reponse will follow paths B_1 and B_2 with the result of path B. Turning points along the path B_1 indicate that governing dynamic equations of certain related Gaussian points change into the pseudo-harmonic type. This can be caused by the following reasons,

1. the strength reaches its residual (linear softening rate) or the softening rate decreases to the critical value (nonlinear softening rate);
2. the positive stiffness (simulated by K_2) increases and so the absolute value of critical softening rate decreases;
3. both 1 and 2.

Therefore, along the loading path, both negative (K_1) and positive (K_2) stiffness will change. If the positive contribution ever exists, finally the system will reach its new equilibrium position, marked with Δu_B as shown in Fig. 2.12.

Group C corresponds to the situation where the positive stiffness vanishes as it changes along the loading path. Then the solution behavior is the same as element 1. With any arbitrarily small incremental force, total collapse will occur at this degree of freedom. A new equilibrium position will be certainly reached in a real structure but the position cannot be determined under the assumption of small deformations.

Because all degrees of freedom are identical in the mathematical form, conclusions can be easily drawn for the whole system as follows.

1. The acceptability of the solution at any degree of freedom depends on the normal solution behavior of all the related degrees of freedom and hence depends on the normal behavior of the whole system.
2. The true solution can be obtained or, at least, defined in certain permissible solution subspaces if and only if no loading criteria are violated at any degree of freedom or at any Gaussian point where strain softening develops.
3. The solution should be discarded if loading criteria are violated.

As mentioned before, it is convenient to use the loading criteria at each Gaussian point to check unstable softening.

Finally, it should be mentioned that infinitesimal load increments are assumed in this discussion. In real calculation, iterations may often be needed to satisfy the consistent condition of yield functions. Therefore, the global stiffness matrix may also change in a loading step. The loading criteria should be obeyed in each iteration. The change of the stiffness matrix towards singularity may cause very large incremental displacements at certain nodes. However, as mentioned before, to determine whether the structure is safe or not depends on engineering judgement.

2.4 Summary

1. The general formulation and material models are introduced for finite element analyses in this research.
2. In the conventional framework of elastoplasticity, the finite element formulation for strain softening can yield correct solutions if and only if the loading criteria are obeyed.
3. Corner problems caused by the intersection of different expressions of the yield and potential functions should be properly treated when tension criteria are used together with frictional yield criteria.
4. In principle stress space, for isotropic elastic constitutive relationships, there exist three positive eigenvalues with three independent eigenvectors corresponding to isotropic stress and pure shear states (Section B.1, Appendix B). For perfect elastoplastic constitutive relationships, one eigenvalue is zero while the other two are positive. The orthogonality of the three corresponding eigenvectors is maintained under the

associated flow law but generally vanishes under the non-associated flow law. For strain softening materials, only the two dimensional situation is studied. When the determinant of the elastoplastic matrix is negative, one eigenvalue is negative and the other is positive. The orthogonality of the eigenvectors depends upon the flow laws as mentioned above. Useful conclusions are summarized for the weak direction. Under moderate softening rate, the weak direction will deviate a little bit from that of the corresponding elastoplastic model. However, when Poisson's ratio is near 0.5, the slip surface will make an angle of nearly 45° with the principal stress during failure in isotropic soils. For ν = 0.5, this failure direction is independent of softening rates.

5. The capacity to capture localized deformation exists in the elastoplastic formulation. For the isotropic region, the initial shear bands often develop in a smeared pattern except for weak layers or special loading and boundary conditions. However, the incipient potential slip surface can be determined by the direction of incremental displacement vectors just before failure. Due to the unstable nature during failure, location of the shear band with material separation and dislocation will be beyond the capacity of the elastoplastic model based on the

incremental theory.

6. The existence of negative eigenvalues may cause all the possible unfavorable conditions of the global stiffness matrix. For a complex problem, at present, the solution behavior can be investigated only from the obtained solution. Absurd solutions can be obtained even for a very simple problem. Therefore, no abnormal solution should be guaranteed before any results are put into use.
7. Violation of the loading criteria indicates that the system cannot seek a new equilibrium position in the vicinity within an infinitesimal distance along the strain and stress path no matter how small the disturbance might be. Such an unstable softening cannot be treated statically in the incremental sense. The theoretical background is re-examined and strengthed in Appendix E.
8. Brittle models can be used to obtain acceptable solutions when unstable softening takes place. However, the solution is approximate since the dynamic behavior of the materials is generally not available. Practical methods are described in Appendix D.

3. ITERATION TECHNIQUES AND MESH DESIGN

The computation cost is very high in analysing complex engineering problems by means of nonlinear finite element analyses. It may be the most important reason to limit wide applications of the method in practice. Therefore, there are two problems for us to study. One is which of the available iteration methods is efficient and hence economical. The other is how coarse a mesh can still yield solutions accurate enough for engineering applications.

The effectiveness and efficiency of the available iteration method are problem dependent and so are the guidelines for mesh design. An extensive study is not intended in this thesis. The discussion is limited to the analyses of rock-earthfill dams and only material nonlinearity is considered.

One purpose of the study is to gain economical benefits in analysing the failure mechanism of the Carsington Dam. It is obvious that experience will be helpful to similar applications of finite element analyses in dam engineering. Moreover, certain conclusions on the effectiveness and efficiency of the selected iteration methods may not lose their generality since nearly all complex material nonlinearity is considered. Improvements of iteration techniques are also made in the following sections.

Another purpose is to summarize guidelines for the mesh design in analysing the failure of the Carsington Dam. They will guarantee reasonable and sufficiently accurate solutions, and hence, reliable conclusions.

All the numerical tests are carried out by modifying the program SAGE, which was developed by Chan (1986) as mentioned in Chapter 1. The formulations of selected iteration methods can be found in Appendix F.

3.1 Iteration Techniques for Material Nonlinearity

3.1.1 Selection of iteration methods

The Newton-Raphson or N-R iteration scheme is the classic method which is generally adopted in non-linear finite element analyses. In a certain loading step, the scheme can be expressed as

$$\begin{aligned} [K]^{i-1}\{\Delta u\}^{i} &= \{R\} - \{F\}^{i-1} , \\ \{u\}^{i} &= \{u\}^{i-1} + \{\Delta u\}^{i} , \end{aligned} \qquad (3.1)$$

in which

$[K]^{i-1}$ is the global stiffness matrix determined by the stress state of the previous iteration i-1,

$\{\Delta u\}^{i}$ is the incremental displacement vector to be solved at the ith iteration,

$\{R\}$ is the external load vector,

$\{F\}^{i-1}$ is the equivalent load vector corresponding to internal stresses at the i-1 th iteration,

$\{u\}^{i}$ and $\{u\}^{i-1}$ are total displacement vectors at the iterations i and i-1.

In the program SAGE, tolerances of both the relative error of displacement norm and stress deviations from the yield surface are adopted to judge the convergence.

The main drawbacks of the standard N-R method are :

1. it is time-consuming and expensive because of repeated reformation and factorization of the global stiffness matrix at every iteration.
2. it is not efficient in dealing with sharply changing stiffness or in determining the critical point at collapse.

Tremendous effort has been made in the past twenty years to develop new iteration methods and improve the solution techniques. However, a brief literature review shows that no universal method has been developed. In selecting the iteration method, only those suitable for material nonlinearity are considered. Besides effectiveness and efficiency, simplicity of formulation is also a main factor for the choices evaluated here.

Although there exist other classifications for the available iteration methods, here, we classify the relevant methods by the way they improve the standard N-R method. They can be classified into three categories:

1. acceleration scheme without reformation and factorization of the global stiffness matrix,
2. update scheme by modifying the original or factorized global stiffness matrix,
3. techniques to capture the critical point in

stability analyses.

The acceleration scheme can be expressed in the form of

$$[K]^i\{\Delta u\}^i = \{R\} - \{F\}^{i-1} \ ,$$
$$\{u\}^i = \{u\}^{i-1} + [a_{jj}]^i\{\Delta u\}^i \ , \qquad (3.2)$$

in which

$[K]^i$ has been factorized previously and will not change,
$[a_{jj}]^i$ is a diagonal matrix of the relaxation factors at the ith iteration. Other notations are the same as in eqn. 3.1.

Factor matrix $[a_{jj}]$ is used in this scheme to lead the solution of the displacement vector in a certain favorable direction, although the methods to determine each factor a_{jj} may be based on different theories. Taking a_{jj} as unity, we have the modified N-R method. However, its slow convergent speed is well known. Among all the acceleration schemes, the Aitken method, line search method, gradient method or conjugate gradient method are often used. However, the gradient methods are often used in geometrically nonlinear problems. By reviewing the literature, it is hard to say which of the other two is superior. The Aitken method is chosen for numerical tests because its formulation is simpler.

The matrix update methods, or the quasi-Newton methods provide a compromise between the standard and modified N-R methods. The convergence speed of the modified N-R method is slow because the actual change of the stiffness is not considered during iteration. The matrix update methods help accelerate the convergence by modifying the global stiffness matrix and reduce the cost by avoiding reformation at each iteration. Several techniques have been developed. One of the famous methods is the BFGS method. It was originally derived for symmetric matrices and the updated stiffness matrix still needs to be factorized. Later, improved methods have been developed. One in common use is the DM method which was developed by Dennis and Marwil (1982). The other one we choose is the TZ method which was presented by Tewarson and Zhang (1987). Those two methods are suitable for unsymmetric matrices and keep the sparcity of the factorized matrix. In the DM method for the LU factorization of [$\dot{K}$] (Appendix F), only matrix U is updated. In th TZ method for the LDU factorization, all the factorized matrices of L, D and U are updated. If L is updated first, we call the method TZ_L. If U is updated first, we call it TZ_U. If TZ_L and TZ_U are used alternately, we call it TZ_{LU}. We choose TZ methods because it has been reported that they require approximately 20% fewer iterations than the DM method.

The formulations of the Aitken, DM and TZ methods are introduced in detail in Appendix F.

Numerical damping, explicit displacement control and modified constant arc length methods are often used to solve the ill-conditioned equations when the system is approaching the critical point. Among those methods, the modified constant arc length method is found to be more effective, but its fomulation is more complex.

None of the above methods are studied due to the limited time available. However, the numerical tests show that the critical elevation can be found in the analyses of the Carsington Dam failure. By using the restart capacity in the program SAGE, the numerical solution can discern the critical elevation just before the failure within a range not more than 0.3m. This is accurate enough for engineering judgement, and the computation cost is not very high either.

3.1.2 Evaluation of effectiveness and efficiency

In the following study, we use the solution obtained by the Newton-Raphson method as the standard in appraising the selected methods, although the solution is approximate. This is because no theoretical solution can be found to include the complex material nonlinearity we are going to deal with. Both effectiveness and efficiency will be compared between different iteration methods. Here, the effectiveness is refered to the stability of convergence and the acceptable deviation of the solution from that of the N-R method. The efficiency is measured in the percentage of the computation time needed by a selected iteration method as compared with the time required by the N-R method.

In the available literature, the efficiency of a developed method is appraised by comparing iteration number or only the computation time required by reformation and solution of nonlinear equations. The actual efficiency in finite element analyses should be evaluated by considering the total time including stress calculation. This is because computation time for the stress calculation is by no means a small portion. As shown in Fig. 3.1, even for a very fine mesh the time needed for stress calculation is still about 30% of the total computation time which cannot be reduced by using any iteration methods in one iteration. The above value of 30% is taken on average from more than 200 examples. Therefore, the total computation time for one loading step is adopted as the base for comparison, and the efficiency is defined as computation time ratio R_t, i.e.

$$R_t = \frac{\text{Time for the selected method}}{\text{Time for the N-R method}} , \qquad (3.3)$$

in one loading step. The time reduction percentage P is also used and $P = (1 - R_t)$.

Obviously, the effectiveness and efficiency of an iteration method are dependent on the complexity of the nonlinearity. It is difficult to define the complexity quantatively. Reflecting on the intermediate results, the complexity of nonlinearity is determined by the change of stiffness, the amount of excess stresses to release after yield and the number of the elements between which the released stresses are distributed. Therefore, in view of the input information, four factors merit attention after the

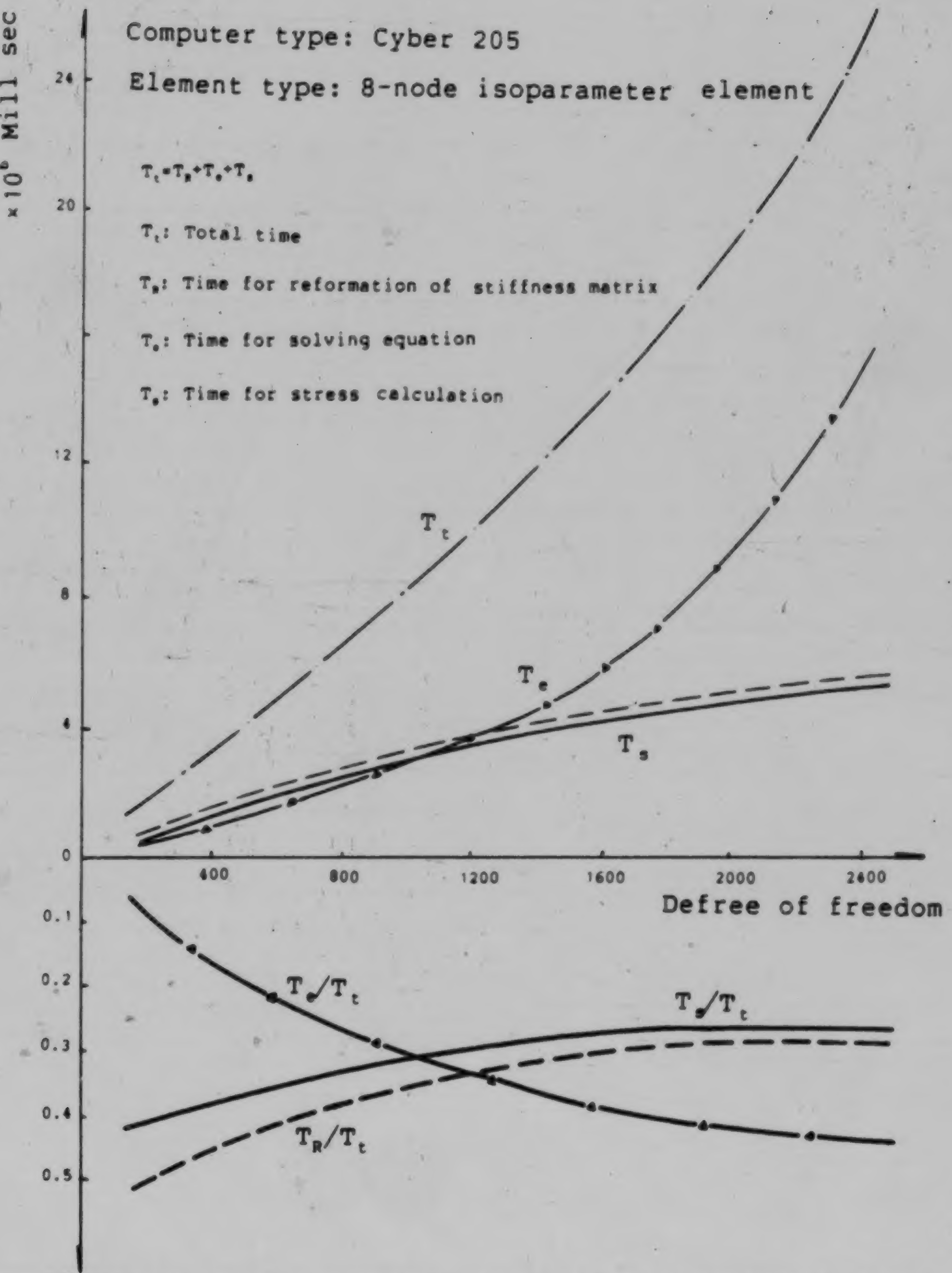

Figure 3.1: Average computing time of Newton-Raphson iteration

problem is clearly defined. They are

1. the prescribed reformation frequency of the stiffness matrix,
2. the total number of elements or the degrees of freedom,
3. the magnitude of load increments,
4. the error tolerance preset for the required accuracy.

The study will be carried out around the above four points.

The material nonlinearity includes non-linear elastic behavior, nonlinear strain-softening after peak, and sharp decreases of stiffness due to local collapses. The above non-linear behavior includes the main features of the meterial properties we may encounter in elastoplastic analyses.

More than 200 trial calculations have been carried out for the selected iteration methods. The performances are investigated through three groups of examples. They include very simple examples of loading tests of soil samples, simulation of the construction of an embankment as shown in Fig. 3.2 and trial analyses of the Carsington Dam failure which is described in detail in Chapter 5.

3.1.3 Improvement of iteration methods and result analyses

The trial calculations show that the standard Newton-Raphson method is the most effective and reliable method although it is generally not efficient. In the case

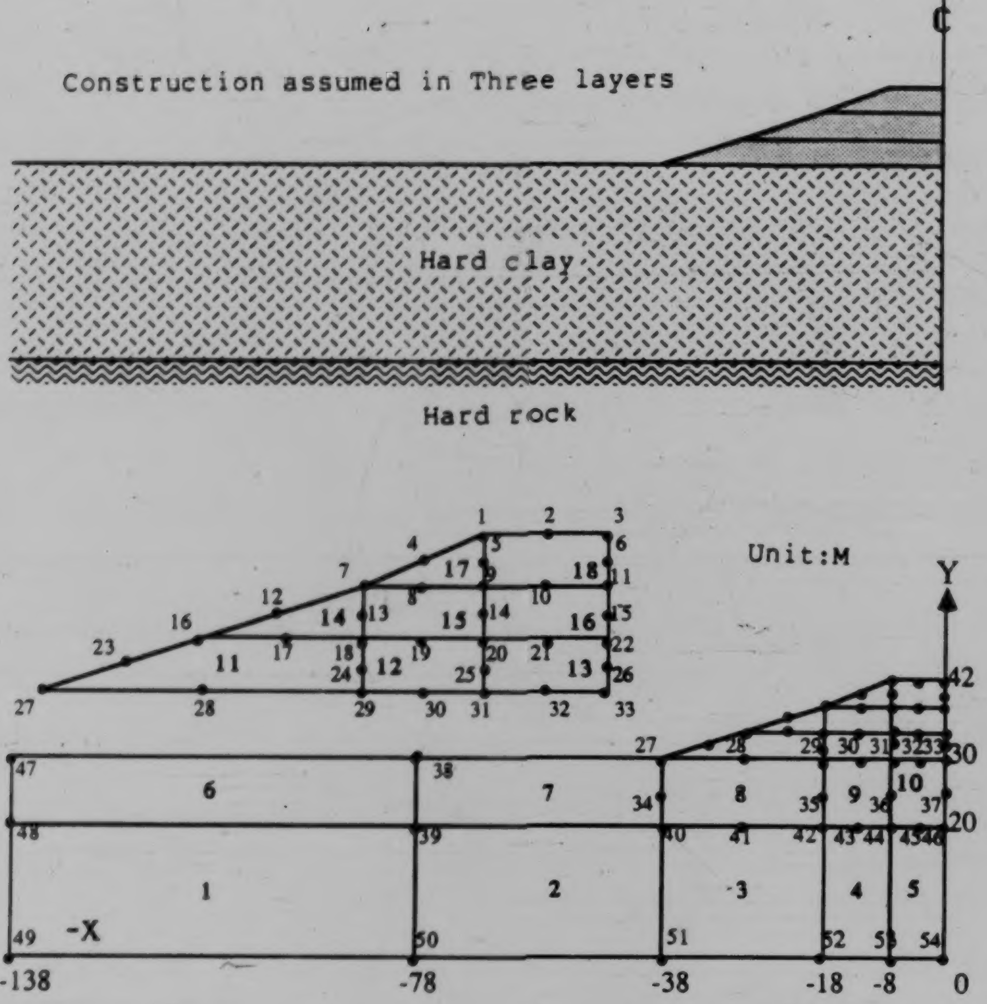
Construction assumed in Three layers
℄
Hard clay
Hard rock
Unit:M
Y
-X
1
2
3
4
5
6
7
8
9
10
11
12
13
14
15
16
17
18
19
20
21
22
23
24
25
26
27
28
29
30
31
32
33
34
35
36
37
38
39
40
41
42
43
44
45
46
47
48
49
50
51
52
53
54
-138
-78
-38
-18
-8
0
20
30
42

Figure 3.2: Construction of an embankment

of the failure of the Carsington Dam, no convergent solution can be obtained by any other selected iteration methods if the standard N-R method leads to divergence.

All other methods are subjected to slow convergence and even divergence if the nonlinearity is very pronounced. If we use any selected iteration method as it is, the only way to improve its performance is to reassemble the global stiffness matrix in time for certain unfavorable situations. Fig. 3.4 to 3.7 show the unfavorable situations for the selected methods. The examples in Fig. 3.4 to 3.7 are calculated with all other conditions being the same. The convergence behaviors shown in the above Figures also indicate that the TZ and DM method are more effective for unfavorable conditions than the Modified N-R method or Aitken method. This conclusion has also been supported by many other examples, e.g. the performance of the TZ and DM method for very complex problem as listed in Table 3.3. Without any improvement, direct use of any selected method is not efficient in unfavorable conditions as compared with the the N-R method.

Certainly, reformation frenquency can be fixed before the calculation. However, the suitable frequency is very difficult to preset. Reassembling the stiffness matrix too frequently will reduce the efficiency while delayed reformation may cause slow convergence or even divergence. In order to reassemble it in due time, the norms of relative displacement errors and unbalanced forces are chosen to

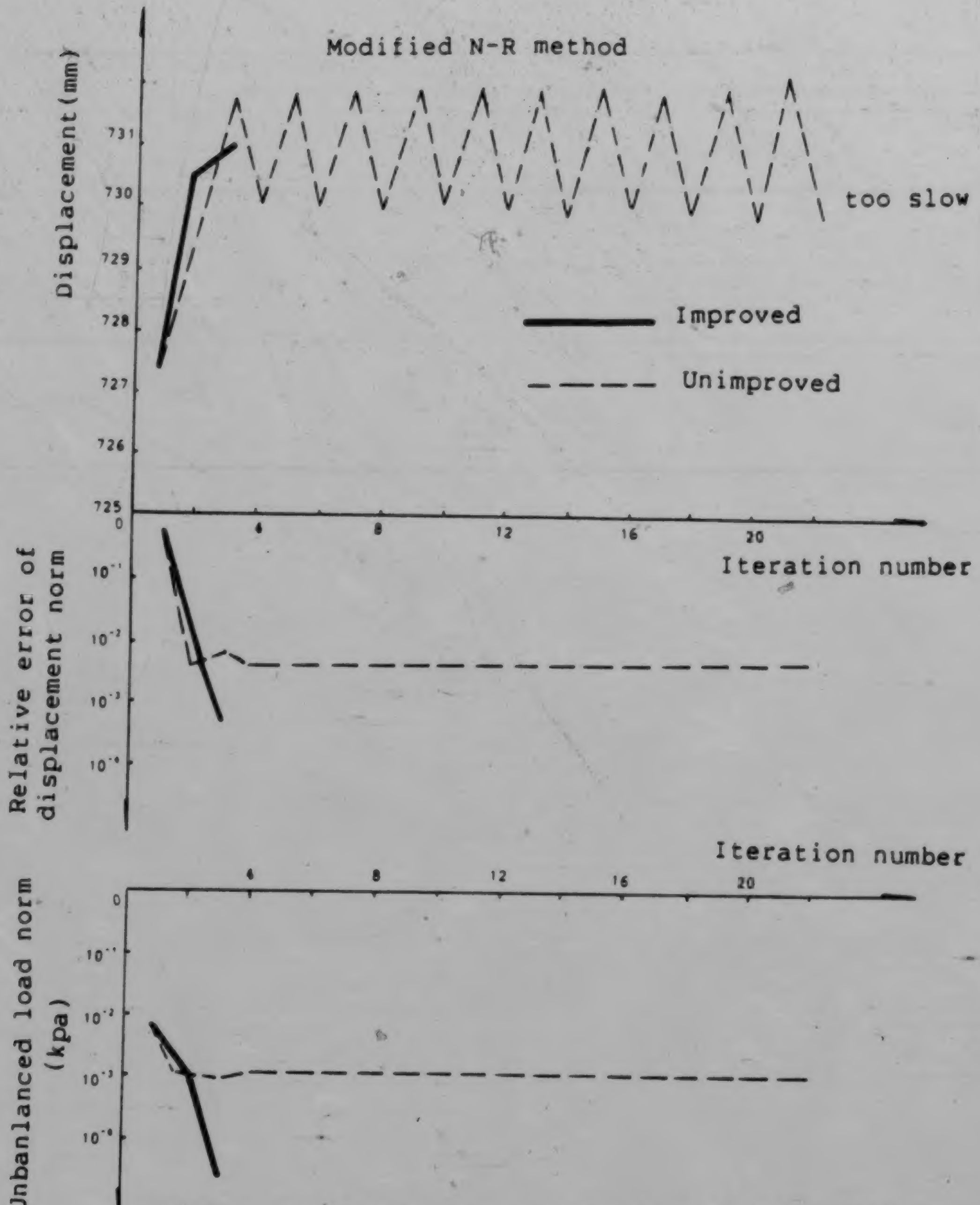

Figure 3.3: Convergence behavior of the modified N-R method (A)

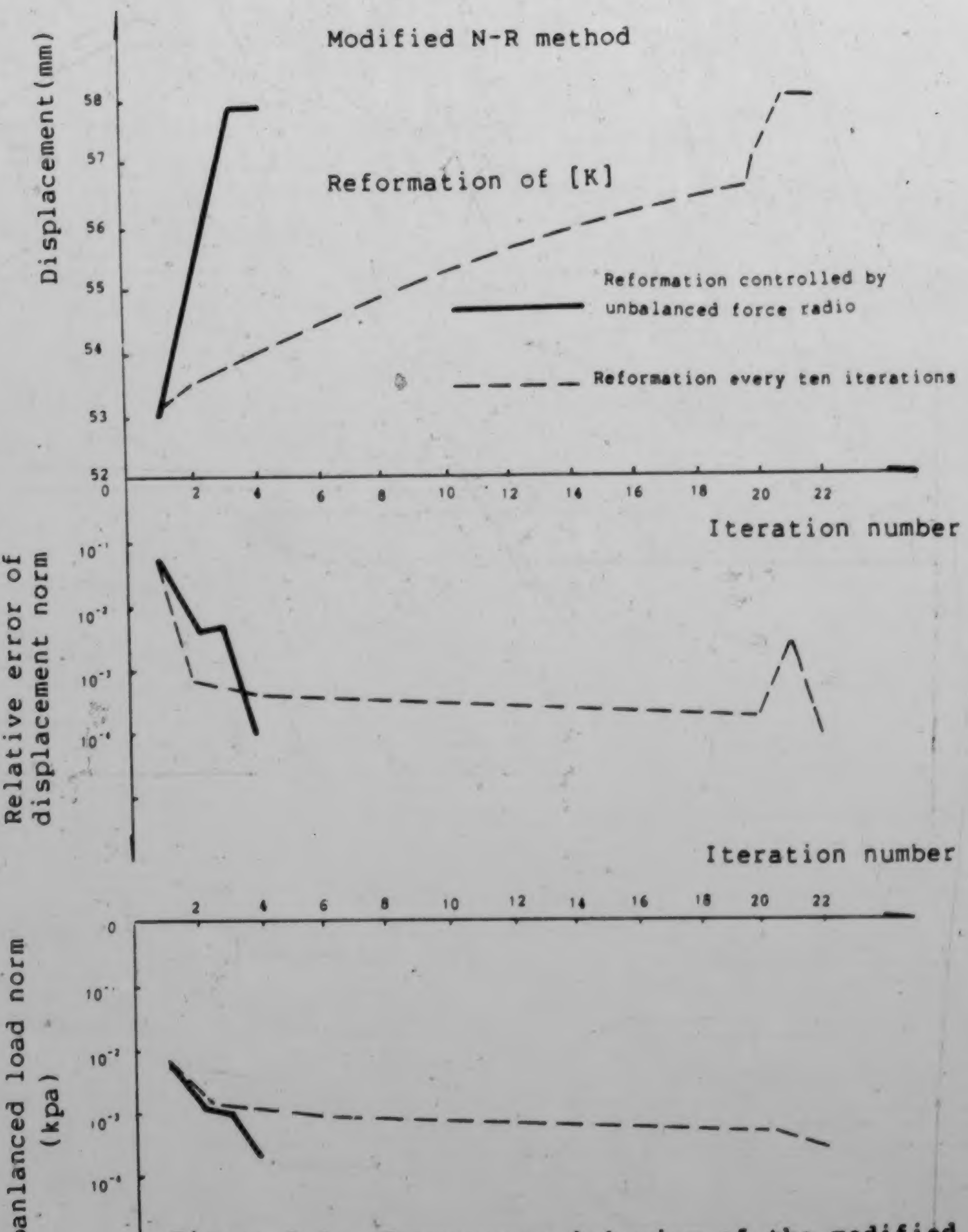

Figure 3.4: Convergence behavior of the modified N-R method (B)

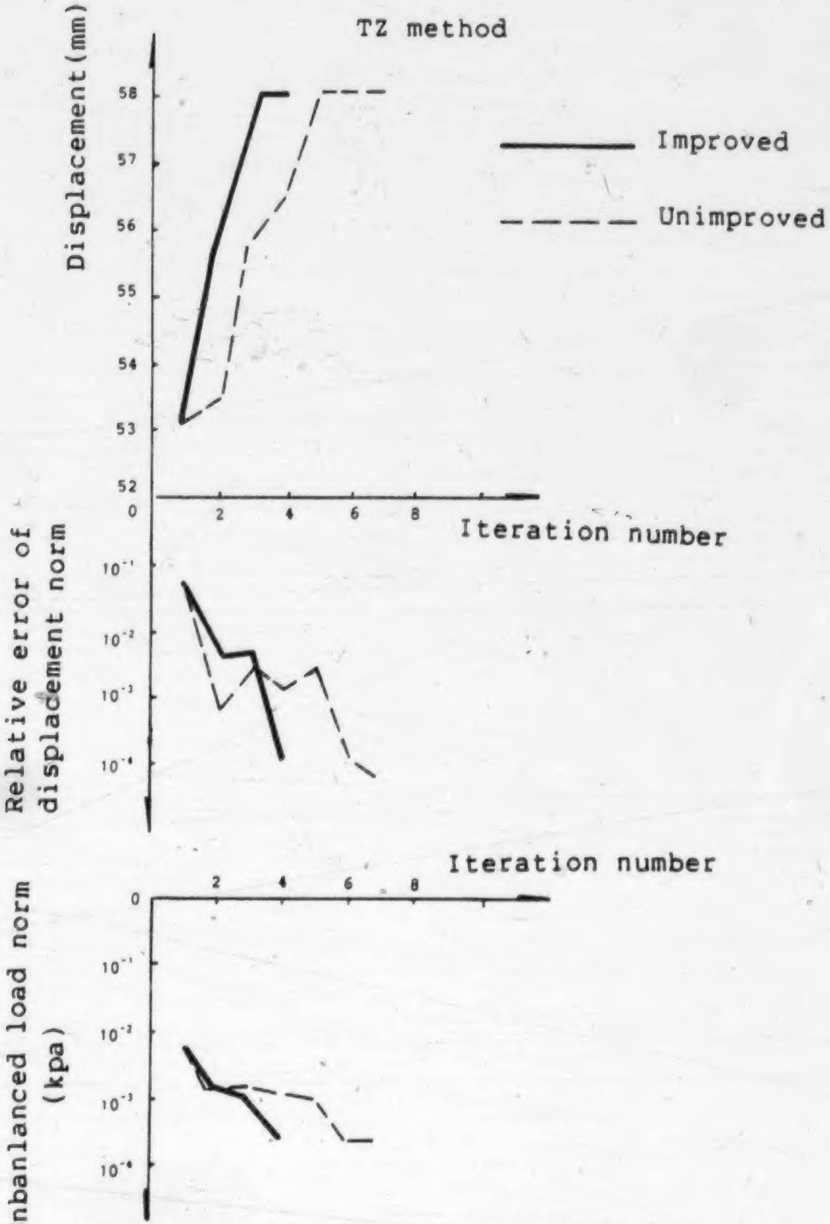

Figure 3.5: Convergence behavior of the TZ method

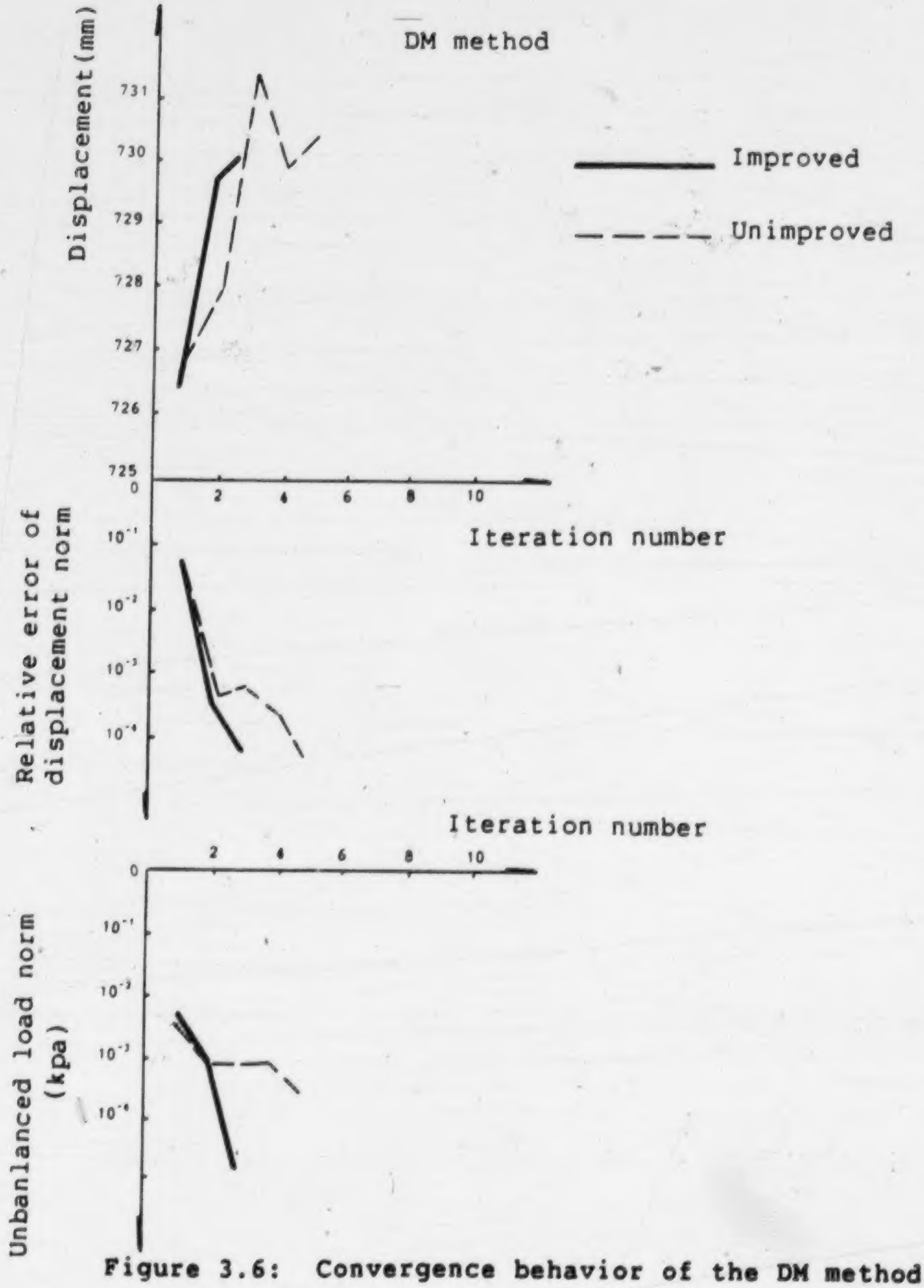

Figure 3.6: Convergence behavior of the DM method

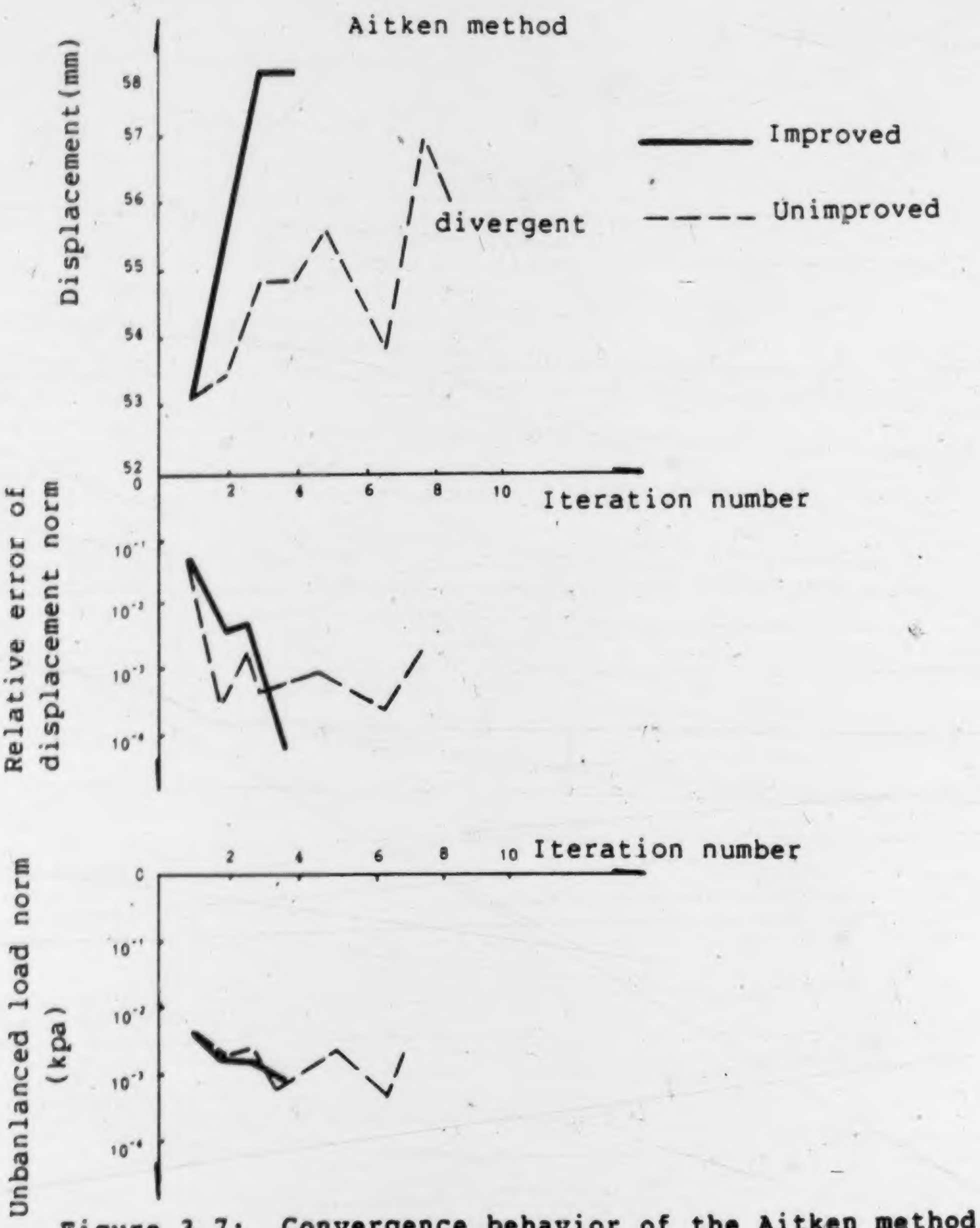

Figure 3.7: Convergence behavior of the Aitken method

control the reformation. The above figures also show the characteristics of these variables in succeeding iterations under unfavorable conditions. For the TZ, DM and Aitken method, by experience, the suitable criteria for updating the global matrix might be

$$e_n^i > 1.1e_n^{i-1}$$
$$F_{unb}^i > 1.1F_{unb}^{i-1} , \qquad (3.4)$$

in which

e_n: norm of the relative displacement error,

F_{unb}: norm of the unbanlanced load,

i and i-1 denote the ith and (i-1)th iterations.

The above criteria are very strict and only a factor of 1.1 is used to allow undulation of e_n and F_{unb}. This is because no undulation of e_n and F_{unb} has been found in any efficient iteration process in all the trial calculations.

As to the modified N-R method, the above criteria are not generally suitable, because e_n and F_{unb} may not undulate under some unfavorable situations as shown in Fig. 3.3. For such cases, the ratio of unbalanced force norm is used to control the reformation frequency of the stiffness matrix. The ratio r_F^i is defined as

$$r_F^i = \frac{F_{unb}^i}{R_{ext}} , \qquad (3.5)$$

in which R_{ext} is the norm of the total external forces applied in this loading step. By experiences, if $r_F^i > 0.2$, reformation is needed. A large value of r_F^i indicates pronounced nonlinearity for which the modified N-R method is not suitable.

After the above techniques were implemented into the program, all the unfavorable cases have been recalculated. The results are satisfactory and the computation time ratio is less than 1.0 for all the selected methods as compared with the N-R method. Fig. 3.3 to 3.7 also shows the performance of the selected methods after improvement. The comparison of results from the trial analyses are listed in Tables 3.1 to 3.3.

From Table 3.1 to 3.3, it can be seen that the percentage of time reduction is between 15 to 30% for simpler problems, and between 10% to 18% for the complex problems. In the above comparison, we use the computation time for the whole loading step because it reflects the real efficiency, although the efficiency for one unfavorable sub-incremental loading step is much higher than that before improvement.

In practice, a large number of degrees of freedom is generally related with a complex stress distribution, and therefore a fine mesh is needed. Although the time percentage for stress calculation will decrease (Fig. 3.1), the efficiency will generally not increase for a fine mesh, especially for the Aitken or modified N-R method as shown in the above tables. For complicated problems with fine meshes,

Table 3.1 Performance of the selected methods, elasto-plastic materials under associated flow law

Trial Calculation: Construction of an Embankment (Final Loading Step)

Method	Before Improved			After Improved		
	Computation Time Ratio	Range of Relative Error		Computation Time Ratio	Range of Relative Error	
		Maximum Displacement	Maximum Stress		Maximum Displacement	maximum Stress
Modified N-R	div.	div.	div.	0.723	3.76×10^{-6}	1.9×10^{-3}
Aitken	div.	div.	div.	0.680	2.6×10^{-5}	2.7×10^{-3}
TZ_L	0.864	1.1×10^{-5}	5.3×10^{-4}	0.860	3.7×10^{-6}	1.7×10^{-3}
TZ_U	1.053	1.4×10^{-5}	3.9×10^{-4}	0.760	1.1×10^{-5}	1.7×10^{-3}
TZ_{LU}	0.900	2.5×10^{-5}	2.6×10^{-4}	0.758	2.2×10^{-5}	1.8×10^{-3}
DM	0.913	1.5×10^{-5}	1.3×10^{-3}	0.753	1.5×10^{-5}	1.3×10^{-4}

Note: Convergence tolerance relative error of displacement norm is 0.0001.
Convergence tolerance yield function F=0 is 0.0005 to 0.005.

Table 3.2 **Performance of the selected methods, elasto-plastic materials under the non-associated flow law**

Trial Calculation: Construction of an Embankment (Final Loading Step)

Method	Before Improved			After Improved		
	Computation Time Ratio	Range of RelativeError		Computation Time Ratio	Range of Relative Error	
		Maximum Displacement	Maximum Stress		Maximum Displacement	Maximum Stress
Modified N-R	0.961	1.1×10^{-5}	7.5×10^{-4}	0.851	1.1×10^{-5}	7.5×10^{-4}
Aitken	0.864	6.9×10^{-5}	7.8×10^{-3}	0.726	6.2×10^{-5}	7.7×10^{-3}
TZ_L	0.948	2.9×10^{-5}	6.0×10^{-4}	0.844	2.9×10^{-5}	4.5×10^{-4}
TZ_U	0.889	1.4×10^{-5}	7.5×10^{-4}	0.805	1.4×10^{-5}	7.5×10^{-4}
TZ_{LU}	0.998	1.1×10^{-5}	7.5×10^{-4}	0.812	1.1×10^{-5}	7.5×10^{-4}
DM	0.832	1.5×10^{-5}	3.0×10^{-4}	0.783	1.4×10^{-5}	3.0×10^{-4}

Note: Convergence tolerance relative error of displacement norm is 0.0001.
Convergence tolerance yield function F=0 is 0.0005 to 0.005.

Table 3.3 Performance of the selected iteration methods for complex problems

Trial Calculation: The Carsington Dam Failure (Loading Step 4)						
Number of Sub-load increment		1	2	3	3	5
Displacement Error Tolerance		0.001	0.001	0.001	0.001	0.001
stress Error Tolerance		0.005	0.005	0.005	0.005	0.001
Prescribed Reformation Frequence		2	2	2-4	set within program	set within program
Computation Time Ratio	N-R	div	div	1.0	1.0	1.0
	Modified N-R	div	div	div	0.895	0.852
	Aitken	div	div	div	0.905	0.858
	TZ	div	div	1.18	0.840	0.830
	DM	div	div	1.15	0.837	0.820
Range of Relative Error	Stress			<2.0%	<2.0%	<0.01%
	Maximum Δu			<1.8%	<1.6%	<0.10%
	Maximum Δv			<1.0%	<1.0%	<0.01%

Note: The solution of N-R method with 5 sub-load increments is taken as the standard.
Δu is horizontal displacement increment.
Δv is vertical displacement increment.

the DM and TZ methods are more suitable.

Increasing the magnitude of load increments means increasing of nonlinearity in each loading or sub-loading step. In simulating dam construction, the load increment is controlled by the thickness of each layer. In order to avoid too fine a mesh, the thickness of each layer cannot be too small. Layers of 3 to 5 meters high are used in the trial calculations. The weight of soils of each layer is further divided into sub-load increments to decrease nonlinearity, e.g. 20% of weight per a sub-increment with 5 sub-increments in all. The influence of load increment magnitude is shown in Table 3.4.

In the further analyses of the Carsington Dam, it is suggested that at least 3 sub-increments for each layer should be used when nonlinear behavior has been developed. Trial calculations also shows that 5 sub-increments are sufficient to cope with the complexity near failure, if the thickness of each layer is less than 3.5m.

Adoptation of large error tolerances will obviously decrease the computation time and lead to easy convergence, but may yield unacceptable solution with excessive errors. Table 3.5 shows the influence of the error tolerances on the accuracy of the final results. The influence of the stress error deviated from the yield function seems very small within the trial tolerance range between 0.01 kpa to 0.0001 kpa. The main influence is caused by the dispacement error tolerance. Its suitable range should guarantee a solution

Table 3.4 Influence of the magnitude of load increments

Model: Brittle Materials with the Associated Flow Law

Trial Calculation: Construction of an Embankment

Number of Sub-load Increment	Equivalent Layer Thickness (m)	Convergence Behavior		Relative Error Range of	
		N-R	Selected Methods	Maximum Displacement	Stress
1	4.00	div	div		
2	2.00	div	div		
3	1.33	good	better after improved	<0.0002	<0.001
5	0.80	good	better after improved	<0.0005	<0.0008
10	0.40	very good	very good	taken as Standard	

Note: Convergence tolerance relative error of displacement norm is 0.0001.
Convergence tolerance yield function F=0 is 0.0005 to 0.005.

with acceptable errors, and save computation time. The relative error of the displacement norm is suggested to be around 0.001 in this research. The tolerance of 0.0001 will decrease the efficiency of the selected methods too much, while tolerance of 0.01 will cause large stress errors of about 5%, which are generally unacceptable.

As mentioned in the previous chapters, the solution will be finite and even infinite when local collapses takes place. For example, stiffnes will change sharply and finite stresses will be released after cracking even with very small load increments. It is not the task of this thesis to study the convergence conditions of such cases. However, experience has shown that the standard N-R methods can yield acceptable solutions for the brittle models. When the automatic reformation of the global stiffness matrix is implemented in the computer program, no trouble has been found in trying other methods. It should be mentioned that the criteria given in eqn. 3.4 and 3.5 are problem dependent. Therefore, theoretical study is needed for the convergence conditions.

Examples of the best selected iteration method are listed in Table 3.6 and 3.7. It can help us to draw the conclusions.

3.1.4 Conclusions on the iteration techniques

1. The Aitken, TZ and DM iteration methods are implemented in the program SAGE. Together with the

Table 3.5 Influnce of the convergence tolerance

Example: Construction of an Embankment
Brittle Material, Non-associated Flow Law

Trial Calculation Group	Convergence Tolerance		Range of Relative Errors for Maximum Values				Total Calculation Time Ratio (Maximum)	
	Relative Error of Displacement	Stress (kpa)	Displacement		Stress			
			N-R	Other Method	N-R	Other Method	N-R	Other Method
1	0.0100	0.0005	$<1.6\times10^{-4}$	$<2.8\times10^{-4}$	$<9.0\times10^{-3}$	$<4.8\times10^{-2}$	0.571	0.545
2	0.0050	0.0005	$<7.0\times10^{-4}$	$<2.0\times10^{-3}$	$<1.2\times10^{-2}$	$<3.0\times10^{-2}$	0.572	0.591
3	0.0010	0.0005	$<7.0\times10^{-5}$	$<4.0\times10^{-4}$	$<3.0\times10^{-3}$	$<1.6\times10^{-2}$	0.824	0.686
4	0.0005	0.0005	$<7.0\times10^{-5}$	$<4.0\times10^{-4}$	$<3.0\times10^{-3}$	$<1.4\times10^{-2}$	0.871	0.722
5	0.0001	0.0100	$<1.0\times10^{-6}$	$<2.0\times10^{-5}$	$<1.0\times10^{-4}$	$<1.8\times10^{-3}$	0.993	0.896
6	0.0001	0.0010	$<1.0\times10^{-6}$	$<1.0\times10^{-6}$	$<1.0\times10^{-4}$	$<1.0\times10^{-4}$	0.998	0.901
7	0.0001	0.0001	taken as standard					0.903

Table 3.6 Examples of the best iteration method in certain situations

Group		1	2	3	4	5	6
Complexity of the Problem		very high	high	high	fairly high	fairly high	low
Error Tolerance	Displacement Stress	0.001 0.001	0.0001 0.0001	0.001 0.005	0.0001 0.0001	0.0001 0.0001	0.005 0.01
Method	Best Method	TZ_{LU}&DM	DM	TZ_U	M-N-R	Aitken	M-N-R
M-N-R	P (%)	11	44	32	29	27	32
	e_s (10^{-3})	9.0	4.6	12.1	0.08	3.8	7.0
	e_d (10^{-4})	7.0	0.04	0.7	0.01	0.04	17
Aitken	P (%)	10	43	32	27	32	29
	e_s (10^{-3})	26.1	7.9	12.5	8.5	3.5	15.4
	e_d (10^{-4})	18.5	1.2	1.1	0.07	0.2	55.3
TZ_L	P (%)	17	34	26	16	23	21
	e_s (10^{-3})	21.2	3.1	8.7	0.05	2.5	10.7
	e_d (10^{-4})	11.8	0.5	0.6	0.03	0.31	60.2

P: Computation time reduction (%).
e_s and e_d: Relative error of the maximum stress and displacement.

Table 3.7 Table 3.6-continued

Group		1	2	3	4	5	6
Complexity of the Problem		very high	high	high	fairly high	fairly high	low
Error Tolerance	Displacement Stress	0.001 0.001	0.0001 0.0001	0.001 0.005	0.0001 0.0001	0.0001 0.0001	0.005 0.01
Best Method Group		TZ_{LU}&DM	DM	TZ_U	M-N-R	Aitken	M-N-R
TZ_U	P (%)	16	44	35	19	24	20
	e_s (10^{-3})	15.4	3.2	8.0	0.08	1.7	8.3
	e_d (10^{-4})	9.6	0.05	0.6	0.01	0.10	55.6
TZ_{LU}	P (%)	16	44	24	19	24	19
	e_s (10^{-3})	15.1	2.8	25.1	0.07	1.8	9.5
	e_d (10^{-4})	9.0	0.55	6.8	0.01	0.22	50.8
DM	P (%)	16	46	31	22	24	21
	e_s (10^{-3})	18.3	4.2	10.4	0.03	1.7	11.4
	e_d (10^{-4})	10.8	0.06	0.5	0.01	0.00	52.7

P: Computation Time Reduction (%).
e_s and e_d: Relative error of the maximum stress and displacement.

modified Newton-Raphson method, their effectiveness and efficiency for material nonlinearity have been investigated by more than 200 trial calculations.

2. Without proper control of the reformation frequency of the global stiffness matrix, the selected iteration methods may cause slow convergence or even divergence in certain complex situations. With the automatical control, all the above methods work effectively and efficiently.
3. If the above methods are applied to similar calculation conditions, the computation time can be reduced by 10-30% as compared with the time needed by using the standard Newton-Raphson method.
4. The suitable convergence tolerance of the norm of relative displacement errors is suggested to be about 0.001 and the stress error tolerance is chosen to be around 0.005 kpa for the effective and efficient applications of the selected methods.
5. The magnitude of load increments should be limited within reasonable range. In simulating the construction of rock-earthfill dams, the rise of the dam height, or equivalent rise ΔH obtained by dividing the weight should not be too large. The suitable range of ΔH is about 0.5 to 1.0 m. This range is suggested only for cases similar to the Carsington Dam.
6. Suitable working conditions for the selected

iteration method are listed in Table 3.8. Although summarized from a limited number of examples, it can guide the selection of suitable iteration methods in this research.

3.2 Mesh Study

3.2.1 Basic requirements for mesh design

Basic requirements and suggestions for the mesh design can be found in many early published papers on the finite element method. The main points are:

1. suitable types of elements should be chosen for the problem concerned,
2. the nodes of each element should be correctly numbered and its shape should be properly designed,
3. gradual transition from very small to very large elements is suggested,
4. the number of elements should be large enough, or the mesh should be dense enough to quarantee a solution with the required accuracy,
5. it is recommended that the density of the elements should reflect the change of stress and strain distribution.

Experience has shown that 8-node isoparametric elements are suitable for elastoplastic finite element analyses. This type of element is mainly used in these analyses. A few 6-node curve-sided triangular elements are also used to fit

Table 3.8 General performances of the selected iteration methods

Method	Working Condition		
	Comlexity of Nonlinearity	Number of D.O.F.	Convergence Tolerance
Modified N-R	Effective except for very high nonlinearity. Convergence speed is slow but very efficient for simple cases.	Most suitable for a small number of D.O.F., suitable for fine mesh only if nonlinearity is low.	probably most stable for small tolerance.
Aitken	Similar to modified N-R method but with higher convergence speed, may cause divergence in complex cases, most suitable for not too complicated cases.	Similar to modified N-R method.	probably most unstable for small tolerance.
TZ	Most suitable for high nonlinearity, less efficient than M-N-R and Aitken method in simple promlems.	Suitable for all cases but less efficient for more degrees of freedom as compared with itself. More suitable than M-N-R & Aitken for very fine mesh with high nonlinearity.	Fairly stable for small tolerance.
DM	Similar to TZ but more efficient than TZ in less complicated cases.	Similar to TZ method.	Same as above.

Note: Reformation of the global stiffness matrix in time is needed for all the above methods in unfavorable situations.

geometric boundaries when necessary.

Badly shaped elements will yield zero or negative values of the Jacobian determinant in local coordinate transformations and hence yield wrong solutions. In elastoplastic analyses, if elements are shaped too far away from a square, even with a positive Jocobian determinant, the convergence behavior in this element will be abnormal.

Numerical tests have been conducted by Chan(1986) to determine the limit of aspect ratio for 8-node isoparametric elements in normal working condition. According to his conclusion, the relative displacement error would not exceed 2% for an aspect ratio as high as 10,000 when double precision arithmetic is used. The corner angle and side curvature of each 6 or 8-node element should be controlled within certain limits. By experience, those limits are suggested to be between 15 and 165 degrees for the corner angles and between 0 to 1/4 for the ratio of arc height to chord length. Here, the chord length is referred to the distance between two corner nodes of a curved side, while the arc height is referred to the distance from the mid-sided node to the chord. Gradual transition from very small to large elements can avoid bad shapes and trace the sharp change of stress and strain distribution.

It is well known that the density of a mesh and the total number of the elements influence the accuracy of the solution. Although the relationship between the element number and obtained accuracy has been studied theoretically for the linear elastic case, there is no available guideline in this repect for practical geotechnical engineering problems such as landslides and dam failures. The density of the mesh seriously affects the computation time, hence, the computation cost, especially for complex nonlinear problems. Therefore, it is important to answer the question how coarse a mesh can still yield an acceptable solution.

If the density of the elements is arranged according to the stress distribution, the sharp stress and strain change can be reflected by a locally densified mesh while economical benefits in computation time can be gained from a coarse mesh design in the area where the stresses are comparatively evenly distributed. However, this technique needs experience.

3.2.2 Objectives and methods of mesh study

The trial calculation has shown that the analysis of the Carsington Dam failure is very expensive. The effective calculation time on the super computer Cyber 205 amounts to about 9,000 seconds for one working condition of the dam, which costs about $4500. Considering the adjustment of parameters and trial calculations to catch the critical point of stability, one analysis needs $10,000. In order to cut down the budget for further reseach, a mesh study is designed. The main objective of the mesh study are

1. to investigate the influence of mesh density on the computational results.

2. to investigate the feasibility of replacement of the conventional large mesh for the foundation by an elastic layer with an equivalent elastic modulus.
3. to study guidelines of mesh design and select suitable meshes for further research.

It should be mentioned here, the conclusions made from the above research are not only problem dependent but also dependent on personal skills in the mesh design. Measures are taken to eliminate the artificial factors.

All meshes for numerical experiments are designed in compliance with the basic requirements. The input information has been checked with a data treatment program so that neither ill-noded nor badly-shaped elements exist. However, no special attention has been paid to the gradual transition from very small to large elements, since experience needed to be gained.

As far as the mesh information is concerned, the computation times are dependent on the number of construction layers designed to simulate the construction sequence and the length of the global stiffness matrix. This length is highly dependent on the node numbering skill of the designers. The CM and RCM methods of band width optimization are adopted in the above program and the length of the global stiffness matrix is optimized to be as short as possible so that the effect on computation time due to personal skill is basically eliminated.

The main characteristics in the failure of rock-earthfill dams are chosen for comparison, including

1. the critical height of the dam beyond which it will fail,
2. displacement and strain distribution,
3. stress distribution,
4. displacement vector increments just before failure.

The very dense mesh used in the first trial calculation of the Carsington Dam is chosen as the first example. The same material models and parameters are adopted for the other less dense meshes. The description of the material models and parameters can be found in Section 5.1.2. The material nonliearity is complicated enough to provide useful guidelines for further calculations. The nonlinearity includes nonlinear elastic behavior and softening rate, brittle models. The adopted strengths are on the safe side. Thus, the calculations until failure can be completed.

3.2.3 Comparison of the results from different meshes

Three meshes with different density are designed for comparison as shown in Fig. 3.8. The large conventional foundation is adopted for all meshes but not shown in the figure. It extends 12 times dam height H in both upstream and downstream directions and 5 times H in depth. The main features of the three meshes are listed in Table 3.9.

The main results obtained from the three meshes are listed in Table 3.10 for comparison. The relative error is

Very dense mesh

521 element 1521 Nodes stiffness matrix size=373,210

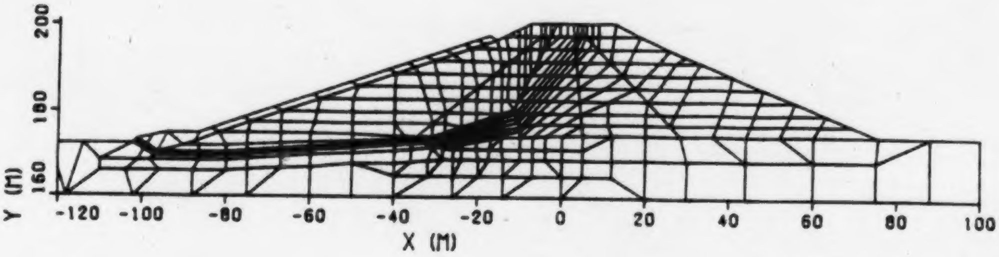
200
180
160
Y (M)
-120
-100
-80
-60
-40
-20
0
20
40
60
80
100
X (M)

Dense mesh

230 element 680 Nodes stiffness matrix size=107,406

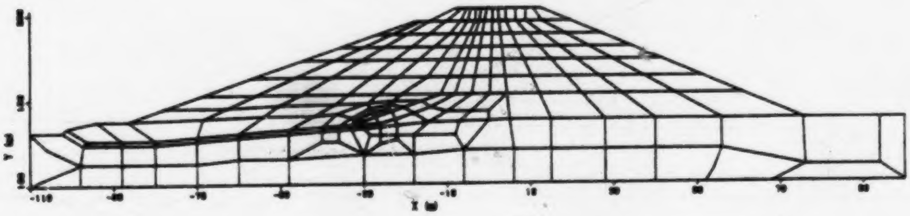

Coarse mesh

115 element 332 Nodes stiffness matrix size=29,322

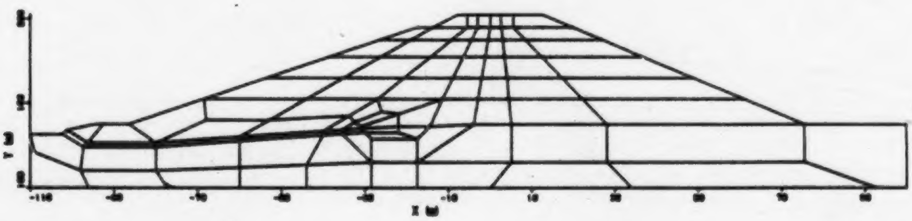

Figure 3.8: Comparison of different meshes

estimated by taking the results from the very dense mesh as the unity. Since the critical dam heights just before the failure are different for the three meshes, the critical loads are also different. Although the difference between the critical loads is very small, only corresponding to 0.30 to 0.6m thick of the fill, its influence on the plastic deformation is appreciable near failure. The relative error is estimated from the construction stage of EL. 195.0m, at which the total load is same for all meshes.

Table 3.9 Main features of the Meshes

Density	Very Dense	Dense	Coarse
Element	521	230	115
Node	1521	680	332
Stiff Matrix Length	373,210	107,404	29,332
Maximum Aspect Ratio	35	10	18
Side Curvature	flat	flat	flat
Corner Angle°	25 to 155	25 to 155	23 to 157
Element Area Transition	good	not good in the boot	bad in the boot

Note: The boot is the extension of the core (Fig. 3.9)

Table 3.10 shows that all the meshes yield acceptable results when they are used to make engineering judgement, though the relative strain and displacement errors of the coarse mesh seem a little bit higher. The computation time by using the coarse mesh is only 6.1% of the time needed by using the very dense mesh.

The critical dam height is determined by the sharp increase of the displacement at node A in the boot as shown in Fig. 3.9. At lower loading levels at which plastic deformations are not pronounced, the coarse mesh looks stiffer since the degrees of freedom are much less. When the loading level goes higher and higher, the plastic deformation develops more quickly than in denser meshes.

Table 3.10 Comparison of main results of meshes with different densities

Density	Very Dense	Dense	Coarse
Computing Time (sec)	9000	1050	550
Critical Height Just before Failure	EL. 198.0m	EL. 197.4m	EL. 197.7m
Relative Error of Max. Displ.	0.0%	3.8%	6.2%
Relative Error of Max. Strain	0.0%	4.2%	7.8%
Relative Error of Max. Stress	0.0%	2.2%	4.6%

As to the dense mesh, displacements increase in the same manner and are much closer to that obtained from the very dense mesh. The same situation can be also found in Fig. 3.10, where the toe movements are compared. The critical height of the coarse mesh is between those of the dense mesh and very dense mesh. A simple conclusion that a coarser mesh

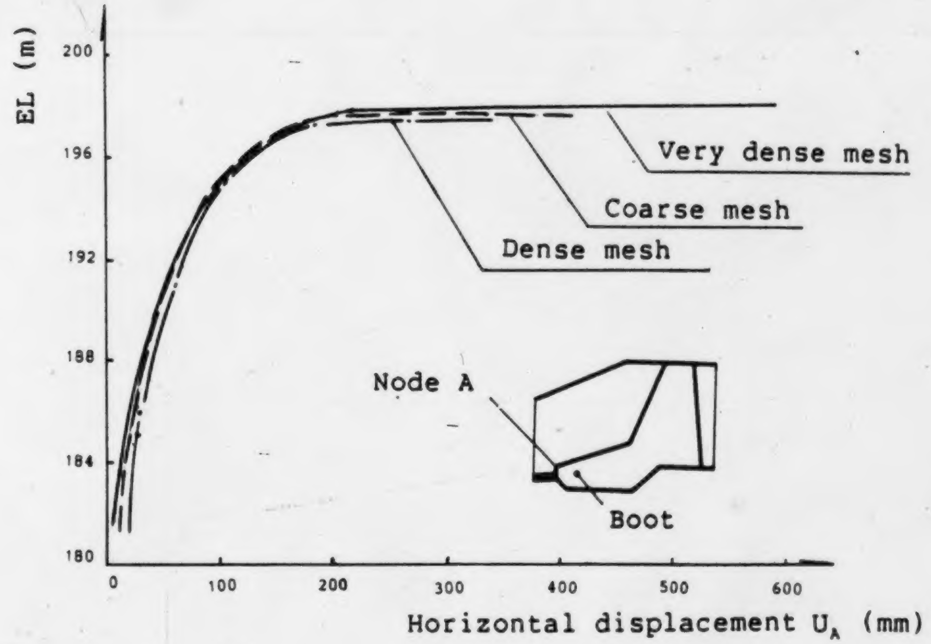

Figure 3.9: Mesh study - comparison of the maximum displacement

causes earlier failure cannot be made. One possible explanation might be that the three meshes are not geometrically similar to each other. Obviously, different arrangements of elements may cause different results. However, the difference between the critical height is within 0.6m. For a dam of 25m high, this is acceptable when used in practice.

Comparison between horizontal and vertical displacement fields before failure are shown in Fig. 3.11. and Fig. 3.12, while the comparison of vertical strains along the dam axis is shown in Fig. 3.13. All the deformation values are taken from one sub-loading step before failure, corresponding to 0.15m of the dam height. The deformation quantities near the critical height are less important. Nevertheless, the deformation patterns are the same for all the meshes, e.g. high shear strain gradients in the yellow clay layer (Fig. 3.11) and large settlement in the middle of the core (Fig. 3.12) can be clearly observed.

The strain distributions in Fig. 3.13 are comparable between the three meshes. The coarser mesh has a less even strain distribution. Larger strains can be found near the foundation, while smaller values can be found near the top of the dam. This also reflects the different response of the three meshes at different loading levels.

Stress distributions of the three meshes are shown in Fig. 3.14. The force equilibrium is always maintained whenever a convergent solution is obtained. The difference

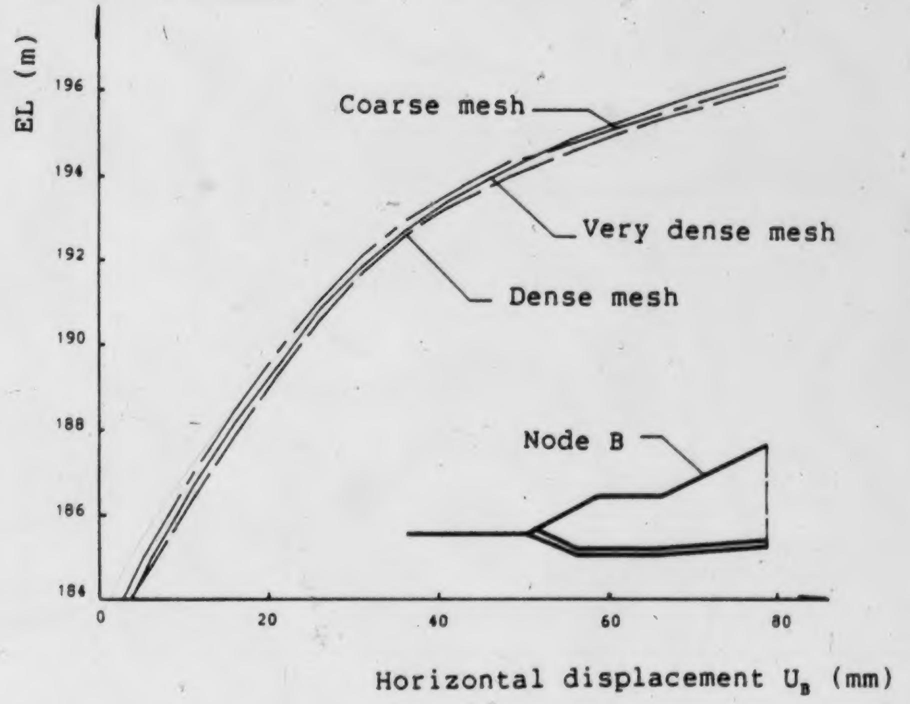

Figure 3.10: Mesh study - Comparison of toe movements

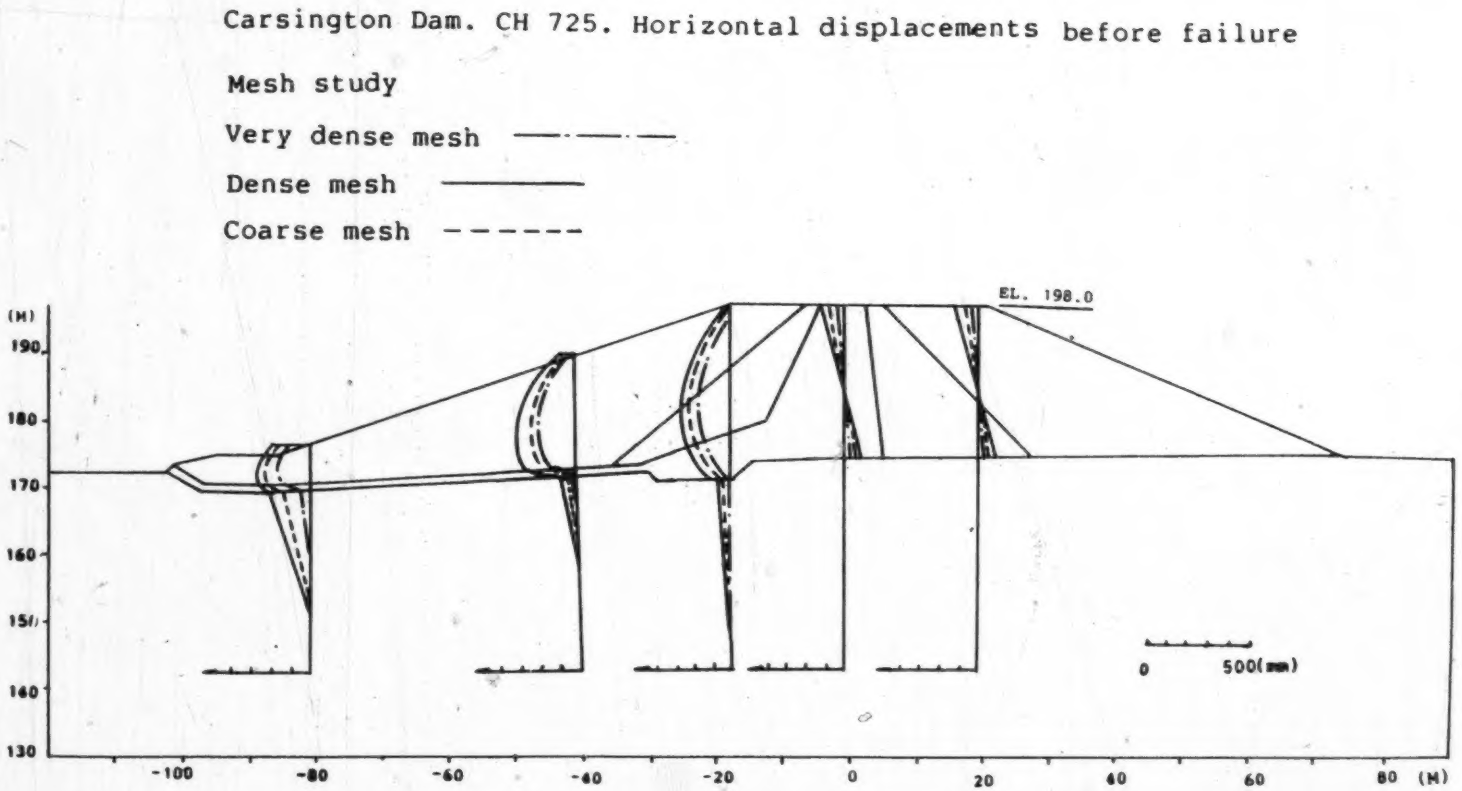

Figure 3.11: Mesh study - Comparison of horizontal displacements

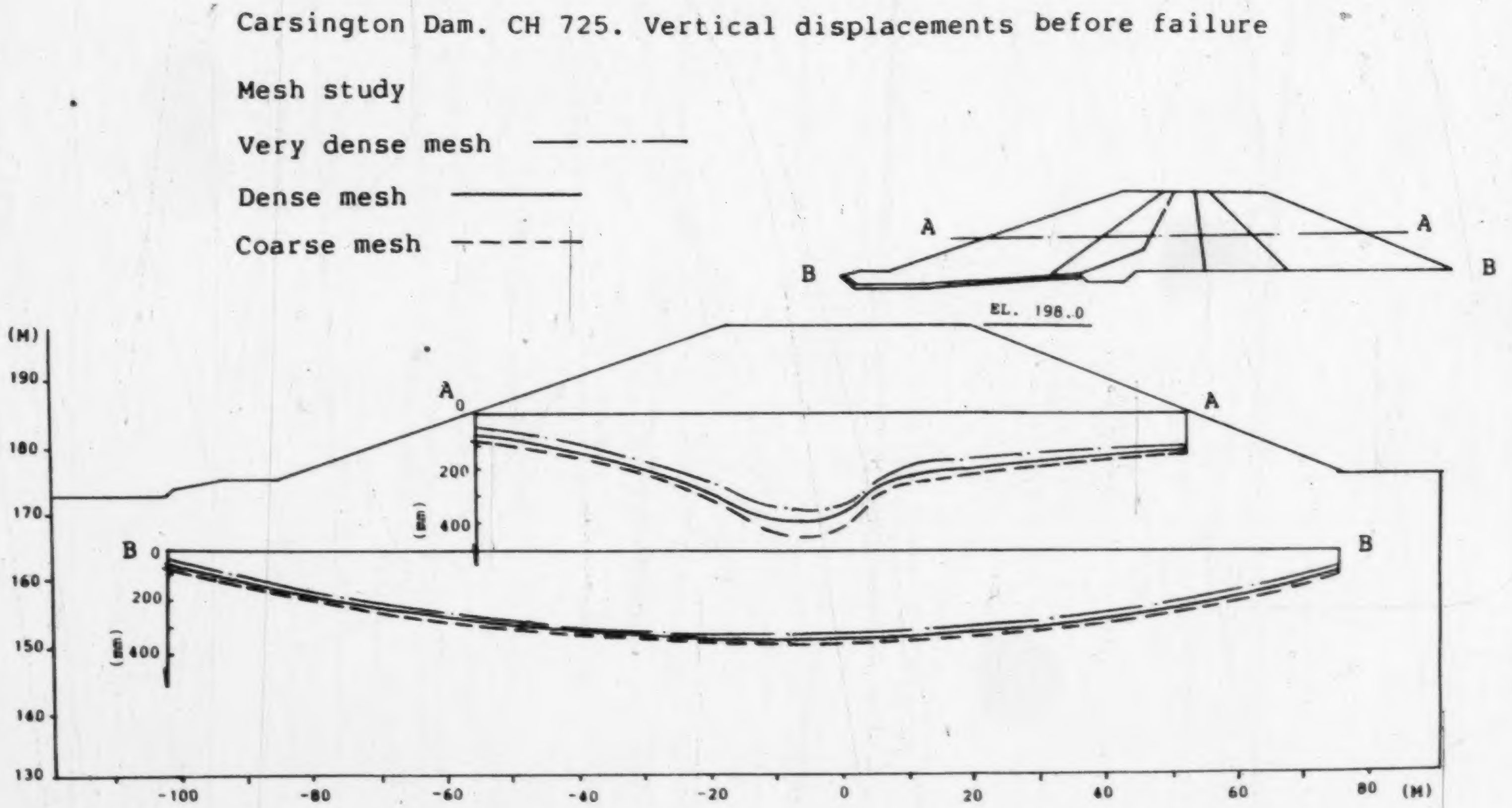

Figure 3.12: Mesh study - Comparison of vertical displacements

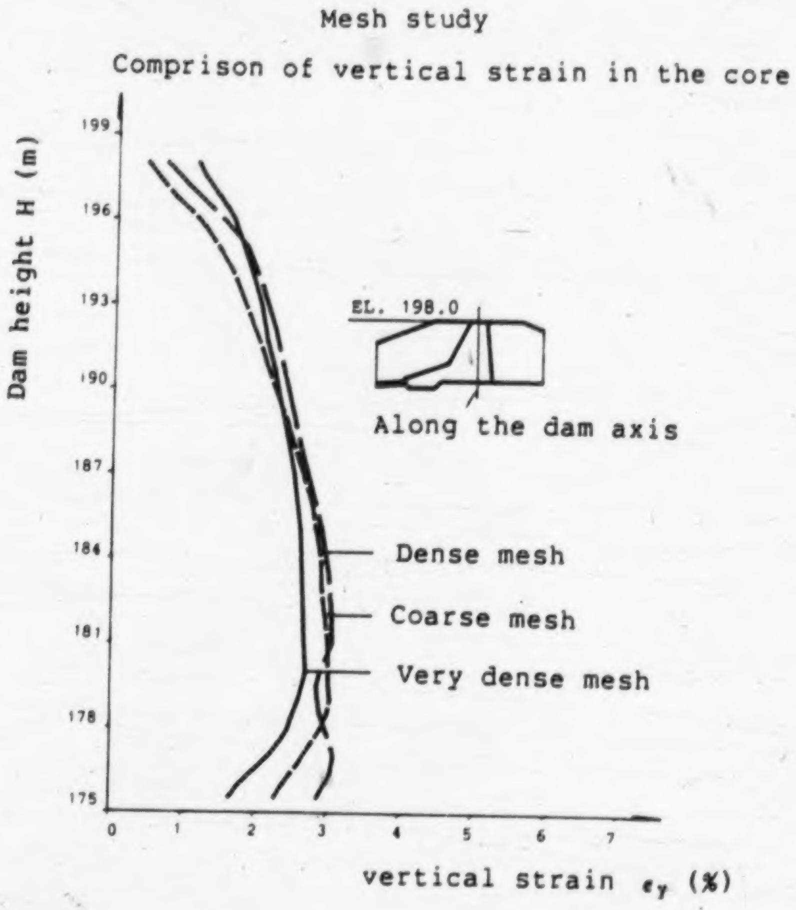

Figure 3.13: Mesh study - Comparison of vertical strains

between the stress distributions is mainly due to the capacity of the mesh to reflect the sharp changes of the stress distribution.

The displacement vector increments near failure are shown in Fig. 3.15 for the very dense mesh. The corresponding plots are also illustrated in Fig. 3.16 and Fig. 3.17 for the dense and coarse mesh. These plots can be used to determine incipient slip surface (Section 6.2). The vectors in the very dense mesh are good enough for this purpose. But, the vector directions in the dense mesh are at random in the part of boot where the transition from small elements to large elements seems too abrupt. The vectors in the coarse meshes can only predict the tendency where the slip surface might go, and they are poor in reflecting the sharp changes of movement directions.

The above comparison shows that an acceptable solution can be obtained even from the coarse mesh except for the displacement vector increment plot which can be used to locate the slip surface. By counting the element number along the possible slip surface, it seems 15 to 20 elements are enough to yield an acceptable solution. In giving the above number of 20, locally densifying the mesh in the boot has been considered. It will improve the plot of displacement vector increments. This number is about two times the slice number of 10 to 12 in the corresponding limit equilibrium analyses.

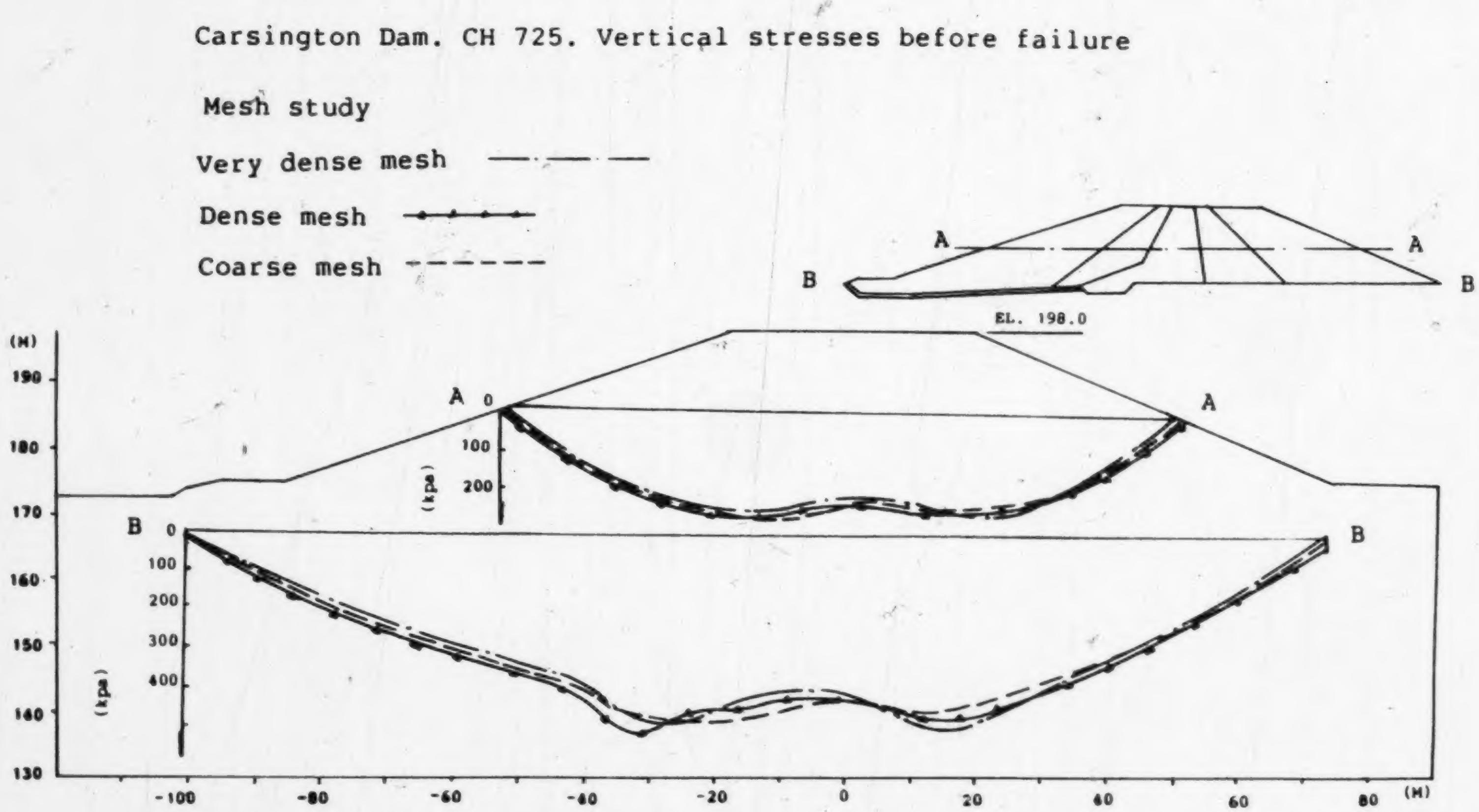

Figure 3.14: Mesh study - Comparison of vertical stresses

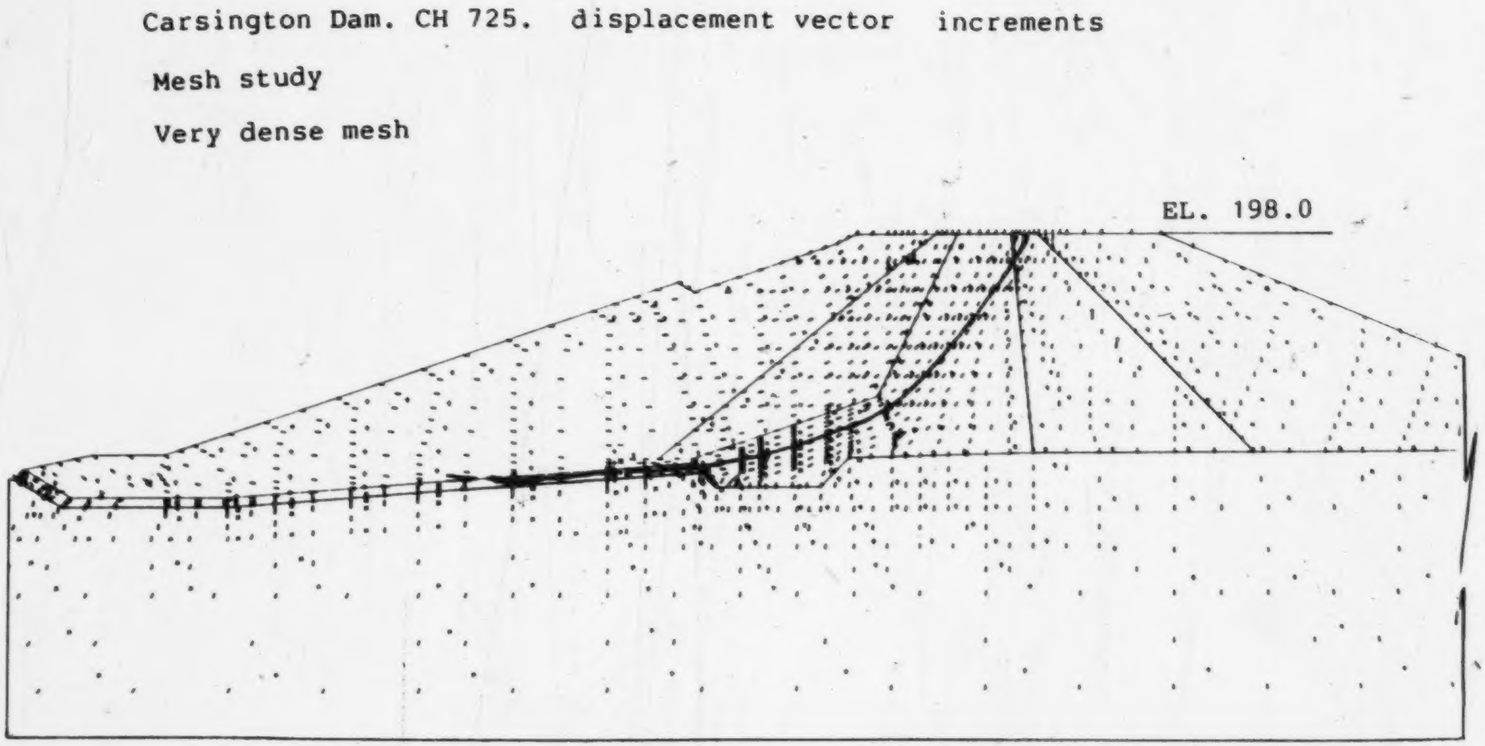
Carsington Dam. CH 725. displacement vector increments
Mesh study
Very dense mesh
EL. 198.0

Figure 3.15: Mesh study - very dense mesh, displacement vector increments

Carsington Dam. CH 725. displacement vector increments

Mesh study

Dense mesh

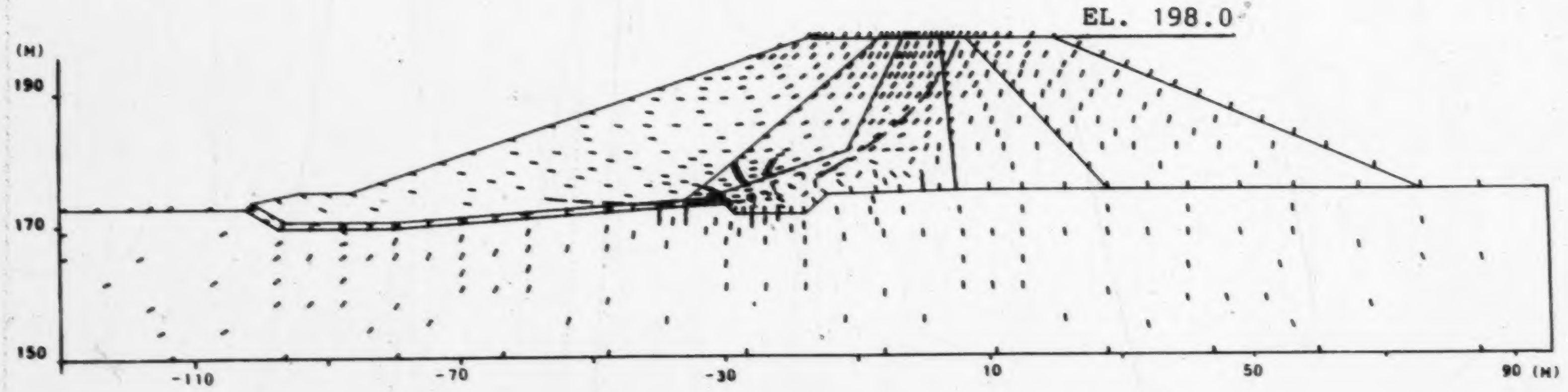
EL. 198.0
(M)
190
170
150
-110
-70
-30
10
50
90 (M)

Figure 3.16: Mesh study - dense mesh, displacement vector increments

Carsington Dam. CH 725. displacement vector increments

Mesh study

Coarse mesh

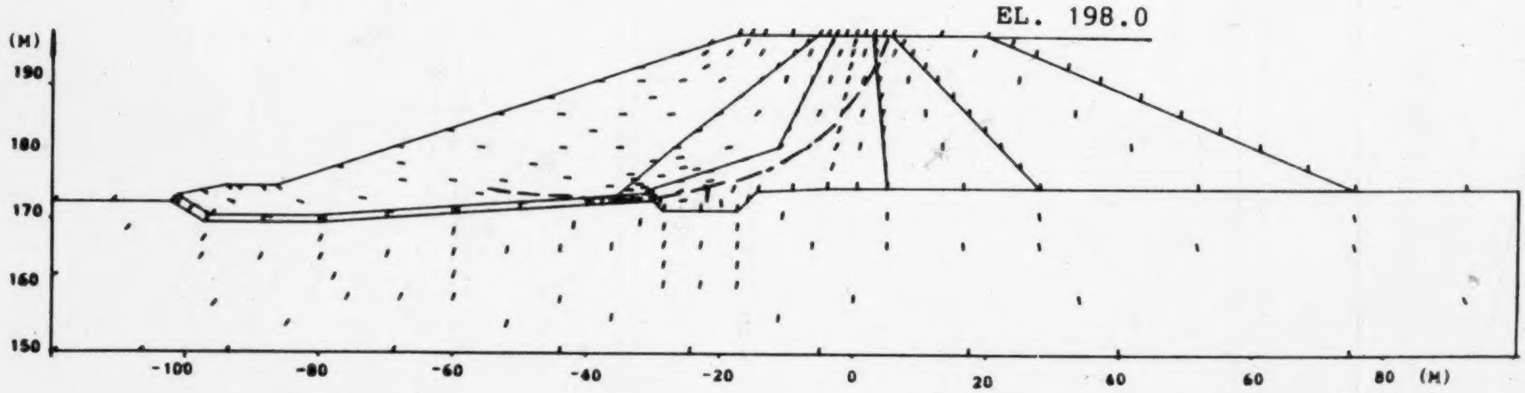
EL. 198.0
(M)
190
180
170
160
150
-100
-80
-60
-40
-20
0
20
40
60
80
(M)

Figure 3.17: Mesh study - coarse mesh, displacement vector increments

In the investigation report of the Carsington Dam Failure (Betie, Shaw, Morton and Skempton, 1986), an elastic layer of elements is used to replace the large conventional foundation mesh. As stated in Chapter 1, we simply mention this report as the "REPORT". The equivalent elastic modulus of this layer is assumed to be 30×p' with a minimum value of 2000 kpa, where p' is the first invariant of the effective stress tensor as described in the "REPORT". In Fig. 3.18, a trial mesh is obtained by deleting most of the foundation elements in the dense mesh (Fig. 3.8), and is analysed for comparison with the conventional meshes.

Table 3.10 gives a comparison of the main results, in which the results obtained from the very dense mesh is still taken as standard. Although about 20% of computation time (columns 3 and 4 Table 3.11) can be saved by using an elastic layer instead of a conventional large foundation, the relative errors seem too large with respect to the strains and displacements.

Fig. 3.19 shows that the errors of horizontal displacements occur from very low loading levels. Theoretically speaking, by using the assumption of an isotropic modulus E=30×p' with a minimum value of 2000 kpa, the horizontal stiffness of the foundation is highly underestimated at lower loading steps. However, the horizontal displacements calculated in the "REPORT" are not so high at the low loading level, but no details of the calculation can be found in the "REPORT". An anisotropic

Dense mesh

Foundation simulated by an elastic layer

174 Elements 577 Nodes

Stiff matrix lenth= 77 ,069

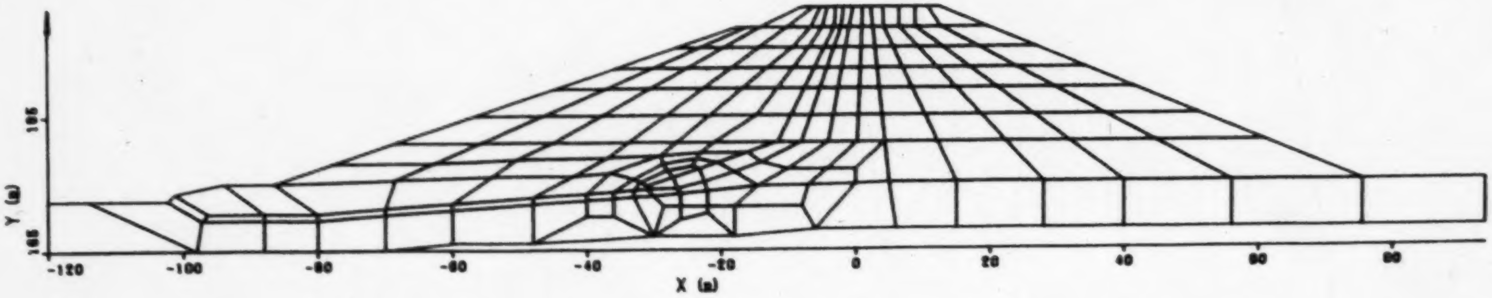
Y (m)
195
165
-120
-100
-80
-60
-40
-20
0
20
40
60
80
X (m)

Figure 3.18: Dense mesh with foundation simulated by an elastic layer

modulus has been tried. Let the ratio of horizontal modulus to vertical modulus be 2.0, the horizontal displacement will decrease by 15% to 20% at lower load levels. But, the assumption here is arbitrary. No further study has been attempted.

Table 3.11 Comparison of main results of different foundations

Foundation	Very Dense Conventional Foundation	Dense Conventional Foundation	Dense Elastic Layer Foundation
Computing Time (sec)	9000	1250	1050
Critical Height Just before Failure	EL.198.00m	EL.197.40m	EL.197.25m
Relative Error of Max. Displ.	0.0%	3.8%	70% to 130%
Relative Error of Max. Strain	0.0%	4.2%	53%
Relative Error of Max. Stress	0.0%	2.2%	6.7%

Fig. 3.20 and Fig. 3.21 illustrate the comparison of displacement fields before failure. The results from two kinds of foundations are comparatively close to each other if the same mesh is used for the dam. In short, the main features of deformation and stress distribution will be basically the same if an elastic layer with an equivalent modulus is used to replace the large conventional foundation. However, without reasonable control of the horizontal stiffness, horizontal displacements will be

Study of meshes for foundation

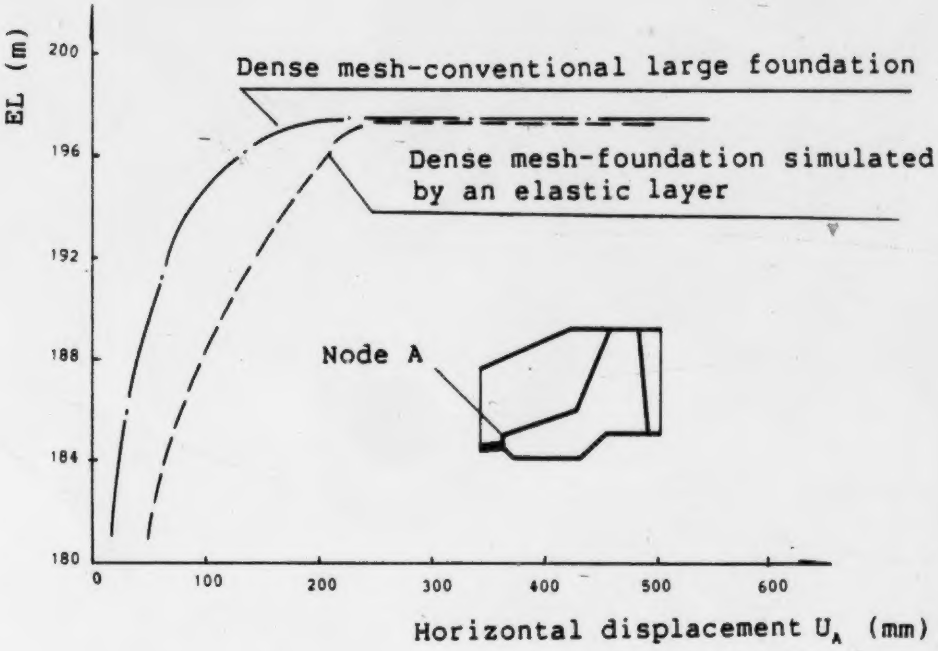

Figure 3.19: Study of meshes for foundation - comparison of the maximum displacement

Carsington Dam. CH 725. Horizontal displacements before failure

Study of meshes for foundation dense mesh

Foundation simulated by

a. conventional large mesh ————

b. An elastic layer -------

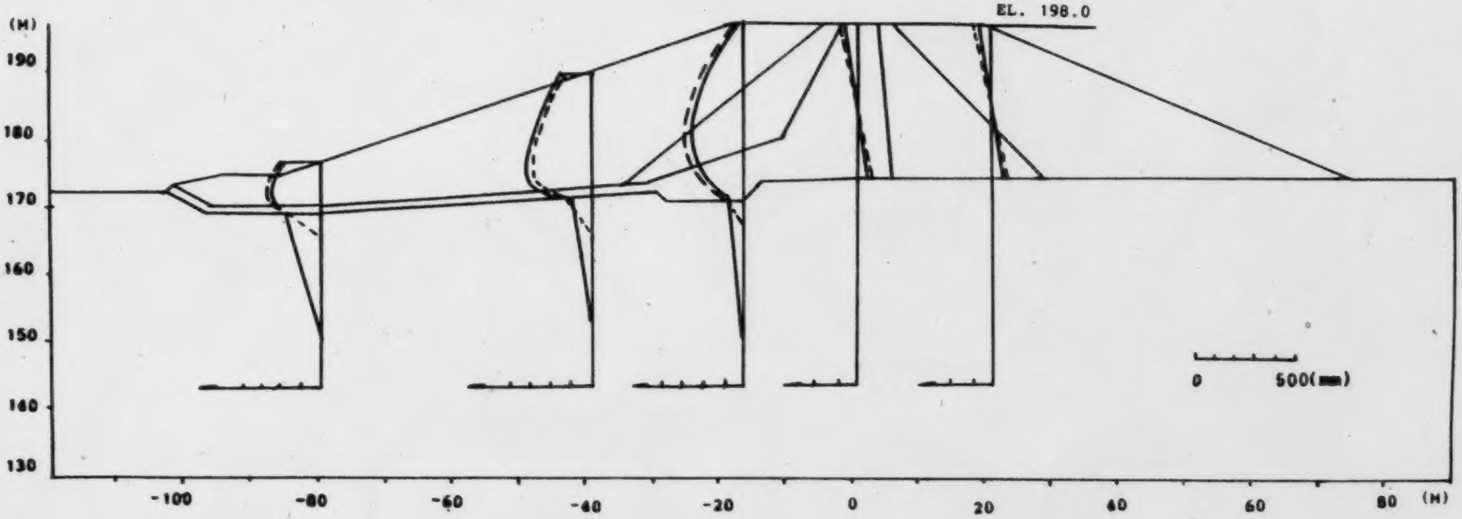

Figure 3.20: Study of meshes for foundation - comparison of horizontal displacements

Carsington Dam. CH 725. Vertical displacements before failure

Study of meshes for foundation dense mesh

Foundation simulated by

a. conventional large mesh —·—·—

b. An elastic layer ------

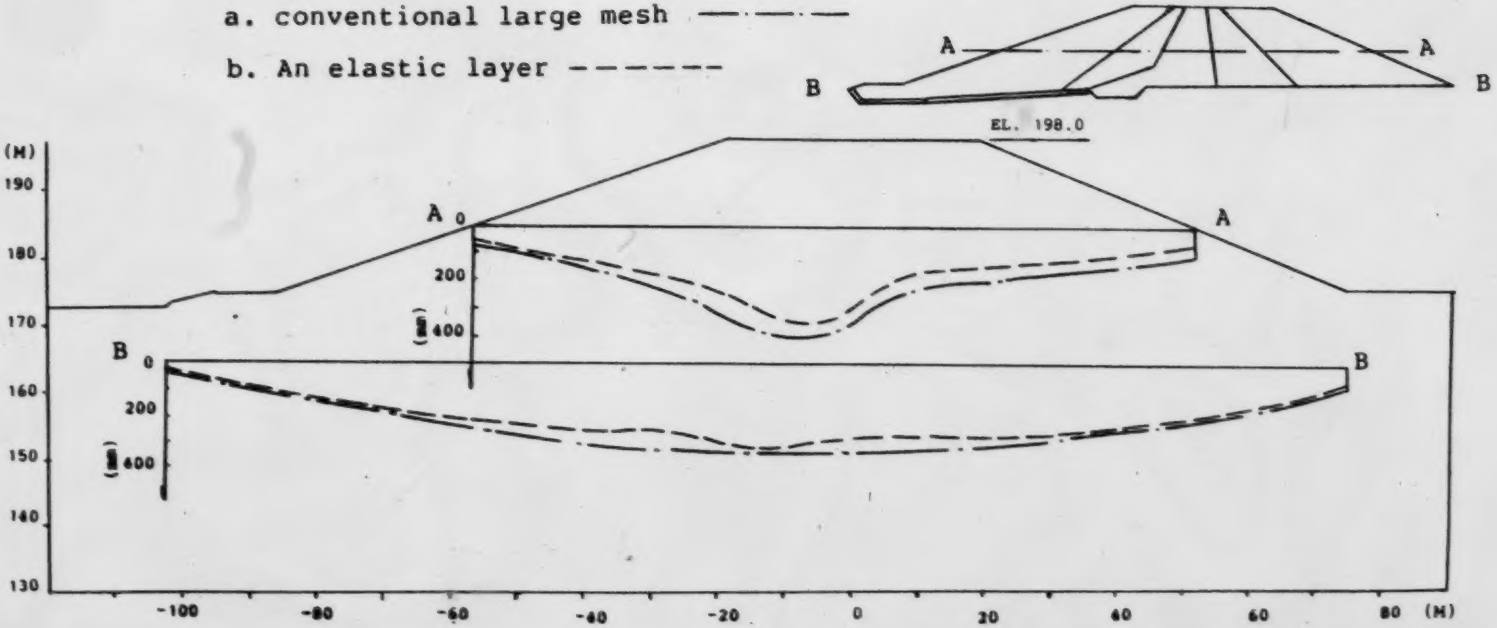

Figure 3.21: Study of meshes for foundation - comparison of vertical displacements

highly exaggerated. Therefore, if the equivalent horizontal modulus is not available, this method is difficult to use in analyses of dams.

3.2.4 Conclusions and recommendations for mesh design

1. Three meshes with different density have been designed to investigate the influence of the density of the mesh upon the results of nonlinear finite element stability analyses for rock-earthfill dams. The feasibility of replacement of the conventional large mesh by an elastic layer in simulating the foundation has also been studied.
2. A revised mesh (Fig. 6.3) with its density between the coarse and dense mesh in Fig. 3.8 is to be adopted for further analyses. Special attention should be paid to the gradual transition from very small to large elements. Reduction of the computation time by 90% can be expected. It is a great economical benefit.
3. An elastic layer with equivalent elastic modulus can be used in simulating the foundation with acceptable results, if the information is available for both horizontal and vertical equivalent stiffnesses. Without the observed data to work out the horizontal stiffness, the horizontal displacements will be highly exaggerated by using an isotropic model only to fit observed vertical settlements.

4. From the results in this chapter, guidelines for the mesh design in analysing the Carsington Dam failure can be summarized as follows:

   (1) Element type: 8-node isoparametric element with 6-node curve-sided triangular elements to fit the geometric boundary if necessary,

   (2) Number of construction layers: not less than 6-8 for a dam section of 25m to 30m high,

   (3) Layer thickness and sub-increment load division: for lower nonlinearity, 3 to 6 meter thick for one layer which is further divided into 2 to 4 load sub-increments with respect to soil density; near failure, 2 to 3 meter thick with 3 to 5 load sub-increments in one layer, (the above guideline is suggested by reviewing Table 3.3 and 3.4),

   (4) Element number along the possible slip surface is suggested to be about 20,

   (6) Attention should be paid to gradual transition from very small to large elements.

4. THE CARSINGTON DAM FAILURE

The failure of the Carsington Dam in 1984 is a very important case history for research into progressive failure due to strain softening. After the failure of the Carsington Dam, extensive field, laboratory and research work has been carried out to explore the failure mechanism. The "REPORT" i.e. "Carsington Dam - The Machanism of Failure" issued by the Severn Trent Water Authority contains three volumes and includes nearly all aspects of the above work.

In this chapter, the failure of the Carsington Dam will be introduced and the previous work on this case history is briefly summarized and disussed. The discussion is focussed on the contents relevant to numerical work.

4.1 Introduction of the Carsington Dam Failure

4.1.1 Geology and construction

The Carsington scheme has been described by Davey and Eccles (1983). The dam (Fig. 4.1) is situated on the Scow Brook near the village of Hognaston in Derbyshire, England and has a maximum design height of 35m. Its longitudinal profile and typical section are shown in Fig. 4.2 and 4.3. Placing of fill at the 1200m long Carsington Dam began in July, 1982 . By the end of May in 1984, the placing of fill material was nearly completed to the maximum intended height. Then, failure over a 500m length occurred on June, 5th.

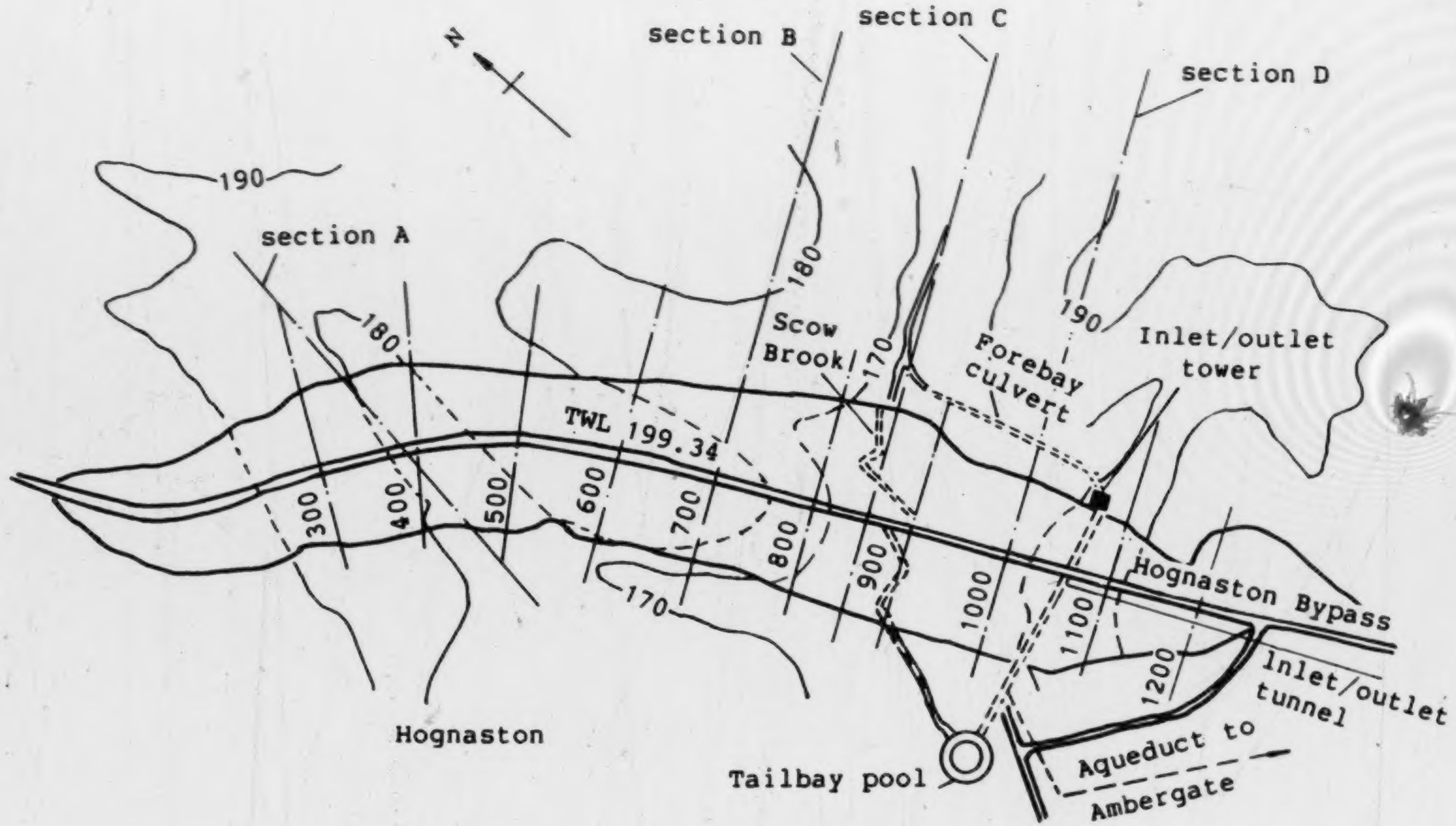
section B
section C
section D
N
190
section A
180
180
Scow
Brook
170
190
Forebay
culvert
Inlet/outlet
tower
TWL 199.34
300
400
500
600
700
800
900
1000
1100
1200
170
Hognaston Bypass
Inlet/outlet
tunnel
Hognaston
Tailbay pool
Aqueduct to
Ambergate

Figure 4.1: Plan of the Carsington scheme

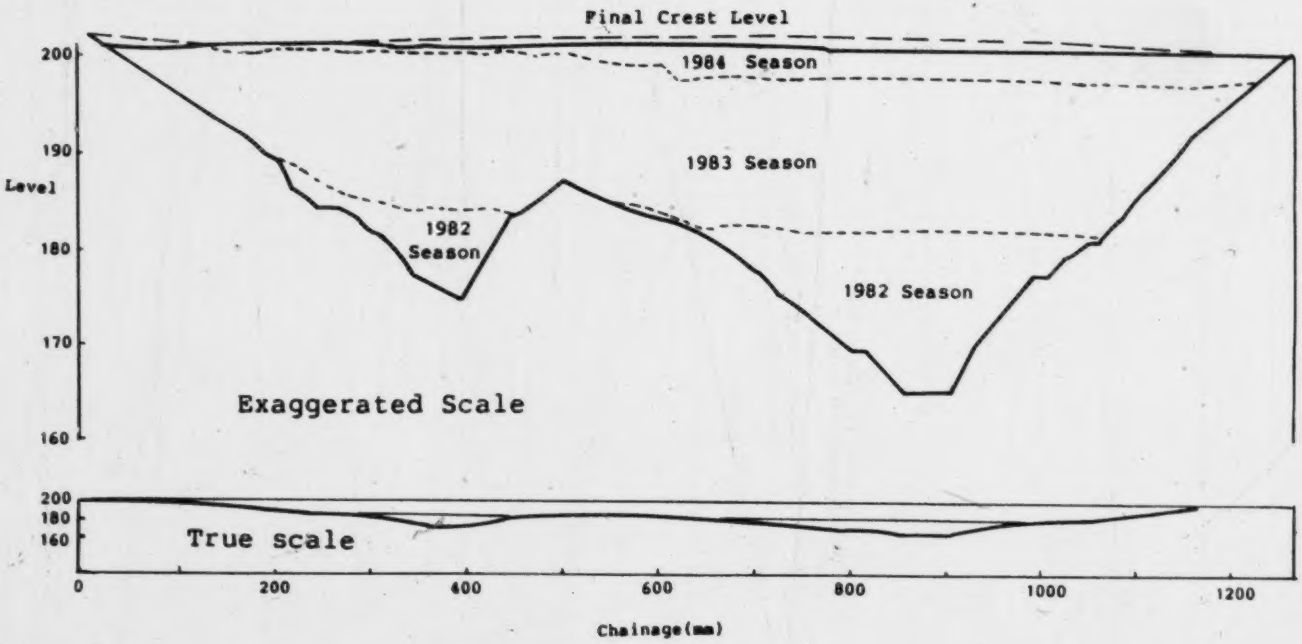

Figure 4.2: Longitudinal profile of the Carsington Dam

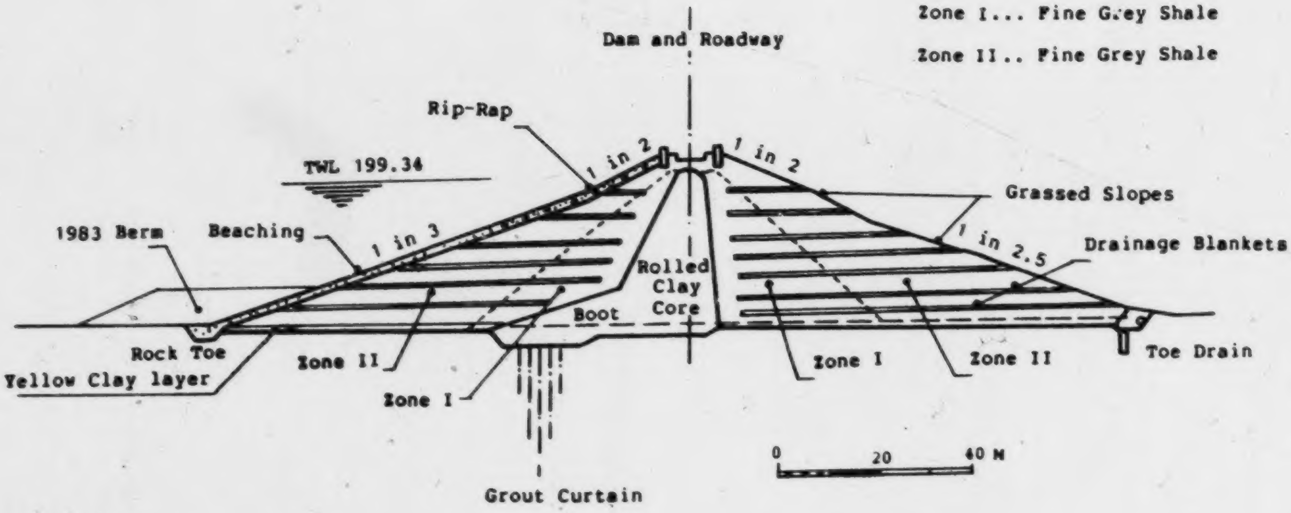
Zone I... Fine Grey Shale
Zone II.. Fine Grey Shale
Dam and Roadway
Rip-Rap
TWL 199.34
1 in 2
1 in 2
Grassed Slopes
1983 Berm
Beaching
1 in 3
1 in 2.5
Drainage Blankets
Rolled Clay Core
Boot
Rock Toe
Yellow Clay layer
Zone II
Zone I
Zone I
Zone II
Toe Drain
Grout Curtain
0
20
40 M

Figure 4.3: Typical cross-section of the Carsington Dam

The valley is broad and cuts through mudstones of Upper Carboniferous age belonging to the Nanurian series. During the long interval of at least 100,000 years before the onset of the last (Devensian) glaciation, erosion enlarged the valley removing most of the glacial deposits which draped the valley slopes, and the mudstones were weathered.

Devensian ice-sheets never reached the dam site. Therefore, the site and its surroundings were not glaciated at this stage but, for a period lasting about 20,000 years, were subjected to periglacial conditions. As a result the mudstone was disturbed by cryoturbation to a depth of several metres and the valley slopes became mantled by Head: clayey material moving downhill by the freeze-thaw process of solifluction. On the lower slopes the Head has an average thickness of about 1.2m. It tends to be thicker at the bottom of the slopes. The downhill movement caused shears to develop at, or more typically just below, the base of the Head.

During the past 10,000 years, since the return of temperate conditions, there has been further weathering and the formation of topsoil, and Scow Brook has widened and deepened its bed, replacing Head and the uppermost weathered mudstone by its own alluvium, in a flood plain generally 50m to 80m in width. From trial pits and trenches both under the dam and in ground beyond the upstream toe, the succession of foundation strata was established as given in Table 4.1.

Table 4.1 Materials at the dam site

Site identification		Symbol in trial pit logs	Classification and description
Topsoil		Ts	Topsoil
Subsoil		a_1	Head deposits Stiff brown and grey friable clay
Yellow Clay	Yellow Clay (a)	a_2	Firm and stiff light grey and yellow/orange mottled clay. Both a_1 and a_2 contain some angular/subangular sand-stone and limestone fragments, and rare rounded quartz pebbles
	Yellow Clay (b)	b_1 & b_2	Weathered Bedrock Soft to stiff grey, brown & yellow mottled clay with rare sandstone and coal fragments [Residual Soil]
Dark clay		b_3	Soft dark grey and black clay with some very weak mudstone peds. [Highly brecciated and completely weathered mudstone]
Brecciated mudstone		b_4	Dark grey laminated, highly weathered mudstone; very weak
Blocky mudstone		b_5	Dark grey laminated, moderately weathered mudstone

Although extensive field and lab work have been carried out after the failure of the dam, only key points relevent to the back analyses are described

1. Two layers can be recognised in the Head. The lower

layer (a_2) is a yellow brown and light grey mottled clay; similar to b_1 though slightly more sandy, and individual samples of a_2 and b_1 cannot easily be differentiated one from another. For geotechnical purposes they are therefore grouped together under the name 'Yellow Clay'. The downslope movement of Head leads to the development of solifluction shear surfaces, in clay, at or below its base. Such shear surfaces have been observed to a greater or lesser extent in all trial pits upstream of the dam, and are presumably characteristic of the whole site. The shears are in most cases smooth, gently undulating, and often gleyed.

2. The foundation for the dam were intended generally to be in shallow excavations with removal of only topsoil and the softer clay over the embankment area. Unfortunately, the Yellow Clay has not been removed around the critical section at CH 700 to 750 (CH is for chainage). It constitutes a weak layer due to the pre-shears as mentioned above. However, except for this layer, the whole foundation has proved to be sound enough since no failure of other foundation materials has been found throughout the extensive field investigation.
3. In order to control seepage, at the upstream edge of the core, a key trench was excavated (Fig. 4.3). Its centreline was coincident with that of the grout

curtain. Thus, an extension of the central rolled clay core was formed and is known as the "boot", which has acted as a strain concentrator in promoting the progressive failure.

4.1.2 Properties of materials

4.1.2.1 Foundation

The main materials in the foundation are highly weathered to moderate weathered mudstones. Since no failure has been found in the foundation after failure, material parameters other than the deformation modulus are irrelevent to the back-analyses. In the finite element analyses given in the "REPORT", an equivalent nonlinear deformation modulus was adopted by fitting the observed settlements.

4.1.2.2 Yellow Clay

This material comprises the soft to firm yellow brown and light grey mottled clays of strata a_2 and b_1, and only a small difference between the two strata can be found in the averages from a large number of tests. Mean values of the index properties of the Yellow Clay are shown in Table 4.2. These properties are typical of an inorganic clay of high plasticity with a moderate proportion of kaolinite in the clay fraction.

The average unit weight is about 20 kN/M_3.

For intact Yellow Clay the peak shear strength parameters are

Table 4.2 Index properties

Stratum	Material	Water Content W	Liquid Limit LL	Plastic Limit PL	Plasticity Index PI	Liquidity Index W-PL/PI	Clay Fraction CF	Activity Ratio PI/CF	Specific Gravity G_s
a_1	Subsoil		69	37	32		30	1.1	
a_2 b_1	Yellow Clay (mean)	40	75	32	43	+0.2	62	0.69	2.67
b_3	Dark grey clay	30	63	31	32	-0.05	47	0.68	2.70
b_4	Brecciated mudstone	20	43	22	21	-0.1	32	0.65	2.75
b_5	Blocky mudstone	15	44	23	21	-0.4	33	0.64	2.75
	Core	33	69	31	38	+0.05	56	0.68	2.68
	Zone II fill	14	45	23	22	-0.3	33	0.66	2.75

$C' = 10$ kpa and $\phi' = 20°$.

Test results, plotted on Fig. 4.4, show no significant difference between various types of test or size of samples. Curves in shear box tests are shown in Fig. 4.5. With the polished and striated slip surface placed exactly in the separation plane of the box, the residual strength is developed after only a few millimetres displacement, and the results of all these (fifteen) tests, give the residual values:

$C' = 0$ and $\phi_r' = 12°$.

In nature, the solifluction shears are nearly parallel to the boundary of the Yellow Clay layer and therefore lie in a nearly horizontal shape characterised by an angle $i=3°$. Hence, at small displacements the equivalent angle of friction on a horizontal plane will be approximately

$\phi_s' = \phi_r' + i = 12 + 3 = 15°$.

Obsevations in the trial pits have shown that the solifluction shears occupy 40% of this total length(L) on average. Let shear length be λL and the remaining length $(1-\lambda)L$ for intact clay with parameters C' and ϕ', the strength of the layer as a whole will be given by

$$\bar{c} = (1-\lambda)C' + 0 ,$$

$$\bar{\phi} = (1-\lambda)\phi' + \lambda\phi_s' . \qquad (4.1)$$

Peak and post-peak parameters of the Yellow Clay are thus reduced and, with $\lambda=40\%$, the "REPORT" gives the average peak strength as $\bar{C}=6$ kpa and $\bar{\phi}=18°$. The triaxial tests on the

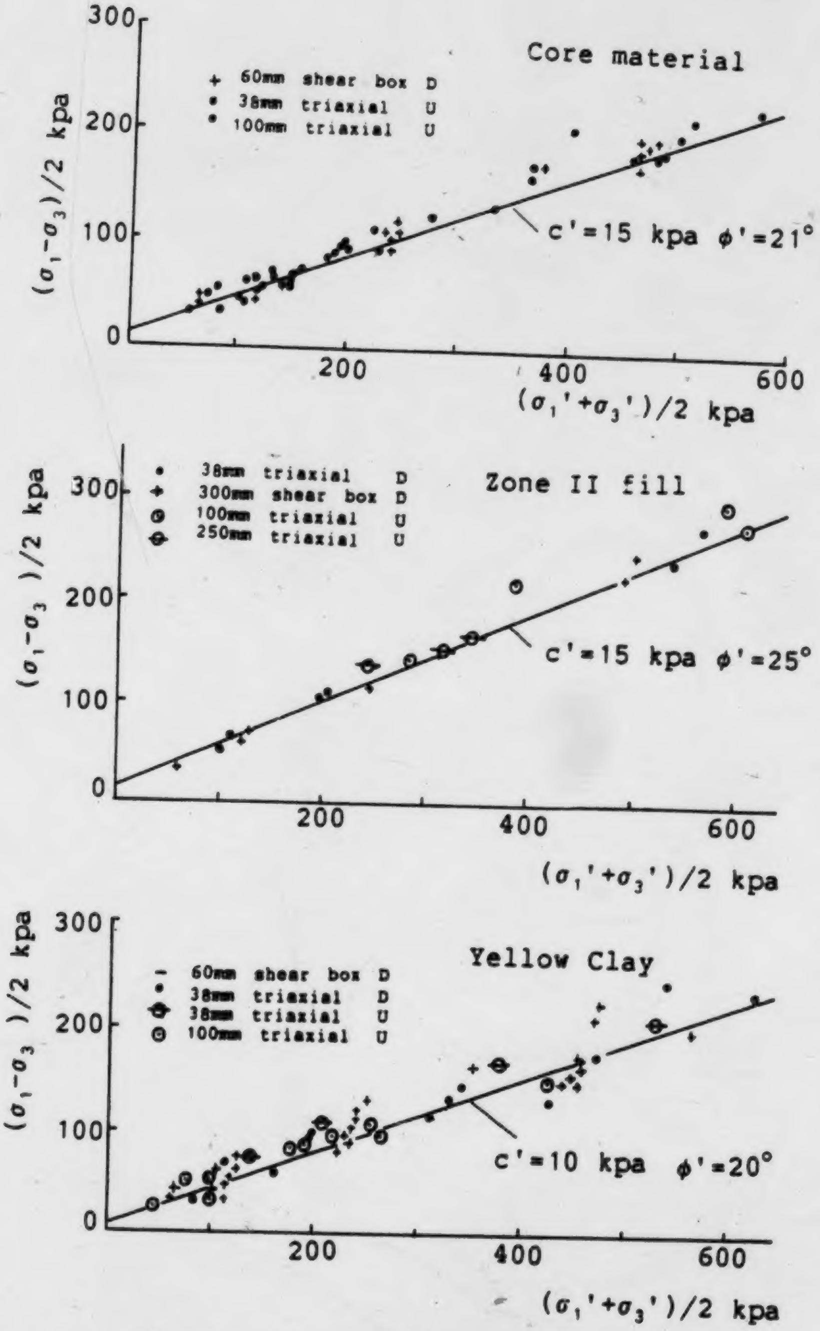

Figure 4.4: Peak shear strength

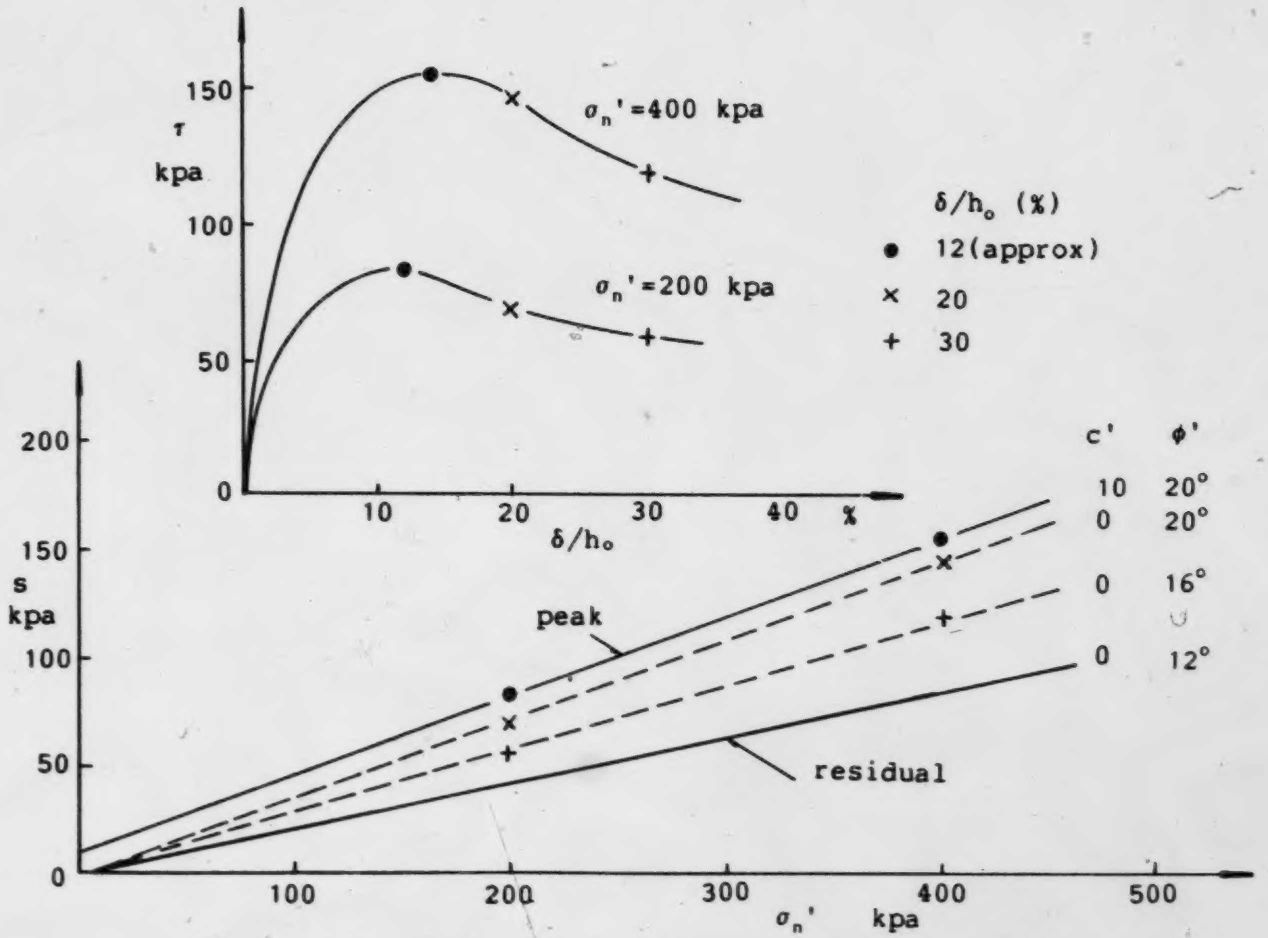

Figure 4.5: Post-peak behavior of intact Yellow Clay

pre-existing shears are shown in Fig. 4.5. Strain softening behavior is obvious with a peak strain of about 2%.

The relationships between the mobilized strain and the reduction strength are not well defined for a soil with defects. However, as reported, a 1m thick layer containing a horizontal pre-existing shear surface develops its 'peak' strength at about 40 to 50 mm displacement (4% to 5% shear strain) and subsequently falls to the residual after a small further displacement as shown in Fig. 4.7.

4.1.2.3 Core material

The core (and boot) consists of Yellow Clay (a_2+b_1) and Dark Grey clay (b_3) compacted at natural water content. Average values of the index properties are also listed in Table 4.2. Numerous tests made during the 1982, 1983 and 1984 construction seasons have shown that the material has an average unit weight of 18.5 KN/m^3 in the main portion. A value of 20.0 KN/m^3 for the fully saturated boot has been adopted in the "REPORT".

The undrained shear strength C_u measured by triaxial tests on 100 mm undisturbed samples has an average value of 65 kpa.

Peak strength parameters of the intact core material, in terms of effective stress, are

$C' = 15$ kpa and $\phi' = 21^\circ$.

Results are plotted on Fig. 4.8.

The residual strength parameters are

$C' = 0$ kpa and $\phi' = 13^\circ$.

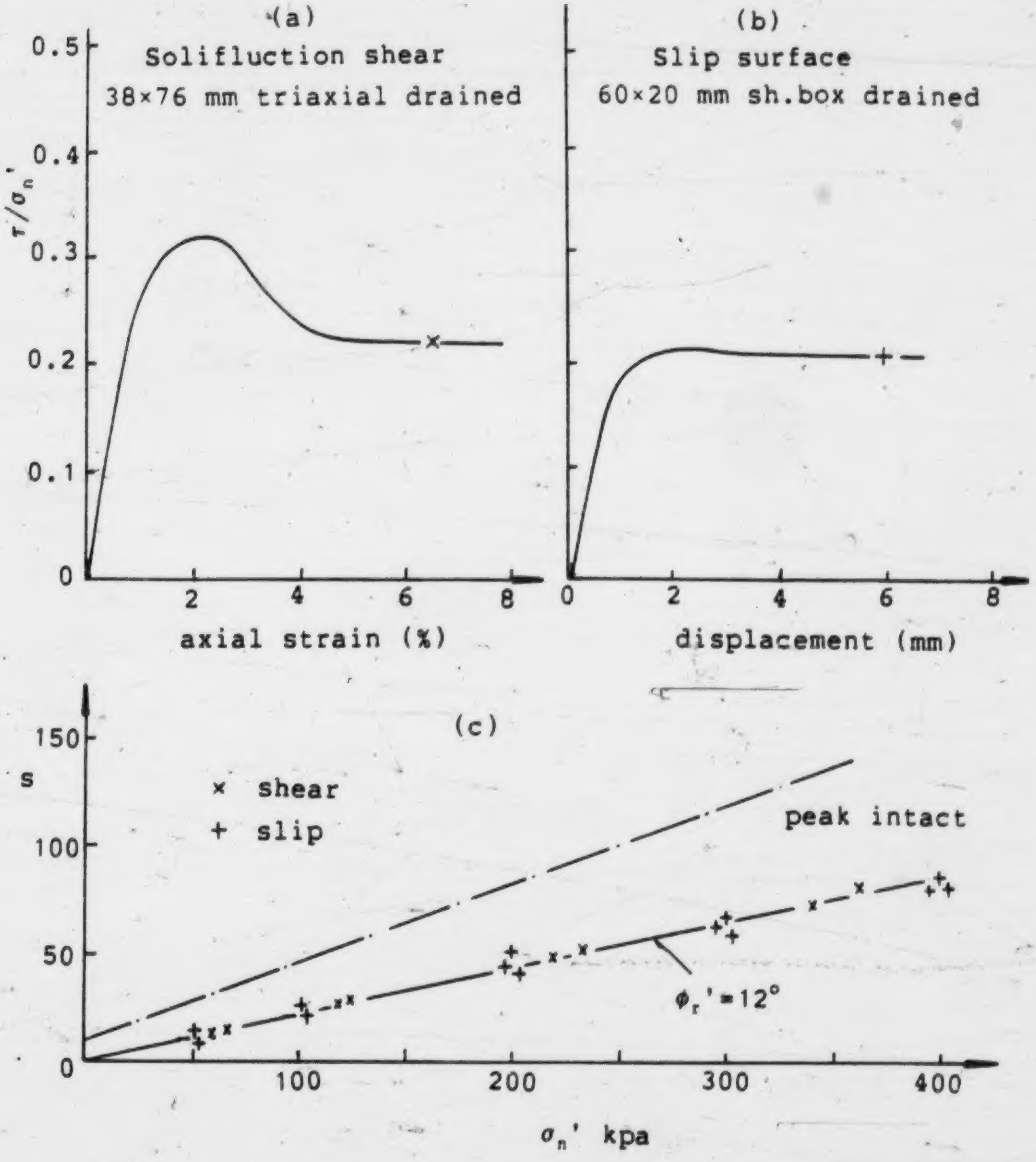

Figure 4.6: Strength along solifluction shears and slip surface

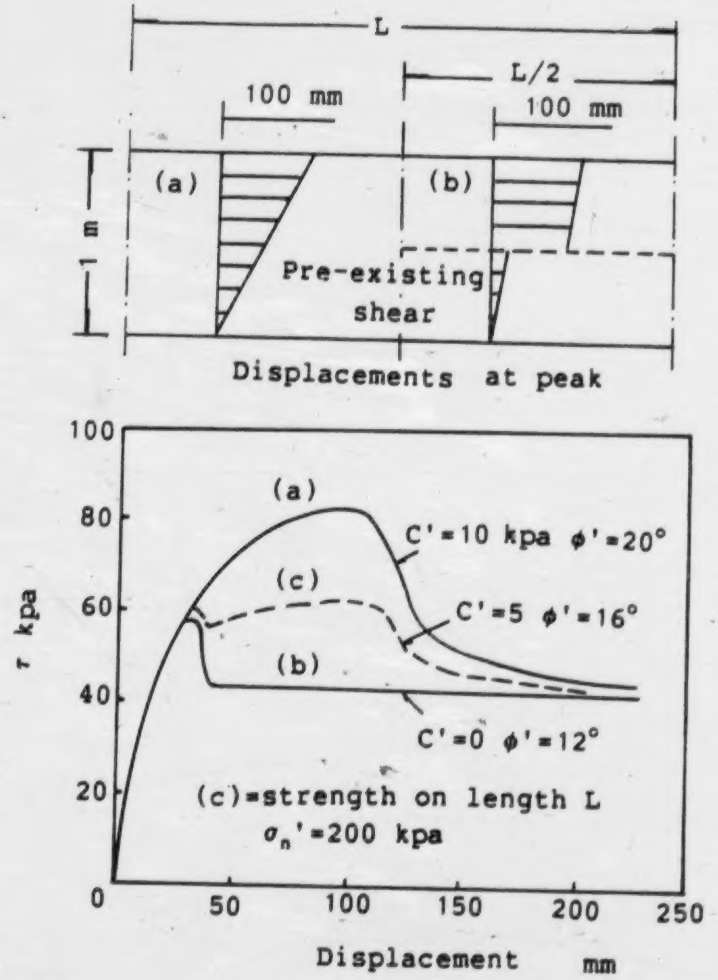

Figure 4.7: **Stress-displacement curves for the Yellow Clay**

During construction, the peak strength was affected by rutting shears, inclined at angles from 0° to 60° with the horizontal direction. Triaxial tests on samples taken diagonally across a rutting shear develop 'peak' strengths represented by $C^{'}=0$ and $\phi^{'}=16^{\circ}$ at axial strains around 2.5% and then fall to a residual strength, with $\phi^{'}_{r}=13^{\circ}$ (see Fig. 4.8). A numerical method has been presented in the "REPORT" to estimate the "bulk" strength including the influences of rutting shears. The average peak "bulk" strengh parameters are estimated to be

$C^{'}$ = 6 kpa and $\phi^{'} = 20^{\circ}$.

Similar to the case of Yellow Clay, the relationship between the post-peak strain and the reduction of strength parameters can not be well-defined for the in-situ soil due to lack of test information.

4.1.2.4 Zone I fill

Zone I fill consists mostly of brecciated Mudstone (b_4) with some Dark Grey Clay (b_3), compacted at natural water content. Only a few tests have been made on this material. Average values of water content and unit weight are about 25 and 20 KN/m^3 respectively.

Peak strength parameters, determined on four 100 mm diameter samples in triaxial tests with pore measurements, are approximately

$C^{'}$ = 10 kpa and $\phi^{'} = 22^{\circ}$.

Very limited information can be found of the zone I fill in the "REPORT". However, as reported, its behavior is

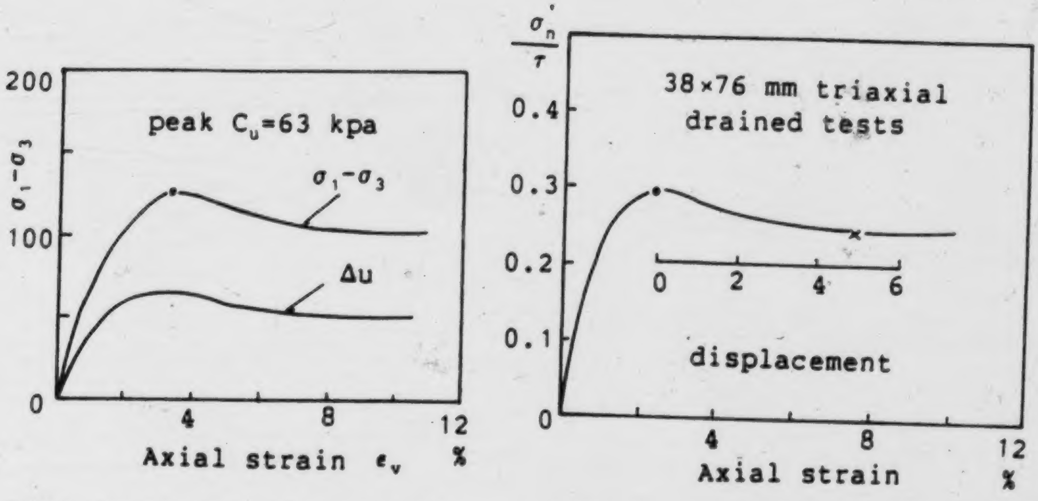

(a) On intact clay (test)

(b) On rutting shears (test)

(c) Core with rutting shears at random direction
(numerical modelling)

Condition	Axial strain	strength parameters					
		Intact		shears		Resultant	
	%	C'	ϕ'	C'	ϕ'_s	$\bar{C}$	$\bar{\phi}$
		kpa	°	kpa	°	kpa	°
Peak	3.5	15	21	0	16	6	20
	6	3	21	0	15	1.5	19
Critical state	8	0	21	0	15	0	19
Residual	large	0	13	0	13	0	13

Figure 4.8: Post peak behavior of the core

very similar to zone II fill.

4.1.2.5 Zone II fill

Zone II fill is composed of b_5 mudstone compacted at natural water content. Average index properties are also listed in Table 4.2. The material consists of 'lumps' of softened mudstone and a 'matrix' of fragments smaller than 5 mm in size. As compared with fresh b_5 mudstone, the fill has undergone some weakening. This effect is due partly to chemical changes and partly to an increase in water content. The latter is particularly important in the fill placed below EL. 170.0m in the valley bottom section of the dam but to a lesser degree is evident throughout.

The unit weight can be taken from 21.5 KN/m^3 to 21.0 KN/m^3 from the bottom to the top of the dam as suggested in the "REPORT".

Tests on undisturbed samples from above EL. 170.0m give peak strength parameters $C'=15$ kpa and $\phi'=27°$ and, for the fill below EL. 170.0m, $C'=15$ kpa and $\phi'=25°$. One group of drained test curves are given in Fig. 4.9 with slightly softening behavior after the peak strain of about 12%. Tests on samples including a polished and striated slip surface in zone II fill show a residual angle $\phi'_r=14.5°$. The peak strength are also affected by construction defects. Compaction surfaces have been observed in zone II fill, which are nearly horizontal and planar. With an average value of 10% for λ in eqn. 4.1, the "bulk" peak strength is suggested to be

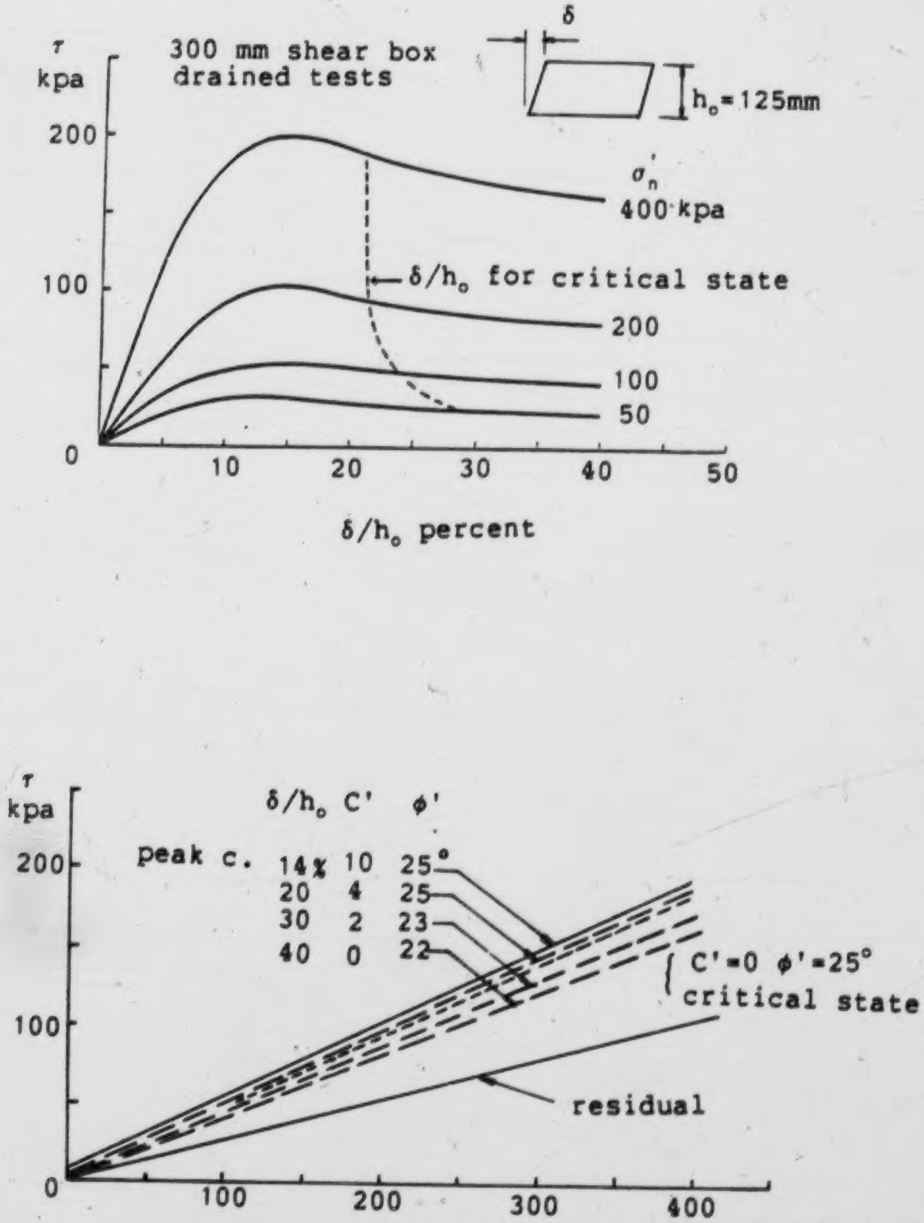

Figure 4.9: Shear box drained test curves for Zone II fill

$C' = 13.5$ kpa and $\phi' = 24°$

below EL. 170.0m, where the observed slip surface passes through this zone.

Also similar to other materials the post peak strength reduction with respect to strains cannot be accurately determined from the information in the "REPORT". Since the peak strain is very high and about 12%, the softening effect generally can be negelected in back-analyses, particular for the case where the slip surface did not develop in the material.

4.1.3 Pore pressure and deformation observation

During construction, instrumentation was incorporated mainly in four instrumented sections CH 390, 705, 850, 995 and comprised Casagrande type piezometers (foundations), Bishop type piezometers (dam), USBR vertical settlement gauges and horizontal magnetic extensometers. Horizontal displacements of 'pegs' on the upstream face were also measured from August 1983 at four monitoring station (CH 675, 750, 875, and 1050).

Piezometer levels at CH 705 and 850 are shown in Fig. 4.10 and the relationship between pore pressure and fill height just before failure is given in Fig. 4.11. In addition to the final pore pressure distribution, the pore pressure changes with the vertical stress on typical sections are also given. This will place the effective stress analysis on a more realistic base. The main points

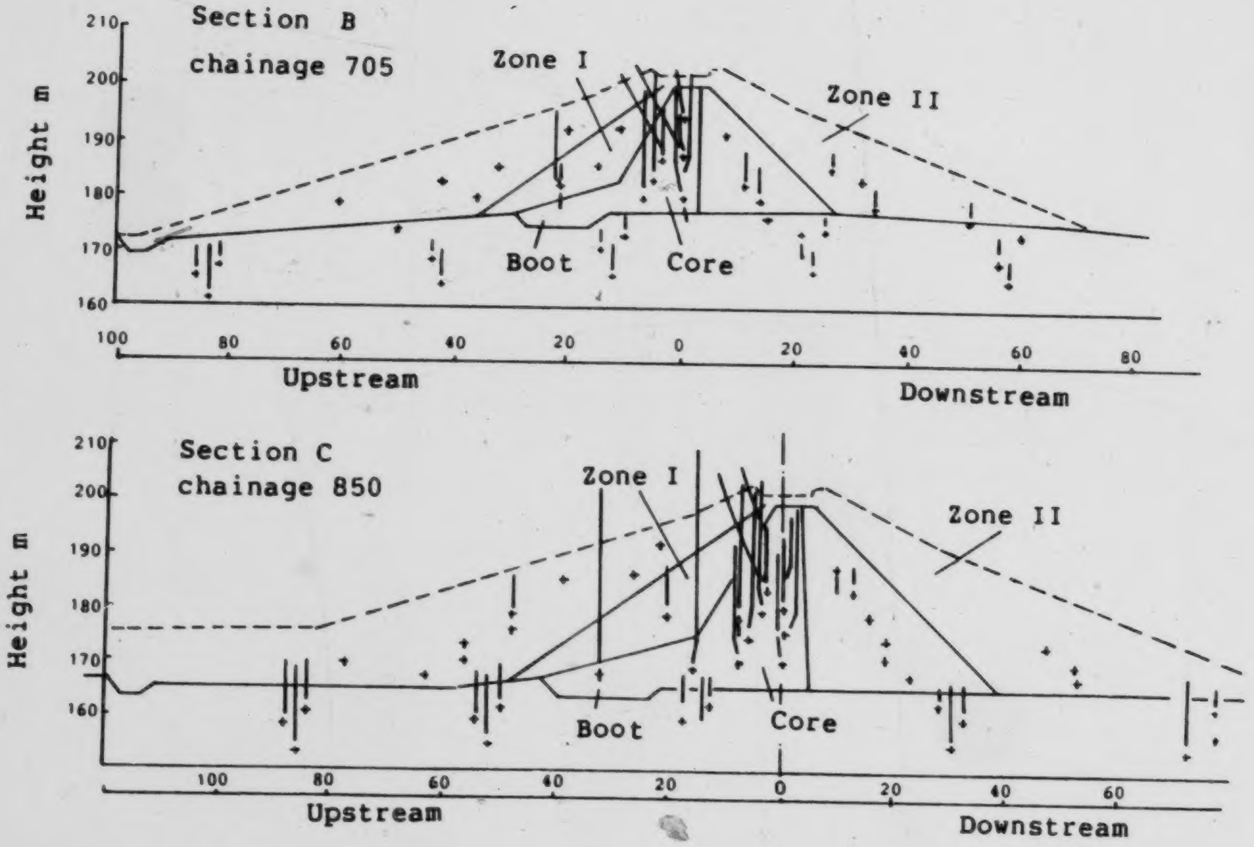

Figure 4.10: Piezometric readings prior to failure

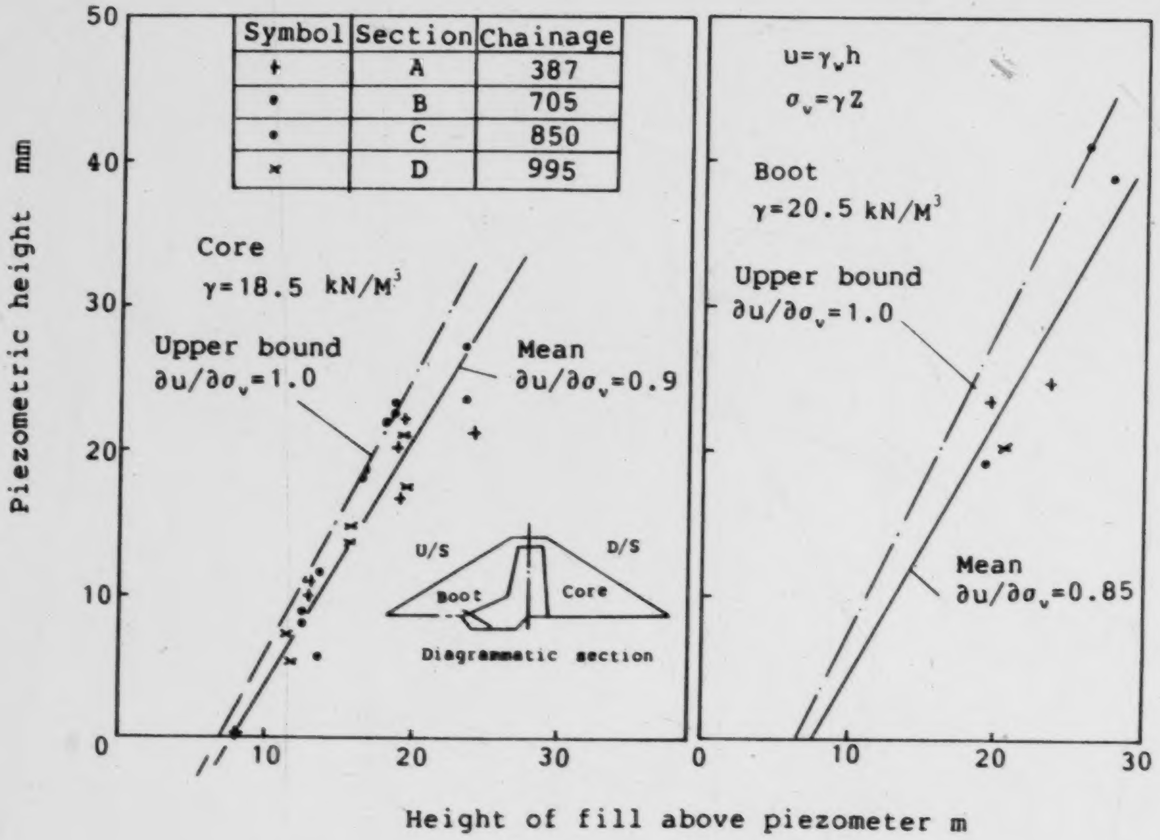

Figure 4.11: Relation between fill height and piezometric height

are summarized as follows:

1. The Core and boot

   In the boot and near the base of the core the material becomes almost full saturated, the piezometers give $du/d\sigma_v = 0.95$.

   For the middle portion of the core (between EL. 175m and EL. 190m), on average, $u=(\sigma_v-\sigma_0)\frac{du}{d\sigma_v}$, $\sigma_0=85$ kpa, $\frac{du}{d\sigma_v}=0.65$

   For the upper part of core, (above EL. 192m), the material appears to have been placed at lower than average water content and piezometers show no positive pore pressure until newly-placed fill height reaches 4m to 7m. The final elevation is about EL. 201m, and so pore pressures built up in the upper part is very small.

2. The zone I fill

   The final pore pressure pattern shows that the pore pressures in zone I ranging from small negative values to roughly half of the mean for the core.

3. The zone II fill

   Because of the rather high content of air voids in zone II fill (about 5% at end of construction), there is no evidence that significant pore pressures were developed at any time when the dam was being built.

4. The Yellow Clay

The observed data of pore pressures in Yellow Clay layer are not available. The pieozometer heads show that ground water level nearly coincides with the base of Yellow Clay and the drainage above it is effective. Thus it can be assumed that no excessive pore pressures exist in this thin layer. The possibility of generation of pore pressures during loading will be discussed in the next chapter.

Fig. 4.12 shows the horizontal movement of the upstream face and Fig. 4.13 shows the vertical strain in the core and horizontal movements along the upstream dam base. They provide bases for comparison with the results from back-analyses.

Limited observed data of vertical settlements are also given in the "REPORT". They have been used to work out an equivalent deformation modulus (eqn. 5.9 and 5.10).

4.1.4 Description of failure

By the end of May, 1984 the placing of fill material was nearly complete. Before this date, the observed data shown that the creep of upstream peg movements is under 1.5 mm/day and the performance of the dam is normal.

Heavy rainfall in the period from 1 to 3, June, 1984, amounting to approximately 40mm, brought earthmoving to a standstill. Due to the wet conditions earthfilling had not commenced on Monday 4 June,1984 when a crack was reported on

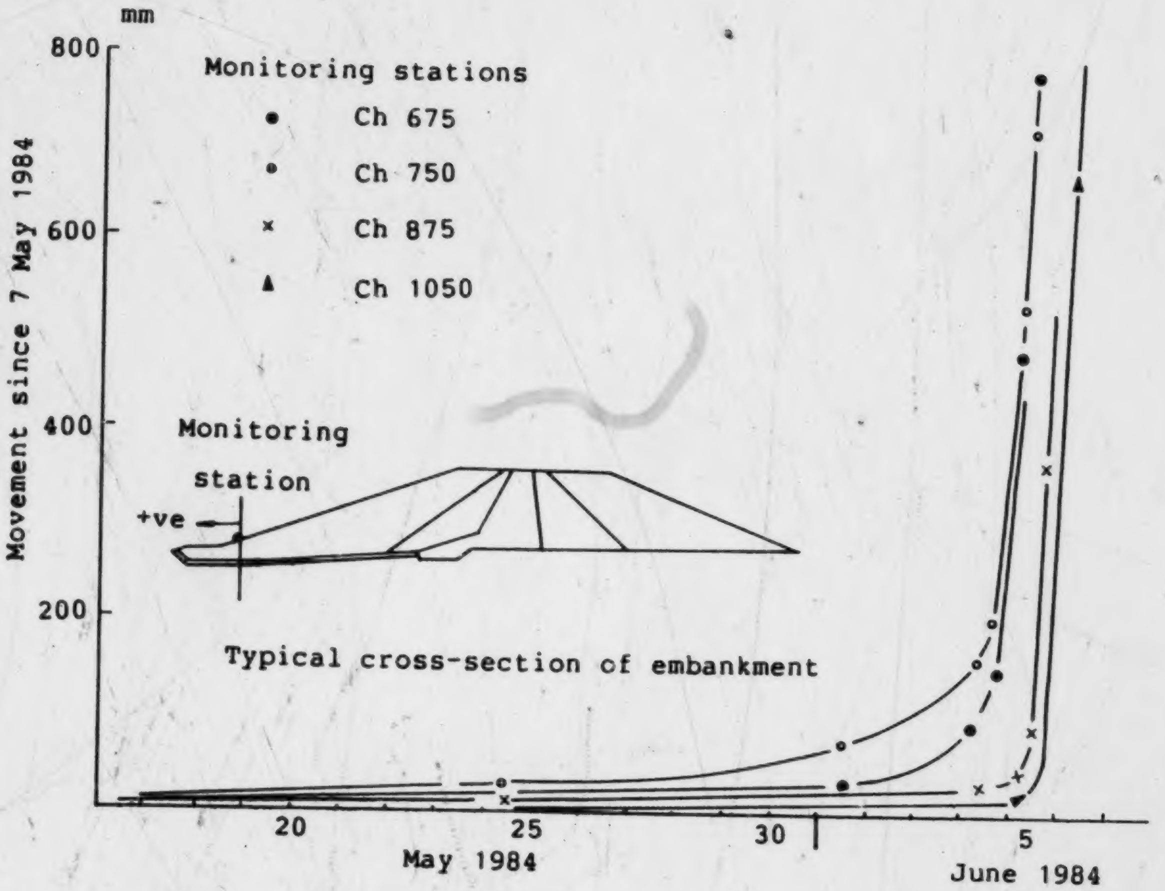

Figure 4.12: Horizontal movement of the upstream face vs. time

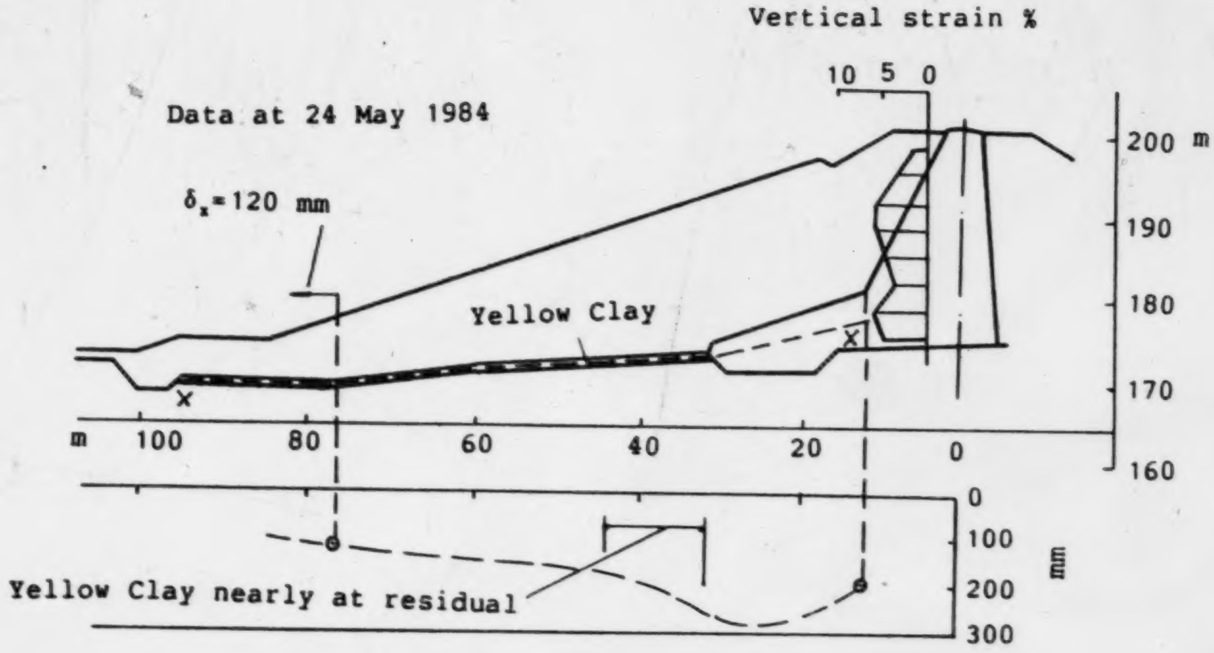
Vertical strain %
10 5 0
Data at 24 May 1984
δ_x=120 mm
Yellow Clay
200 m
190
180
170
160
m 100
80
60
40
20
0
0
100
200
300
mm
Yellow Clay nearly at residual
X
X

Figure 4.13: Observed vertical strains and estimated horizontal displacements

the dam crest at 07:30 hours. Later a 50 mm crack was recorded parallel to the dam centreline and 2m into the downstream shoulder. The crack extended from chainage 675m to 740m with lesser widths beyond. At this time no noticeable differential vertical movement was apparent.

During this period, sudden increases of upstream peg movements with the creep rate as high as about 30 mm/day were observed. Increases of pore pressure between CH 600 and CH 800, especially the disproportionate increases in the boot have been reported.

As an emergency measure, enlargement of the existing berm (Fig. 4.14) between chainages 650m and 950m commenced at about 15:40 hours on 4, June. By evening (21:00 hours) the crack width reached 130mm, but still with little vertical differential movements until 7:30 pm, 5, June.

By late afternoon 5th June, the main crack was widening at a rate of 150mm per hour. The original crack widened to 3m maximum and on the upstream side between chainages 650m and 800m had dropped 3m by the close of the day's operations. A second crack 2m downstream of the original opened rapidly and the wedge between these cracks collapsed. Fissures also opened on the upstream slope and crumpling was seen at the toe. Cracks at the dam crest now extended south to chainage 1050m. Work on the berm enlargement continued throughout this day.

By the end of this day, the creep rate of upstream peg movement reached as high as 310 mm/day with a total movement

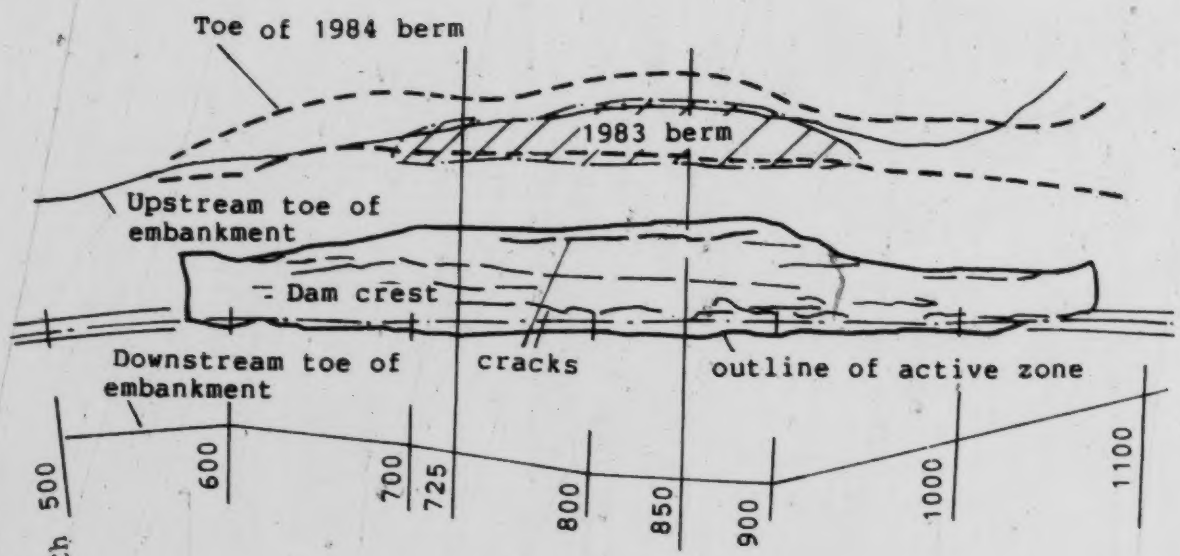
Toe of 1984 berm
1983 berm
Upstream toe of embankment
Dam crest
Downstream toe of embankment
cracks
outline of active zone
Ch 500
600
700
725
800
850
900
1000
1100

Figure 4.14: Plan of the dam during failure

of 620 mm at the most critical section (about CH 725). After the sudden drop of the crest, pore pressures began to drop sharply as shown in Fig. 4.15.

During the night of 5 to 6, June, the crest dropped 10m exposing a striated scarp face. Parts of the upstream toe had moved 13m laterally and had lifted by about 2.5m at chainage 675m and disruption of the upstream slope was severe. Although movement of the dam virtually stopped on 6 June, berm enlargement continued for a few days. Horizontal movements (Fig. 4.12) illustrate the progression from about chainage 750 to the both sides. During the total collapse of the upstream portion of the dam, pore pressure in the boot underwent about a 10 m reduction.

The upstream part of the dam before and after the failure is illustrated in Fig. 4.16 for CH 725 and in Fig. 4.17 for CH 825. The position and nature of the slip surface were explored by means of trial pits, shafts excavated through the upstream shoulder of the dam, and by large diameter borings through core. Part of the main slip surface is highly polished and striated, passing through the Yellow Clay into the boot in the most critical section around CH 725. This indicates that stain softening has taken place to bring the strength down to a level much lower than the peak, even near the residual.

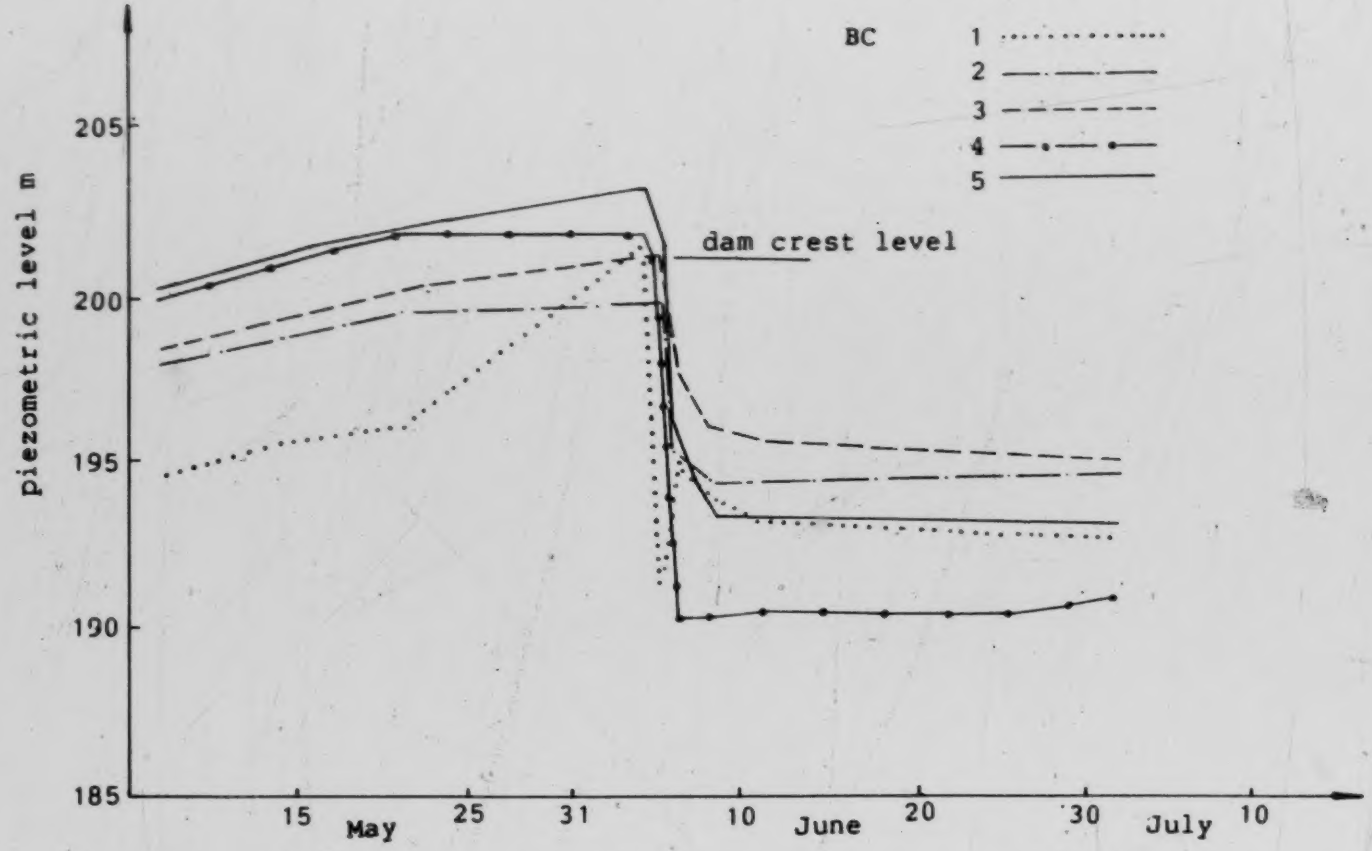

Figure 4.15: Sudden reduction of pore pressures after failure

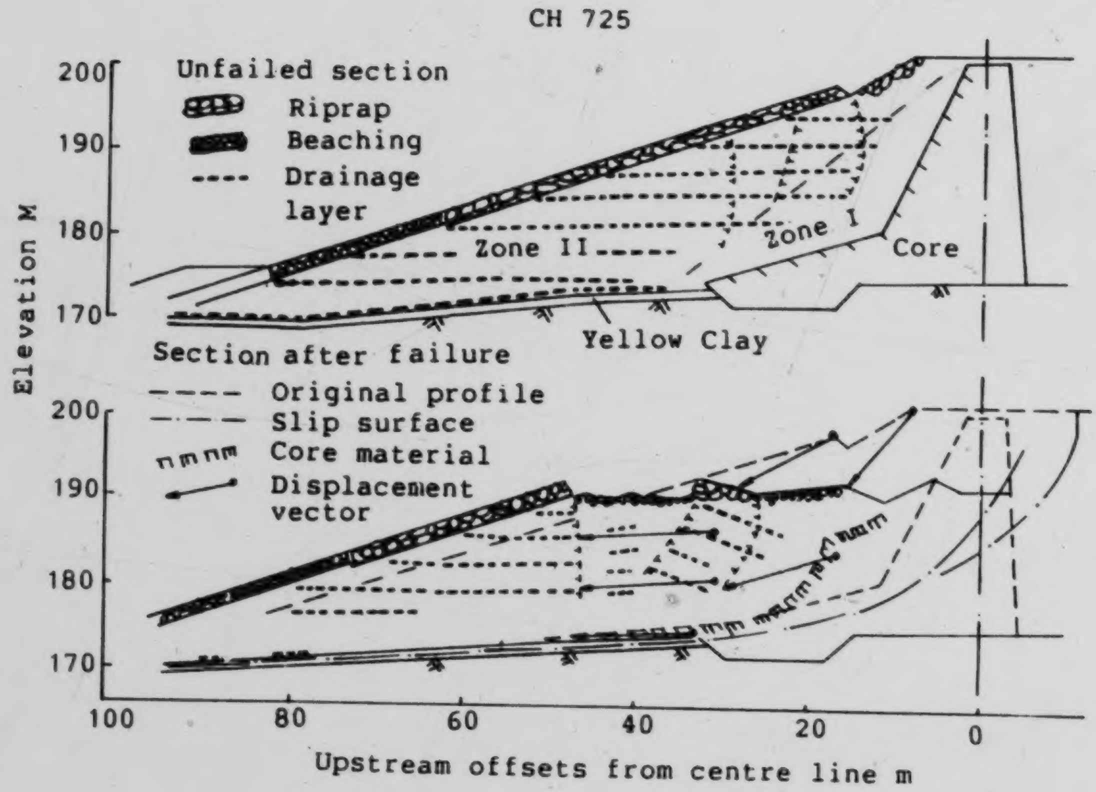
CH 725
Elevation M
200
190
180
170
Unfailed section
Riprap
Beaching
Drainage layer
Zone II
Zone I
Core
Yellow Clay
Section after failure
Original profile
Slip surface
Core material
Displacement vector
200
190
180
170
100
80
60
40
20
0
Upstream offsets from centre line m

Figure 4.16: Investigative section at CH 725

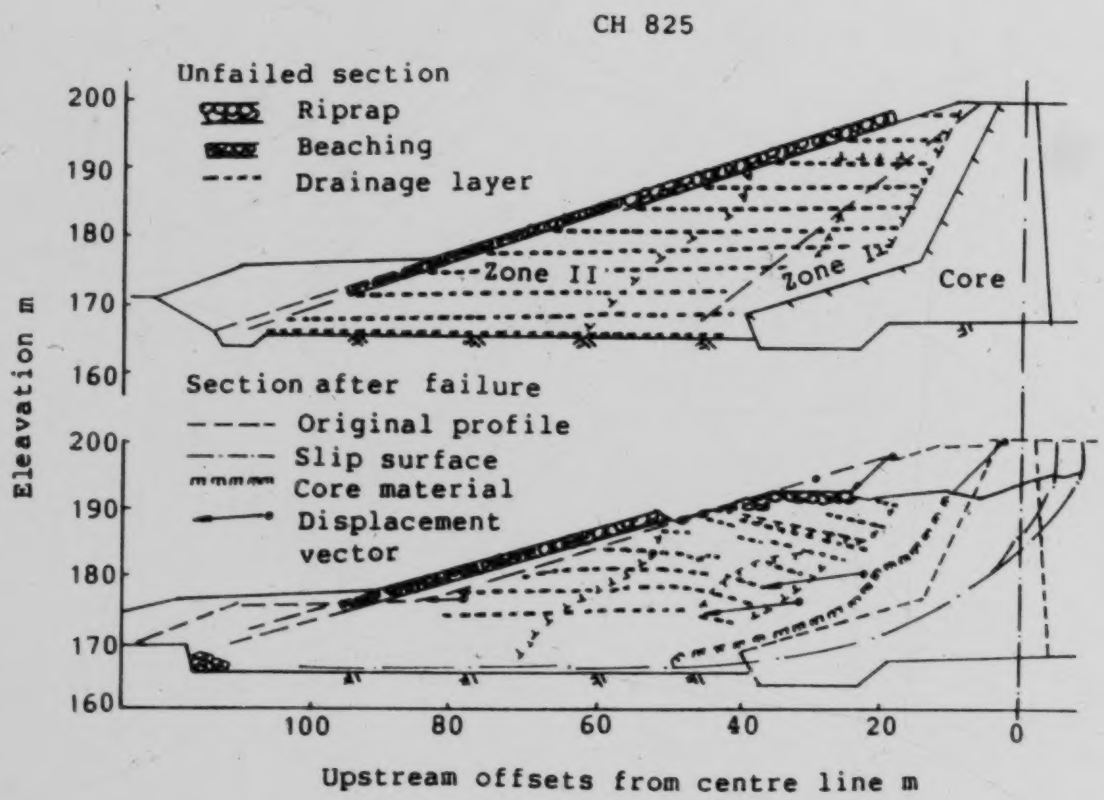
CH 825
Unfailed section
Riprap
Beaching
Drainage layer
Zone II
Zone II
Core
Section after failure
Original profile
Slip surface
Core material
Displacement vector
Eleavation m
200
190
180
170
160
200
190
180
170
160
100
80
60
40
20
0
Upstream offsets from centre line m

Figure 4.17: Investigative section at CH 825

4.2 Summary of Previous Reserach

The three volumes of "Carsington Dam - The Machanism of Failure" have described the field investigation and laboratory tests as well as numerical work in back-analysing the failure machanism. In order to direct our further research, it is necessary to identify what they have done, what results they have obtained and how they arrived at their conclusions. First, a brief introduction of their main conclusions is given. Then, a short comment is made and lastly recommendations for the new work are also discussed. Emphases are placed only upon the aspect of numerical analyses.

4.2.1 Main conclusions

Using the unmodified results from laboratory tests (intact peak strength) on materials taken from Carsington Dam after Failure, the factor of safety (F) was 1.41 around the most critical section (CH 725) and was 1.55 in the valley bottom (CH 850).

Since failure occured, influences reducing the above F to 1.0 must be identified. The "REPORT" concludes that the failure is mainly caused by progressive failure due to strain softening in the core, boot and Yellow Clay layer. The main influences are

1. solifluction shears pre-existing in the Yellow Clay layer which is the significant effect,
2. numerous shears in the core and boot caused by

construction plant which are minor weakening effects,

3. unscarified nearly horizontal construction surfaces in the zone II which are also minor effects,
4. lateral load transfer which accounts for the propagation of the failure from the initial failure section to lateral sections.

The "REPORT" also points out that if shears (pre-existing or due to construction defects) were taken into consideration, the factor of safety would be reduced to 1.21 (CH 725) and 1.44 (CH 825). As defined in the "REPORT", the "critical state of a soil is reached due primarily to an increase in water content leading to an almost total loss in C', without any appreciable change in ϕ'. The strengths in this state are used to accommodate strain softening. By using "critical state" strength: $C'=0$, $\phi'=\phi'_{peak}$, a further reduction of SF to 1.07 for CH 725 and to 1.29 for CH 825 can be obtained.

The proportion of the main influences upon the factor of safety is evaluated as given in Table 4.3.

Other influences have been suggested in addition to the above to explain the mechanism of failure, e.g. the weakening of material due to chemical changes. But, as pointed in the "REPORT", they were not required because the dam would fail in any case without invoking them.

A safe dam can be constructed at the Carsington site provided that the redesign is based upon the principles

Table 4.3 Reduction of factors of safety due to different factors

	Intact strength		CH. 725	CH. 850
	2-D analysis		SF=1.41	SF=1.55
	Percentage due to			
a	Progressive failure	in Yellow Clay	12%	
		in core material	3%	4%
		in Zone I & II		15%
b	Solifluction shears in Yellow Clay		10%	
c	Rutting shears in core		4%	4%
d	Construction surfaces			3%
e	Lateral load transfer			10%
	Total		29%	36%
	Check		(1.41-1.0)/1.41=29% Ok	(1.55-1.0)/1.55=36% Ok

elucidated in the "REPORT", i.e. the strength parameter reduction due to defects and pre-existing shears incorporated, and conventional factors of safety applied.

Limit equilibrium analyses were carried out to give factors of safety along the dam length without considering the effect of load transfer. The results are shown in the Table 4.4.

Table 4.4 Factors of safety at different sections

	Foundation	Chainage	F	
North slope	Yellow Clay	580		Final extent of slip
		600	1.06	
		650	1.02	
		700	1.06	
		725	1.00	
		750	1.05	
Valley bottom	Grey weathered mudstone	825	1.15	
		850		
		900		
South slope	Yellow Clay	1000	1.11	
		1050	1.18	
		1075		

The strengths used in above calculation are taken from the most critical section (CH 725), and F=1.0 is defined for this section. These results accord with the field records in the following manner: failure started from around CH 725, then extended to the north slope, subsequently, the south slope began to fail due to load transfer.

4.2.2 Brief comments on the previous work

Limit equilibrium analyses are the primary means used in the "REPORT" to draw the conclusions. Multiple-wedge analyses were adopted with the interface force inclination comparable with the results of finite element analyses. The results have also been compared with those obtained from the Morgenstern-Price method. The difference is small.

Analyses were carried out in term of effective stresses. The determination of the pore pressure ratio were based upon the observed piezometric data.

The principles used in the "REPORT" to estimate percentage influences of major factors upon the factor of safety is very simple. First, three values of factor of safety are defined as:

F_1 for intact strengths,

F_2 for peak strengths reduced by construction defects and pre-existing shears,

F_3 for strengths further reduced by progressive failure due to strain softening.

Then, it can be obtained that

$(F_1-F_2)/F_1$ = reduction due to pre-existing shears

$(F_2-F_3)/F_1$ = reduction due to progressive failure

$(F_3-1.0)/F_1$ = reduction due to load transfer

Obviously, these definitions can be extended to consider other influencing factors. Thus, the conclusions in Table 4.3 can be made. Although the above definitions are simple in form, it is difficult to apply them in practice.

In the most critical section CH. 725, the factor of safety is assumed as 1.0 under the assumption of no lateral load transfer. With $F_3=1$, the influence of progressive failure can be easily estimated. However the above assumption (F=1.0) needs to be checked by analysing the three dimensional effects. In other sections where safety factor are greater than 1.0 just before failure, the operational strengths reduced by progressive failure need to be estimated from finite element analyses in calculating F_3.

Therefore, if used independently, limit equilibrium analyses are powerless to discern the influence of various factors upon the factor of safety. At least two dimensional finite element analyses are needed to estimate the operational strength and provide a guide for the assumption on interface force inclination. In addition, three dimensional effects should be investigated in estimating the influence of lateral load transfer.

The only merit of the above method is to give a conventional basis for comparison of factors of safety. Nevertheless, the physical meaning here is not clear because the operational strength parameters are not inherent material properties. Strictly speaking, the degree of safety cannot be measured by using operational strength parameters.

As we know, spontaneous softening will influence the degree of safety. Let us examine a very simple example. In Fig. 4.18, suppose $C_{u\ peak}$=100 kpa, $C_{u\ residul}$=50 kpa, the resultant external force is 75 KN, and this slip surface length is 1m. Four cases (a, b, c and d) are illustrated with the same total external force for a, b and c. Due to different distributions caused by different stress history, the difference between the degrees of safety is large. Here, linear stress distributions are assumed for the sake of simplicity, but all cases are kinematically possible, in equilibrium and do not violate the yield criteria.

From case b to c, no extra loading is needed theoretically, while from case a to b both loading and unloading should be needed. This reflects the influence of loading history upon the factor of safety.

From case a to d, the shear stress increases uniformly from 50 to 90 kpa. The factor of safety is reduced to 1.11, less than F=1.25 in case b. However, the situation can be considered more stable than case b.

Case c shows that a small disturbance may reduce the factor of safety by a certain amount, the extreme situation is that the safety factor is reduced to 1.0. For real dams, this disturbance may be rain water filling some cracks, some relaxation at the toe, small earthquakes or a layer or two of fill placed upon the top of dam.

In short, when the above definition of safety factor is used as a basis for comparison, the same value may not imply the same degree of stability. To solve this problem, the only way is to introduce deformation behavior into an analysis.

At present, one possible and reasonable way to measure the degree of safety is to reduce the peak-strength by a factor of safety according to Bishop's definition, and keep the residual strength unchanged in finite element analyses.

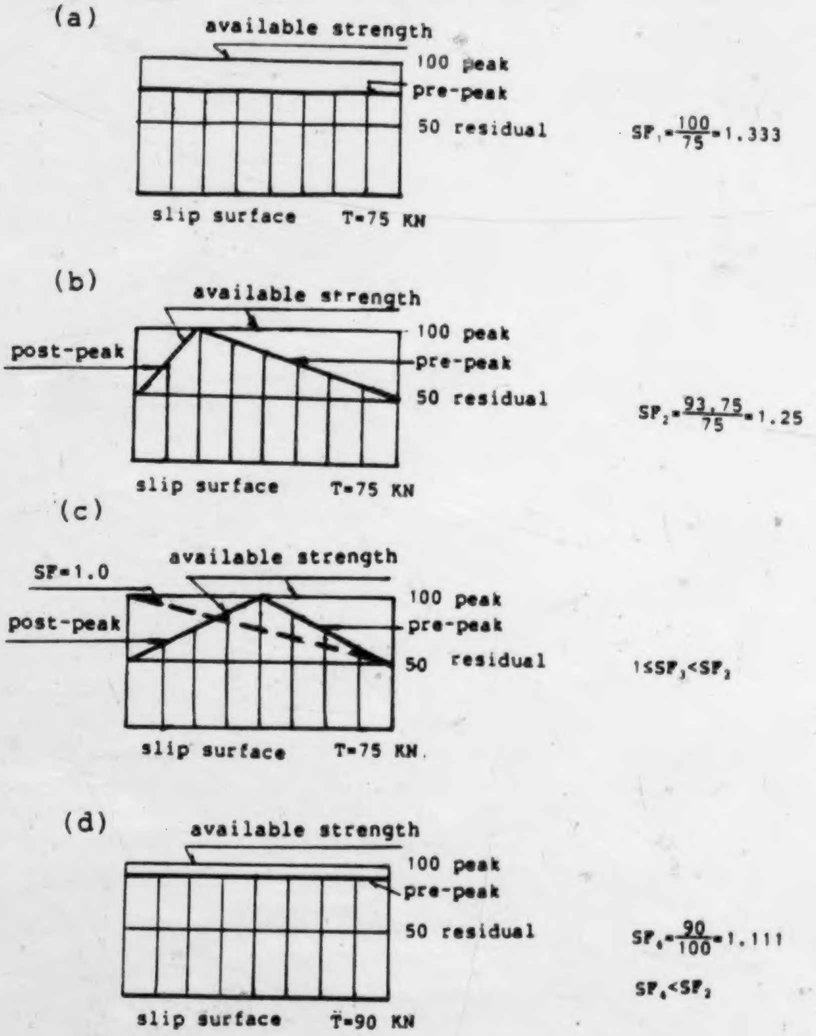
(a)
available strength
100 peak
pre-peak
50 residual
slip surface
T=75 KN
$SF_1 = \frac{100}{75} = 1.333$
(b)
available strength
post-peak
100 peak
pre-peak
50 residual
slip surface
T=75 KN
$SF_2 = \frac{93.75}{75} = 1.25$
(c)
SF=1.0
available strength
post-peak
100 peak
pre-peak
50 residual
slip surface
T=75 KN
$1 \leq SF_3 < SF_2$
(d)
available strength
100 peak
pre-peak
50 residual
slip surface
T=90 KN
$SF_4 = \frac{90}{100} = 1.111$
$SF_4 < SF_2$

Before peak: available strength = peak strength
After peak: available strength = operational strength

Figure 4.18: Definition of safety factors

In using the results, there are two choices. One way is to use the results from finite element analyses alone. For each sufficiently large strength reduction factor, we can find a critical height of failure. By trial and error or by interpolation, the strength reduction factor corresponding to failure at the designed height can be found and taken as the factor of safety. However, this method is obviously very expensive. Another way is to use the calculated strain distribution at the design height to work out the operational strength parameters, then to find a conventional factor of safety. The factors of safety obtained from the above two approaches may generally be different, and problems in both theory and calculation merit study. More discussion will be given in Chapter 6.

Three dimensional effects have also been investigated by using a very simple mechanical model. The study yields the conclusion that the lateral load transfer does not affect the initial failure at the critical section. In other words, the factor of safety should be about 1.0 at this section. The dam is treated as a beam with a uniform section lying on a horizontal foundation without vertical settlements. This is far from the reality. It seems that a sufficiently accurate estimate can be obtained only by three dimensional finite element analyses.

4.2.3 Recommendations for further nonlinear analyses

The main objectives of this research are focussed on the study of numerical methods in analysing progressive failure due to strain softening by using the case history of the Carsington Dam as an example. It is not intended to try to fit the results with the observed deformation data by adjusting material parameters. Since the information on deformation moduli and post-peak behavior is not enough, little can be gained by varing too many parameters. Only two dimensional nonlinear analyses will be undertaken. Therefore, the critical height just before failure for certain sections may not be entirely accurate. However, the results from two dimensional analyses are conventionally sufficient for dam engineering. Generally speaking, a factor of safety less than 1.3 is not acceptable for any isolated section during the construction of rock-earthfill dams.

The main tasks for the numerical analyses in this research are as follows,

1. Trial finite element and limit equilibrium analyses are suggested in order to check the main conclusions drawn in the "REPORT" and examine the performance of program SAGE by comparing with the results obtained in the "REPORT". Then the program will be revised to meet the requirements for further analyses. The influences of various factors upon the factor of safety will also estimated and so parametric studies can be planned for those important parameters which

are not well defined in the "REPORT".

2. The boundary problem for finite element analyses should be defined as clearly as possible based on the previous work in the "REPORT" and trial calculations.
3. Limited groups of both effective and total stress analyses are planned for different working conditions to achieve three main objectives: firstly, to put the formulations and principles in theoretical study into practice and prove their effectiveness; secondly, to make conclusions on the failure mechanism of Carsington Dam; thirdly, to investigate the influence of certain major factors upon the reliability of the final results.
4. Limit equilibrium analyses are also to be made to estimate the Factor of safety.

5. DEFINING THE CARSINGTON DAM FAILURE FOR FINITE ELEMENT ANALYSES

The finite element method is intended to be used as the main tool in studying the mechanism of the Carsington Dam failure, in which progressive failure has played a major role. If we wish to carry out finite element analyses with confidence, the following questions should be answered:

1. to what extent can the whole process from construction to the end of failure be formulated in the framework of the adopted theories,
2. based on the laboratory and field data, which kinds of material model will fit the behaviour of each material best,
3. whether the external loads are defined accurately enough or not,
4. whether or not the material parameters to be adopted are reliable and accurate enough to obtain acceptable results,
5. whether or not the mesh design, construction sequence simulation and solution procedure are appropriate to quarantee a sufficiently accurate answer.

The last question has been answered in Chapter 3. In this chapter, we mainly try to define the problem of the Carsington Dam failure for finite element analyses as clearly and reasonably as possible by reviewing the information available in the "REPORT" and analysing results from trial calculations.

5.1 Summary of Preliminary Numerical Studies

5.1.1 Trial limit equilibrium analyses

Limit equilibrium analyses have been carried out to check the main conclusions in the "REPORT" and estimate the influences of various factors upon the factor of safety. The calculations were carried out by means of Sarma's method. The results are in good agreement with those given in the "REPORT" with a relative error less than 1% if all the conditions are the same. Hence, the same conclusions can be drawn. Only some useful implications will be mentioned in this section, the analyses can be found in detail in Appendix G. In Table 5.1 the influences of certain material parameters upon factors of safety are listed.

Table 5.1 Influence of some material parameters

Material	Parameter		Change of parameter	Change of F.o.S.
Zone I & II	Unit weight	γ	+0.5 kN/M^3	+1.0%
Core	Unit weight	γ	+0.5 kN/M^3	-0.4%
	Undrained strength	Cu	+5.0 kpa	+3.5%
	Friction angle	Ø'	+1°	+4.5%
Yellow Clay	Friction angle	Ø'	+1°	+4.5%

As shown in Table 5.1, a variation of the unit weight by 0.5 kN/M^3 only leads to a change of SF by no more than

1%. Therefore, the average unit weight can be used with confidence. The influence of the undrained strength C_u is not small, since an error of 5 or even 10 kpa may not be avoided in estimating an average value including the effect of strain softening. In real situations this value depends on the total stress and pore pressure development. C_u is different at different elevations and is especially unsuitable for the top construction layers of the dam where observed pore pressures were zero or very small and the soil was really not saturated. Hence, it is not reasonable to determine the main slip surface in the top layers if an average C_u is used. However, for a preliminary study, total stress analyses are acceptable by experience.

Further limit equilibrium analyses with effective strength parameters C' and ϕ' have been carried out for comparison. The results show that a 3m reduction of the dam height from EL. 201m to EL. 198m will cause an increase of the safety factor by 12% if total stress analyses is used. However, the corresponding amount will be 16.5% if effective stress analyses are used. The influence is noticeable. It is simply because the observed pore pressures at EL. 198m are considerably smaller than that at EL. 201m. Since the failure height predicted by two dimensional analyses may nct be correct, an effective stress analysis based on observed pore pressure data is more reliable.

A decrease of the friction angle has been used in limit equilibrium analyses in the "REPORT" to study the effect of the softening process. The influence is important as shown in Table 5.1. The operational friction angle during softening is mainly affected by the softening rate and elastic modulus, if the residual strength is reliable. In view of the limited information on this aspect, the influence of their changes within the possible range should be examined by finite element analyses, before we can use the results to draw conclusions with confidence.

5.1.2 Trial finite element analyses

The Program SAGE was used for the first run of a two dimensional analysis at CH 725 of the Carsington Dam. Limited by the original capacity of the Program SAGE, comparatively simple material models were adopted. A very fine mesh was adopted in the trial runs as shown in Fig. 3.8 as compared with that used in the "REPORT" (Fig. 5.1).

In Fig. 3.8 a conventional large foundation is used which is not completely shown as described in Section 3.2.3, while only a non-linear elastic layer is used in the " REPORT " to simulate the foundation. Ten construction layers above the foundation are used to simulate the construction sequence while six layers have been used in the "REPORT".

All the analyses are in terms of total stresses including those presented in the "REPORT". The adopted models are listed in Table 5.2 for comparison.

Linear elastic moduli before the peak and associated flow laws are adopted for all nonlinear materials in trial

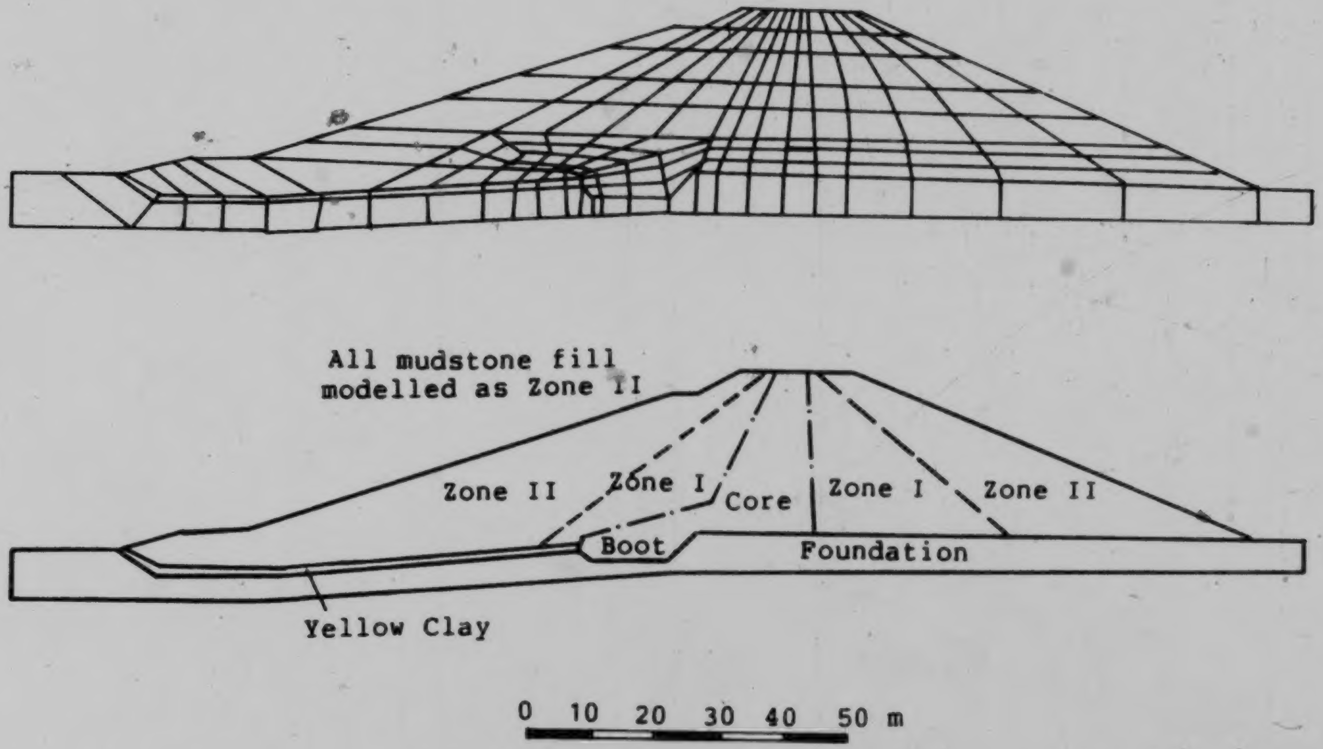
All mudstone fill
modelled as Zone II
Zone II
Zone I
Core
Zone I
Zone II
Boot
Foundation
Yellow Clay
0 10 20 30 40 50 m

Figure 5.1: Geometry and mesh for CH 725 in the REPORT

runs. Failures due to tension have been considered in the "REPORT", while we assume that all the materials could take tensile stresses.

Table 5.2 Comparison of Material Models

Material	Present Model	Model in "REPORT"
Core	Von Mises, Associated flow, Hyperbolic softening	Von Mises, Non-associated, without softening
Yellow Clay	Mohr-Coulomb, Associated flow, Brittle	Mohr-Coulomb, Linear softening, Non-associated.
Zone I & II	Mohr-Coulomb, Associated flow, Brittle	Mohr-Coulomb, Linear softening, Non-associated.
Foundation	Large usual mesh, Linear elastic	Nonlinear elastic cushion

The material parameters as shown in Table 5.3 are selected from the latest recommendations in the "REPORT". In Table 5.3, the parameters in the "REPORT" are also given in the parentheses for comparison. The strength reduction due to the geological pre-shears or construction defects has been taken into account in determining the strength parameters (Section 4.1.2).

The main differences between the two sets of input data will be described for each material as below.

1. A linear elastic foundation is assumed in the trial run, with an elastic modulus E=125,000 kpa and Poisson's ratio μ=0.35. Therefore, a back-check against the observed settlement is needed. In the "REPORT", a nonlinear modulus has be adopted, which

was obtained by fitting the observed settlements.

2. For the core material, the von-Mises yield criterion is adopted in both studies. Hyperbolic softening is assumed in our calculations with the peak undrained strength C_u=52 kpa and the residual strength C_{ur}=28 kpa, while no softening for the core was considered in the "REPORT". An average peak strength (C_u=52 kpa) is estimated by following effective elastic stress paths until they intersect with the Mohr-Coulomb failure envelope in an elastic analysis. It is impossible to follow the stress path during strain softening in an elastic analyis. The residual strength is roughly estimated by studying the possible stress paths and pore pressure changes for a typical element of the core. A moderate softening rate is selected for the trial calculation. The initial rate gives a reduction of peak strength by 10% due to 2.5% principal plastic strain after the peak. The Poisson's ratio is assumed to increase from 0.43 at first to 0.49 after the construction of two 3m layers.
3. For the Yellow Clay layer and Zone I & II fills, a brittle elastoplastic model with the Mohr-Coulomb failure criterion and associated flow law is used in our calculation. Obviously, in assuming an infinite softening rate, the brittle model gives a lower bound. However, in the "REPORT" non-associated flow

Table 5.3 Comparison of material parameters

Soil Type	Unit Weight KN/M^3	Young's Modulus kpa	Poisson's Ratio	Cp kpa	Øp °	Cr kpa	Ør °
Foundation (drained)	20.0 (20.0)	125,000 ($30 \times p'$)	0.35 (0.35)	Elastic			
Core & Boot (undrained)	18.5 (18.5)	2500 (2500)	0.43-0.49 (0.46)	52 (51)	0 (0)	28 (51)	0 (0)
Yellow Clay (drained)	19.5 (20.0)	3000 ($20 \times p'$)	0.42 ($f_1(J_2)$)	6 (0)	18 (20)	0 (0)	12 (11)
Zone I & II (drained)	21.0 (22.0)	60,000 ($370 \times p'$)	0.38 ($f_2(J_2)$)	13.5 (10)	24 (25)	0 (10)	14.5 (25)

note (1) Values without parentheses are used in trial run.
- a) All materials can take tensile stress .
- b) Strain and displacement are set to be zero in foundation before construction.

note (2) Values in parentheses are used in "REPORT",
- a) Dilation angle=0 for all elasto-plastic materials.
- b) MOnimum E=2000kpa,unload Eu=(1 to 4)E.
- c) P'=mean effective principal stress.
- d) J_2=the second invariant of stress tensor.

laws with a zero dilation angle have been used and strain softening in the Yellow Clay layer has been simulated by using a linear relationship between strength and strain.

4. Average elastic parameters are used in our calculation. One thing which should be mentioned is that the elastic modulus of E=40,000 to 80,000 kpa for the Zone I & II fills seems higher than that in real situations. In the "REPORT", the elastic modulus is assumed as a linear function of the first invariant of the effective stress tensor and Poisson's Ratio is obtained from a linear function of the second invariant based on the observed test or field data. The influence of the unloading modulus upon the progressive failure has also been studied in the "REPORT".

Our results show that the dam fails when it reaches EL. 198.0m, i.e. at the end of the construction of Layer 9 in total 10 layers. It is not strange that our calculated failure height is about 3 meters lower than that of EL. 200.95m as calculated in the "REPORT", because brittle models are used for both the Yellow Clay layer and Zone I & II fills and the strain softening process is simulated for the core in our calculation. Because of the differences between the two set of input data, only the comparison between main features of the failure mechanism is meaningful.

The settlement of 0.325m was observed under the core in the foundation at CH 705. The calculated settlement at the corresponding location at CH 725 is about 0.3 to 0.33 m. Since no observed distribution of vertical displacements is available at the dam base, the value of 125,000 kpa is the best assumption we could make for the equivalent elastic modulus.

The incremental displacement vector plot may be used to determine the location of the slip surface. Kinematically possible slip surfaces can be integrated by taking the incremental direction as the tangent. The most dangerous slip surface can be discerned among all the kinematically possible ones (see detail in the next chapter). The incremental displacement field in Fig. 3.11 shows less rotational characteristics than that given in the "REPORT" (Fig. 5.2). Strictly speaking, neither of the two vector plots reproduces the observed fact that the general slip surface goes through the whole length of the Yellow Clay layer without appreciable heave of upstream surface when failure starts. Because there exist pre-shears in the Yellow Clay layer, and the shears extend nearly parallel to the layer boundaries, occupying about 40% of the total length, the material exhibits anisotropic characteristics. An isotropic model may be not good enough to simulate the slip surface parallel to the the layer boundaries.

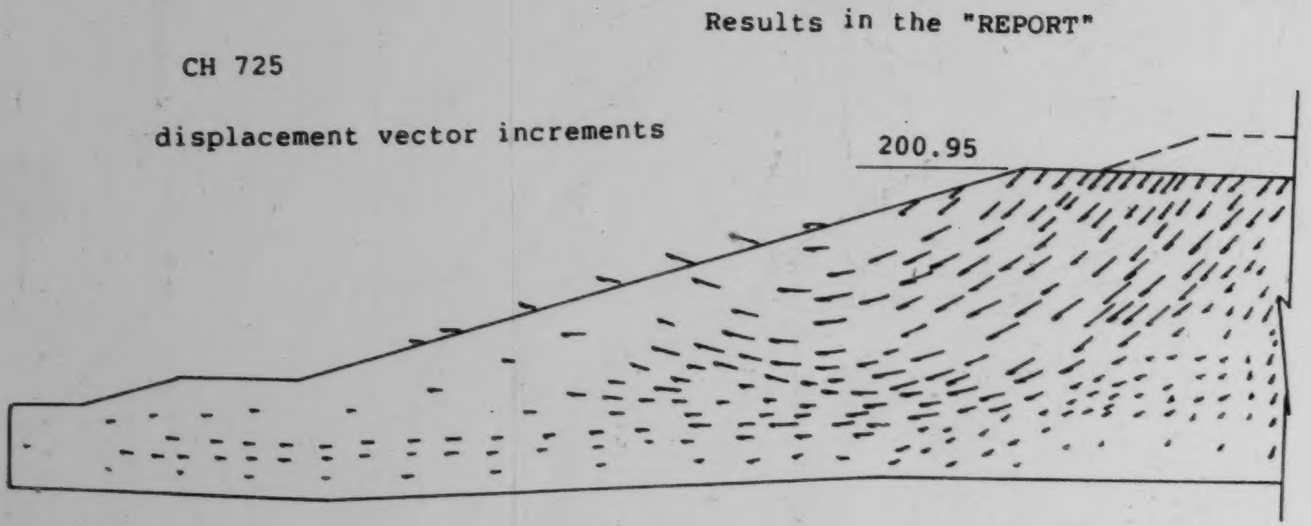
Results in the "REPORT"
CH 725
displacement vector increments
200.95

Figure 5.2: Results in REPORT - displacement vector increments

In Fig. 5.3, vertical stresses at the loading stage of layer 8+9/10 are plotted. The arching action in our results is highly exaggerated due to higher average elastic moduli selected for Zone I & II fills. It is better to use the assumption of nonlinear elastic moduli which fits the observed settlements.

By examining the output loading history it can be found that the stress level along the observed slip surface is past peak in the boot, but it is still pre-peak at the top portion of the dam. It is easy to understand that the slip surface cannot be simulated correctly within the top portion of the dam by doing a total stress analysis with a constant undrained strength C_u. In the real situation, no pore pressure has been observed in the top layers and the stress level is very low. Hence, an effective stress analysis is more suitable.

The calculated results have shown that the maximum tension stress is developed in the top layers and amounts to about 100 kpa under the assumption that all materials are capable of taking tensile stresses. Therefore the influence of tension cracks upon the failure mechanism should not be neglected in the future calculation.

In Fig. 5.4, the movement of the upsteam peg near the toe is plotted for comparison. Although the observed data include deformation due to creep, the dam simulated

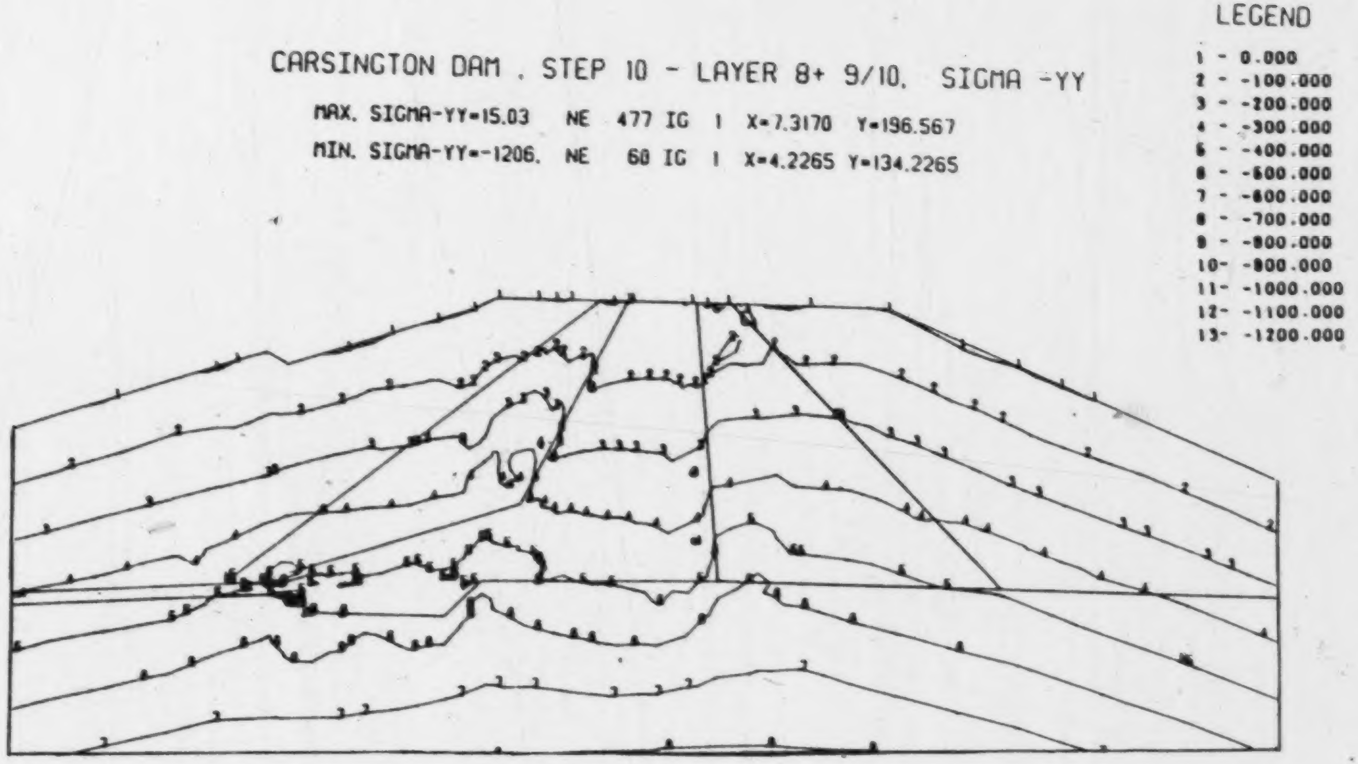
CARSINGTON DAM . STEP 10 - LAYER 8+ 9/10. SIGMA -YY
MAX. SIGMA-YY=15.03 NE 477 IG 1 X=7.3170 Y=196.567
MIN. SIGMA-YY=-1206. NE 60 IG 1 X=4.2265 Y=134.2265
LEGEND
1 - 0.000
2 - -100.000
3 - -200.000
4 - -300.000
5 - -400.000
6 - -500.000
7 - -600.000
8 - -700.000
9 - -800.000
10- -900.000
11- -1000.000
12- -1100.000
13- -1200.000

Figure 5.3: Trial F.E.A.- vertical stress contour

in the trial run still looks much stiffer. In Fig. 5.5, the calculated vertical strains in the core are compared with those given in the "REPORT" and with the measured values in the core at Gauge BS1 at CH 705. The result presented by us seems of about the same magnitude as the observed data at EL 198.0m. However the dam fails at EL 198.0m in our case. The predicted deformations are still much smaller when compared with those observed just before failure.

As mentioned in the "REPORT", the horizontal moduli of Zone I and II may be underestimated by comparing the predicted and observed horizontal displacements. An anisotropic model can easily simulate this feature.

In conclusion, the trial calculation has shown that the Program SAGE is capable of tackling the complex problem in practical engineering projects such as the the progressive failure of the Carsington Dam, if necessary revisions are made. The assumed equivalent elastic modulus for the large conventional foundation is acceptable. It is better to use the same assumption of nonlinear elastic moduli in the "REPORT" for zone I and zone II fills. More suitable material models and parameters should be adopted in SAGE to cover the main features influencing the failure mechanism of the Carsington Dam, including anisotropic models, cracking models and strain softening models for post-peak behavior. In addition, effective stress analyses are

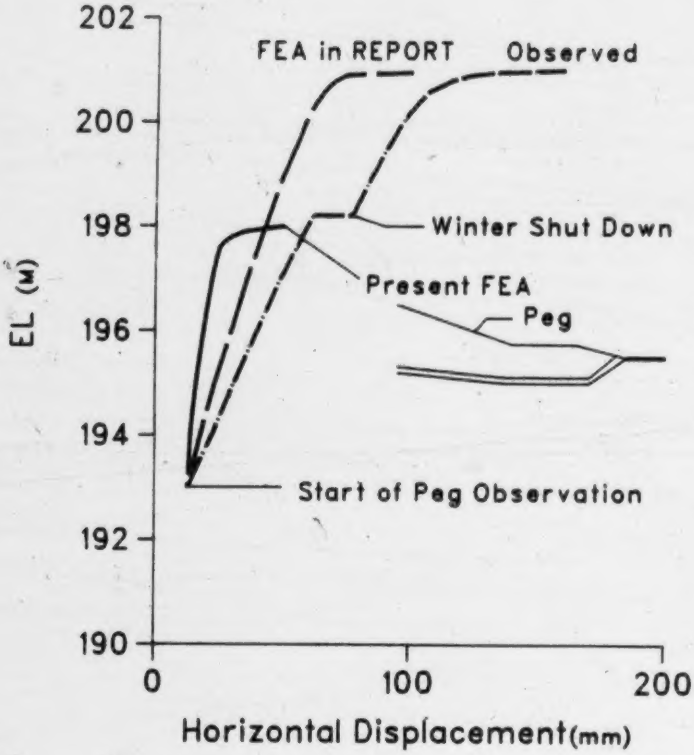

Figure 5.4: Trial F.E.A.- peg movements

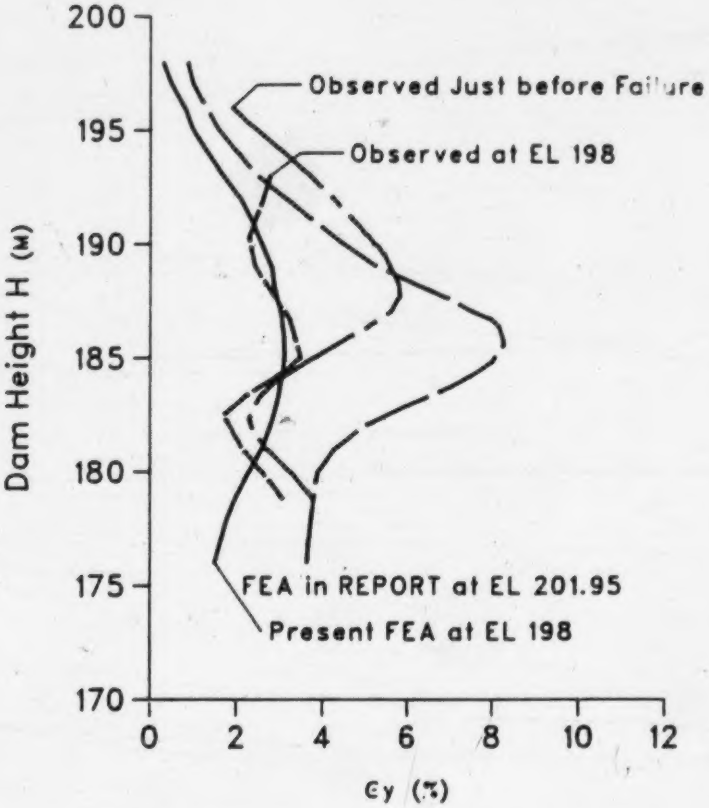

Figure 5.5: Trial F.E.A.- vertical strains in the core

more suitable.

5.2 Defining the Boundary Problem for Back-analyses

In order to simulate the Carsington Dam failure, the boundary problem is to be defined by answering the five basic questions raised in the beginning of this chapter. The definition is based on the information given in Chapter 4 and the results gained in the preliminary numerical studies. The section is chosen at CH 725, where the failure started.

5.2.1 Feasibility of formulating the problem in plasticity

Based on the recorded failure events (Section 4.1.4), the whole process from the begining of construction to the total failure of the Carsington Dam can be divided into the following stages,

1. the strain-stress level normally developed before failure as the dam went up nearly to the design elevation,
2. the creep rate increased suddenly and abnormally and cracks was observed on the surface of the dam. This indicated a critical state in stability,
3. starting from the most critical section and extending longitudinally, large deformation took place, wedges dropped down, grabens formed and the upstream dam body was thrusted horizontally along more than 500m length of the dam. The collapse movement finally stopped, mainly due to the new

geometric configuration and the sharp decrease of pore pressures.

In dam engineering, what we are most concerned with is the working performance of the dam and the prediction of the critical state if the design is not safe.

The deformation before failure was caused by the gravitational force of newly-built layers and the increase of pore pressures. Although strain softening processes might develop in certain regions, they were limited. The observed creep rate was less than 1.5 mm/day, peg movements were less than 0.2m and no abnormal behavior of the dam had been reported during this stage. Generally speaking, it was a typical quasi-static loading process and the compatibility conditions were satisfied in the macro sense. According to the basic theory in Chapter 2, the process before failure can be formulated in the framework of plasticity with small strain and deformation assumptions.

At the critical state, the sudden increase of the creep rate were caused by spontaneous progressive failure due to certain disturbances in the highly strained areas along the potential slip surface. The disturbance might be small pore pressure changes due to heavy rain or one or two newly-placed layers of fill. Since no pore pressure changes were observed in the section without further placing, it is reasonable to simulate the disturbance only by increasing the dam height.

Along the deformation curve, the critical state is represented only by a point. The deformation after the peak will be inevitably involved in the back-analyses. Although the compability in the most part of the dam body was still satisfied, it was not so in cracks and might not be so along certain parts of the most critical potential slip surface, where local collapses might cause dislocations of materials in the macro sense. However, we can still formulate the problem in plasticity by introducing brittle models.

In short, it can be expected to isolate the critical state by unacceptably large displacements at failure, but the calculated deformations only indicate failure and their absolute values are less important.

The failure process to a new equilibrium position involved exceptionally large deformations without compability, total break-down of materials and rigid body motion of separated wedges. Up to now, no effective theories and methods have been developed to tackle it. However, its numerical analysis is irrelevant in dam engineering practice. No further analyses of post-failure behavior are intended in this research.

5.2.2 Evaluating the pore pressure distribution

The loads for the back analyses during the construction stage are caused by gravitational body forces and generated pore pressures. The latter are transformed into equivalent nodal forces. Since the given density for each material is reliable, the task left here is to make reasonable assumptions of the pore pressure distribution generated during loading.

Only zero or small pore pressures have been observed in Zone II. Zero pressures are assumed for this region.

The observed pore pressures just before failure in Zone I is between -2 to 7 meters on average (Fig. 5.6). However, at CH 725 the observed general potential slip surface did not pass through Zone I fill but the Yellow Clay layer below it. Besides, the observed piezometric heights (-2m to 7m) are much lower than those of 20 to 30m in the adjacent region of the core. Therefore, the assumption of zero pressures in zone I fill is reasonable.

As to the Yellow Clay layer, the possibility of pore pressures being generated during construction has been discussed in the "REPORT". No fill was placed between October, 1983 and April, 1984. By using the Terzaghi consolidation theory and adopting an experimental value of the parameter C_v, the "REPORT" made the conclusion that the layer was fully consolidated by April 1984. The pore pressures built up during the 1984 loading, were calculated by using tested pore pressure parameters and stress changes obtained from finite element analyses. The estimated pore pressure takes its maximum value of about 45 kpa (4.5m head) and decrease sharply below 10 kpa within 25m in the upstream direction form the boot. The effect on the safety factor is about 2%. We neglect this minor effect in further

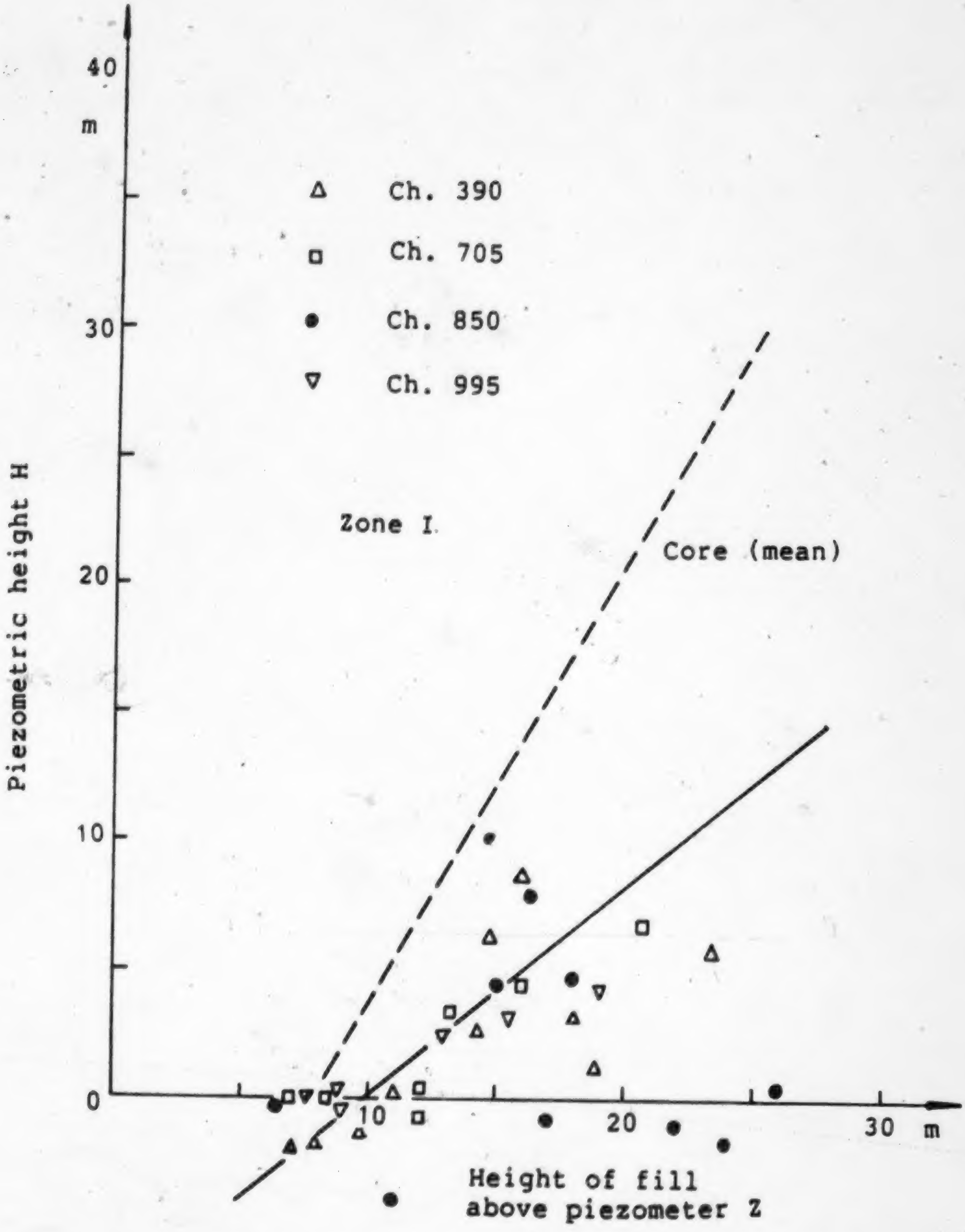

Figure 5.6: Piezometric observation in Zone I fill

calculations in view of the limited accuracy of the input information.

Zero pore pressure is assumed throughout the rest of foundation, since no failure has ever been found in it.

Because of the above simplifications, only the pore pressures in the core and boot need to be evaluated. The pore pressures dissipated during the standstill between Oct. 1983 and April, 1984. During this period, the pore pressure decreased by 2-3 meters in total height, then went up after the 1984 loading. This implies not only changes of effective stress but also changes of volume. At present, it is impractical to incorporate consolidation into the non-linear stress analyses for such a complex problem as the Carsington Dam failure. To simplify the calculation, we assume the pore presure goes up linearly as the dam height goes up.

Fig. 4.11 shows the simplified linear relationship. A program has been compiled to give incremental change of pore pressure at each loading step for finite element analyses. Thus, we can have

$$\begin{aligned} p &= 0 && (H < H_i) \ , \\ p &= B_p \gamma_w (H - H_i) && (H \geq H_i) \ , \end{aligned} \qquad (5.1)$$

where

p is the generated pore pressure during loading,

B_p is an average proportional factor based on observed data,

H is the fill height above the point in consideration as the dam goes up,

H_i is the average observed intial height above which pore pressure will be generated,

γ_w is the density of water.

and so the incremental expressions will be

$$\Delta p = 0 \ (H<H_i) \quad \text{and} \quad \Delta p = B_p \gamma_w \Delta H \ (H \geq H_i) \ . \tag{5.2}$$

For the section at CH 725, B_p and H_i in eqn. 5.1 and 5.2 are estimated for different elevations with the help of Fig. 5.7, which is for the nearby section at CH 705. The calculated pore pressure distribution before failure is checked against the observed data in Fig. 4.10. At all the observation points, the errors in head are less than 1.0m.

Possible error due to the above linear asumption can be seen from Fig. 5.7. If an average value of B_p is used between zero and final pore pressures, the complex history of the pore pressure generation and dissipation cannot be reflected. Although it is not difficult to follow the observed unloading curve of pore pressures without further placing of fill, the results are doubtful. This is because all the observed data show that deformation continuously increased. In reality, the soil underwent very complex processes of pore pressure dissipation and structural changes which resulted in continuous creep. By neglecting the time effect, our present approach is powerless to deal

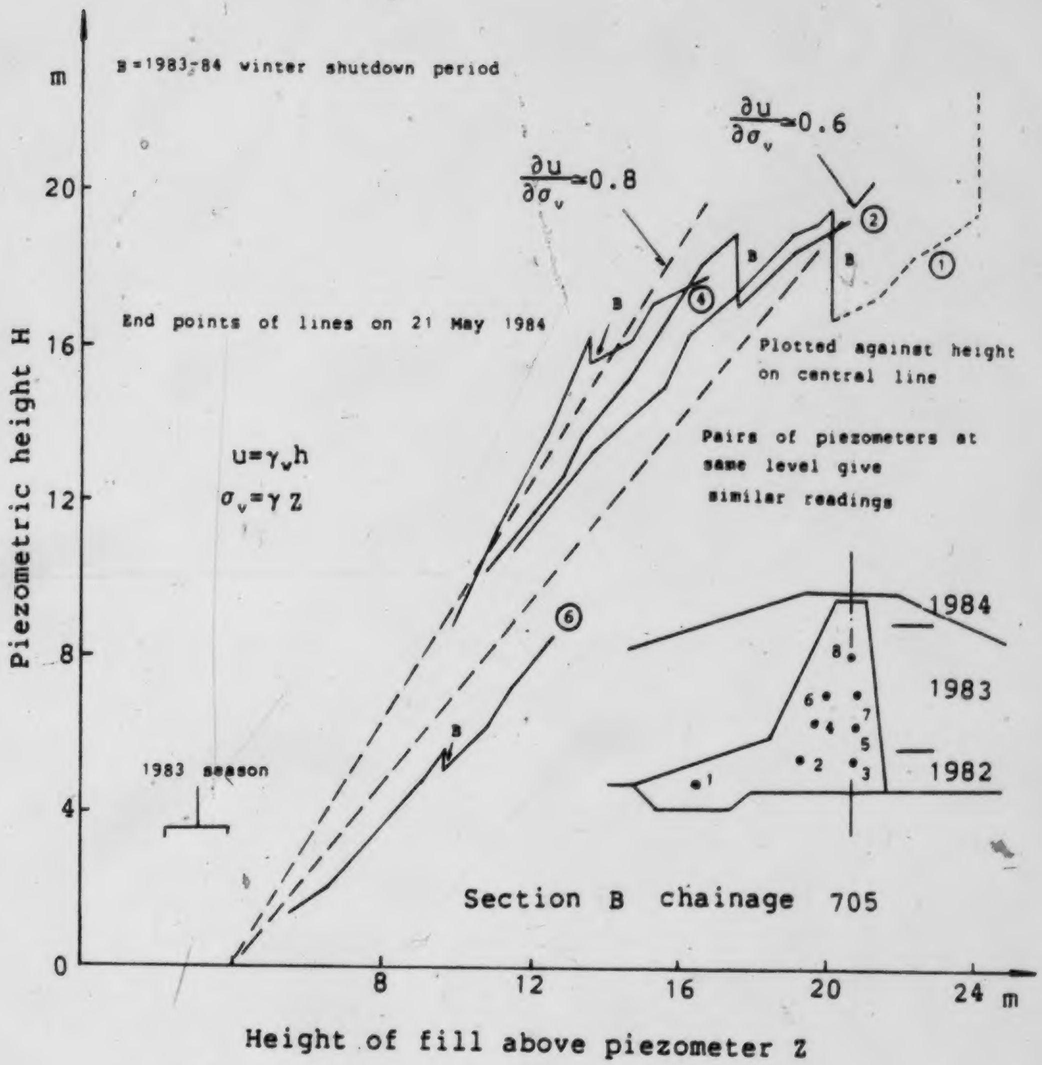

Figure 5.7: Typical piezometric line for the core and boot

with this situation.

Due to the complicated process of pore pressure generation and dissipation, the above evaluation is approximate. A parametric study of B_p is needed in back-analyses.

5.2.3 Selecting suitable material models

We mainly use effective stress analyses in the further study and list selected material models and the main reasons briefly in Table 5.4.

Experience and trial calculations have shown that too many Gaussian points fail at the very low stress level near zero when the Mohr-Coulomb model is used, especially when used together with cracking models. This does not reflect the real situation in dam construction. Elastic models are suggested in the first loading step.

Cracking models are to be adopted for all the materials except the foundation according to the theories introduced in Section 2.3.

The anisotropic material may fail outside the weak plane. When this situation is found, an isotropic yield criterion will be used.

Total stress analyses are theoretically acceptable for undrained conditions. The pore pressure observation has shown that most lower parts of the core fulfill this condition. Except the core material, there is no difference between total and effective stress analyses, since the pore

Table 5.4 Selected material models

Material	Selected Model	Reasoning & Notes
Foundation	linear elestic	1) no failure in it 2) proved to be acceptable by trial calculation
Yellow Clay layer	Mohr-Coulomb	1) only parameters C' & Ø' are availble
	hyperbolic softening	2) brittle after peak
	orthogonally anisotropic	3) effect of horizontal pre-shears
	non-associated	4) to limit dilation at failure
Core	Mohr-Coulomb	1) only parameters C' & Ø' are reliable
	hyperbolic softening	2) brittle after peak
	non-associated	3) to limit dilation at failure
	isotropic	4) defects distributed at random
Zone I & II fill	Mohr-Coulomb without softening	1) only parameters C' & Ø' are availble 2) slightly brittle 3) failure mainly occurs in yellow clay layer and core
	isotropic (final results)	4) anisotropic moduli are not available
	orthogonally anisotropic (parametric study)	5) horizontal construction defects 6) effect of horizontal stiffness upon deformation
	non-associated	7) to limit dilation at failure

pressure is assumed to be zero. Total stress analyses will also be undertaken for comparison.

5.2.4 Determining material parameters

Except for unit weights and strength parameters, the deformation parameters $E'(\sigma'_{ij})$ and $\nu'(\sigma'_{ij})$, especially softening rate $a'(\epsilon_{peak})$ are not well defined and the available supporting test data are also not sufficient. Here, "'" denotes the formulation in an effective stress sense. It is very difficult to evaluate them accurately. Simplification and rough estimation are unavoidable in determining their values. The suggested values used in the "REPORT" will be adopted after reviewing whenever possible. The discussion on their reliability will be given in the next chapter by analysing the results. Obviously, a good agreement between the calculated deformations and the observed data cannot be expected. This is because no special effort has been ever made in the field and laboratory tests to provide information for deformation prediction by means of numerical methods.

5.2.4.1 Unit weight and strength parameter

Unit weights and strength parameters for effective stress are well defined in the "REPORT". They are based on careful laboratory and field investigation before and after failure. Therefore, they are reliable as listed in Table 5.5 and Table 5.6.

Table 5.5 Unit weight

Material	Foundation	Yellow clay layer	Core	Zone I	Zone II
Selected values	20.0 kN/M³	20.0 kN/M³	18.5 kN/M³	20.0 kN/M³	21.3 kN/M³

The strength parameters below have included all defects in the materials.

For the core material, an average undrained strength C_u of 52 kpa is suggested for the peak value while 27 kpa is suggested for the residual. As mentioned before, they are not accurate enough to accommodate the complex stress-strain analyses. A back-check of the results is necessary.

Table 5.6 Strength parameters C' & Ø'

Material	Selected values			
	Cp'	Øp'	Cr'	Ør'
Core	6 kpa	20°	0	13°
Yellow clay	6 kpa	18°	0	12°
Zone I	13.5 kpa	24°	0	14.5°
Zone II	13.5 kpa	24°	0	14.5°

5.2.4.2 Poisson's ratio

In the "REPORT", Poisson's ratios have been estimated from the limited test data. For total stress analyses in the core and boot, an average value of 0.46 was adopted. It was considered to model the compression of 1% air voids in the partly saturated fill. We change this value to values from

0.43 at a lower stress level increasing to 0.49 near failure. This seems more reasonable.

In another expression for Poisson's ratio, the yield ratio R_y is used to measure the extent towards yielding from an elastic state. R_y is equal to 1.0 at peak. The expression takes a linear form with respect to R_y as

$$\nu = \nu_0(1-R_y) + \nu_{max}R_y \ ,$$
$$R_y = J/J_f \qquad \text{for the von-Mises model,}$$
$$R_y=(\sigma_1-\sigma_3)/(\sigma_1-\sigma_3)_f \qquad \text{for the Mohr-Coulomb model,} \qquad (5.3)$$

where J is the second stress invariant and subscript $_f$ denotes failure. J_f and $(\sigma_1-\sigma_3)_f$ can be calculated by assuming the first stress invariant unchanged.

For isotropic models used in the "REPORT". It is suggested to adopt

$\nu_0 = 0.26$, $\nu_{max} = 0.49$

for the Yellow Clay, and

$\nu_0 = 0.167$, $\nu_{max} = 0.49$

for the Zone I and Zone II fill to fit the volume changes of limited observed data.

When the anisotropic model is used, the above assumption is regarded as valid for ν_1 which corresponds with isotropic plane deformation, but, for ν_2, $(\nu_2)_{max}$ is calculated by using condition B.10 so as to keep the elastic relationship positive definite. In order to evaluate ν_1 and ν_2 by using eqn. 5.3, we define

$$R_y = \frac{\tau}{\sigma'_n \tan\phi' + C'} , \qquad (5.4)$$

before peak. After peak we use $\nu=\nu_{max}$ with $R_y=1$.

5.2.4.3 Elastic modulus

In the "REPORT", linear elastic behavior up to failure was assumed for the core material in the total stress analyses. For other materials, non-linear elastic models were adopted. With zero pore pressure, they also apply to the effective stress analyses.

For core material, a Young's modulus of 2550 kpa was adopted in the "REPORT". This gives an axial strain at failure of 2%, which makes a reasonable fit to the test data. A value of 2500 kpa is adopted in this research for total stress analyses.

Information from test curves is not sufficient to formulate E', ν' for the core in effective stress analyses. Here, approximate methods are used.

To formulate the expressions for the elastic modulus, at least 3 test curves of $(\sigma_1'-\sigma_3')$ vs. ϵ_1 are generally needed for different stress levels, for example, of σ_3', and the test is better if performed under plane strain conditions. The above requirements cannot be met by available data and therefore we give a rough estimation. As we know, for the plain strain condition, the tangential modulus takes the form of

$$E(\sigma_{ij})' = \frac{(1-\nu^2)\Delta\sigma_1' - \nu(1+\nu)\Delta\sigma_3'}{\Delta\epsilon_1} \; . \tag{5.5}$$

By assuming a linear relationship before peak, and ν to be approximately 0.5, a rough estimate is

$$E'(\sigma_3') = \frac{(1-\nu^2)(\sigma_1'-\sigma_3')_{peak}}{(\epsilon_1)_{peak}} \; . \tag{5.6}$$

Further, we suppose $(\epsilon_1)_{peak}$ is constant for all stress levels. This assumption is acceptable since the range of $(\sigma_1'-\sigma_3')$ at peak is not large, being between 35 and 60 kpa in the core material.

At peak, the relationship between σ_1' and σ_3' can be found from the Mohr-Coulomb criteria as

$$(\sigma_1') = \left[\frac{\sigma_3'(1+\sin\phi')}{(1-\sin\phi')} + \frac{2C'\cos\phi'}{(1-\sin\phi')}\right]_{peak} . \tag{5.7}$$

Initially, we assume that $\sigma_3'=0$ when fill is first placed. Then E' can be evaluated with the increasing stress level. If E' is estimated from triaxial test data

$$E'(\sigma_3') = \frac{(\sigma_1'-\sigma_3')_{peak}}{(\epsilon_1)_{peak}} \tag{5.8}$$

The non-linear elastic modulus is adopted for the Yellow Clay, Zone I and II fill by fitting the observed settlement data. In the vertical direction the recommended expressions in the "REPORT" are

$$E_v = 20 \left(\frac{\sigma_1'+\sigma_2'+\sigma_3'}{3}\right) \tag{5.9}$$

for the Yellow Clay and

$$E_v = 370 \left(\frac{\sigma_1'+\sigma_2'+\sigma_3'}{3}\right) \tag{5.10}$$

for Zone I and II fill with a minimum value of 2000 kpa.

No observed data are available for the horizontal modulus E_h, $E_h=E_v$ is assumed in the analyses and E_h will be changed in the parametric study to check the reliability of the results.

Whenever perfect elastoplastic models are used, the independent shear modulus G_2 is assumed as

$$G_2 = E_2/[2(1+\nu_2)] \tag{5.11}$$

When softening models in weak layers are used, it is better to control the peak shear strain γ^p in the weak plane. Similar to the isotropic case for the core, we use

$$G_2 = \frac{\tau(\sigma_n')_{peak}}{\gamma_{peak}} = \frac{(\sigma_n'\tan\phi'+C')_{peak}}{\gamma_{peak}} \tag{5.12}$$

where, γ^p is taken as 4% (Fig. 4.7) for the Yellow Clay layer.

5.2.4.4 Strain softening rate

Because it is impossible to work out softening rates directly from observed data, estimation of parameter a in eqn. A.8, A.10 and A.14 is made for hyperbolic softening partly from the incomplete information, partly by using the assumptions made in the "REPORT".

For total stress analyses, a mean value of 0.1 for a is used in eqn. A.8 for the core material. This value corresponds to a decrease of undrained strength C_u by 10% with 1% plastic axial strain after peak. For effective stress analyses, mean values of 0.5 for a_ϕ and 0.01 for a_c are assumed. The two values are based by fitting the post peak behavior listed in the Fig. 4.8. As we know, 1/a is an indicator of softening rate (Fig. A.1), the small mean value of 0.01 for a_c will make the cohesion decrease sharply by more than 95% within the development of 2 % plastic axial strain.

It should be mentioned here that the axial strain ϵ_1 is not equal to the equivalent strain $\bar{\epsilon}$ in the plane strain condition. By assuming μ to be 0.5, i.e. no volume change with $\epsilon_{kk}=0$, we have $\bar{\epsilon} = 115\% \ \epsilon_1$. Within the range of μ from 0.40 to 0.50, the difference is under 15% and we neglect this difference. The reason is that both the peak strain and the softening rate have been roughly estimated.

The softening rate for the Yellow Clay layer is obtained by fitting the assumed linear relationship given in the "REPORT" (Fig. 5.8). The fitting of test data together with the observed data is illustrated in Fig. 5.9. The adopted a_ϕ is between 0.2 to 0.4. The parameter a_c is simply taken as 0.01 to simulate a quick reduction of the cohesion to the residual.

Since the estimated softening rates is very rough, a parametric study is desirable to investigate possible errors in the results.

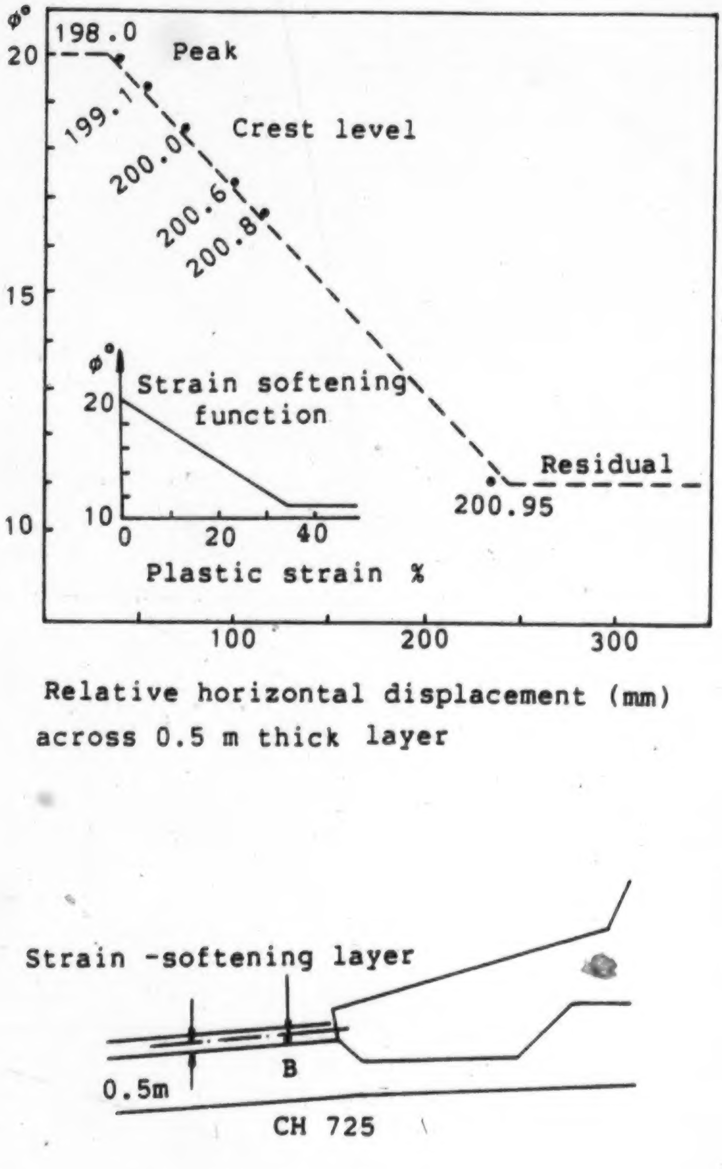

Figure 5.8: Strain softening at point B in the Yellow Clay

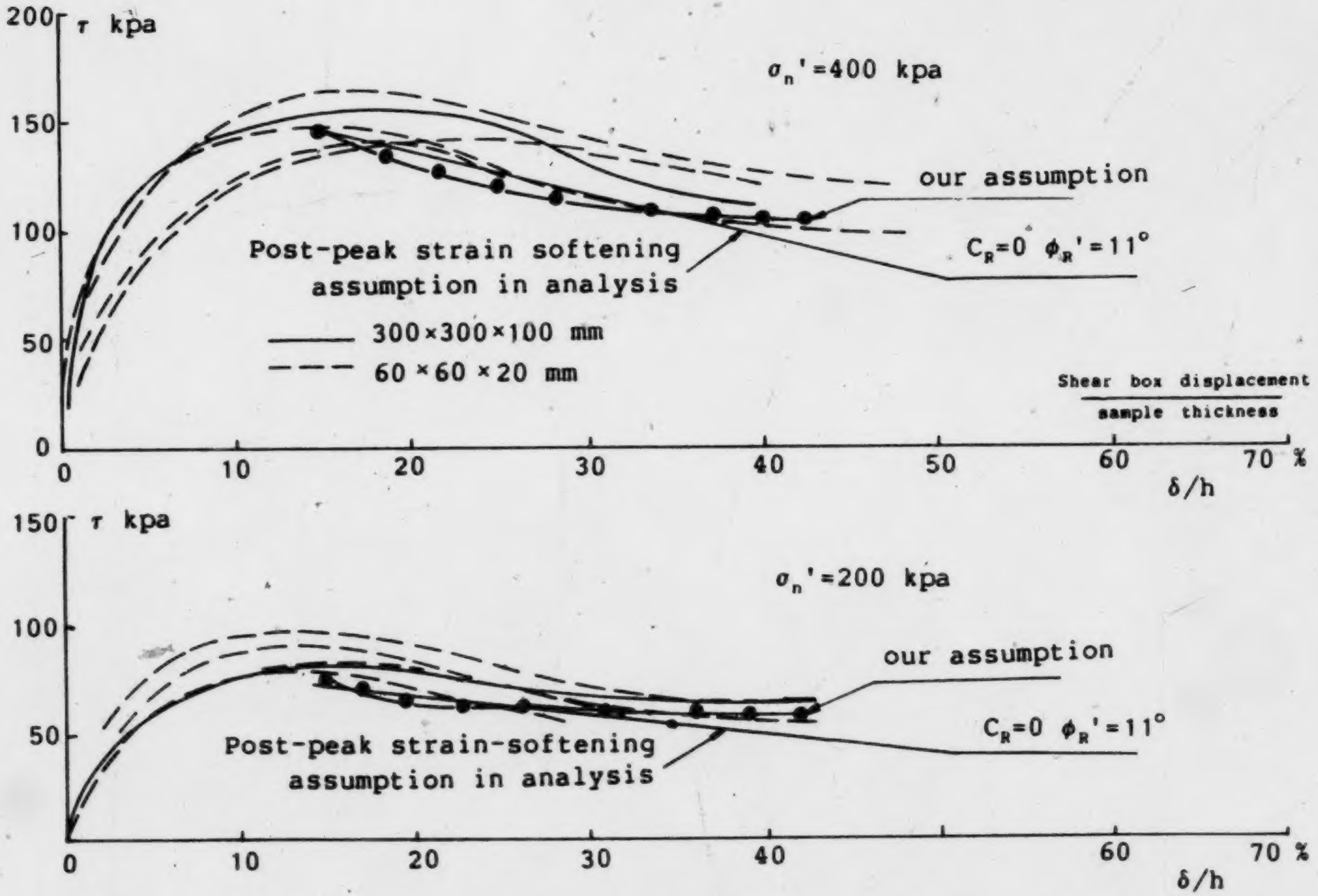

Figure 5.9: Assumed post peak strain softening rate for the Yellow Clay

6. ANALYSES OF THE CARSINGTON DAM FAILURE

6.1 Introduction

In this chapter, finite element analyses are undertaken to investigate the mechanism of the Carsington Dam failure, and the effectiveness of the finite element formulation and material models are evaluated. In addition, efforts are made to improve the techniques in treating the calculated results so as to better our understanding of the failure mechanism and facilitate making reasonable engineering judgements.

In treating the results, one question is how to locate the most critical slip surface more accurately. New techniques are developed to determine this critical slip surface. The relationship between the so-determined critical surface and the observed one is also discussed.

Another question is how to use the results in determining factors of safety. For progressive failure due to strain softening in a complex structure, the available strength parameters for limit equilibrium methods can be obtained only from finite element analyses at present. Therefore, this topic is very important in practice. Methods to determine factors of safety are discussed.

The calculation is carried out on the critical section at CH 725 from where the failure of the dam started. Although effective stress analyses are preferred in obtaining the final results, total stress analyses are also carried out for comparison. The adopted material models and parameters are the same as described in Chapter 5. The representative results are plotted by using a newly-developed program RESTRE for treatment of results.

Limited runs for parametric studies have been performed. The main purpose is to evaluate the reliability of the presented results. Since many factors are involved in predicting deformations, no trials have been made to fit the observed data. Although a much better fit can be obtained by just modifying one or two parameters after trial calculations, the results may be of limited implications for use in design. The true solution depends on the advance of field investigation and laboratory test procedures. Analyses in a history-matching mode will be more helpful by changing deformation parameters based on observations during construction.

6.2 Techniques for Result Treatment

Programs are available to plot contours of stress and strain components and displacement vectors, and so provide visual help in understanding the response of the whole body. However, those plots are not convenient to examine the distribution of the variables in concern along a section or slip surface, especially in comparison with the results obtained from different runs. Besides, it is very difficult to locate the critical slip surface accurately from the incremental displacement vector plot.

Program RESTRE has been developed to overcome the above shortcomings. This 4000 sentence program is comparatively complex in providing many useful and flexible options to create sections, paths and potential slip surfaces as well as to give the distribution of any variable output from the program SAGE. An introduction can be found in the internal report submitted by the author to the Department of Civil Engineering, University of Alberta (1989). Here only key points are briefly introduced.

6.2.1 Creating section

Since variables along a chosen path are interpolated by using shape function with local coordinates ξ and η, nonlinear equations need to be solved to find ξ and η from the given global coordinates x and y with

$$x = \sum N_i(\xi,\eta)\ x_i \qquad (i=1,\text{Node}) \ , \tag{6.1}$$

$$y = \sum N_i(\xi,\eta)\ y_i \qquad (i=1,\text{Node}) \ , \tag{6.2}$$

in which N_i is the shape function, x_i and y_i are coordinates of the element nodes. The above nonlinear equations are solved by linear interpolation. The key point is to find a good set of initial values, especially when the shape of the element is far from a square. Here, a half division method is adopted. The initial values of ξ and η are first searched in each quarter of a transformed square element in the local system by comparing the error of global coordinates of the corners of this quarter with the given values. Then, similar procedures are taken for the selected quarter until the error is less than a tolerance, say 0.10 to 0.05 in the local system. The search is expensive and so the line interpolation approach is used for further solution.

6.2.2 Interpolation techniques

The stress and strain components are output at each Gaussian integration point. Before interpolation by means of any chosen shape function, the components at nodes are found by means of the least square smoothing method (Hinton,1973).

Let $\bar{\sigma}_1$, $\bar{\sigma}_2, \ldots \bar{\sigma}_m$ be the smoothed stress components at element nodes, then, at any point inside the element, the smoothed value is

$$\bar{\sigma}(\xi, \eta) = \sum_{i=1}^{m} \bar{N}_i \bar{\sigma}_i \ , \tag{6.3}$$

where $\bar{N}_i$ is a suitablly chosen shape function. For 2×2 Gaussian points, we chose

$$\bar{N}_1 = \frac{(1-\xi)(1-\eta)}{4} \ , \quad \bar{N}_2 = \frac{(1+\xi)(1-\eta)}{4} \ ,$$

$$\bar{N}_3 = \frac{(1+\xi)(1+\eta)}{4} \ , \quad \bar{N}_4 = \frac{(1-\xi)(1+\eta)}{4} \ , \tag{6.4}$$

The error between the original and the smoothed value is

$$e(\xi, \eta) = \sigma(\xi, \eta) - \bar{\sigma}(\xi, \eta) \ . \tag{6.5}$$

The least square solution of $\bar{\sigma}$ will make the following functional take a minimum.

$$\phi = \int_D e^2(\xi,\ \eta)dxdy\ . \tag{6.6}$$

Therefore, it needs

$$\frac{\partial\phi}{\partial\bar{\sigma}_i} = 0\ , \qquad i=1,2,...m\ , \tag{6.7}$$

or

$$\frac{\partial\phi}{\partial\bar{\sigma}_i} = \int_D (\sigma-\bar{\sigma})\bar{N}_i\bar{\sigma}_i dxdy = 0 \qquad i=1,2,...m\ . \tag{6.8}$$

Hence, the equations for smoothed values at nodes takes the form of

$$\int\int (\sigma-\bar{\sigma})\bar{N}_1|J|d\xi d\eta = 0\ ,$$

$$\int\int (\sigma-\bar{\sigma})\bar{N}_2|J|d\xi d\eta = 0\ ,$$

$$\int\int (\sigma-\bar{\sigma})\bar{N}_3|J|d\xi d\eta = 0\ ,$$

$$\int\int (\sigma-\bar{\sigma})\bar{N}_4|J|d\xi d\eta = 0\ , \tag{6.9}$$

in which, $|J|$ is the Jacobian determinant for coordinate transformation.

For 2×2 Gaussian points and the chosen function, the solution is

$$\begin{bmatrix} \bar{\sigma}_{n^1} \\ \bar{\sigma}_{n^2} \\ \bar{\sigma}_{n^3} \\ \bar{\sigma}_{n^4} \end{bmatrix} = \begin{bmatrix} a & b & c & b \\ b & a & b & c \\ c & b & a & b \\ b & c & b & a \end{bmatrix} \begin{bmatrix} \sigma_{g^1} \\ \sigma_{g^2} \\ \sigma_{g^3} \\ \sigma_{g^4} \end{bmatrix} \tag{6.10}$$

in which subscript n denotes smoothed values at nodes, g denotes original values at the Gaussian points and

$$a = 1 + \frac{\sqrt{3}}{2}, \quad b = -\frac{1}{2}, \quad c = 1 - \frac{\sqrt{3}}{2}.$$

The program RESTRE also provides the option to smooth variables further by averaging the node values among the related elements. Experience has shown that the so-smoothed distribution fit the observed data much better, especially for shear stresses and strains.

6.2.3 Description of instantaneous movement

The incremental displacement vectors represent the movement tendency of the body subjected to incremental loads. Similar to the streamline in fluid mechamics, the "streamlines" integrated by taking the vectors for "velocities" will give a better picture of the movement. Let us call these "streamlines" movement paths.

Kinematically possible slip surface obtained by integrating streamline of incremental displacement vectors

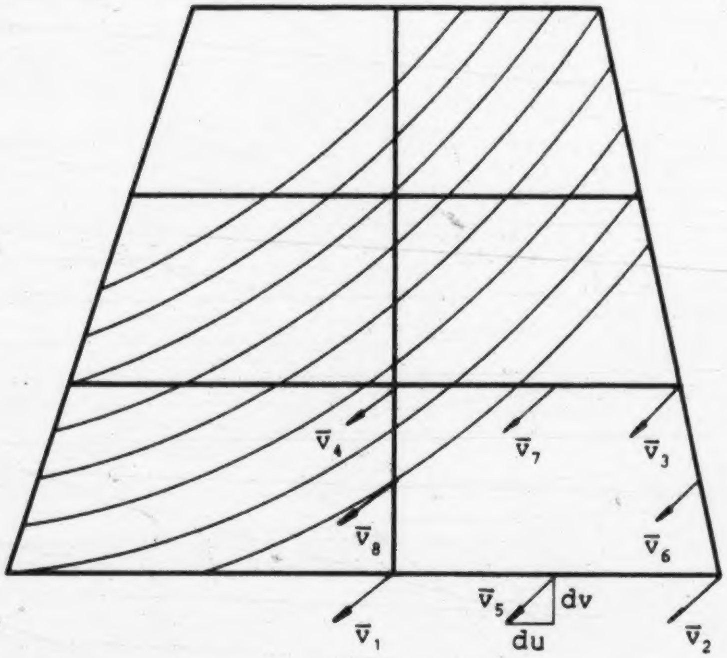

$\overline{v}_4$
$\overline{v}_7$
$\overline{v}_3$
$\overline{v}_8$
$\overline{v}_6$
$\overline{v}_5$
dv
du
$\overline{v}_1$
$\overline{v}_2$

Figure 6.1: Kinematically possible slip surface

As shown in Fig. 6.1, in any element, we have the incremental horizontal and vertical displacements du and dv, which define the direction of movement. By interpolation with the shape function, the movement direction of any point is known. Let the function defining the movement path be

$$Y = f(X) \ . \qquad (6.11)$$

Then the basic equation is

$$\frac{dY}{dX} = \frac{du}{dv} \ . \qquad (6.12)$$

Since

$$\frac{dY}{dX} = (\frac{\partial Y}{\partial \xi}d\xi + \frac{\partial Y}{d\eta}d\eta)/(\frac{\partial X}{\partial \xi}d\xi + \frac{\partial X}{\partial \eta}d\eta) \ , \qquad (6.13)$$

we have

$$\frac{d\xi}{d\eta} = (\frac{\partial Y}{\partial \eta} - \frac{du\partial X}{dv\partial \eta})/(\frac{du\partial X}{dv\partial \xi} - \frac{\partial Y}{\partial \xi}) \ , \qquad (6.14)$$

in which $\frac{\partial X}{\partial \xi}, \frac{\partial X}{\partial \eta}, \frac{\partial Y}{\partial \xi}, \frac{\partial Y}{\partial \eta}$ can be easily obtained from derivatives of the shape functions.

The Runge-Kutta method is adopted and the integrated paths are shown in Fig. 6.1. To check the error, integration has been carried out from two different ends of the same path. The error of local coordinates is less than 10^{-6} if 15 steps are used in one element. The results are reliable.

6.2.4 Locating the critical slip surface

The critical slip surface is determined from the movement paths just before failure. It is defined as that movement path which is kinematically possible and along which the mean yield ratio $\bar{R}_y$ is the highest. The yield ratio R_y at a point is a measure of the extent of the stress level as compared with the yielding state (R_y=1.0) (see eqn. 5.3 and 5.4). Obviously, $0 \leq R_y \leq 1$. For cracks, the yield ratio is set to be 1.0. For the whole movement path, the mean yield ratio $\bar{R}_y$ is defined as

$$\bar{R}_y = \int_L R_y ds / \int_L ds \tag{6.15}$$

where integration is applied to the whole length.

Fig. 6.2 shows the distribution of R_y along a movement path. It should be noted that $R_y<1$ may not indicate the elastic state of the whole element, but the elastic state of at least one Gaussian point inside the element. The cohesion ratio R_c and friction angle ratio R_ϕ are also defined to examine the extent of strain softening. The ratio is defined as the reduced value over the the peak value. The interpolated R_c and R_ϕ will be less than 1.0 if softening is developed at certain Gaussian points. Examples will be given in Section 6.3.3 in presenting the final results.

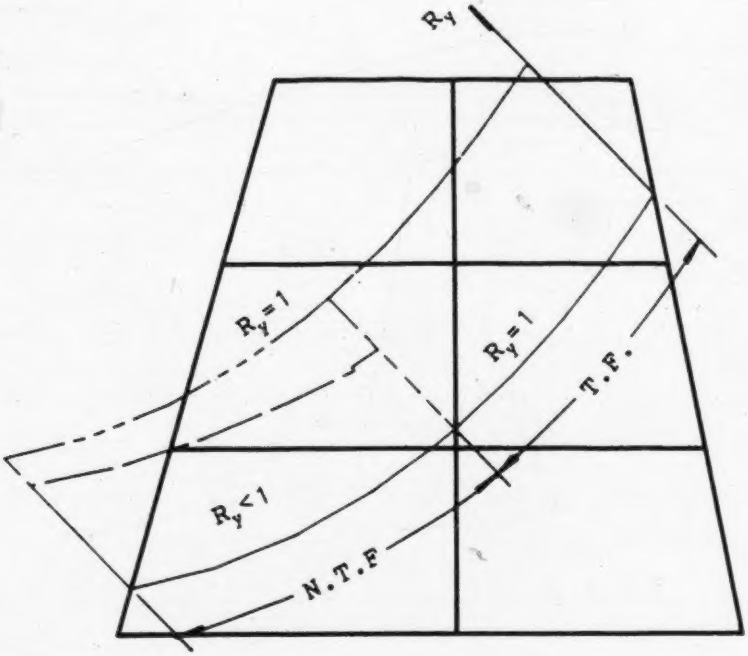

T.F.----- Totally failed

i.e. failed at all Gaussian points

N.T.F.----- Not totally failed

i.e. elastic or failed at some but not all Gaussian points

Figure 6.2: Illustration of yield ratio along a slip surface

6.3 Results and Discussions

The mesh for section CH 725 is shown in Fig. 6.3 with 162 8-node elements and 479 nodes. The final results obtained from the effective and total stress analyses will be discussed in this section.

6.3.1 The critical dam height

The failure of the dam is indicated by a sudden increase of the displacement. In Fig. 6.4 and Fig. 6.5, the horizontal movements of the peg at the upstream toe and at the edge of the boot are selected to illustrate this feature.

For the effective stress analysis, the dam fails at EL. 200.1m, about 0.9m lower than that in the real situation. As far as the reliability of input data is concerned, the error seems to be caused mainly by the rough estimate of the pore pressure distribution and the elastic modulus. It is hard to say which of those is more important. However, the overall result is certainly satisfactory for a dam of 25 meters high.

The results obtained from the total stress analysis shows that the dam does not fail by using the selected model and parameters. At least two major factors, i.e. undrained shear strength C_u and elastic modulus would affect the critical dam height, therefore, no further trials by modifying the material parameters are attempted to fit the observed critical height. In order to study failure

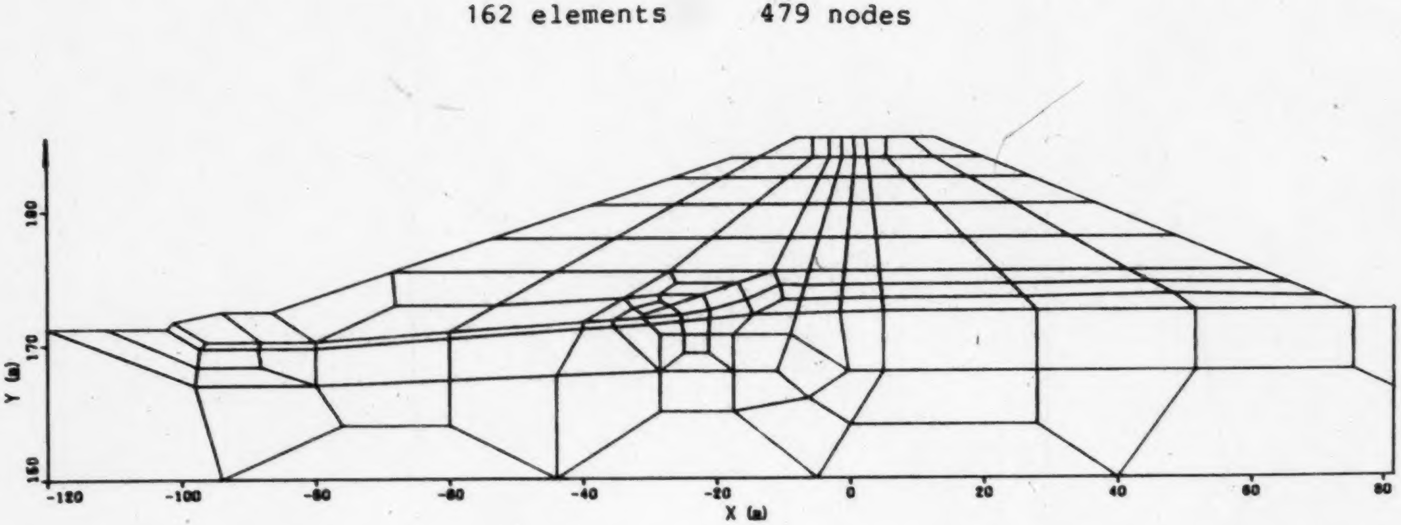
162 elements 479 nodes
160
170
180
Y (m)
-120
-100
-80
-60
-40
-20
0
20
40
60
80
X (m)

Figure 6.3: Finite element mesh for CH 725

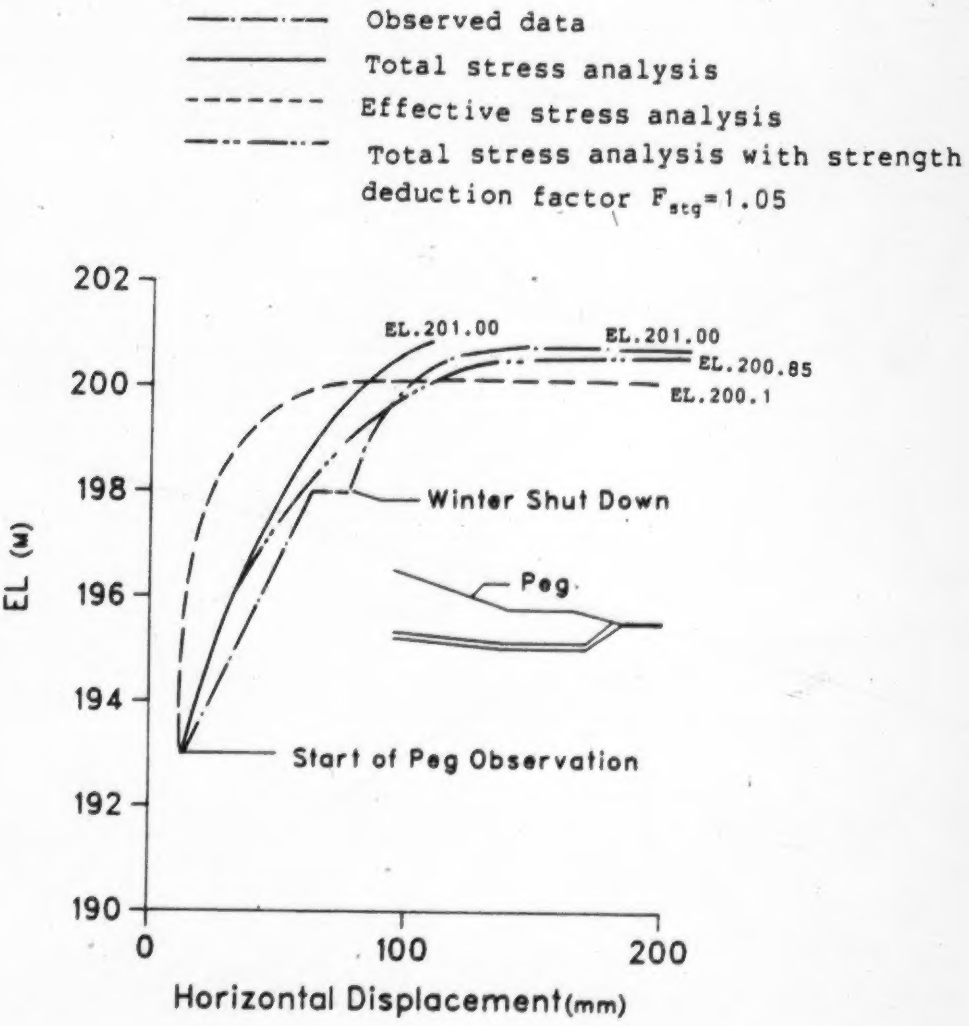

Figure 6.4: Comparison of results of peg movements

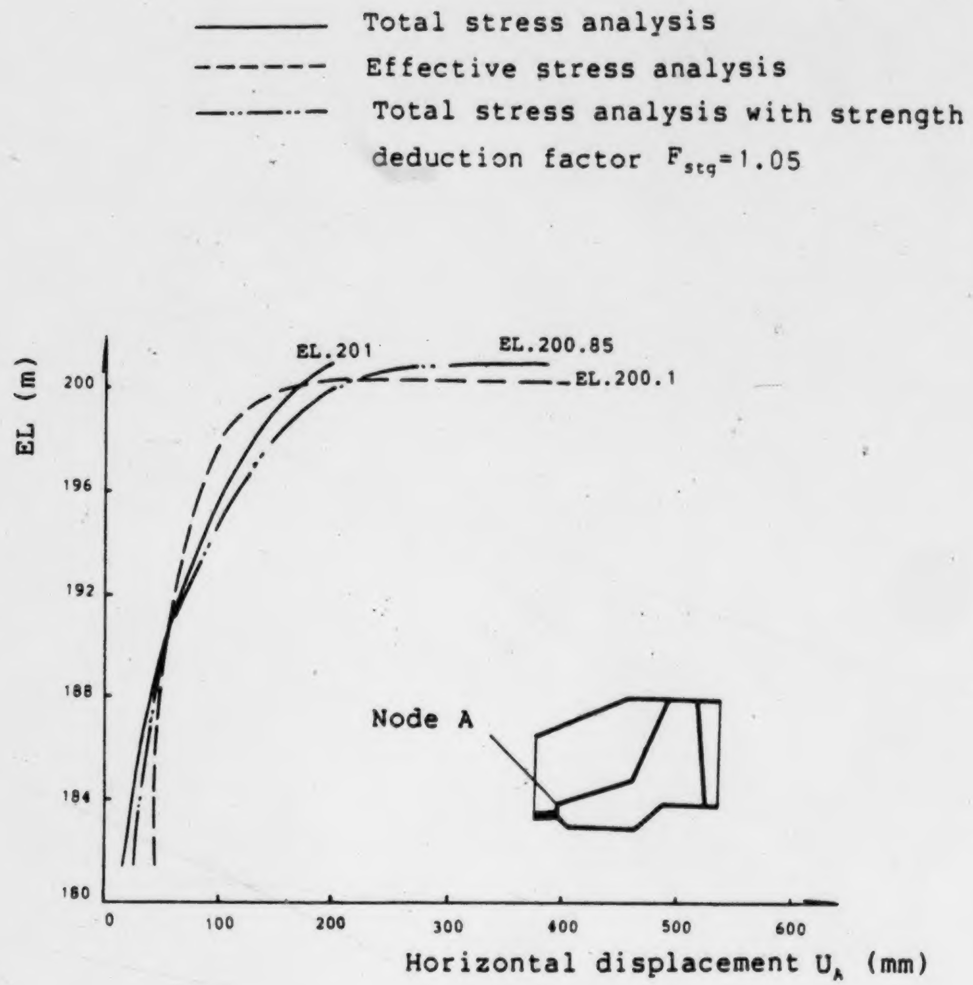

Figure 6.5: Determination of the critical dam height

mechanisms, two conventional ways can be chosen to force the dam to undergo progressive failure.

One way is to apply additional load, e.g. to increase the design height to an assumed value. The other is to reduce the strength parameters by a strength reduction factor F_{stg}, then re-calculate the problem. The latter method is adopted to conform with the concept of safety factor. With the strength reduction factor being equal to 1.05, the dam fails at EL.200.85m, only 0.15m below the real failure height.

In short, both the effective and total stress analysis indicate the original design of the Carsington Dam is unsafe, and the calculated critical height is not far from the observed one. Hence, the results are acceptable for practical use.

6.3.2 Comparison of typical deformation and stress quantities

Except those indicating failure, all the quantities for comparison are taken from the convergent results before failure, since divergent results are not reliable. The distribution of vertical stress along horizontal sections just before failure is shown in Fig. 6.6. It is not strange that there is little difference between the results of the effective and total stress analyses, because the vertical load is same for both analyses. Another reason will be given later in discussing the vertical displacement distribution.

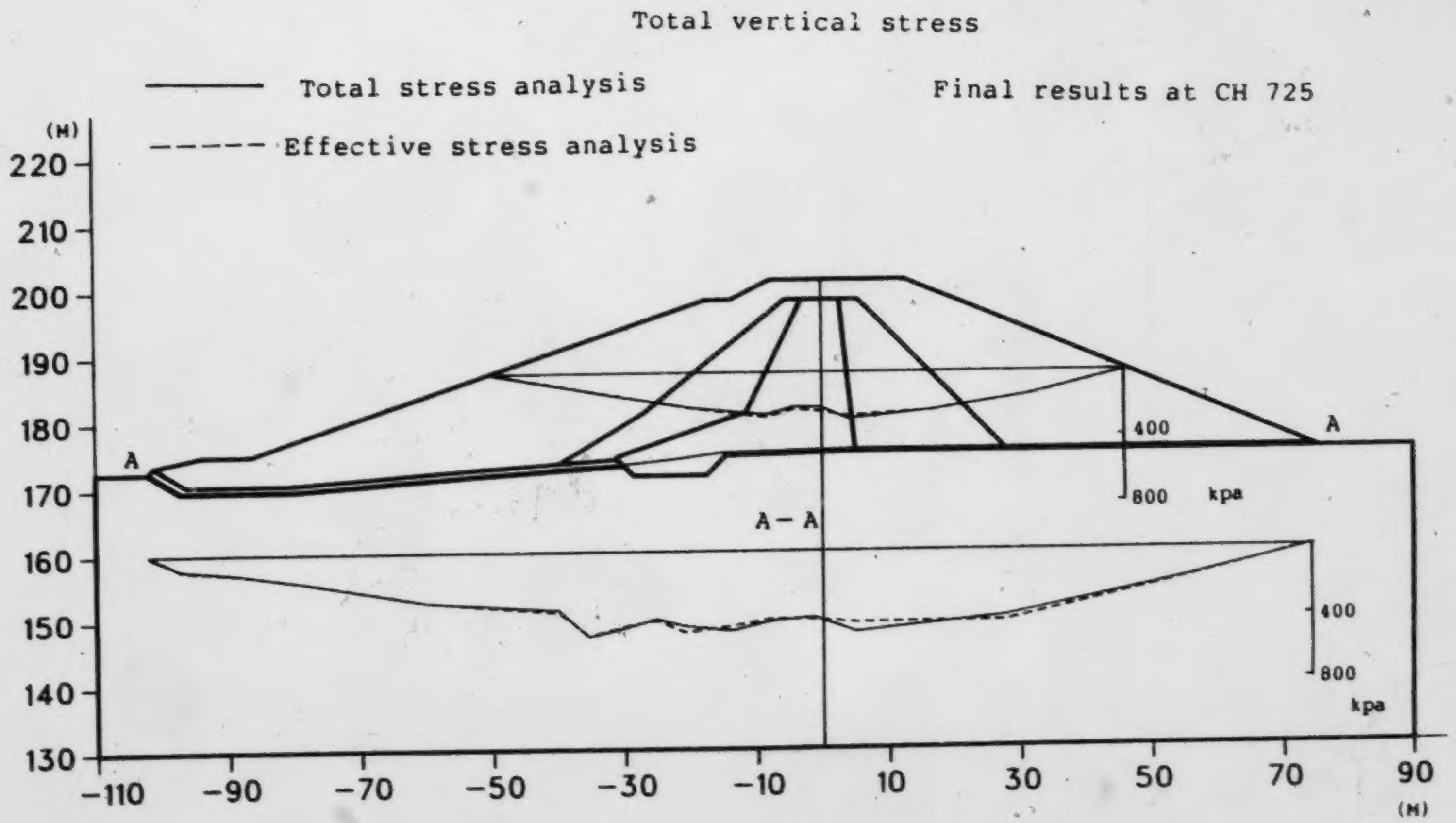

Figure 6.6: Results of total vertical stresses

As to the vertical displacement distribution just before failure, there is also little difference as shown in Fig. 6.7, although different models with different elastic moduli have been adopted for the core material in the two analyses. A constant elastic modulus of 2500 kpa is used in the total stress analysis, while a nonlinear elastic modulus is adopted in the effective stress analysis, which depends on the peak strain and peak strength parameters C' and ϕ'. The average elastic modulus is about 3700 kpa before the dam reaches the horizontal section at EL.186.0m, and about 5200 kpa when the dam reach the critical height. This large difference of elastic modulus (by about 50% to 110%) in the core only causes a little difference in the vertical displacement distribution. The first reason is that the same elastic foundation is used, which seems to play a significant part in controlling the settlements. The second reason is that the materials in most parts of the dam, i.e.. filter and shell are the same and vertically constrained by the same elastic foundation with comparatively high elastic modulus.

In view of the results from other runs in this thesis, it can be concluded that reasonable models and parameters will yield similar distributions of vertical displacements and stresses.

Without constraints in the horizontal direction, the results of horizontal displacements just before failure exhibit large differences (Fig. 6.8). From Fig. 6.4 and Fig.

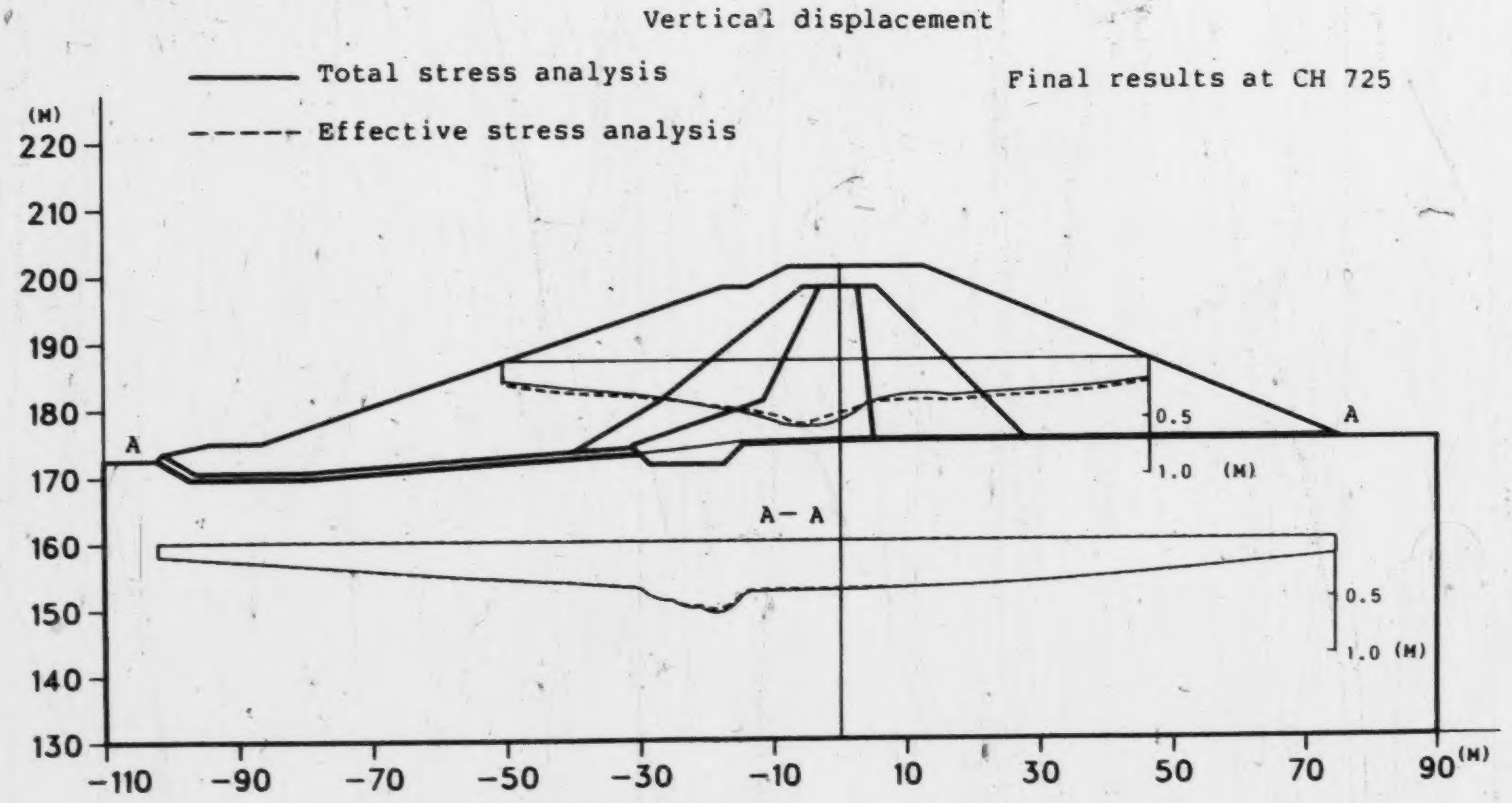

Figure 6.7: Results of vertical displacements

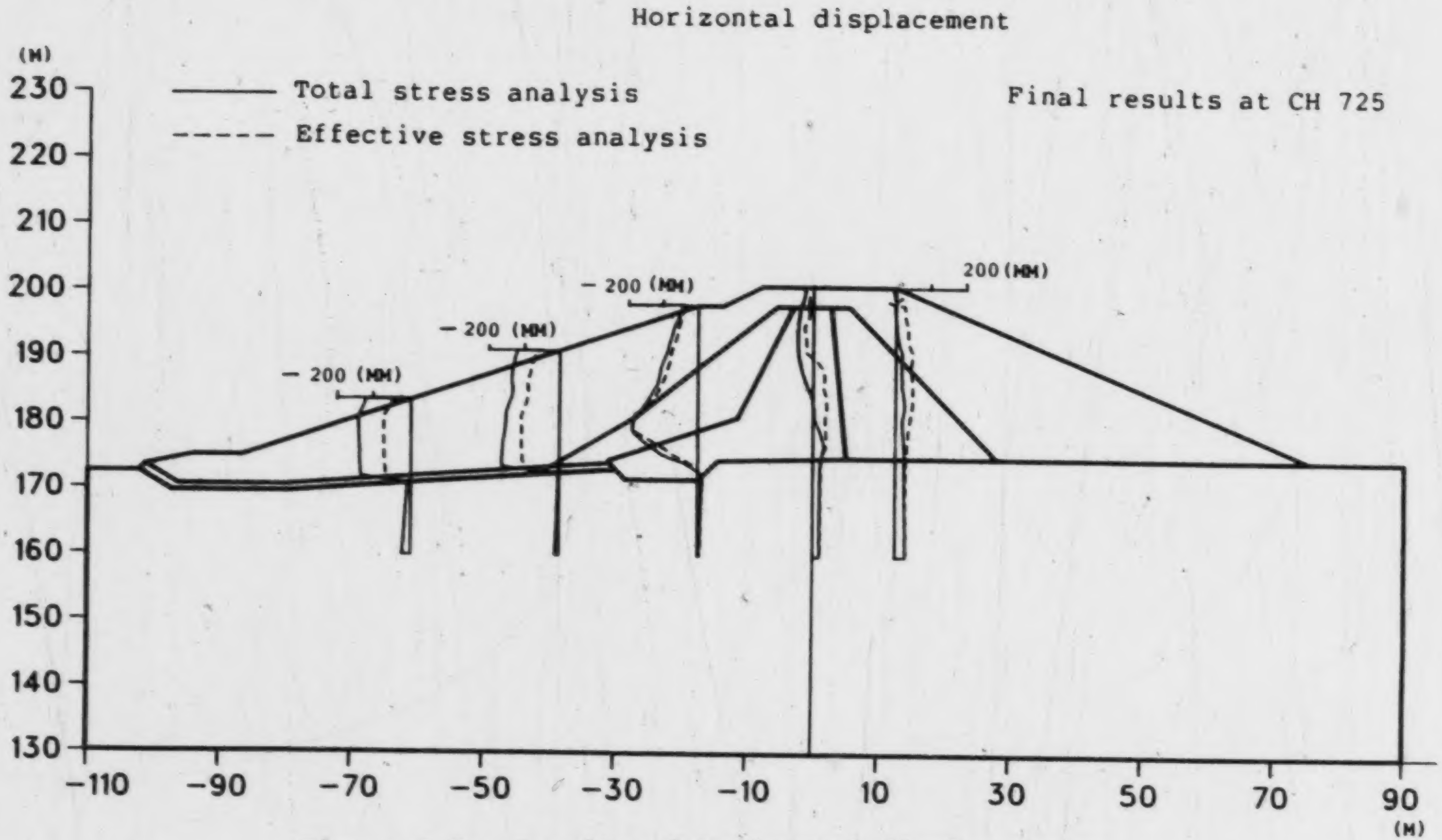

Figure 6.8: Results of horizontal displacements

6.5, it can be seen that the difference starts from the very low stress stage just by using the different models and elastic moduli in the core. This reveals the difficulties in predicting the deformation quantities. However, both sets of results have truly reflected the high shear deformations in the Yellow Clay layer.

The comparison of the calculated deformation with the observed data can be found in Fig. 6.4. and Fig. 6.9. Fig. 6.4 shows that elastic moduli in the effective stress analysis may be too high to predict horizontal displacements accurately. However, the vertical strain distribution is acceptable in the average sense for both analyses (Fig. 6.9). In this figure, horizontal displacements along the clay layer are also compared. Taken as a whole, the distribution patterns are basically similar, but the calculated displacements are much smaller than the observed. The sharp changes in the calculated curve are caused by cracking near the edge of the boot.

On the one hand, the capacity of finite element analyses to predict deformations is still low at present. At least a 50% to 100% relative error may be encountered even in the average sense. Satisfactory prediction of deformations in both the vertical and horizontal directions cannot be expected before striking advance of the field investigation and laboratory techniques. On the other hand, the predicted deformation patterns generally reflect the true situation if the input information is reasonable. This

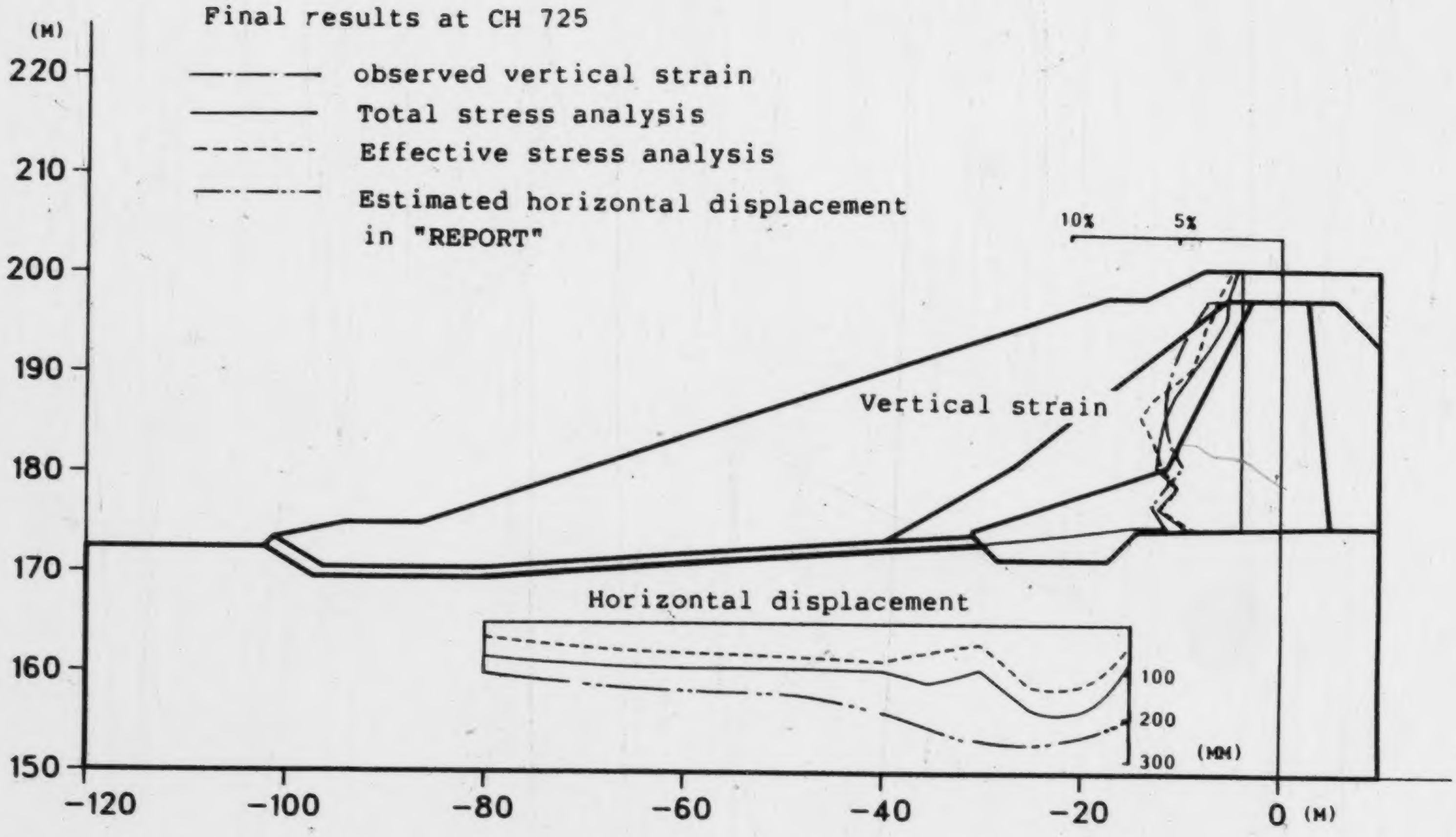

Figure 6.9: Comparison of results with observed data

provides a sound foundation in predicting or back-analyzing the failure mechanism. If observed data are available during the construction, they can provide a reliable basis for adjusting the material parameters. The finite element analyses would be more effective in a history-matching mode.

6.3.3 The critical slip surface and failure mechanism

Fig. 6.10 shows the incremental displacement vectors just before failure obtained from the effective stress analysis. The corresponding increment load is equivalent to a 0.15m rise of the dam height from EL.199.85m to EL.200.10m. The integrated movement paths are illustrated in Fig. 6.11.

It should be mentioned that difficulties may be encountered in integration, if there exist cracks in the way of an integration path. Cracks may cause sharp turning of the movement path, e.g. around the geometrical corner along the boundary of the boot (marked with A and B in Fig. 6.10). To cope with this situation, the integration is completed section by section, then the whole path is smoothed through the section where cracks exist. Since only two paths have been so smoothed, and the smoothed length is less than 5% of the total length, the results can still be considered reliable for further use. However, it shows that the recommended integration techniques only apply to failure dominated by shear. Without cracking, very beautiful smooth lines can be obtained as shown by most of the paths.

Incremental displacement vectors just before failure

Final results at CH 725

Effective stress analysis without strength deduction

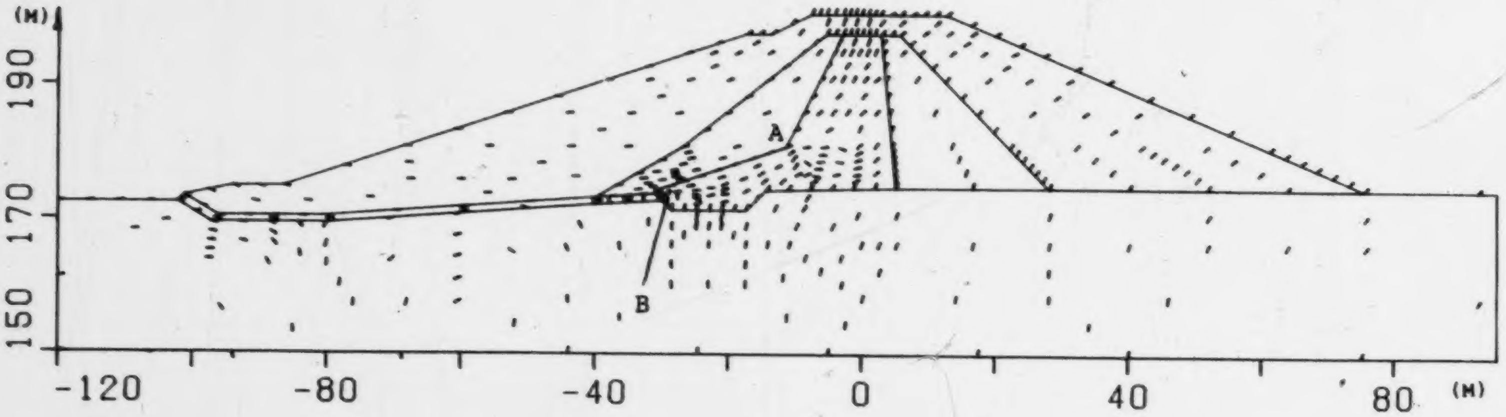
(M)
190
170
150
-120
-80
-40
0
40
80
(M)
A
B

Figure 6.10: Incremental displacement vectors -effective stress analyses

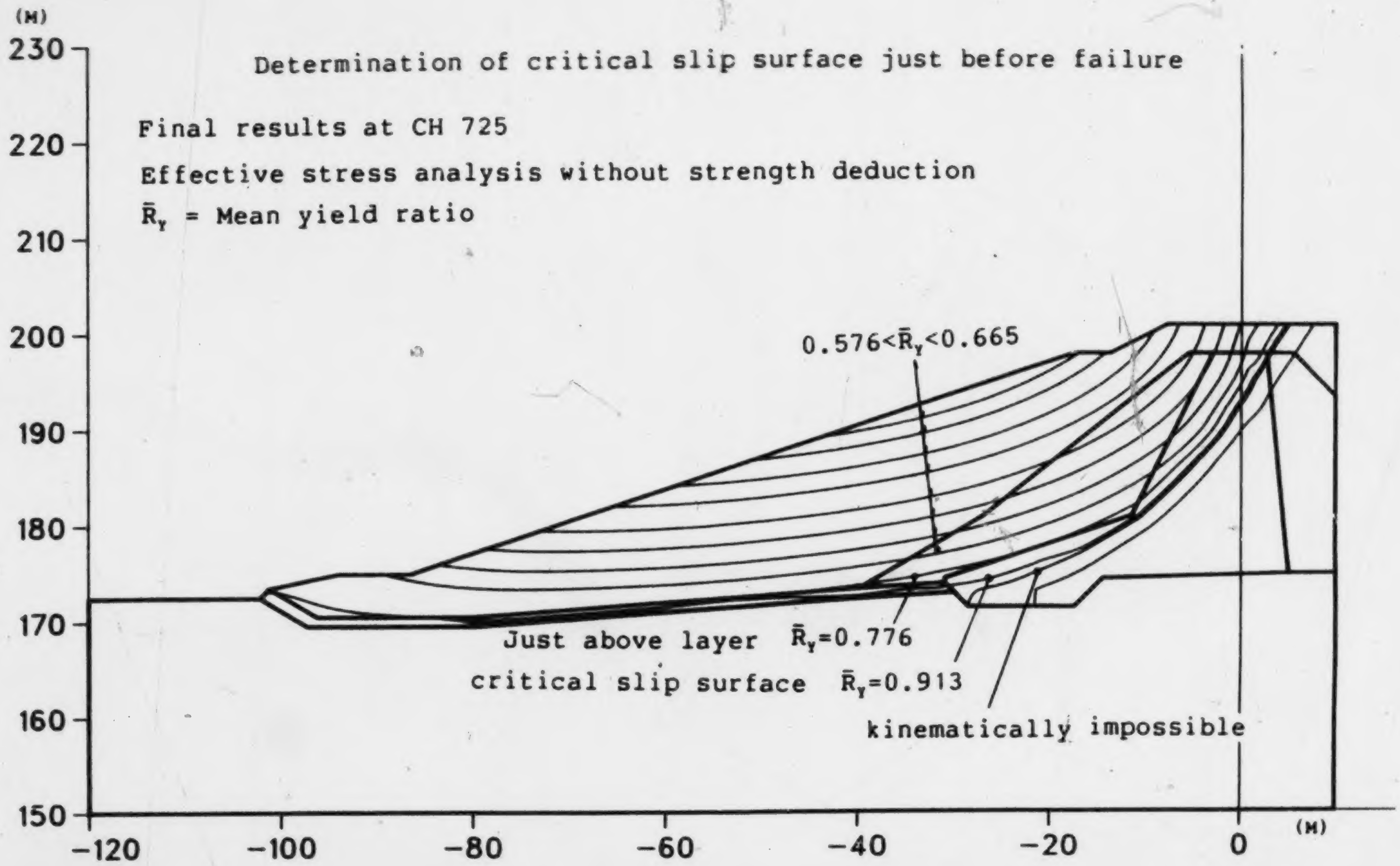

Figure 6.11: Determination of the critical slip surface -effective stress analyses

The mean yield ratios of the potential slip surfaces are also listed in Fig. 6.11. The critical slip surface can be located between another two movement paths. One is above the critical slip surface with a smaller mean yield ratio although it is kinematically possible, while the other below the critical one is kinematically impossible. Trial calculations have shown that it is easy to determine the location of the critical slip surface as accurately as required for practical use. The distance between the critical slip surface and the neighboring two paths is a little bit large in the figure. It is intended for visualization in choosing the paths.

It is interesting to investigate the pattern of the movement paths under lower loading levels. Fig. 6.12 shows the movement paths, one sub-loading step before failure, i.e. from EL. 199.80m to EL. 199.95m. All the movement paths in the lower upstream portion are kinematically impossible to form a slip surface, while the mean yield ratio of all those in the upper portion is below 0.6. These features indicate a typical stable deformation. An additional height of 0.15m leads the deformation to an unstable pattern (Fig. 6.11). The solution for critical dam height is accurate enough.

Fig. 6.13 allows us to examine the tendency of the movement paths to advance through the yellow clay layer so as to form the slip surface in the successive loading stages. Similar to the Lagrangian description in fluid

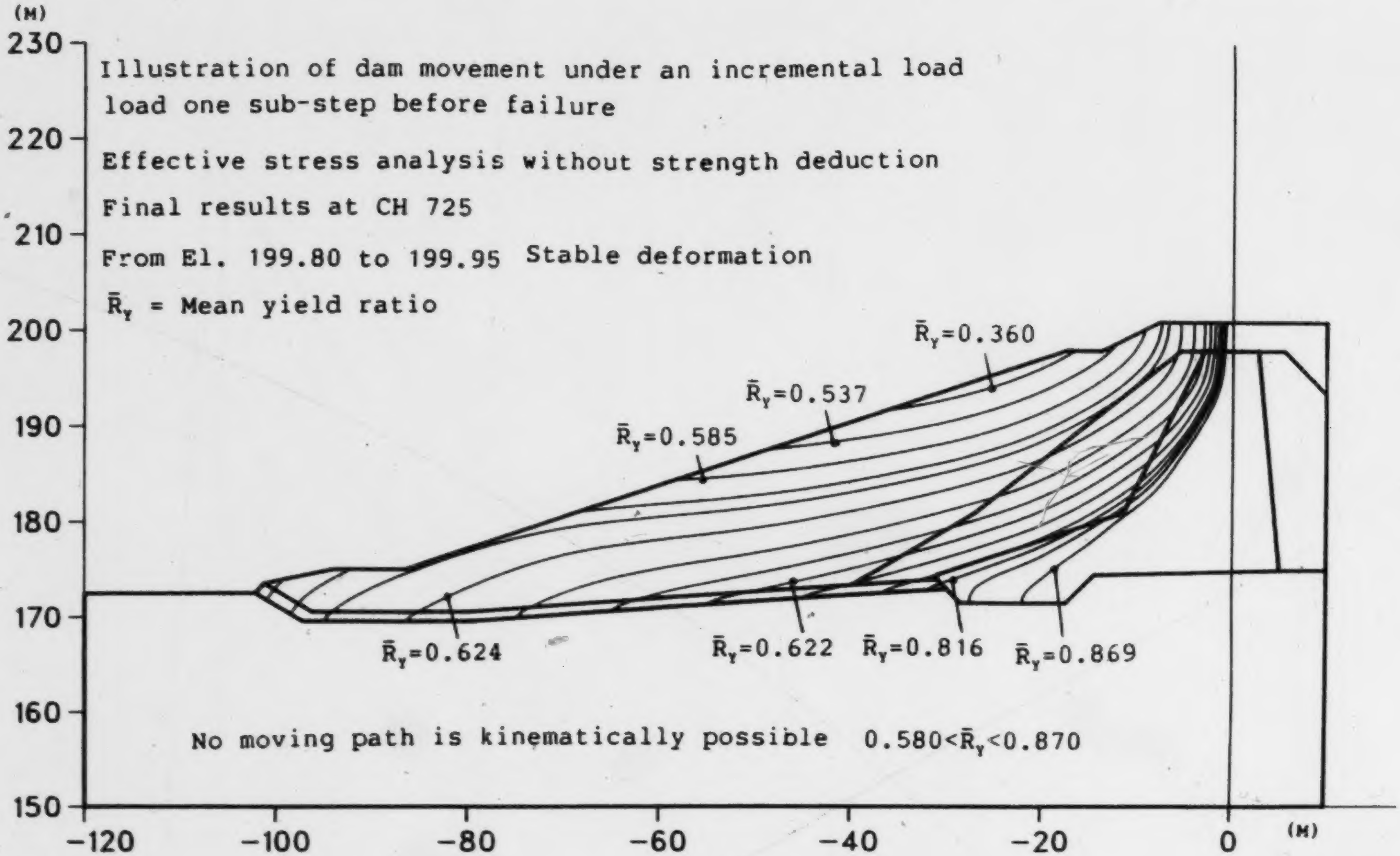

Figure 6.12: Illustration of stable deformation

mechanics, movement paths passing point A at the entrance of the Yellow Clay are illustrated as the dam goes up. Before the critical height is reached, no movement path is kinematically possible and each path goes down into the elastic foundation just after it enters the Yellow Clay layer with the mean yield ratio in the core gradually increasing. The critical slip surface is formed suddenly, exhibiting a totally different pattern and direction. This indicates the feature of a sudden failure.

The yield status along the critical slip surface just before failure is shown in Fig. 6.14. The yield ratio distribution shows that nearly all the points totally fail or almost totally fail except for the portion near the toe berm. As explained in section 5.2.3.4, average observed softening rates are adopted for the friction angle and very high values are adopted for the cohesion. Fig. 6.14 shows that the reduction of friction angle is not appreciable but the cohesion is reduced by a very large amount where failure occurs. The reduction distribution of material parameters will be used to evaluate the conventional factor of safety later. By examining the intermediate results during the iteration process just after failure, the failure is still governed by the shear. Fig. 6.15 shows the further reduction of the strength parameters and the yielding status. However, this figure only shows the tendency to progressive failure, the calculated value cannot be considered reliable due to the divergence. The distribution is still plotted along the

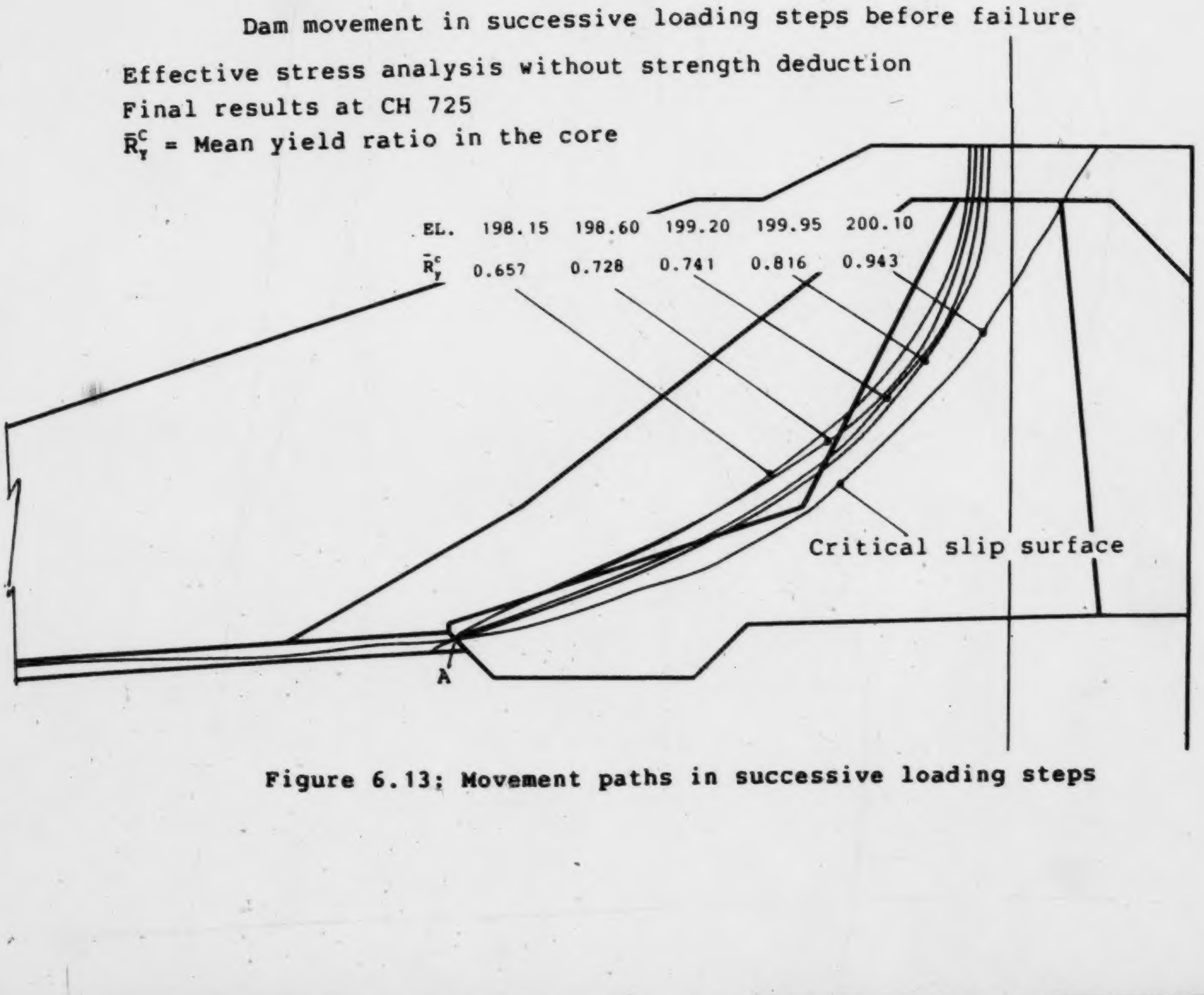

Dam movement in successive loading steps before failure

Effective stress analysis without strength deduction

Final results at CH 725

$\bar{R}_Y^C$ = Mean yield ratio in the core

EL. 198.15 198.60 199.20 199.95 200.10
$\bar{R}_Y^c$ 0.657 0.728 0.741 0.816 0.943
Critical slip surface
A

Figure 6.13: Movement paths in successive loading steps

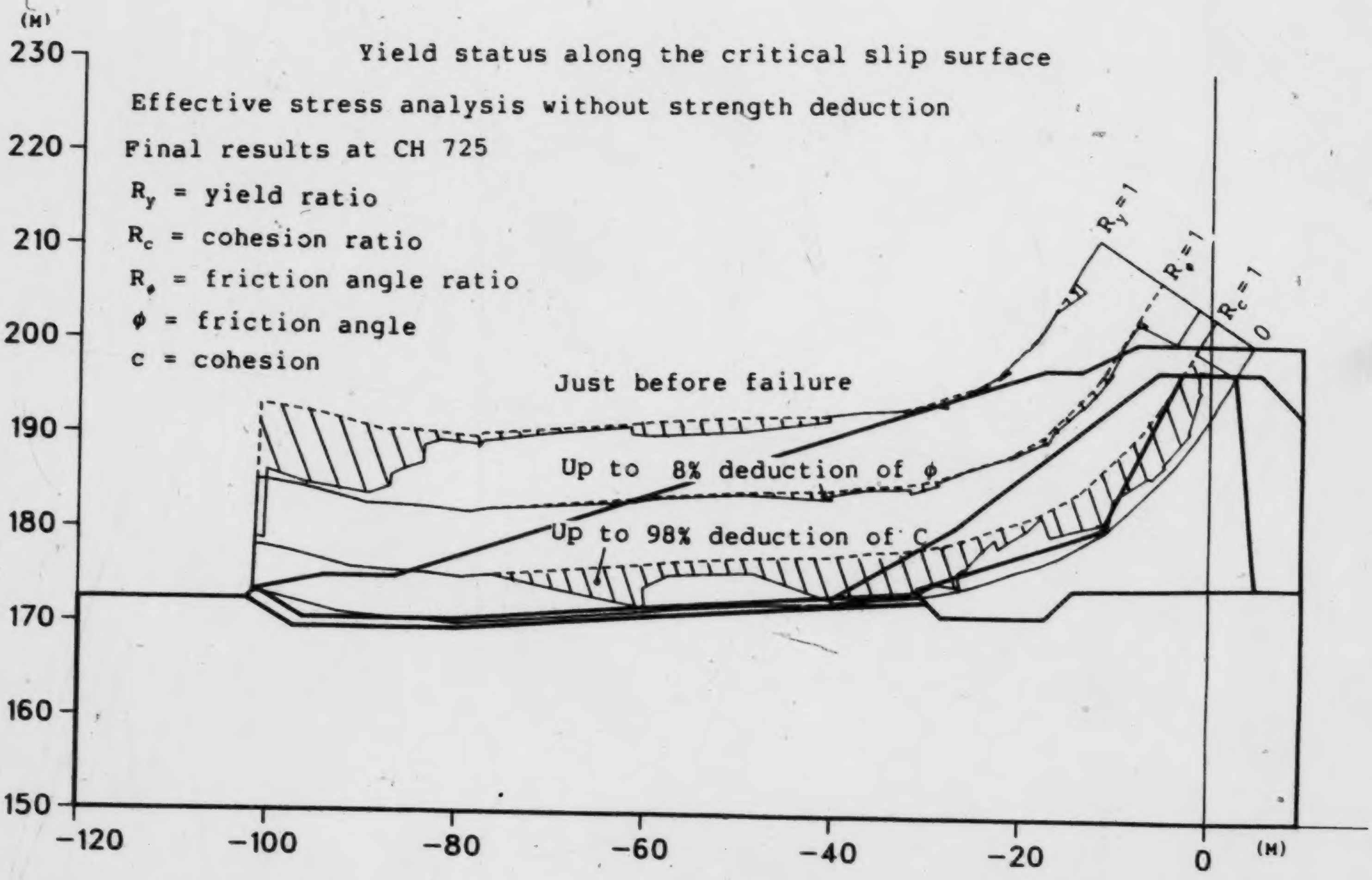

Figure 6.14: Yield status(a) along the critical slip surface-effective stress analyses

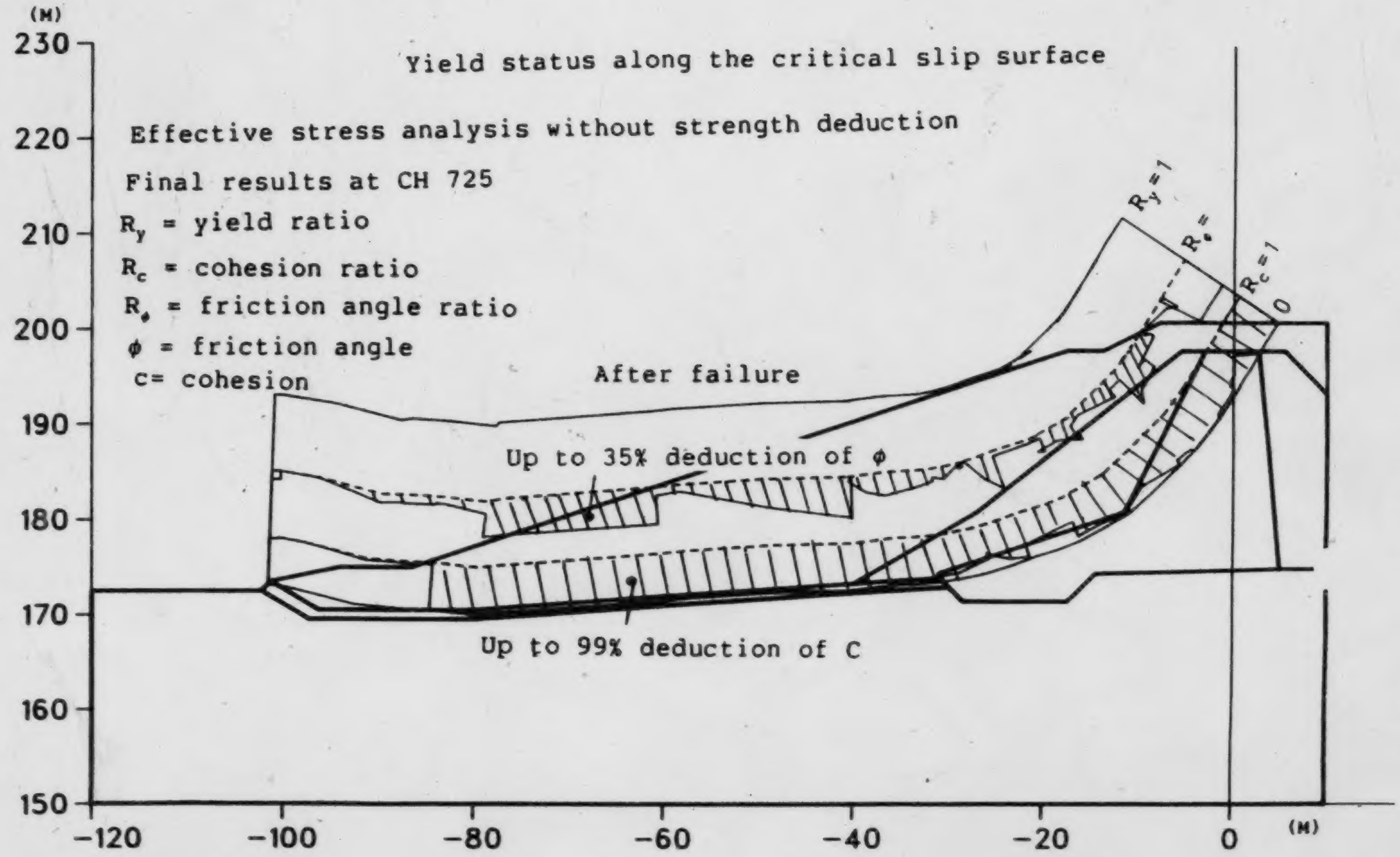

Figure 6.15: Yield status(b) along the critical slip surface-effective stress analyses

surface just before failure, since the reliable slip surface cannot be obtained by integration from results which are not convergent.

By reviewing the failure sequence recorded in the loading history, the failure starts from the contact area of the boot and the yellow clay layer as shown in Fig. 6.16. Especially high straining can be found in this area. Then, the failure extends both in the direction through the weak clay layer and in the direction through the core. The cracks open on the top of the dam, not far from the central line. The above features agree with the observation during and after the failure of the Carsington Dam.

The comparison of the location between the calculated critical slip surface and the observed slip surface is also shown in Fig. 6.16. The adopted finite element formulation is effective in simulating the slip surface in Yellow Clay, since there exists an oriented weak layer. However, the two slip surfaces do not coincide in the core. If we review the movement paths in Fig. 6.13, it seems that the critical surface tends to get close to the observed one as the dam goes up but cannot reach it. The movement of the failure plane can be attributed to changes of principle stress orientations. Theoretically speaking, the observed slip surface corresponds with large deformations and discontinuous shear band formation together with opening of cracks inside the dam. Therefore, limitations of the assumptions of continuity and small deformation prevent us

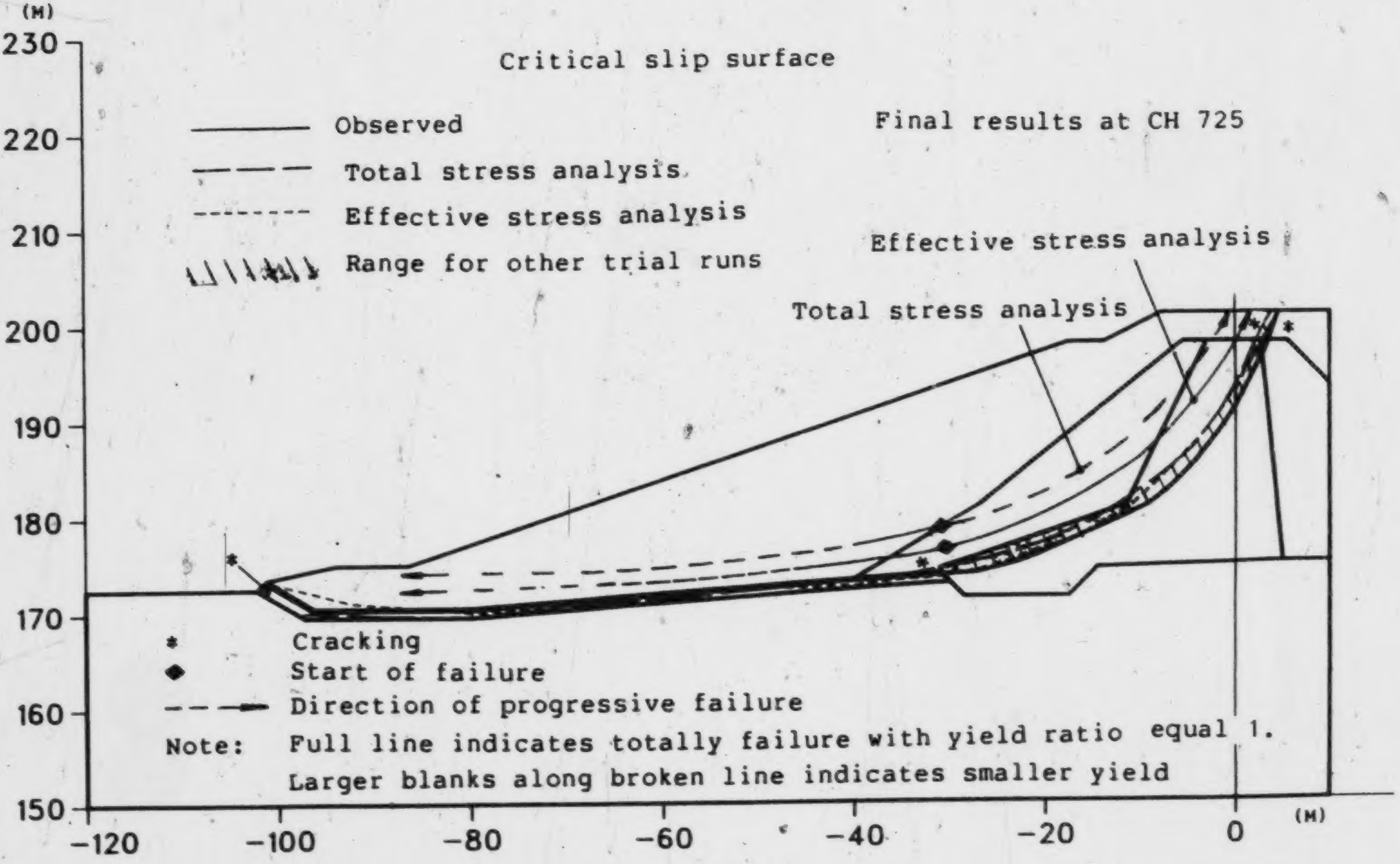

Figure 6.16 Comparison of the critical slip surfaces

from simulating the whole process of progressive failure.

Since the theoretical formulation for the dislocation of shear bands and large openings is far from reliable for practical use, the so-determined critical slip surface may be the best approximation we can obtain. In fact the critical slip surface is the most dangerous potential slip surface at the loading stage just before failure. Fig. 6.17 shows the yield ratio and strength reduction distribution along the observed slip surface. By comparing Fig. 6.14, it is easy to see that the degree of yielding level and strength reduction along the observed surface is really lower than that along the critical slip surface. Except for back-analyses, the final slip surface is generally not available. The above techniques can approximately predict the final slip surface, if the dam does fail due to the further disturbance.

Now, let us examine the results from the total stress analysis. The results are generally acceptable for engineering use, but not so satisfactory as those from the effective stress analysis. For brevity, we concentrate the discussion on the shortcomings of the total stress analysis.

The incremental displacement vectors just before failure are illustrated in Fig. 6.18. The movement paths are obtained as shown in Fig. 6.19. It should be born in mind that the strength parameters used here have been reduced by a factor F_{stg} (F_{stg}=1.05). The mean yield ratio along the determined critical slip surface is only 0.847, which

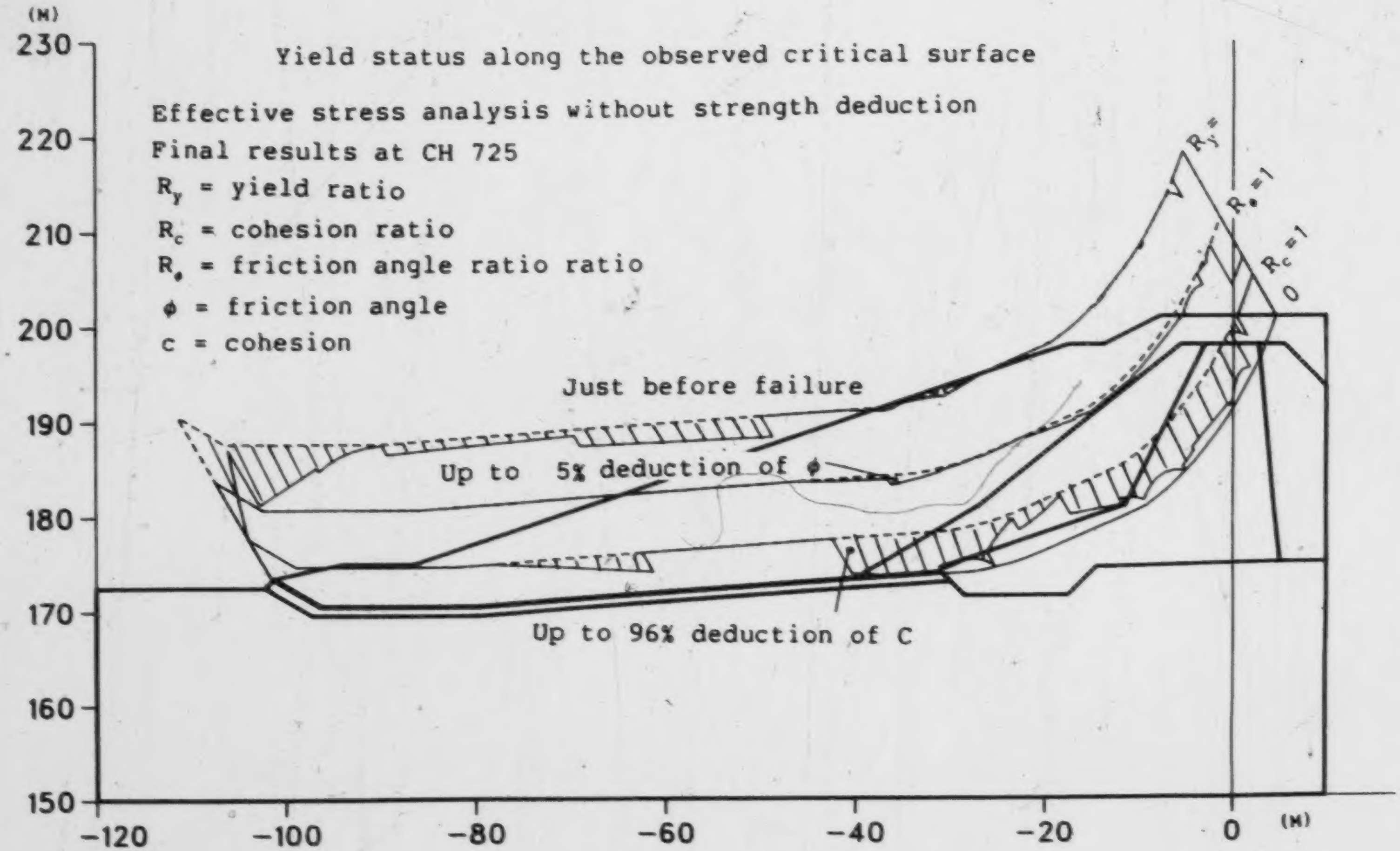

Figure 6.17: Yield status along the observed slip surface-effective stress analyses

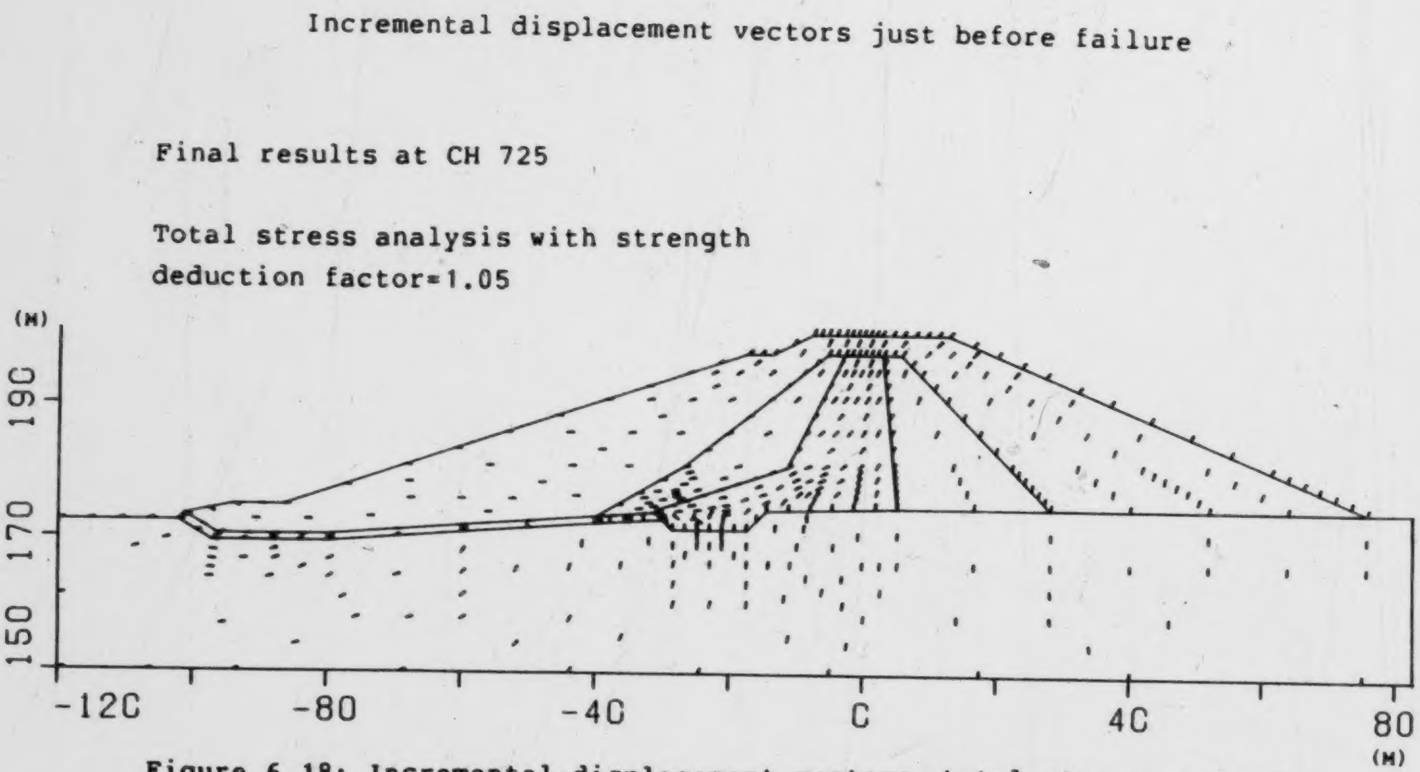

Incremental displacement vectors just before failure

Final results at CH 725

Total stress analysis with strength
deduction factor=1.05

(M)
190
170
150
-120
-80
-40
0
40
80
(M)

Figure 6.18: Incremental displacement vectors -total stress analyses

implies the degree of yield is comparatively low. In comparison, a value of 0.913 is obtained in the effective stress analysis (Fig. 6.11). The location of the critical slip surface is somewhat further from the observed one and above that one obtained from the effective stress analysis, although the development of progressive failure agrees with the observation too.

Fig. 6.20 shows the yield status just before failure. Because an average undrained strength C_u is used in the core, the yield ratio is much lower than that in the effective analysis at the corresponding point. Therefore, the main defect is that the failure process cannot be truly simulated by using the undrained strength C_u, especially in the upper portion of the core at lower stress levels. The intermediate results just after failure show that failure is further promoted not only by shear but also by severe cracking. This is because progressive failure was further promoted in the Yellow Clay layer, but frictional failure is not attainable in the upper core. To accommodate further deformations, a lot of cracks are developed.

Fig. 6.21 illustrates the yield status along the observed slip surface. By comparing Fig. 6.19, the yielding degree is also lower than that along the critical slip surface. Trial calculations also show the so-determined critical slip surface is the most dangerous one among the assumed slip surfaces nearby. The reduction of strength parameters in the above two figures will be used to

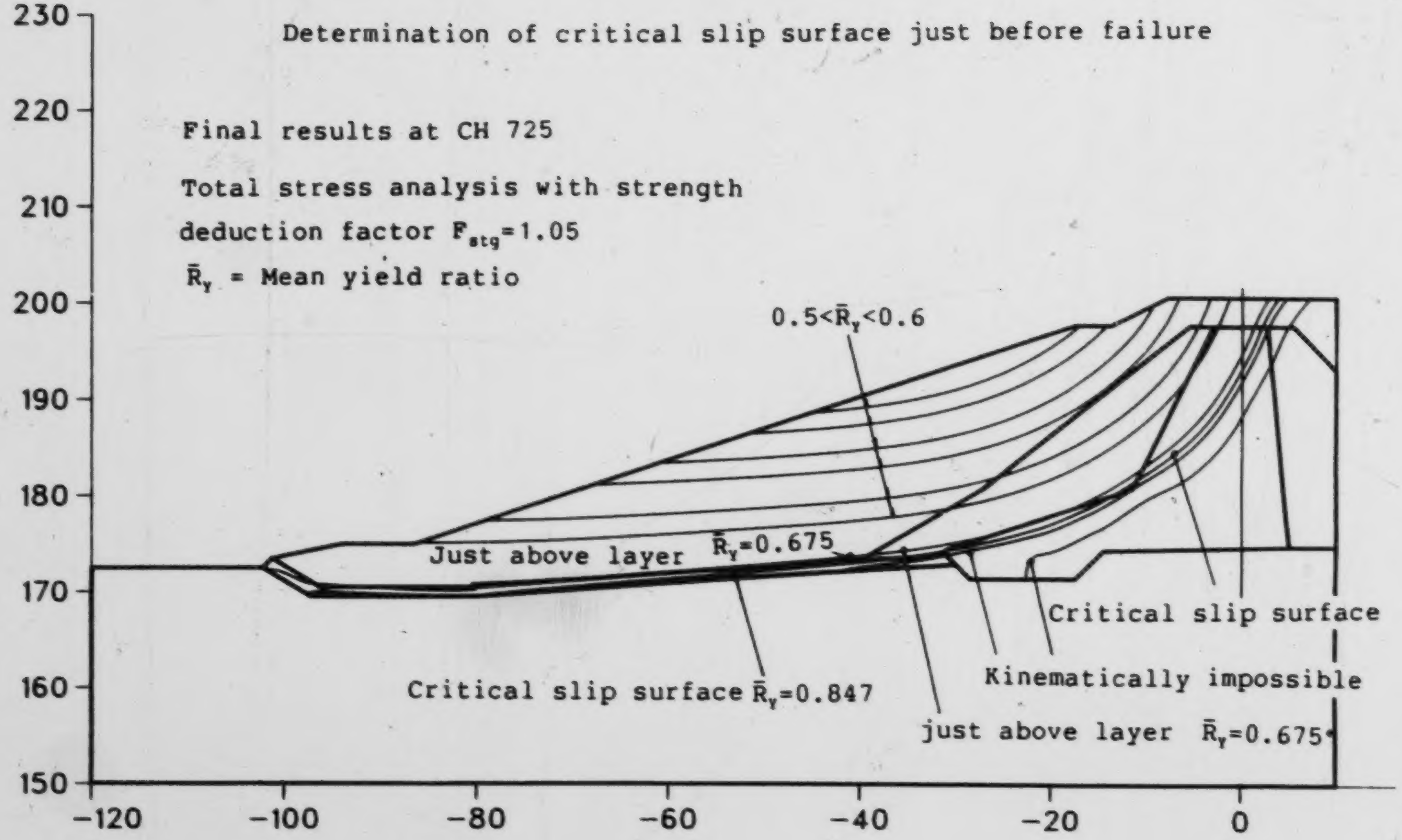

Figure 6.19: Determination of the critical slip surface -total analyses

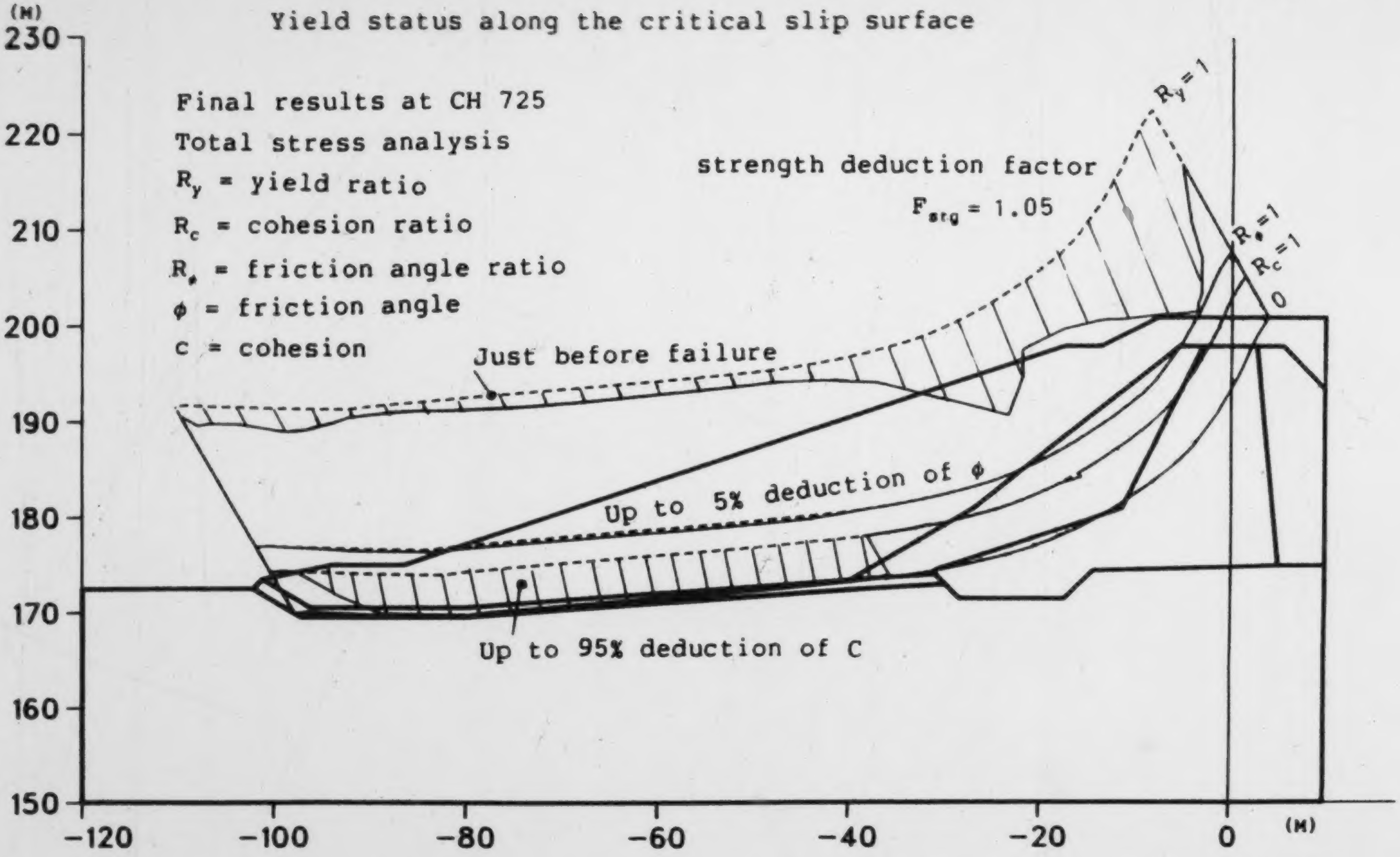

Figure 6.20: Yield status along the observed slip surface-total stress analyses

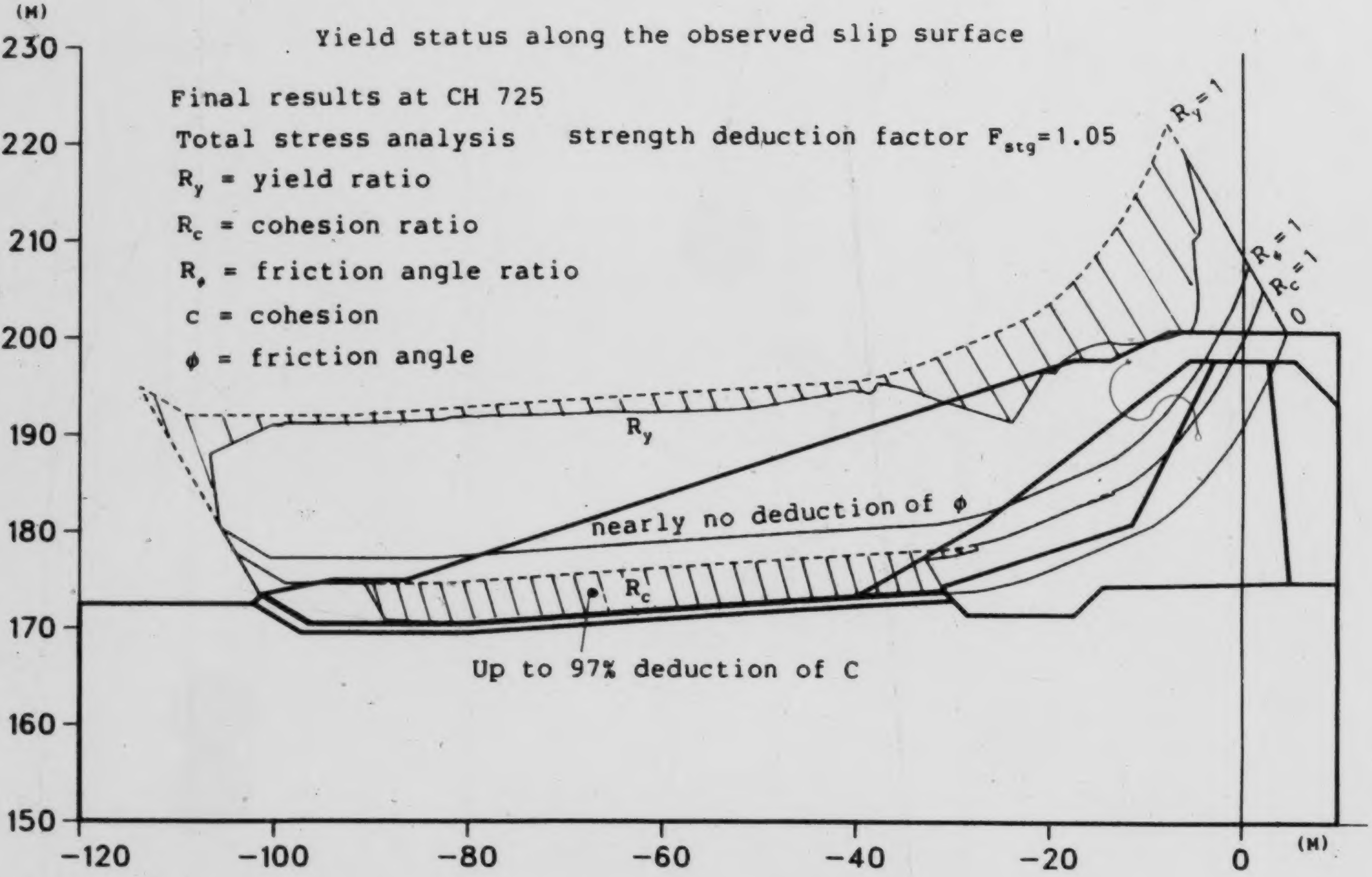

Figure 6.21: Yield status along the critical slip surface-total stress analyses

determine the conventional factor of safety in the next section.

6.3.4 Discussion of factors of safety

If the limit equilibrium method is used directly, the factor of safety is hard to determine for the structure in which progressive failure due to strain softening develops, since the reduction of the strength parameters is unknown. The finite element method can be used to determine the reduction but provides no factor of safety. When the estimated reduction of strength from finite element analyses is used in determining factors of safety, some theoretical and numerical aspects need to be mentioned.

Experience has shown that the so-determined factor of safety might be on the unsafe side. Models used in limit equilibrium analyses corresponds with layered models. The corresponding definitions of failure criteria are generally different from those used in finite element analyses. For example, a point which fails under the von-Mises criterion might not fail in a limit equilibrium analysis when the same undrained strength is adopted. Besides, we need strain distributions to estimate strength reduction. However, at present, prediction of deformation by finite element analyses is not accurate enough. Finally, the reliable strength reduction distribution can be taken from the converged results just before failure and so the error in determining the critical load may also lead to a factor of safety on the unsafe side. Clarification of the above theoretical and numerical problems is beyond the scope of this thesis. What is intended here is to give a try and see what experience we can gain.

The calculations of factors of safety are done by the Sarma method while the reduction of strength parameters is based on the corresponding finite element results. The pore pressure distribution is taken from the interpolated data output from program RESTRE (Fig. 6.22). The factors of safety for the effective stress analysis are listed in Table 6.1.

Table 6.1 Factor of safety - effective stress analyses

Strength	Observed slip surface	Critical slip surface
Peak(intact)	1.46	1.47
Bulk	1.16	1.17
Reduced due to softening	1.04	1.05
Critical dam height is EL.200.10m, $F_{stg}=1.00$		

The bulk strength in Table 6.1 corresponds to the peak strength used in finite element analyses. The bulk strength parameters can be found in Table 5.6. In giving those parameters, all defects in the soils have been considered. The corresponding factor of safety is lower than that of 1.22 given in the "REPORT" due to the following reasons.

Firstly, higher pore pressures are adopted by reviewing all the observed data. Secondly, lower strength parameters are used in the berm at the toe and in the top of the dam where cracking develops.

The first experience gained from the results is that the critical slip surface obtained in finite element analyses may not be the most critical potential slip surface in limit equilibrium analyses. This may be mainly due to differences in defining the failure criteria. In other word, a point which fails under the two dimensional Mohr-coulomb criterion in finite element analyses, now, may not fail under the same one dimensional criterion along the slip surface.

The expected factor of safety obtained from the reduced strength due to softening should be 1.0, since the dam fails at this height. But, the result is about 5% higher than we expect. Although the possible reasons have been listed at the beginning it is hard to tell which one is important. It is better just to consider this difference as an experience, since we have just done one trial with one set of input data. It is meaningless in practice to find the factor of safety at the design height EL.201.0m, since such a design should be revised.

The factors of safety for the total stress analysis can be found in Table 6.2 and 6.3. In Table 6.2, the dam does not fail at the real height EL. 201.0m. With the available strength, the safety factor is between 1.17 to 1.19, this

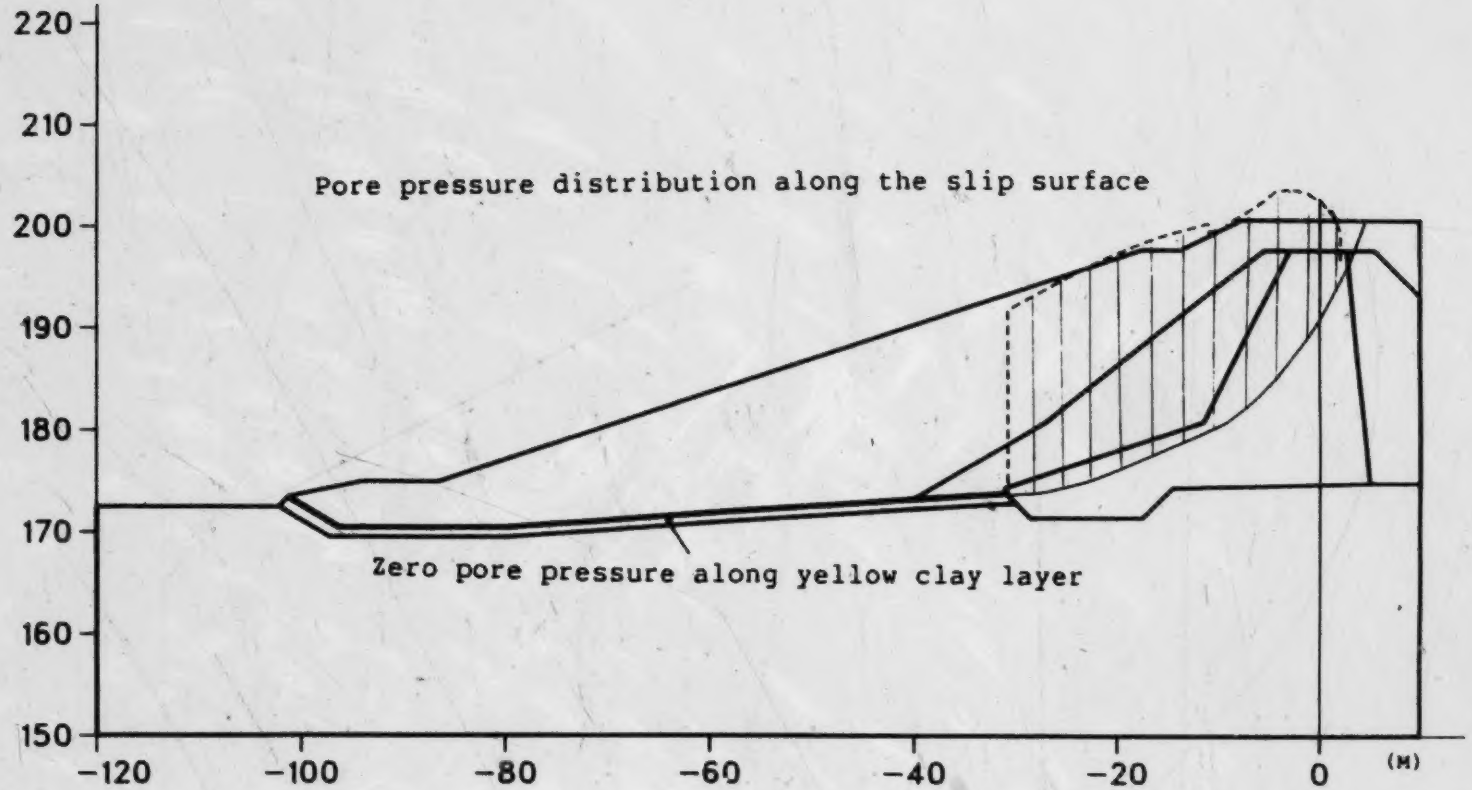

Figure 6.22: The assumed pore pressure distribution along the observed slip surface

value is totally unreliable. If the strength is reduced by a factor of 1.17, the dam will fails at an elevation much lower than EL. 201.0m. In fact, the dam will fail at EL. 200.85m with a strength reduction factor (F_{stg}) of only 1.05 in the finite element analyses.

Table 6.2 Factor of safety - total stress analyses(a)

Strength	Observed slip surface	Critical slip surface
Bulk	1.22	1.24
Reduced due to softening	1.17	1.19
Critical dam height is EL.201.00m, F_{stg}=1.00		

It is difficult to estimate an intact peak strength for the core in total stress analyses. The average bulk strength for the Core is given as explained in Section 5.2.4.1. For other materials, defects in soils have been considered in giving the bulk strength (Table 5.6).

Table 6.3 Factor of safety - total stress analyses(b)

Strength	Observed slip surface	Critical slip surface
Bulk	1.18	1.20
Reduced due to softening	1.10	1.13
Critical dam height is EL.200.85m, F_{stg}=1.05		

In the Table 6.3, the bulk strength is calculated by using the reduction factor (F_{stg}=1.05).

After using the reduction factor (F_{stg}) of 1.05 in the analysis the dam fails and so the expected factor of safety should be 1.0 in the corresponding limit equilibrium analyses. Unfortunately, this time, we have an even larger error of about 0.10 to 0.13 on the unsafe side. Beside other reasons, another important reason lies in the poor performance of the total stress analysis in simulating the yield status in the upper portion of the dam.

It seems much more reliable to find the factor of safety at EL. 201.0m by interpolation with respect to F_{stg} and the dam height. In other words, only the finite element results are used. Since EL. 200.85m is very close to EL. 201.00m, no interpolation is needed, a factor of safety can be taken as about 1.05. This value is still about 5% higher than the real case. As a general example, suppose that H_c=200.8, if F_{stg}=1.05, and H_c=200.2, if F_{stg}=1.07, then, if H_c=201.0, we have

$$(F_{stg})_{EL.201} = 1.05 + (1.05-1.07) \times \frac{201.0-200.8}{200.8-200.2} = 1.043$$

Now, the above value of F_{stg} can be taken as an estimated value of factor of safety.

To use the above estimation, at least, three runs of finite element analyses are generally needed. It is very expensive and the error is still about 5% according to our experience. However, if it is used with caution, say, with an allowance of 5%-10% for effective stress analyses, it may be used safely in practice. It is difficult to explain this error clearly in view of both the uncertainty in theories and problems in calculations. If the mobilized strengths from one finite element analysis are used in limit equilibrium analyses for the designed height, an allowance of about 15%-20% may be needed according to our experience. The true solution of this problem depends on the accumulated experience in the future.

6.4 Parametric study

Since there exist uncertainties in determining the material parameters, parametric studies have been done to evaluate the reliability of the final results described in the foregoing section. However, computation funds and time are limited, hence, only a few trial runs have been carried out. Within reasonable ranges of the material parameters, all runs are successful and the same conclusions on failure mechanism can be drawn. Certainly the critical dam heights at failure are different because different parameters are used. As shown in Fig. 6.15, all the critical slip surfaces are located above the observed one in a narrow shaded area in the core and pass through the Yellow Clay layer. This implies the effectiveness of the formulation and the reliability of the final results. Here, only the main implications concerning the reliability of the results are described.

Three runs of total stress analyses have been carried out to test the influence of softening rates. Factors to increase initial rates are 1.0, 2.0 and 4.0 in sequence. The dam does not fail at El. 201.0m for factors 1.0 and 2.0 and fails at EL. 199.20m for a factor of 4.0. By applying further load on the top of the dam, equivalent to a height at El. 202.05, the dam will fail for a factor of 1.0. If the factor is 4.0, the softening rates of any material is beyond the range given by the limited test data. However, the influence on the critical height is small. Therefore, the adopted softening parameters can be considered reliable. Probably, the small influence can be attributed to the stiff support provided by the filter and shell materials. On average, their elastic moduli are 10 to 20 times of that of the core material. An even stiffer foundation also provides constraints to limit strain softening.

The influence of the dilation angle ψ' is also investigated by changing ψ' from 0 to ϕ'. With ψ' being equal to ϕ', we obtain the associated flow law. The results of the effective stress analysis for the non-associated flow law (i.e. $\psi' = 0$) have been described in detail before, with the critical height (H_c) reached at EL. 200.1m. However, with $\psi' = \phi'$, the critical height is only EL. 195.6m when using cracking models in which closures of cracks are considered. But, the height can reach to EL. 197.85m by using perfect elastoplastic tension models in which cracks are assumed to remain open near failure. Severe cracking can be observed when cracking models are used near failure. As explained in Chapter 2, oscillation of the results occurs during iteration, unreasonably high compressive stresses (-10^4 to -10^5 kpa) can be found and tension spreads quickly to most of the upstream dam body, leading to a divergent solution. The perfect models yield better results, but the critical height is still too low as compared with the observed height at EL. 201.0m.

The above results may be caused by larger dilations, hence larger strains, which depart from the continuous deformation in many places in the core and then in the whole upstream dam body. It may also be caused by poor performance of iteration methods in treating regional cracking. No further study has been made. At least, the conclusion that the non-associated model is suitable can be drawn for our case history.

By decreasing all the elastic moduli to half in another trial effective stress analysis, the critical height is reached at EL. 198.75m, about 1.35m lower than that in the recommended results. It is because softer materials provides less constraint to the development of the plastic strain in the core and Yellow Clay layer, hence cause larger reduction of material strengths. The horizontal displacements increase by 2.1 to 2.3 times on average and fit the observed displacement better. But the vertical deformation, especially in the core are not satisfactory, e.g. the vertical strains are about 1.4 to 1.7 times higher as compared with the observed values. If the horizontal elastic moduli of the filter and shell are decreased to half, both the horizontal displacements and vertical displacements agree with the observed data much better, but the critical height is determined at EL. 198.90m, 1.20m lower than that of the original one, and 2.10m than the observed height. There are many other factors which will affect the deformation quantities. Therefore, the above results cannot be used as a back-analysis of elastic moduli.

The magnitude of the pore pressure affect the results a great deal. If a factor of 1.1 is used to increase the pore pressure. The calculated critical dam height is as low as 196.05m, nearly 5m lower than the real situation with a lot of cracks in the core. A factor of 0.9 make the dam stable even if a further load increment (equivalent to a 2m high fill) is applied above the real dam height. It seems that the adopted pore pressure distribution is acceptable.

Our objective is only to evaluate the reliability of the results presented in the beginning of this chapter. The changes of the parameters in the above trial runs, strictly speaking, are a little bit arbitrary. Therefore, none of the trial results are plotted and recommended as final results.

In conclusion, the finite element formulation in Chapter 2 are effective, the mesh and iteration procedures suggested in chapter 3 are appropriate, the selected models and adopted parameters are basically suitable, and all these make the recommended results in this chapter satisfactory and reliable in analysing the failure mechanism of the Carsington Dam. However, post failure behavior cannot be simulated due to the limitations of the adopted theories, and accurate prediction of deformations is not attainable due to lack of enough information. Effective stress analyses are superior to total stress analyses and are recommended whenever pore pressures are available. At present, more effective applications can be found in a history-matching mode. By adjusting material parameters from observed data during construction, more fruitful results can be obtained by finite element analyses and useful experiences can be accumulated for the future. The use of safety factor still remains as a problem for the structure with strain softening involved.

7. CONCLUSIONS

7.1 Conclusions

The effectiveness of the nonlinear finite element analysis to simulate the mechanism of progressive failure due to strain softening has been proved for such a complex engineering problem as the Carsington Dam failure. However, satisfactory prediction of deformations still remains as a major problem in view of the cost invested for each run on the computer.

An effective and efficient application of the non-linear finite element methods comprises a series of links, including adoption of proper theories for the formulation, determination of reliable material models and parameters, design of a mesh with suitable density, division of sufficiently small load increments, selection of appropriate iteration methods and accurate enough criteria for convergence as well as correct interpretation of the numerical results. The conclusions and implications obtained from the research will be described below. Although certain conclusions are problem dependent, they are helpful in demonstrating a proper way to use the non-linear finite element analyses and can be used for reference to other rock-earthfill dams.

The Lagrangian formulation based on the incremental theory of plasticity for small strain and deformation can reveal the failure mechanism from low loading stages to the formation of the incipient slip surface provided that local collapses due to cracking or dislocation do not occur or are simulated by brittle models in limited and very small areas. In the framework of the adopted theory the true solution can be obtained in the incremental sense if and only if the loading criteria are obeyed. Brittle models can be used to avoid absurd solutions when the loading criteria are violated. The conditions of small strain and deformation are generally satisfied in a man-made structure. Otherwise, either the design may be revised if in the design stage or other theories should be used. The adopted formulation is powerless to simulate the post-failure mechanism and unable to reveal the formation of eventual slip surface except in weak layers. There exists a transition from the incipient slip surface to the eventual slip surface due to the change of principle stress orientations under large deformation, accompanied by dislocations in shear bands and large openings.

Theoretical eigenvalue analyses are made with respect to the elastoplastic matrix (Chapter 2, Appendix B). This helps check the correctness of material parameters in agreement with the desired behavior and reveals the capacity of the elastoplastic model to capture localized deformations. The solution behavior of a system with negative stiffness inside a body is also studied from theory to practice(Chapter 2, Appendix D and E). By using the brittle model, theoretically , any complex problem can be solved with rèasonable results for engineering judgement, if it can be defined within the scope of the above theories. Complex examples or case histories are needed to validate the theories and recommended methods.

The Mohr-Coulomb model is not suitable at very low stress levels near zero, especially when no tension analyses are used. It is better to use an elastic model at the first incremental step. The stiff foundation and stiff materials of the filter and shell limit strain softening in our case history. Therefore, the influence of softening rate is not appreciable before failure and the hyperbolic softening model with two parameters is acceptable. More complicated models which fit the test data better should be adopted when strain softening plays a greater part. By using both the criteria for cracks in the stress space and the criteria for their closure in the strain space, bad convergent speed and unreasonably high stresses may be encountered because of tremendous modulus difference before and after closure and also because of errors in calculating the strain just at closure. However, the bad performance occurs only when the structure is near failure and cracks open seriously in a region. At lower loading levels, the cracking model yields more reasonable solutions than the model derived only in the stress space by using elastoplastic theory. The latter seems more effective when the structure is near failure, since the cracks remain open in our case history. Neither of the two cracking models can garantee satisfactory solution for any situation. In the final analysis, modelling cracks is beyond the scope of continuum mechanics. The present treatment of cracks under the assumption of continuity can only help us to obtain more reasonable results under the condition that the failure is dominated by shear.

Effective stress analyses are superior to total stress analyses in simulating the failure mechanism. The main reason is the conditions for the tests of undrained strength C_u cannot reflect the real situation in the core, especially in the upper portion where the stress level is low and the undrained condition is not maintained. The main shortcomimg of effective stress analyses is that the pore pressure distribution must be known or must be calculated from reliable pore pressure parameters. Effective stress analyses are recommended whenever possible and effort should be made both in laboratory tests and field investigation to help gather necessary data for an engineering project. However, by experience, the results of total stress analyses are acceptable and can be used in preliminary study since less information is needed.

Guidelines for mesh design, division of load increments, selection of iteration method and criteria for convergence are given in Chapter 3. They are problem dependent but useful for similar analyses in dam engineering. For reliable results, considerations of those links are necessary. Conclusions of general significance are listed as follows,

1. Ecnomical benefits can be gained more from a mesh with suitable density than from improvement of iteration methods. For repeated runs on different working conditions or similar sections, a mesh study is suggested.
2. The replacement of the conventional large foundation by an elastic layer with equivalent vertical deformation modulus may yield similar deformation patterns and failure mechanism, but errors of horizontal deformations cannot be controlled without knowing the equivalent modulus in this direction.
3. The error tolerance for a convergence displacement solution is important in determining the critical load just before failure. Trial calculations are less expensive and should be carried out to quarantee reliable results.

The recommended results from the effective and total stress analyses show that the sudden failure of the Carsington Dam is promoted by strain softening, starting from the highly strained boot (Fig. 6.16). The determined incipient slip surface from an effective stress analysis can be considered as a good approximation as compared with the observed one. The error of conventional factor of safety is less than 2% along these two slip surfaces. The vertical deformations fit better with the observation data, but considerable error of 50% to 100% can be found in predicting horizontal deformations.

The newly-developed integration techniques (Chapter 6) are proved to be effective in locating the incipient slip surface. They only apply to shear failure.

Experience should be accumulated for a confident use of conventional factors of safety when the reduced strength is estimated from finite element analyses. The so-determined factor of safety seems on the unsafe side. Theoretically, this is because the thoeries backing up the limit equilibrium and finite element analyses are totally different. Practically, factors in calculation will also affect the value of factor of safety. The most important factors are the division of increment steps and the error tolerance for convergence. They will influence the critical dam height, hence the extent of the development of plastic strains along the slip surface.

7.2 Recommendations

The uncertainty of the input information prevents the nonlinear finite element analysis from finding wider application in practice. On the one side, techniques of field investigation and laboratory tests should be improved, especially in determining the material parameters related to deformation such as deformation moduli and strain softening rates and in clarifying in-situ conditions such as pore pressure and in-situ stress distributions. On the other hand, before the design, during and after the construction of a major project, special effort should be made to gather useful information. Otherwise, the situation that case histories can be rarely found might not be changed. Here, the cooperation of scientists and engineers are very important. At present, analyses in history-matching mode during construction may be more effective and fruitful, therefore are highly recommended.

Although the research shows promising results in understanding the progressive failure due to strain softening, more case histories need to be analysed to obtain more comprehensive knowledge. Especially, case histories in which strain softening has fully developed along the softening curve needs to be studied.

There exist a lot of case histories in which cracks may open here and there but the failure is dominated by shear and the strain and deformation is small except around cracks. The cracking model may improve the solution, but, the regional cracking predicted near failure is often not true. What we observed during failure is two or more continuous bodies separated by primary cracks and shear bands which may or may not be dislocated. A combined solution method with both continuous and discontinuous models needs to be studied. By using or modifying the available contact elements, internal degrees of freedom, re-meshing techniques, or pseudo-dynamic approach, the solution seems feasible. Although the formulation is more complicated, no more material parameters are needed and the results may be more reasonable.

The transition from the incipient failure to eventual failure cannot be solved by the present formulation. The simulation of post-failure behavior is generally not important for a man-made structure. However, it might be important for natural structures such as landslides. The incipient failure is not allowed for any dam, but it might not cause an unacceptable failure of a natural slope from the engineering point of view. More complicated formulations and discontinous models need to be developed to tackle this interesting problem.

Experience in this research shows that unstable solutions or slow convergence will occur when cracking models are used near failure. Little work has been done in this research to analyse the reasons. Numerical methods may be improved or other iteration methods may be tried.

BIBLIOGRAPHY

Aitken, A.C. The Evaluaton of the Latent Roots and Latent Vectors of a Matrix. Proc. Roy. Soc. Edinburgh, Vol. 57: 269-304, 1937.

Babtie Shaw & Morton, Skempton A.W. Carsington Dam - The Mechanism of Failure. Severn-Trent Water Authority, 1986.

Bathe, K.J. and Cimento, A.P. Some Practical Procedures for the Solution of Nonlinear Finite Element Equations. Computer Methods in Applied Mechanics and Engineering, Vol. 22, pp. 59-85, 1980.

Bathe, K.J. Finite Element Procedures in Engineering Analysis. Prentice Hall Inc, 1982.

Bergan, P.G., Horrigoe, G., Krakeland, b. and Soreide, T. H. Solution Techniques for Non-linear Finite Element Problems. Int. J. Numer. Meths. Eng. Vol. 12, pp. 1677-1696, 1984.

Bjerrum, L. Progressive Failure in Slopes of Over-concolidated Plastic Clay and Clay Shales. Journal of the Soil Mechanics and Foundation Division, A.S.C.E., Vol. 93, SM 5, PP. 3-49, 1967.

Bland, D.R. The Associated Flow Rule of Plasticity. Journal of the Mechanics and Physics of Solids, Vol. 6, pp. 71-78, 1957.

Borst, R. de. Numerical Simulation of Shear Band Bifurcation in Sand Bodies. 2nd International Symposium on Numerical Models in Geomechanics, Ghent. pp. 91-98, 1986.

Boyle, E.F. and Jennings, A. Accelerating the Convergence of Elastic-plastic Stress Analysis. Int. J. Num. Meth. Eng. Vol 7, pp. 232 -235, 1973.

Broodlie, K.W, Gourlay, A.R. and Greenstadt, J. Rank-one and Rank-two Corrections to Positive Definite Matrices Expressed in Product Form. J. Inst. Maths. Applics, Vol. 11, pp. 73-78, 1973.

Broydem, C.G. The Convergence of an Algorithm for Solving Sparse Nonlinear Systems. Mathematics of Computation, Vol. 25, No. 114, pp. 285-294, 1971.

Burland, J.B., Londworth, T.I. and Moore, J.F.A. A Study of Ground Movement and Progressive Failure Caused by a Deep Excavation in Oxford Clay. Geotechnique, Vol. 27, No.

4, pp. 557-591, 1977.

Chan, D.H.K. Finite Element Analysis of Strain Softening Material. Ph.D. Thesis, University of Alberta, 1986.

Chen, W.F. and Suzuki, H. Constitutive Models for Concrete. Computers and Structures, Vol. 12, pp. 23-32, 1980.

Chen, W.F. and Baladi, G.Y. Soil Plasticity-Theory and Implementation. Elvesier Science Pub, 1985.

Chow, Y.K. and Kay, S. On the Aitken Acceleration Method for Nonlinear Problems. Int. J. Num. Meth. Eng., Vol. 1, pp. 275-278, 1983.

Christian, J.T. and Whitman, R.V. A One Dimensional Model for Progressive Failure. Proceeedings of the Seventh International Conference on Soil Mechanics and Foundation Engineering, Mexico City, Vol. 2, pp. 541-545, 1969.

Christoffersen, J. and Hutchinson, J.W. A class of Phenomenological Corner Theories of Plasticity. Journal of the Mechanics and Physics of Solids, Vol. 27, pp. 465-487, 1979.

Davey, P.G. and Eccles P.G. Technical Report of Carsington Dam. Journal IWES Vol. 37, 1983 pp. 215-239, 1983.

De Alencar, JR. Deformation of Dams on Sheared Foundations. Ph.D. Thesis, University of Alberta, 1988.

Den Hartog, J.P. Forced Vibrations with Combined Coulomb and Viscous Damping Trans. ASME, Vol. 53, P. APM-107, 1931.

Dennis, J.E. and Marwill, E.S. Direct Secant Updates for Highly Structured Systems of Non-linear Equations. SIAM J. Numer. Anal. Vol. 16, pp. 260-269, 1983.

Desai, C.S. and Christian, J.T. Numerical Method in Geotechnical Engineering. New York: McGraw Hill, 1977.

Drucker, D.C. and Prager, W. Extended Limit Design Theories for Continuous Media. Quarterly of Applied Methematics, Vol. 9, pp. 381-389, 1951.

Drucker, D.C. On Uniqueness in the Theory of Plasticity. Quarterly of Applied Mathematics, Vol. 14, pp. 35-42, 1956.

Drucker, D.C. A Defination of Stable Material. Int. Appl. Mech. Vol. 26, pp. 101-106, 1959.

Gadala, M.S. and Oravas, G. AE Numerical Solutions of Nonlinear Problems of Continua-I, Survey of Formulation Method and Solution Techniques. Computers & Structures, Vol 5/6, pp. 856-877, 1984.

Ghaboussi, J., Wilson, E. and Isenberg, J. Finite Element for Rock Joints and Interfaces. Journal of the Soil Mechanics and Foundation Division, A.S.C.E., Vol. 99, SM 10, pp. 833-848, 1973.

Goodman, R.E., Taylor, R.L. and Brekke, T.L. A Model for the Mechanics of Jointed Rock. Journal of the Soil Mechanics and Foundation Division, A.S.C.E., Vol. 94, SM 3, pp. 637-659, 1970.

Harris, M. Cyril and Crede, E. Charles. Handbook of Dynamics. New York: McGraw-Hill Company, 1976.

Hill, R. The Mathematticl Theory of Plasticity. London: Oxford at the Clarendon Press, 1953.

Hill, R. Bifurcation and Uniqueness in Non-linear Mechanics of Continua. Problem of Continuum Mechanics, Editor: Laurentev M.A., Society of Individual and Applied Mathematics, 1961.

Hinton, E. and Campbell, J.S. Local and Global Smoothing of Discontinuous Finite Element Functions Using a Least Squares Method. Int. J. Num. Meth. Eng. Vol. 8, pp. 461-480, 1974.

Hinton, E., Scott, F.C. and Ricketts, R.E. Local Least Squares Stress Smoothing for Parabolic Isoparametric Elements. Int. J. Num. Meth. Eng. Vol. 9, pp. 235-256, 1975.

Knopp, J.P. Linear Algebra, Santa Babara. California: Hamilton Publishing Company, 1974.

Law, K.T. and Lumb, P. A Limit Equilibrium Analysis of Progressive Failure in the Stability of Slopes. Canadian Geotechnical Journal, Vol. 15, pp. 113-122, 1978.

Lo, K.Y. An Approach to the Problem of Progressive Failulure. Canadian Geotechnical Journal, Vol. 9, pp. 407-429, 1972.

Lo, K.Y. and Lee, C.F. Stress Analysis and Slope Stability in Strain Softening Material. Geotechnique, Vol. 23, pp. 1-11, 1973.

Magnus, K. Vibrations. Glasgou, Blackie &Son ltd, 1965.

Mandel, J. Conditions de Stabilité et Postulat de Drucker. Rheology and soil Mechanics. Grenoble, Symposium, pp. 58-68, 1964. and P. M. Sirieys.)

Martin, J.B. Plasticity: Fundmentals and General Results. Mit Press, Cambridge, Mass, 1975.

Morgenstern, N.R. and Tchalenko, J.S. Microscopic Structure in Kaolin Subjected to Direct Shear. Geotechnique, Vol. 17, pp. 309-328, 1967.

Morgenstern, N.R. and Simmons, J.V. Analysis of the Movements of Gardiner Dam. Proceedings 4th International Conference on Numerical Methods in Geomechanics, Vol. 3, pp. 1003-1027, 1982.

Palmer, A.C. and Rice, J.R. The Growth of Slip Surfaces in the Progressive Failure of Over-Consolidated Clay. Proceedings of the Royal Society of London, A 322, pp. 527-548, 1973.

Pietruszczak, S. and Stolle, F. E. A constitutive Model for Jointed and fissured materials. 2nd International Symposium on Numerical Models in Geomechanics, Ghent. pp. 191-201, 1986.

Qu, S. and Yin, Y. Drucker's and Ilyushin's Postulate of Plasticity. Beijing: No.5, Transaction of Mechanics. Vol. 5, pp. 465-473, 1981.

Rice, J.R. The Localization of Plastic Deformation. Theoretical and Applied Mechanics, Edited by Koiter W.T., North-Holland Publishing Company, pp. 207-220, 1976.

Skempton, A.W. Long Term Stability of Clay Slope. Geotechnique, Vol. 14, No. 2, pp. 77-102, 1964.

Skempton A.W. Carsington Dam Failure. Proc. of symp. on Failures in Earthwork (1985: London), Thomas Telford ltd. pp. 203-220, 1985.

Tewarson, R.P. and Zhang, Yin. Sparese Quasi-Newton LDU Updates. Int.J. Num. Eng., Vol 24, pp.1093-1100, 1987.

Vardoulakis, I. Shear Band Inclination and Shear Modulus in Biaxial Tests. International Jounral for Numerical and Analytical methods in Geomechanics. Vol. 4, pp. 103-119, 1980.

Wang, R. Foundation of Palasticity. Beijing, Science Publishing House, 1982.

Zienkiewcz, O.C. Humpheson, C. and Lewis, R.W. Associated and Non-Associated Visco-Plasticity and Plasticity in Soil Mechanics. Geotechnique, Vol. 25, No. 4, pp. 671-689, 1975.

Zienkiewicz, O.C. The Finite Element Method. London: McGraw Hill, 1977.

A. APPENDIX - THE MOHR-COULOMB MODEL WITH HYPERBOLIC STRAIN SOFTENING

Chan (1986) introduced hyperbolic strain softening into the von-Mises model and gave the specific expressions in detail. In this model, linear elastic behavior is assumed before peak, the yield surface will contract in the stress space, and the decrease of shear strength to its residual is simulated by a hyperbolic function measured in terms of equivalent strain as shown in Fig. A.1. Since we need the basic expressions of this model to extend similar softening behavior to the Mohr-Coulomb model, we still list them as follows.

The yield function is defined as

$$F = q - \kappa = 0 \ , \tag{A.1}$$

in which

$$q = \sqrt{3J_2} \ , \tag{A.2}$$

$$\kappa = \kappa_p \left(1 - \frac{\bar{\epsilon}^p}{a + b\bar{\epsilon}^p} \right) \ , \tag{A.3}$$

where

κ_p is the uniaxial compressive peak strength with the residual value being κ_r. For the strength parameters below, subscripts $_p$ and $_r$ are for the peak and residual values respectively. And

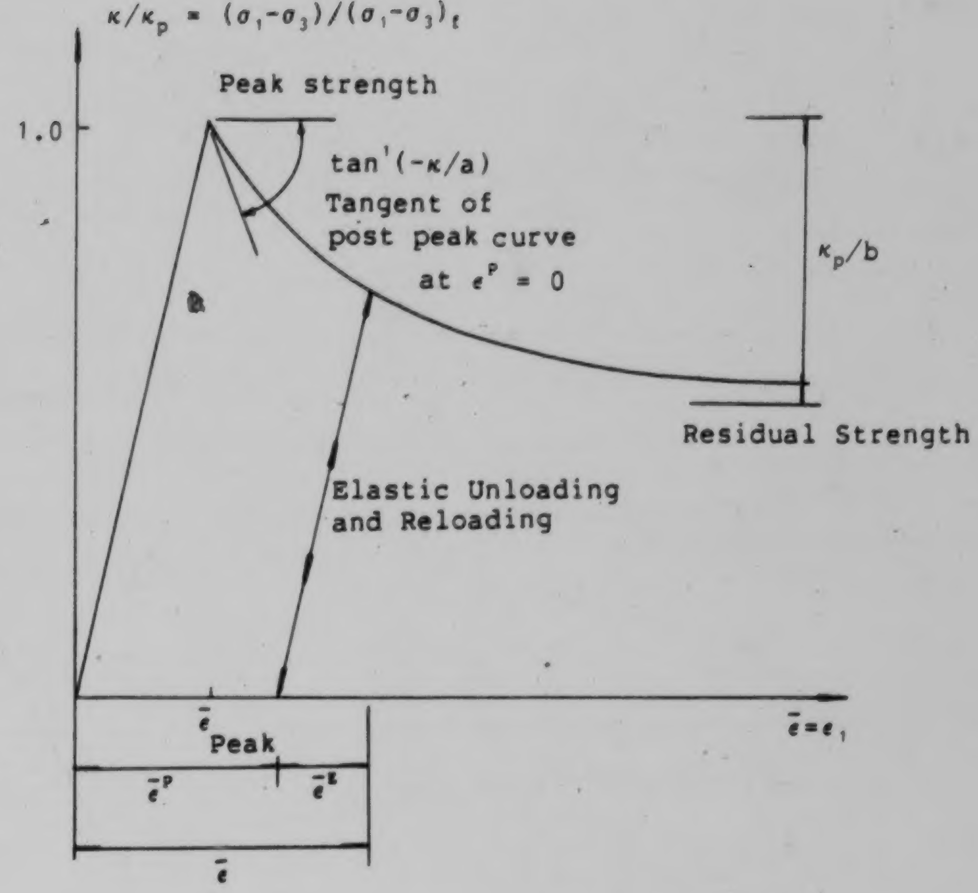
$\kappa/\kappa_p = (\sigma_1-\sigma_3)/(\sigma_1-\sigma_3)_f$
Peak strength
1.0
$\tan^{-1}(-\kappa/a)$
Tangent of
post peak curve
at $\epsilon^p = 0$
κ_p/b
Residual Strength
Elastic Unloading
and Reloading
$\bar{\epsilon}$ Peak
$\bar{\epsilon}=\epsilon_1$
$\bar{\epsilon}^p$
$\bar{\epsilon}^E$
$\bar{\epsilon}$

Figure A.1: Hyperbolic strain softening model

$$\bar{\epsilon}^p = \int d\bar{\epsilon}^p = \text{equivalent plastic strain},$$
$$d\bar{\epsilon}^p = (\tfrac{2}{3}de^p_{ij}de^p_{ij})^{1/2},$$
$$de^p_{ij} = d\epsilon^p_{ij} - d\epsilon^p_{kk}\delta_{ij}/3,$$
$$d\epsilon^p_{ij} = \text{increment of plastic strain tensors}, \tag{A.4}$$

with a and b being material parameters,

$$b = 1/(1-\kappa_r/\kappa_p) \ , \tag{A.5}$$

or by introducing the brittleness index

$$I_B = \frac{\kappa_p-\kappa_r}{\kappa_p} \ . \tag{A.6}$$

Then,

$$b = \frac{1}{I_B} \ . \tag{A.7}$$

Therefore, b only depends on the peak and residual strengths. The parameter a can be obtain from the expression:

$$\frac{\partial\kappa}{\partial\bar{\epsilon}^p} = -(\frac{\kappa}{a}) \ , \qquad \text{at} \quad \bar{\epsilon}^p = 0 \ . \tag{A.8}$$

This indicates that κ_p/a is the tangent of the initial slope for softening just after peak. This model is simple to use since only one parameter , i.e. a, needs to be determined in addition to those obtained from conventional laboratory tests.

The specific expressions for the Mohr-Coulomb model are known. We only discuss how to use two extra parameters, a_c for the cohesion C and a_ϕ for the friction angle ϕ in introducing softening behavior into the Mohr-Coulomb model. Its yield function takes the form:

$$F = \sigma_m \sin\phi + \bar{\sigma}\cos\theta_0 - \frac{\bar{\sigma}}{\sqrt{3}}\sin\phi\sin\theta_0 - C\cos\phi ,$$

in which

$$\sigma_m = \sigma_{kk}/3, \qquad \bar{\sigma} = \sqrt{J_2},$$

$$\theta_0 = \frac{1}{3}\,\mathrm{arsin}[(-3\sqrt{3}J_3)/2J_2^{3/2}] . \tag{A.9}$$

By following Chan's definition, we define

$$C = C_p\left(1 - \frac{\bar{\epsilon}^P}{a_c + b_c\bar{\epsilon}^P}\right) , \tag{A.10}$$

$$b_c = 1/(1 - C_r/C_p) , \tag{A.11}$$

$$I_{Bc} = (1 - C_r/C_p) , \tag{A.12}$$

and a_c can be found from

$$\frac{\partial C}{\partial \bar{\epsilon}^P} = -\left(\frac{C}{a_c}\right) , \qquad \text{at} \quad \bar{\epsilon}^P = 0 . \tag{A.13}$$

Then, we define

$$\phi = \phi_p\left(1 - \frac{\bar{\epsilon}^p}{a_\phi + b_\phi \bar{\epsilon}^p}\right) , \qquad (A.14)$$

$$b_\phi = 1/(1-\phi_r/\phi_p) , \qquad (A.15)$$

$$I_{B\phi} = 1-\phi_r/\phi_p , \qquad (A.16)$$

and a_ϕ can be found from

$$\frac{\partial \phi}{\partial \bar{\epsilon}^p} = -\left(\frac{\phi}{a_\phi}\right) , \qquad \text{at} \quad \bar{\epsilon}^p = 0 . \qquad (A.17)$$

Now, the only task is to derive the specific expressions of $<\frac{\partial F}{\partial \epsilon^p}>\{\frac{\partial Q}{\partial \sigma}\}$ for the hardening term in the general eqn. 2.17. Here, the conventional assumption for the potential function Q is adopted by replacing the friction angle ϕ in eqn. A.9 by another angle ψ. Its range is defined as

$$0 \le \psi \le \phi .$$

If $\psi=\phi$, we have the associated flow law. With a smaller value of ψ than ϕ, the calculated dilation may fit field or laboratory observations much better.

By indroducing the equivalent plastic strain (eqn. A.4), it can be obtained that

$$<\frac{\partial F}{\partial \bar{\epsilon}^p}>\{\frac{\partial Q}{\partial \sigma}\} = \frac{\partial F}{\partial \bar{\epsilon}^p}\bar{Q} , \qquad (A.18)$$

in which

$$\bar{Q} = \frac{\sqrt{2}}{\sqrt{3}} \left[\frac{\partial Q}{\partial \sigma_{ij}} \frac{\partial Q}{\partial \sigma_{ij}} - \frac{1}{3} \frac{\partial Q}{\partial \sigma_{mm}} \frac{\partial Q}{\partial \sigma_{nn}} \right]^{1/2} . \qquad \text{(A.19)}$$

The derivation of the above expressions and the specific expression of $\bar{Q}$ for the Morh-Coulomb model can be found in the thesis of Chan (1986), while the expressions for $\{\frac{\partial F}{\partial \bar{\epsilon}^p}\}$ are given as follows. Since

$$\frac{\partial F}{\partial \bar{\epsilon}^p} = \frac{\partial F}{\partial \phi} \frac{\partial \phi}{\partial \bar{\epsilon}^p} + \frac{\partial F}{\partial C} \frac{\partial C}{\partial \bar{\epsilon}^p} , \qquad \text{(A.20)}$$

by using eqn. A.9, A.10 and A.14, we have

$$\frac{\partial F}{\partial \phi} = \sigma_m \cos\phi - \frac{\bar{\sigma}}{\sqrt{3}} \cos\phi \sin\theta_0 + C \sin\phi , \qquad \text{(A.21a)}$$

$$\frac{\partial \phi}{\partial \bar{\epsilon}^p} = -a_\phi \phi_p / (a_\phi + b_\phi \bar{\epsilon}^p)^2 , \qquad \text{(A.21b)}$$

$$\frac{\partial F}{\partial C} = -\cos\phi , \qquad \text{(A.21c)}$$

$$\frac{\partial C}{\partial \bar{\epsilon}^p} = -a_c c_p / (a_c + b_c \bar{\epsilon}^p)^2 . \qquad \text{(A.21d)}$$

Therefore,

$$\frac{\partial F}{\partial \bar{\epsilon}^p} = (\sigma_m \cos\phi - \frac{\bar{\sigma}}{\sqrt{3}} \cos\phi \sin\theta_0 + C \sin\phi) \times$$

$$\left[\frac{-a_\phi \phi_p}{(a_\phi + b_\phi \bar{\epsilon}^p)^2} \right] + \cos\phi \left[\frac{a_c c_p}{(a_c + b_c \bar{\epsilon}^p)^2} \right] . \qquad \text{(A.22)}$$

B. APPENDIX - ANALYTICAL EIGENVALUE ANALYSES

The derivations of eigenvalues and eigenvectors are very long and need certain techniques. For brevity, only main expressions are listed. However, the proof of the correctness of the results will be much easier by using back-subsitutions into basic equations.

B.1 Eigenvalue Study on Elastic Constitutive Relationship

The elastic matrix in principal stress space takes the form:

$$[C^E] = E(1-\nu)/[(1+\nu)(1-2\nu)]\begin{bmatrix} 1 & \nu/(1-\nu) & \nu/(1-\nu) \\ \nu/(1-\nu) & 1 & \nu/(1-\nu) \\ \nu/(1-\nu) & \nu/(1-\nu) & 1 \end{bmatrix} \qquad (B.1)$$

The equations for eigenvalues are given by the condition that the following linear equations have non-trival solutions.

$$\begin{bmatrix} C^E_{11}-\lambda & C^E_{12} & C^E_{13} \\ C^E_{21} & C^E_{22}-\lambda & C^E_{23} \\ C^E_{31} & C^E_{32} & C^E_{33}-\lambda \end{bmatrix} \begin{bmatrix} \Delta\epsilon_1 \\ \Delta\epsilon_2 \\ \Delta\epsilon_3 \end{bmatrix} = 0 \qquad (B.2)$$

or the determinant of $([C^E]-\lambda[I])$ is zero ($[I]$ is identity). And so we obtain

$$\lambda^3 + p\lambda^2 + q\lambda + s = 0 \ , \qquad (B.3)$$

in which

$$p = -3a, \qquad q = 3(a^2-b^2), \qquad s = -a(a-b)^2(a+2b) ,$$
$$a = E(1-\nu)/[(1+\nu)(1-2\nu)], \qquad b=E\nu/[(1+\nu)(1-2\nu)] .$$

By solving the above equation, we obtain

$$\lambda_1 = a+2b = E/(1-2\nu) ,$$

$$\lambda_2 = a-b = E/(1+\nu) ,$$

$$\lambda_3 = a-b = E/(1+\nu) . \qquad (B.4)$$

Since $\nu>0$, the sufficient and necessary condition for the positive definite nature of $[C^E]$ is $-1<\nu<0.5$. If $\nu=0.5$, the material becomes imcompressible. By substituting λ_1 into eqn. B.2, it is easy to find the corresponding normalized eigenvetor to be

$$<\Delta\epsilon_1 \ \Delta\epsilon_2 \ \Delta\epsilon_3>^T = <\frac{1}{\sqrt{3}} \quad \frac{1}{\sqrt{3}} \quad \frac{1}{\sqrt{3}}>^T , \qquad (B.5)$$

which corresponds to an isotropically stressed state. For the double roots (λ_2 and λ_3), we have

$$\Delta\epsilon_1 + \Delta\epsilon_2 + \Delta\epsilon_3 = 0 , \qquad (B.6)$$

which corresponds to pure shear states without volume change. Three typical eigenvetors for pure shear are

$$<\Delta\epsilon_1\ \Delta\epsilon_2\ \Delta\epsilon_3>^T = <\frac{1}{\sqrt{2}} \quad 0 \quad -\frac{1}{\sqrt{2}}>^T ,$$

$$<\Delta\epsilon_1\ \Delta\epsilon_2\ \Delta\epsilon_3>^T = <0 \quad \frac{1}{\sqrt{2}} \quad -\frac{1}{\sqrt{2}}>^T ,$$

$$<\Delta\epsilon_1\ \Delta\epsilon_2\ \Delta\epsilon_3>^T = <\frac{1}{\sqrt{2}} \quad -\frac{1}{\sqrt{2}} \quad 0>^T . \tag{B.7}$$

Only two of the above three are independent.

When a new constitutive relationship is adopted, an eigenvalue analysis is very helpful, even for elastic models. We take the orthogonally anisotropic model as an example. In a plane strain problem, the elastic matrix is

$$\begin{bmatrix} a & b & 0 \\ b & d & 0 \\ 0 & 0 & G_2 \end{bmatrix} \quad \text{in which,} \quad \begin{aligned} a &= E_2(1-nv_2^2)/\beta , \\ b &= E_2nv_2(1+v_1)/\beta , \\ d &= E_2/(1-v_1^2)/\beta , \\ \\ \beta &= (1+\nu_1)(1-\nu_1-2n\nu_2^2) . \end{aligned} \tag{B.8}$$

The notations of the parameters are shown in Fig. 2.3 and eqn. 2.23. It can be found that

$$\lambda_1 = \frac{1}{2}(a+d) + \frac{1}{2}[(a-d)^2+b^2]^{1/2} ,$$

$$\lambda_2 = \frac{1}{2}(a+d) - \frac{1}{2}[(a-d)^2+b^2]^{1/2} ,$$

$$\lambda_3 = G_2 . \tag{B.9}$$

It is easy to see all the eigenvalues are real. The condition for three positive eigenvalues can be found as

$$1 - v_1 - 2\left(\frac{E_1}{E_2}\right)v_2^2 > 0 \ . \tag{B.10}$$

Improper selection of elastic parameters may destory the postive definite nature.

B.2 Eigenvalue Study on Perfect Elastoplastic Relationship

First, let us work on the perfect elastoplastic relationship under the associated flow law, i.e. F=Q. In the principal stress space, the elastic matrix has been given in eqn. B.1. We write the gradient of the yield function as

$$<\frac{\partial F}{\partial \sigma}> = <\frac{\partial F}{\partial \sigma_1}\ \frac{\partial F}{\partial \sigma_2}\ \frac{\partial F}{\partial \sigma_3}> = <f'_1\ f'_2\ f'_3> \ . \tag{B.11}$$

By calculation, we have

$$[C^{EP}] = E_a \begin{bmatrix} (f'_2)^2+(f'_3)^2+2\nu f'_2 f'_3 & \nu f'_3(f'_3-f'_2-f'_1)-f'_1 f'_2 & \nu f'_2(f'_2-f'_1-f'_3)-f'_1 f'_3 \\ & (f'_1)^2+(f'_3)^2+2\nu f'_1 f'_3 & \nu f'_1(f'_1-f'_2-f'_3)-f'_2 f'_3 \\ \text{SYM.} & & (f'_1)^2+(f'_2)^2+2\nu f'_1 f'_2 \end{bmatrix} \tag{B.12}$$

in which,

$$E_a = \frac{E}{(1+\nu)}/[(1-\nu)((f'_1)^2+(f'_2)^2+(f'_3)^2)+2\nu(f'_1 f'_2+f'_2 f'_3+f'_3 f'_1)] \ . \tag{B.13}$$

Here, E_a is a stiffness factor and will always be positive during loading. It can be proved by using the loading criterion l_3 (eqn. 2.9, 2.10, 2.15 and Table 2.1). By solving basic equations, we have

$$
\begin{aligned}
\lambda_1 &= 0 \ , \\
\lambda_2 &= E/(1+\nu) \ , \\
\lambda_3 &= E_a(1+\nu)[(f'_1)^2+(f'_2)^2+(f'_3)^2] \ ,
\end{aligned}
\qquad \text{(B.14)}
$$

Both λ_2 and λ_3 are positive, and the corresponding eigenvectors are

$$
\begin{bmatrix} f'_1 \\ f'_2 \\ f'_3 \end{bmatrix}
\qquad
\begin{bmatrix} f'_2-f'_3 \\ f'_3-f'_1 \\ f'_1-f'_2 \end{bmatrix}
\qquad
\begin{bmatrix} f'_2(f'_1-f'_2)-f'_3(f'_3-f'_1) \\ f'_3(f'_2-f'_3)-f'_1(f'_1-f'_2) \\ f'_1(f'_3-f'_1)-f'_2(f'_2-f'_3) \end{bmatrix}
\qquad \text{(B.15)}
$$

for λ_1, λ_2, and λ_3 respectively (Fig. 2.4a). Normalization is omited for brevity.

It is easy to prove the orthogonality of the above three vectors by calculating the dot products.

The derivation for the non-associated case is more complicated, but same procedure can be followed as above. Let the gradients of the yield and potential functions be expressed as

$$
<\frac{\partial F}{\partial \sigma}> \; = \; <\frac{\partial F}{\partial \sigma_1} \; \frac{\partial F}{\partial \sigma_2} \; \frac{\partial F}{\partial \sigma_3}> \; = \; <f'_1 \; f'_2 \; f'_3> \ ,
$$

$$<\frac{\partial Q}{\partial \sigma}> = <\frac{\partial Q}{\partial \sigma_1}\ \frac{\partial Q}{\partial \sigma_2}\ \frac{\partial Q}{\partial \sigma_3}> = <q'_1\ q'_2\ q'_3> \ . \qquad (B.16)$$

Then, the elastoplastic matrix takes the form:

$$[C^{EP}] = E_{una}\left[\begin{matrix} q'_2f'_2+q'_3f'_3+\nu(q'_2f'_3+q'_3f'_2) \\ \nu(-q'_2f'_3-q'_3f'_1+q'_3f'_3)-q'_2f'_1 \\ \nu(-q'_3f'_2-q'_2f'_1+q'_2f'_3)-q'_3f'_1 \end{matrix}\right.$$

$$\left.\begin{matrix} \nu(-q'_1f'_3-q'_3f'_2+q'_3f'_3)-q'_1f'_2 & \nu(-q'_1f'_2-q'_2f'_3+q'_2f'_2)-q'_1f'_3 \\ q'_1f'_1+q'_3f'_3+\nu(q'_1f'_3+q'_3f'_1) & \nu(-q'_2f'_1-q'_1f'_3+q'_1f'_1)-q'_2f'_3 \\ \nu(-q'_3f'_1-q'_1f'_2+q'_1f'_1)-q'_3f'_2 & q'_1f'_1+q'_2f'_2+\nu(q'_1f'_2+q'_2f'_1) \end{matrix}\right] . \qquad (B.17)$$

in which

$$\begin{aligned} E_{una} = \frac{E}{(1+\nu)}/[&(1-\nu)(f'_1q'_1+f'_2q'_2+f'_3q'_3) \\ &+\nu(q'_1f'_2+q'_1f'_3+q'_2f'_1+q'_2f'_3+q'_3f'_1+q'_3f'_2)] \ . \end{aligned} \qquad (B.18)$$

E_{una} is a stiffness factor for the non-associated case and will always be positive during loading as proved for the associated case.

The three eigenvalues can be solved as

$$\lambda_1 = 0 \ ,$$

$$\lambda_2 = E/(1+\nu) \ ,$$

$$\lambda_3 = E_{una}(1+\nu)(f'_1q'_1+f'_2q'_2+f'_3q'_3) \ . \qquad (B.19)$$

It is no doubt that λ_2 is positive. λ_3 should be positive for the perfect case. This requires that $\{\frac{\partial F}{\partial \sigma}\}$ and $\{\frac{\partial Q}{\partial \sigma}\}$ make an acute angle.

The corresponding eigenvectors are

$$\begin{bmatrix} q'_1 \\ q'_2 \\ q'_3 \end{bmatrix} \qquad \begin{bmatrix} f'_2-f'_3 \\ f'_3-f'_1 \\ f'_1-f'_2 \end{bmatrix} \qquad \begin{bmatrix} f'_2(q'_1-q'_2)-f'_3(q'_3-q'_1) \\ f'_3(q'_2-q'_3)-f'_1(q'_1-q'_2) \\ f'_1(q'_3-q'_1)-f'_2(q'_2-q'_3) \end{bmatrix} \qquad \text{(B.20)}$$

for λ_1, λ_2 and λ_3 respectively. The normalization is also omitted here.

The first eigenvector $<\frac{\partial Q}{\partial \sigma}>$ for $\lambda_1=0$ may no longer be perpendicular to the other two (Fig. 2.4b), since the elastoplastic matrix is generally not symmetric. However, the other two eigenvectors together with the gradient of the yield surface constitute three orthogonal bases in the stress space.

B.3 Eigenvalue Study on Elastoplastic Model with Strain Softening

The study is carried out only in the two dimensional stress space. The focus is concentrated on the strain softening materials. For convenience, in eqn. 2.17 we define the perfect elastoplastic term k^{perf} as

$$k^{perf} = <\frac{\partial F}{\partial \sigma}>[C^E]\{\frac{\partial Q}{\partial \sigma}\} \ . \qquad \text{(B.21)}$$

The plastic hardening (or softening) parameter h^P may be expressed as the ratio of the hardening term to the perfect term, i.e.

$$h^P = -\frac{1}{k^{perf}} \langle \frac{\partial F}{\partial \epsilon^P} \rangle \{\frac{\partial Q}{\partial \sigma}\} \ , \qquad \text{(B.22)}$$

and hardening (or softening) parameter h is defined as

$$h = \frac{h^P}{1+h^P} \qquad \text{or} \qquad h^P = \frac{h}{1-h} \ . \qquad \text{(B.23)}$$

We rewrite the elastic matrix (eqn. 2.17) as

$$[C^{EP}] = [C^E] - \frac{(1-h)}{k^{perf}}[C^E]\{\frac{\partial Q}{\partial \sigma}\} \{\frac{\partial F}{\partial \sigma}\} [C^E] \ . \qquad \text{(B.24)}$$

In a two dimensional stress space, the form of the elastoplastic matrix including strain softening can be formulated from eqn. B.23 and B.24 with the result:

$$[C^{EP}] = E(1-\nu)/(1+\nu)(1-2\nu)\begin{bmatrix} 1 & \nu/(1-\nu) \\ \nu/(1-\nu) & 1 \end{bmatrix}$$

$$- 1/[k^{perf}(1+h^P)]\begin{bmatrix} ad & bd \\ ae & be \end{bmatrix} \qquad \text{(B.25a)}$$

in which, k^{perf} is the perfect elastoplastic term, h^P is the strength softening parameter, and

$$a = \frac{E}{(1+\nu)(1-2\nu)}[(1-\nu)f'_1+\nu f'_3] \ , \qquad \text{(B.25b)}$$

$$b = \frac{E}{(1+\nu)(1-2\nu)}[\nu f'_1+(1-\nu)f'_3] \ , \qquad \text{(B.25c)}$$

$$d = \frac{E}{(1+\nu)(1-2\nu)}[(1-\nu)q'_1+\nu q'_3] \ , \tag{B.25d}$$

$$e = \frac{E}{(1+\nu)(1-2\nu)}[\nu q'_1+(1-\nu)q'_3] \ , \tag{B.25e}$$

Let

$$k_0 = (1-\nu)(f'_1q'_1+f'_3q'_3) + \nu(f'_1q'_3+f'_3q'_1) \ . \tag{B.26}$$

We further define

$$E_h = \frac{E}{k_0(1+h^P)(1+\nu)(1-2\nu)} \ . \tag{B.27}$$

which is a stiffness factor for the strain softening case.

Now,

$$[C^{EP}] = E_h[C] = E_h\begin{bmatrix} C_{11} & C_{12} \\ C_{21} & C_{22} \end{bmatrix}$$

By actual calculations, we obtain,

$$[C] = \begin{bmatrix} (1-\nu)k_oh^P+(1-2\nu)f'_2q'_2 & \nu k_oh^P-(1-2\nu)f'_2q'_1 \\ \nu k_oh^P-(1-2\nu)f'_1q'_2 & (1-\nu)k_oh^P+(1-2\nu)f'_1q'_1 \end{bmatrix} \tag{B.28}$$

The equation for the eigenvalues of $[C^{EP}]$ can be derived as

$$\left(\frac{\lambda}{E_h}\right)^2 - (C_{11}+C_{22})\left(\frac{\lambda}{E_h}\right) + (C_{11}C_{22}-C_{12}C_{21}) = 0 \ . \tag{B.29}$$

It can be shown that if

$$\det[C^{EP}] = E_h^2(C_{11}C_{22} - C_{12}C_{21}) < 0 \ , \tag{B.30}$$

the above equation has two real roots and one is positive and the other is negative, the expressions of the two roots are

$$\lambda_1 = E_h\{\frac{C_{11}+C_{22}}{2} - [(\frac{C_{11}-C_{22}}{2})^2+C_{12}C_{21}]^{1/2}\} \ , \tag{B.31}$$

$$\lambda_2 = E_h\{\frac{C_{11}+C_{22}}{2} + [(\frac{C_{11}-C_{22}}{2})^2+C_{12}C_{21}]^{1/2}\} \ , \tag{B.32}$$

in which $\lambda_1<0$ and $\lambda_2>0$ and expressions of E_h, C_{11}, C_{22}, C_{12} and C_{21} can be found in eqn. B.27 to B.28.

If the determinant of $[C^{EP}]$ is greater than or equal to zero, the above expressions may include strain hardening, strain softening in two directions and perfect case. The specific conditions depend on many prameters. No further discussion is given.

By solving the equation for eigenvectors for λ_1 and λ_2, the normlized eigenvectors are

$$\overline{v}_1^{eig} = <\cos\beta \ \ \sin\beta>^T \ \text{ and } \ \overline{v}_2^{eig} = <\cos\gamma \ \ \sin\gamma>^T \ , \tag{B.33a}$$

respectively, in which

$$\tan\beta = \{(\frac{C_{22}-C_{11}}{2}) - [(\frac{C_{22}-C_{11}}{2})^2+C_{12}C_{21}]^{1/2}\}/C_{12} \ . \qquad (B.33b)$$

$$\tan\gamma = -C_{21}/\{(\frac{C_{22}-C_{11}}{2}) - [(\frac{C_{22}-C_{11}}{2})^2+C_{12}C_{21}]^{1/2}\} \ . \qquad (B.33c)$$

Both β and γ are measured from the positive direction of axis σ_1. Although the notations used above are convenient for the derivation, they are not convenient in plotting the weak direction. The convenient forms can be obtained by using the directional numbers of $\{\frac{\partial F}{\partial \sigma}\}$ and $\{\frac{\partial Q}{\partial \sigma}\}$. In the two dimensional stress space, we use

$$<\cos\beta_f \quad \sin\beta_f>^T \quad \text{and} \quad <\cos\beta_q \quad \sin\beta_q>^T \ ,$$

in which

$$\cos\beta_f = \frac{f'_1}{R_f}, \quad \sin\beta_f = \frac{f'_2}{R_f}, \text{ and } \quad R_f = [(f'_1)^2+(f'_2)^2] \ ,$$

$$\cos\beta_q = \frac{q'_1}{R_q}, \quad \sin\beta_q = \frac{q'_2}{R_q}, \text{ and } \quad R_q = [(q'_1)^2+(q'_2)^2] \ . \qquad (B.34)$$

Then, by using trigonomitric identities, we will obtain

$$\lambda_1 = \frac{(1-h)ER_fR_q}{k_{fq}(1+\nu)(1-2\nu)}\Big[\{(1-\nu)k_{fq}h^p + \frac{1}{2}(1-2\nu)\cos(\beta_f-\beta_q)\} -$$

$$\frac{1}{2}\{(1-2\nu)^2\cos^2(\beta_q-\beta_t)-4\nu k_{tq}h^P[(1-2\nu)\sin(\beta_q+\beta_t)-\nu k_{tq}h^P]\}^{1/2}\Big] \tag{B.35a}$$

$$\lambda_2 = \frac{(1-h)ER_tR_q}{k_{tq}(1+\nu)(1-2\nu)}\Big[\{(1-\nu)k_{tq}h^P + \frac{1}{2}(1-2\nu)\cos(\beta_t-\beta_q)\} + \frac{1}{2}\{(1-2\nu)^2\cos^2(\beta_q-\beta_t)-4\nu k_{tq}h^P[(1-2\nu)\sin(\beta_q+\beta_t)-\nu k_{tq}h^P]\}^{1/2}\Big] \tag{B.35b}$$

$$\overline{v}_1^{eig} = \langle\cos\beta \quad \sin\beta\rangle^T , \qquad \overline{v}_2^{eig} = \langle\cos\gamma \quad \sin\gamma\rangle^T , \tag{B.35c}$$

with

$$\tan\beta = \Big[\{(1-2\nu)\cos(\beta_t+\beta_q)\} - \{(1-2\nu)^2\cos^2(\beta_q-\beta_t)-4\nu k_{tq}h^P \times [(1-2\nu)\sin(\beta_q+\beta_t)-\nu k_{tq}h^P]\}^{1/2}\Big]/2\Big[\nu k_{tq}h^P-(1-2\nu)\sin\beta_t\cos\beta_q\Big] \tag{B.35d}$$

$$\tan\gamma = \Big[\{(1-2\nu)\cos(\beta_t+\beta_q)\} + \{(1-2\nu)^2\cos^2(\beta_q-\beta_t)-4\nu k_{tq}h^P \times [(1-2\nu)\sin(\beta_q+\beta_t)-\nu k_{tq}h^P]\}^{1/2}\Big]/2\Big[\nu k_{tq}h^P-(1-2\nu)\sin\beta_t\cos\beta_q\Big] \tag{B.35e}$$

in which

$$k_{tq} = (1-\nu)\cos(\beta_q-\beta_t) + \nu\sin(\beta_q+\beta_t) \ . \tag{B.35f}$$

Under the associated flow law, the above results for eigenvectors take much simpler forms due to the symmetry of matrix $[C^{EP}]$. With $\beta_t=\beta_q$, two eigenvectors become orthogonal and

$$\bar{v}_1^{eig} = \langle \cos\beta \quad \sin\beta \rangle^T \ , \tag{B.36a}$$

$$\bar{v}_2^{eig} = \langle -\sin\beta \quad \cos\beta \rangle^T \ , \tag{B.36b}$$

with

$$\tan(2\beta) = \tan(2\beta_t) - \frac{2h^P}{1-2\nu}\left[\frac{\nu(1-\nu)}{\cos(2\beta_t)} + \nu^2\tan(2\beta_t)\right] \ . \tag{B.36c}$$

Since $\lambda_1 \neq \lambda_2$, let

$$[T_v] = [\bar{v}_1^{eig} \quad \bar{v}_2^{eig}] \ , \tag{B.37a}$$

we have the transformation equation:

$$[T_v]^{-1}[C^{EP}][T_v] = [\lambda_i] \ , \tag{B.37b}$$

in which, $[\lambda_i]$ is a diagonal matrix with the eigenvalues λ_1 and λ_2 as the diagonal elements.

Now, let us discuss briefly how to illustrate the weak direction in plots. For convenience, the weak direction is defined by angle β in the σ_1-σ_3 space (Fig. B.1). β is the angle measured from the first principal stress σ_1 to the weak direction. To keep the generality, the generalized Mohr-coulomb criterion is illustrated in Fig. B.1. It takes the form of

$$F = q + mp - \kappa \ , \tag{B.38}$$

in which

$$q = \frac{1}{2}(\sigma_1-\sigma_3) \qquad \text{and} \qquad p = \frac{1}{2}(\sigma_1+\sigma_3) \ . \tag{B.39}$$

According to the incremental theory, m and κ are constants in an incremental loading step. By using the concept of the apparent friction angle ϕ_f and cohesion C_f as shown in the Mohr diagram (Fig. B.1), the image of ϕ_f can be obtained in the p-q space (marked as a_f) and in the σ_1-σ_3 space (marked as β_f). And, the image of weak direction in the σ_1-σ_3 space can also be obtained in the p-q space (marked as a) and in the Mohr diagram (marked as ϕ). The relationships among angle β, a and ϕ for the weak direction are

$$\tan a = \sin\phi \qquad \text{and} \qquad a = \beta + \frac{\pi}{4} \ . \tag{B.40}$$

The above relationships also apply to ϕ_f, a_f and β_f.

It should be pointed out that the Mohr circle diagram is not a plot of stress space. Mathematically, the images

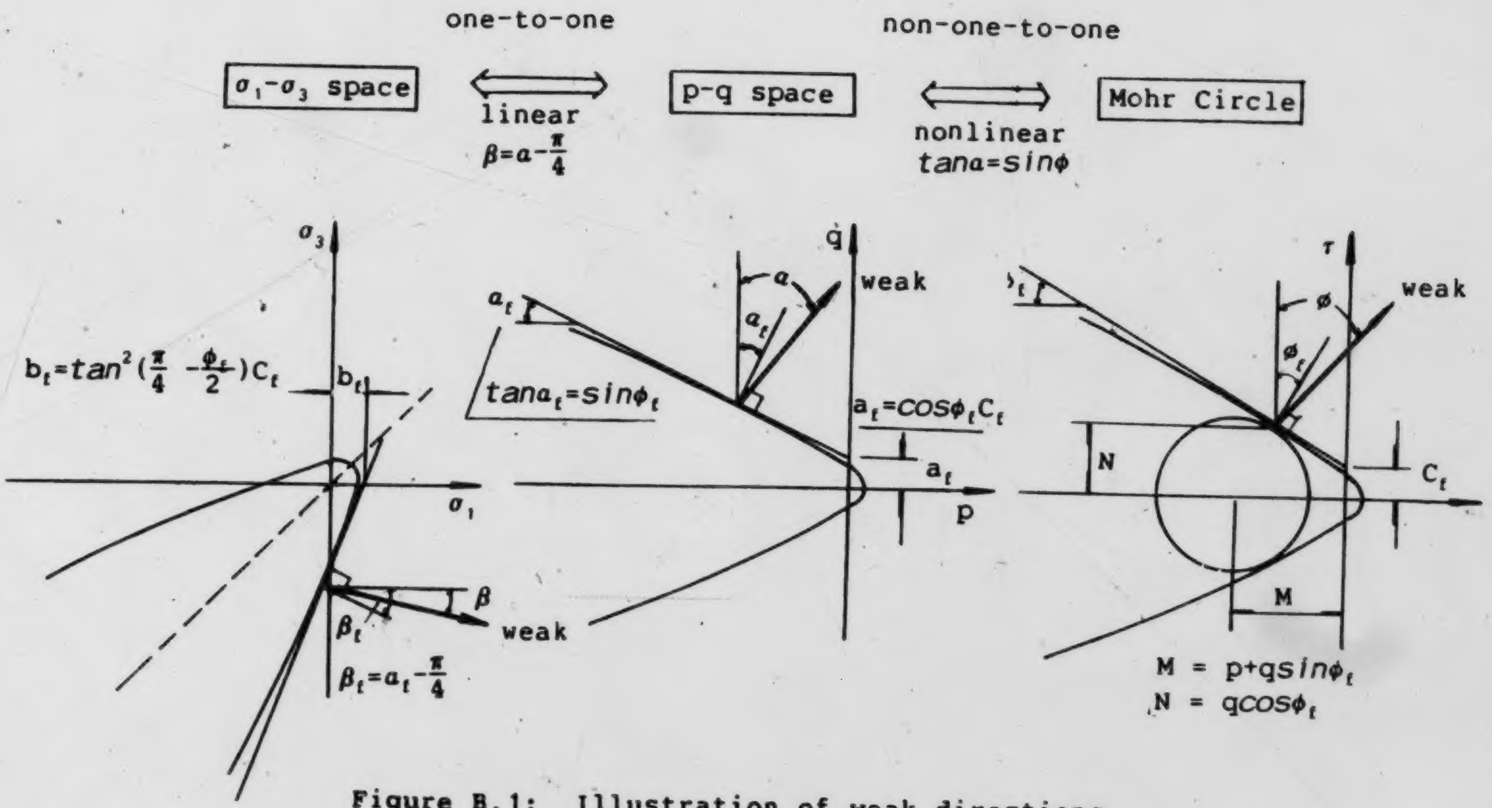
one-to-one
non-one-to-one
σ_1-σ_3 space
linear
$\beta = a - \frac{\pi}{4}$
p-q space
nonlinear
$\tan a = \sin\phi$
Mohr Circle
σ_3
$b_t = \tan^2(\frac{\pi}{4} - \frac{\phi_t}{2})C_t$
b_t
σ_1
β
β_t
weak
$\beta_t = a_t - \frac{\pi}{4}$
a_t
$\tan a_t = \sin\phi_t$
q
a
a_t
weak
$a_t = \cos\phi_t C_t$
a_t
p
τ
ϕ
ϕ_t
weak
N
C_t
M
$M = p + q\sin\phi_t$
$N = q\cos\phi_t$

Figure B.1: Illustration of weak directions

between the Mohr diagram and space σ_1-σ_3 are not one to one and the transformation is nonlinear. In soil machanics it is better to use p-q stress space. Between space σ_1-σ_3 and p-q, the images are one to one and the transformation is linear.

B.4 The Impact of Strain Softening on the Global Stiffness Matrix

Since the value of h may tend to +∞ due to very high softening rate, the eigenvalue λ may tends to -∞ (eqn. B.35). Its influence on the global stiffness matrix can be studied as follows. Substituting eqn. B.37b into eqn. 2.2, the general expression of the global stiffness matrix becomes

$$[K] = \sum_{e=1}^{ne} \int_{\Omega} B^T[T_\sigma][T_V]^{-1}[\lambda][T_V][T_\sigma]^T[B]\, d\Omega \ , \qquad (B.41)$$

in which $[T_\sigma]$ is the transformation matrix from the principal stress space to the stress space defined in the X-Y-Z system with other notations as mentioned before. When we use the Gaussian method to integrate the above equation, for the stiffness matrix $[K_{ij}]_e$ of each element,

$$(K_{ij})_e = \sum_{NG=1}^{NGP} W_{NG} d_{NG} [B_{ki}(T_\sigma)_{kl}(T_V^{-1})_{lm}\lambda_{mn}(T_V)_{no}(T_\sigma)_{op}B_{pj}] \ , \qquad (B.42)$$

in which, W_{NG} is the weighted factor of the related Gaussian points with a total number of NGP, d_{NG} is the three dimensional volume factor (or two dimensional area factor), the result inside the square bracket follows the law of summation by using dummy suffixes with each variable being the element of the corresponding matrix. Particularly, $\lambda_{mn}=0$, if $m\neq n$.

The above expression indicates that $(K_{ij})_e$ can be considered as a linear combination of the eigenvalues i.e.

$$(K_{ij})_e = \Sigma a_k \lambda_k \;, \tag{B.43}$$

in which the summation is with respect to the eigenvalues (λ_k) of all the related Gaussian points, and a_k is a finite number if the shape of each element is properly designed. With the related node displacements as prescribed boundary conditions, the stiffness matrix for each node can be studied by eigenvalue analyses in checking an obtained solution. If there is no minus contribution from any related Gaussian point, the stiffness matrix of this node is positive definite. Otherwise, by using coordinate transformation, we can find the stiffness along any direction, since we already know the displacement solutions. We still call this stiffness as K_{ii} for simplicity. In assembling the global stiffness matrix, the minus and positive contributions will make K_{ii} take the form

$$K_{ii} = (K_1)_{ii} + (K_2)_{ii} \quad (-\infty < K_1 \leq 0, \quad 0 \leq K_2 < +\infty) \;. \tag{B.44}$$

Here, we divide the stiffness contribution into two parts for the convenience of the further study. $(K_1)_{ii}$ is negative taking zero as its limit, and $(K_2)_{ii}$ is positive also taking zero as its limit. If the negative part prevails, then K_{ii} will become negative. Here we only want to point out that

1. No matter how weak the softening process is, the global stiffness matrix may not remain positive definite, since softening may exist at an isolated corner without other support or with regional softening or cracking developing around the degree of freedom concerned.
2. The positive definite nature of the global stiffness matrix may be destoryed even if the strain softening exists only at one Gaussian point, since the range of the negative eigenvalue can be between 0 and $-\infty$.

Therefore, an indefinite stiffness matrix may be encountered when strain softening is considered in the calculation.

C. APPENDIX - SOLUTION OF THE ELASTICALLY CONNECTED COULOMB DAMPING MODEL

When the system is transformed into a series of independent degrees of freedom, under the action of generalized forces defined by prescribed displacement boundary conditions, each equation is the same in mathematical form. For convenience, subscripts $_{ii}$ or $_{i}$ and superscript ^{g} for each degree of freedom (Fig. 2.5) are omitted, and subscripts $_{1}$ or $_{2}$ are used to indicate the damping and elastic elements. The basic equation is

$$\Delta T = K\Delta u = (K_1+K_2)\Delta u \ . \tag{C.1}$$

For positive stiffness contribution, $K_2>0$ with unloading elastic stiffness k_2, and if $K_2=0$, no positive contribution exists (Fig. 2.6); for minus contribution, $K_1<0$ with unloading elastic stiffness k_1. We only study the case with minus contribution. Before we give further discussion, it should be mentioned that what we are doing is to check an obtained solution. Therefore, all the expressions below can be presented. For example, in trying loading directions by using elastic models, we can obtain the elastic incremental displacement Δu^E. After convergence, we have the total incremental displacement Δu and so we can have the incremental plastic displacement Δu^P at each degree of freedom. By using the principle of virtual work, we can have the nodal force increments ΔT, ΔT^E and ΔT^P from $\Delta\sigma$, $\Delta\sigma^E$ and $\Delta\sigma^P$. The yield function for the damping element is assumed to be

$$F_1 = T_1 - [T_1^{peak}+h_1^P k_1 u_1^P] \qquad (u_1 < u_1^{res}) \ . \qquad (C.2a)$$

T_1^{peak} is the nodel force at which strain softening just begins at one or more related Gaussian integration points.

The global stiffness matrix can be assumed as constant and it is independent of the past strain-stress history but depends only on the present strain-stress state and loading directions. Therefore, the above model is a general model in the incremental sense, no matter how complex the material models are or the loading history has been. We use $(T_0)_1$ to replace T_1^{peak} in all the figures and formulations in order to maintain the generality. Here, $(T_0)_1$ reflects the stress state at the end of last incremental step.

We use linear assumption in one incremental step. If the displacement exceeds a residual value u_1^{res},

$$F_1 = T_1 - T_1^{res} \qquad (u_1 \geq u_1^{res}) \ . \qquad (C.2b)$$

This residual state is assumed under the linear softening assumption. However, the obtained implications can be extended to nonlinear cases as discussed in Section 2.3.4. In eqn. C.2a, u_1^P is assumed to be the plastic deformation and represented by the relative movement between the piston and shell (Fig. 2.5), h^p is a minus eqivalent softening factor, and k_1 is used to keep the dimension consistent.

Let,

$$h_1 = \frac{h^p}{1+h_1^p} \qquad (-\infty < h_1 < 0 \text{ and } -1 < h^p < 0) \ . \tag{C.3}$$

The above range is determined by a parametric study (Fig. C.1). Beyond this range, the model either behaves like a strength hardening one or the yield surface will contract in the strain space. From the general equation 2.17, it can be obtained that

$$K_1 = h_1 k_1 \qquad (F = 0,\ u_1 < u_1^{res}) \ , \tag{C.4a}$$

$$K_1 = 0 \qquad (F = 0,\ u_1 \geq u_1^{res}) \ . \tag{C.4b}$$

All the possible values of K_1 and K_2 will studied to keep completeness. As shown in Fig. 2.7, there exists a critical minus stiffness $(K_1)_{cr}=-K_2$ or a critical softening parameter $(h_1)_{cr}=-K_2/k_1$, which corresponds with a zero stiffness of this two element system.

If K<0, under stable displacement boundary conditions, ΔT will in unloading direction opposite to that indicated in the Fig. 2.5, but Δu will be in compliance with $(T_1)_0$ so that the solution is permissible. However, it is can be judged only after we have obtained the solution. Therefore,

Yield Function:

$F = \tau - (\tau^{peak} + h^{P}G\gamma^{P})$

Constitutive relationship:

$\tau = G\gamma \qquad (F < 0)$

$[C^{EP}] = \frac{h^{P}}{1+h^{P}} G = hG \qquad (F=0)$

Strength:

$[\tau] = \tau^{peak} + h^{P}G\gamma^{P}$

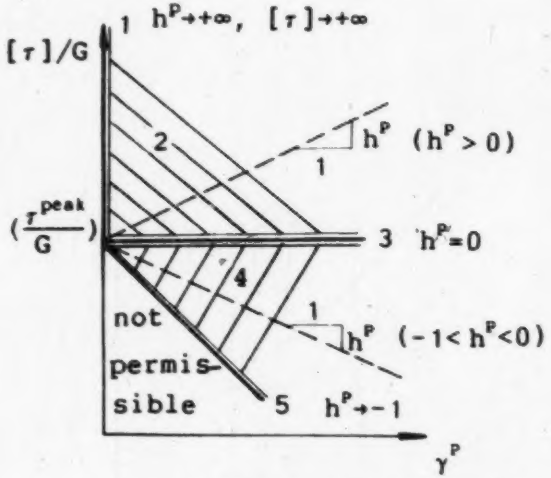
1 $h^{P} \to +\infty$, $[\tau] \to +\infty$
$[\tau]/G$
2
1
h^{P} $(h^{P} > 0)$
$(\frac{\tau^{peak}}{G})$
3 $h^{P}=0$
4
1
h^{P} $(-1 < h^{P} < 0)$
not permissible
5 $h^{P} \to -1$
γ^{P}

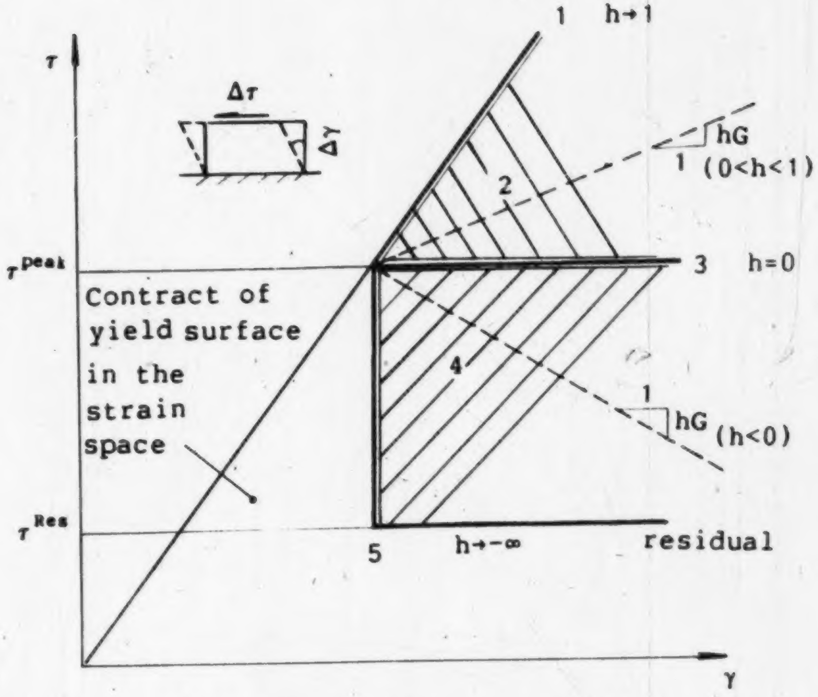
τ
$\Delta\tau$
$\Delta\gamma$
1 $h \to 1$
2
1
hG
(0<h<1)
τ^{peak}
3 h=0
Contract of yield surface in the strain space
4
1
hG
(h<0)
τ^{Res}
5
$h \to -\infty$
residual
γ

1.elastic 2.hardening 3.perfect 4.softening 5.extremely brittle

Figure C.1: One dimensional strain softening or hardening

a full study on solution behavior is necessary.

Here, we only consider the case of ΔT in the direction of $(T_1)_0$. The complete displacement solutions are listed in Table C.1. It shows that the consitency condition will always be satisfied, even if $K_1+K_2<0$. The stable solution is shown in Fig. 2.6.

Table C.1 Complete solution of displacements

$\Delta u=\Delta T/(K_1+K_2)$

	Total displacement	Elastic displacement	Plastic displacement	Consistent condition
System	Δu	$h_1\Delta u$	$(1-h_1)\Delta u$	$\Delta u=\Delta u^E+\Delta u^P$
EL.1	Δu	$h_1\Delta u$	$(1-h_1)\Delta u$	$\Delta u_1=\Delta u_1^E+\Delta u_1^P$
EL.2	Δu	Δu	0	$\Delta u_2=\Delta u_2^E+\Delta u_2^P$
Consistent condition of the system				$\Delta u=\Delta u_1=\Delta u_2$

The complete solutions of incremental nodal forces are listed in Table C.2. The equilibrium conditions are also satisfied even if $K_1+K_2<0$.

If we check the energy conservation of element 1, it is also kept in the mathematical form, because

$$\Delta W_1^{ext} = (T_1)_0\Delta u + \frac{1}{2}(\Delta T_1)(\Delta u) \quad \text{(extenal work)} ,$$

(C.5a)

$$\Delta W^P = (T_1)_0\Delta u^P + \frac{1}{2}(\Delta T_1)(\Delta u^P) \quad \text{(plastic work)} ,$$

(C.5b)

$$\Delta E^{E} = (T_1)_0 \Delta u^{E} + \frac{1}{2}(\Delta T_1)(\Delta u^{E}) \quad \text{(elastic energy increment)} \ . \tag{C.5c}$$

Table C.2 Complete solution of nodal forces

$\Delta u = \Delta T/(K_1+K_2)$

	Total Force	Elastic Force	Plastic Force	Yield condition	Consistency condition
System	$\Delta T=$ $(K_1+K_2)\Delta u$	$\Delta T^E=$ $(k_1+K_2)\Delta u$	$\Delta T^P=$ $(k_1-K_1)\Delta u$		$\Delta T=\Delta T^E-\Delta T^P$
EL.1	$\Delta T_1=$ $K_1\Delta u$	$\Delta T_1^E=$ $k_1\Delta u$	$\Delta T_1^P=$ $(k_1-K_1)\Delta u$	$\Delta F_1=0$	$\Delta T_1=\Delta T_1^E-\Delta T_1^P$
EL.2	$\Delta T_2=$ $K_2\Delta u$	$\Delta T_2^E=$ $k_2\Delta u$	$\Delta T_2^P=$ 0		$\Delta T_2=\Delta T_2^E-\Delta T_2^P$
Equilibrium condition of the system					$\Delta T=\Delta T_1+\Delta T_2$

Note: Only element 1 yields. $\Delta F=\Delta T_1-k_1 h^P \Delta u^P$

But, if we check the sign of the above three terms, we will find that for $K=K_1+K_2<0$, every thing is wrong. Due to the impermissible direction of Δu, the plastic work (eqn. C.5b and Fig. 2.8) is negative. Besides, the strength also increases due to the increase of elastic deformation.

Since $<\frac{\partial F}{\partial \sigma}>^T$ in the loading criteria (eqn. 2.13 to 2.15) now is equivalent to $\frac{\partial F}{\partial T_1}$ with the value 1, $l_1=\Delta T$, $l_2=\Delta T^E$ and $l_3=\Delta T^P$. It is easy to check out that all the loading criteria are violated. The solution behavior under further loading of external forces is listed in Table C.3.

Table C.3 Solution behavior

K_1+K_2	h_1	Δu	Plastic work	Loading criteria	$\delta^2(\Pi)$	Strength
>0	$h^+_{cr}<h_1<0$	>0	>0	Kept	>0	decrease
0^+	h^+_{cr}	$+\infty$	>0	Kept	0^+	decrease
$^-0$	h^-_{cr}	$-\infty$	<0	Violated	$^-0$	increase
<0	$-\infty<h_1<h^-_{cr}$	<0	<0	Violated	<0	increase

Note: Superscripts + and - denote the direction of a limit value.

The above table provides the criteria for us to judge the solution behaviors.

A further understanding of unstable softening needs studying this system in dynamics. We use equivalent gravitational forces to replace the node forces, i.e.

$$M = T_0/g \qquad \text{and} \qquad \Delta M = \Delta T/g \ , \qquad\qquad (C.6)$$

in which g is the gravitational accelaration.

Set the initial position of the movement at $u=u_0$, then the dynamic equation in the force equilibrium form becomes

$$(M+\Delta M)\Delta\ddot{u} = (M+\Delta M)g - T_1 - T_2 \ ,$$

in which,

$$T_1 = (T_0)_1 + h^P k_1 \Delta u^P \quad \text{and} \quad T_2 = K_2 \Delta u \ .$$

By using $T_1 = (T_0) + K_1 \Delta u$,

$$\Delta \ddot{u} = \frac{\Delta M}{(M+\Delta M)} g - \frac{K_1+K_2}{(M+\Delta M)} \Delta u$$

Let

$$a = \frac{\Delta M}{(M+\Delta M)} g \ . \tag{C.7}$$

The physical meaning of a is the accelaration of the mass $(M+\Delta M)$ under the weight ΔT. Note that $a>0$ in this case.

Let

$$P^2 = \left| \frac{K_1+K_2}{(M+\Delta M)} \right| \ . \tag{C.8}$$

The dynamic equation will fall into three types according to the value of K_1+K_2, ie

$$\Delta \ddot{u} = a - P^2 \Delta u \qquad (K_1+K_2 > 0) \ , \tag{C.9a}$$

$$\Delta \ddot{u} = a \qquad (K_1+K_2 = 0) \ , \tag{C.9b}$$

$$\Delta \ddot{u} = a + P^2 \Delta u \qquad (K_1+K_2 < 0) \ . \tag{C.9c}$$

All of the above equations have the same initial conditions: $t=0$, $\Delta u=0$ and $t=0$, $\Delta\dot{u}=0$. The first equation belongs to the stable pseudo-harmonic type, while the other two are not.

Note that the discontinuity between $^{-}0$ and 0^{+} vanishes here, because both eqn. C.9a and C.9c take eqn. C.9b as the limit. The above equations are of the Coulomb damping type. A complete solution of these simple equations is far more complicated than those of the viscous damping type even with constant Coulomb forces (Den Hartog, 1931). However, only the first response and final equilibrium position are necessary for us to interpret the unstable softening process.

The solutions of the first response are listed in Table C.4. In Fig. 2.9, the dynamic strain-stress paths are also given for unstable softening. From the above table, we can clearly see that a stable solution can be obtaned if and only if $K>0$ and the final equilibrium position is same as predicted in statics. Note that we are only taking the response under the action of external force in the further softening direction. If $K\leq 0$, the infinite displacement in the same direction of ΔT indicates that a local collapse will occur. By neglecting the inertial term, Δu will be obtained in the wrong direction, which is impermissible in statics. The above concepts are closely related to the concept of a quasi-static process (see Appendix E in detail).

Table C.4 **The first dynamic response of Coulomb damping model**

$t=0$, $\Delta u=0$ and $t=0$, $\Delta\dot{u}=0$

	Displacement	Velocity	Acceleration	
$x=\Delta u$	x	dx/dt	d^2x/d^2t	$t\to+\infty$
$K>0$	$a[1-\cos(pt)]/p^2$	$a\sin(pt)/p$	$a\cos(pt)$	$\Delta u=\Delta T/K$
$K=0$	$1/2(at^2)$	$a\,t$	a	$\Delta u\to+\infty$
$K<0$	$a[ch(pt)-1]/p^2$	$a\,sh(pt)/p$	$a\,ch(pt)$	$\Delta u\to+\infty$

$ch(pt)=1/2(e^{pt}+e^{-pt})$ and $sh(pt)=(1/2)(e^{pt}-e^{-pt})$

Certainly, after the first response, displacements cannot increase unlimitedly. In our simple linear model, the dynamic equation will change its type until and only until the strength is lowered down to the residual with $K_1=0$ and $K=K_2>0$. Then, the motion is governed by the stable dynamic equation C.9a until the final equilibrium position is reached due to damping (Fig. 2.9).

D. APPENDIX - APPLICATION OF BRITTLE MODELS TO UNSTABLE SOFTENING

As explained in the section 2.3.3, brittle models can be used to obtain meaningful results in unstable equilibrium analyses when local collapses occur inside the structure. In order to put the idea into practice, we shoud

1. use the loading criteria to judge local unstable softening;
2. choose appropriate solution methods to eliminate the possible effects of singularity of the global equilibrium equation;
3. formulate the procedure for the application of brittle models;
4. judge whether the results are on the safe side or not.

In practice, the loading criteria for permissible solution (Table 2.1) should be set up in the program with respect to each Gaussian point.

Since all the unfavorable effects may caused by the minus stiffness contribution, the Gaussian elimination method by using primary elements is most suitable to transform the global stiffness matrix into an upper trianglar matrix. Unfortunately, most of computer programms do not adopt the above solution procedure for the sake of ecomomy. Nevertheless, by experience, the Gaussian elimination method by using diagonal elements can generally yield a complete solution for further judgement, but the accuracy may be worse than that by using primary elements. To avoid singularity, the following techniques are suggested

1. do not use any zero modulus in cracking models, but use a very small postive number (say, 10^{-4} to 10^{-6} times elastic modulus)
2. if zero diagonal element is detected during elimination, assign a very small positive number to it. In this case, we can not tell 0^{+} from 0^{-} if softening is present. It can be determined in the next iteration or incremental step.

After using bittle models, unstable solutions may vanish, but may not due to collapses or further softening at other Guass points. If we want to get a solution as accurate as possible, we have no other choice but to try again and again until the solution is stable.

Provided that the structure could be considered near failure, we might use brittle models to all the related Guassian points round the abnormal degree of freedom. If the structure does fail, the solution is acceptable, since the displacement values during failure are of less importance, but we obtain a reasonable displacement field to study the failure mechanism. If the structure does not fail, trials should be made. Obviously, this technique needs experience.

The stiffness contribution (K_1 and K_2) may change during the local collapse. If all those changes are incorporated into iterations, we are, in fact, seeking an equivalent secant stiffness for the system. By experience, it is easy to deal with linear relationship, including constant E and ν, linear yield or potential function with respect to principal stress, linear softening (or hardening) rate. But it is very difficult to deal with nonlinear relationships. Limited by the computation budget, it is often impractical to seek the exact equilibrium position when all the nonlinear relationships are included. It is suggested that E and ν and softening (hardening) rates not be modified in one incremental step. Therefore, errors will be caused.

Although a strict theoretical error analysis is too profound to present in this thesis, Fig. D.1 provides the basic concepts for us to judge whether the results obtained from brittle models are on the safe side or not for a bar system. More general situations may be imagined concerning the possible deviation of a solution in light of Fig. D.1 as follows.

1. By using constant elastic parameters E and ν, the dislpacement solution may be on the safe side if E increases with external loads and ν increase as yield functions tends to zero. Otherwise the results may be on the unsafe side.
2. The deformation modulus of a strain hardening material will be decreased after yield. Therefore, without changing hardening rates, the results may be on the unsafe side.
3. By using a brittle model to replace a strain

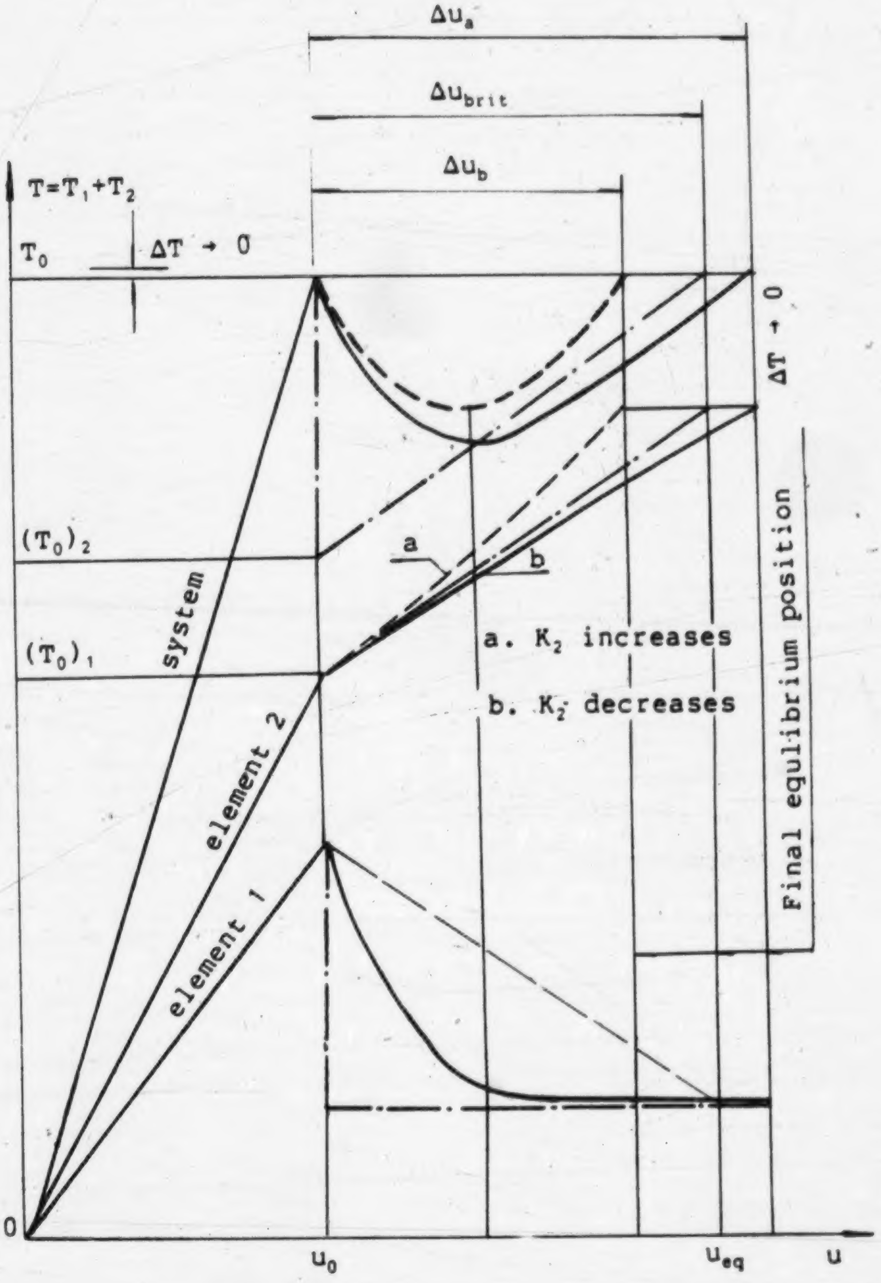

Δu_a
Δu_{brit}
Δu_b
$T=T_1+T_2$
T_0
$\Delta T \to 0$
$(T_0)_2$
$(T_0)_1$
a
b
a. K_2 increases
b. K_2 decreases
system
element 2
element 1
$\Delta T \to 0$
Final equlibrium position
0
u_0
u_{eq}
u

Figure D.1: Possible errors in using brittle models

softening model with hyperbolic softening rates, the results will always be on the safe side, because the residual strength can never be reached in such models.

In short, an error analysis may be needed, at least, by a parametric study. The steps to use brittle models are listed as follows

1. Techniques to treat singular and ill-conditioned global equilibrium equations should be used to quarantee a complete mathematical solution.
2. Use the loading criteria to make sure that the solution is permissible at each Gaussian point. If the solution is normal, do next incremental step. Otherwise,
3. check the correctness of the selected models and the range of material parameters as well as the singularities in mesh design. In design stage, check the design. If something needs revising, redo the analysis after revision. If nothing needs modifying, then,
4. use corresponding brittle models to replace softening models at all the Gaussian points where abnormal solutions have been found.
5. Repeat the calculation until the solutions at all Gaussian points are normal, then do next step.
6. Follow the above procedure step by step until the solution becomes divergent or unacceptable in view

of the structure safety or the most unfavorable loads have been applied to their maximum values.

The above steps are illustrated in a flow chart (Fig. D.2).

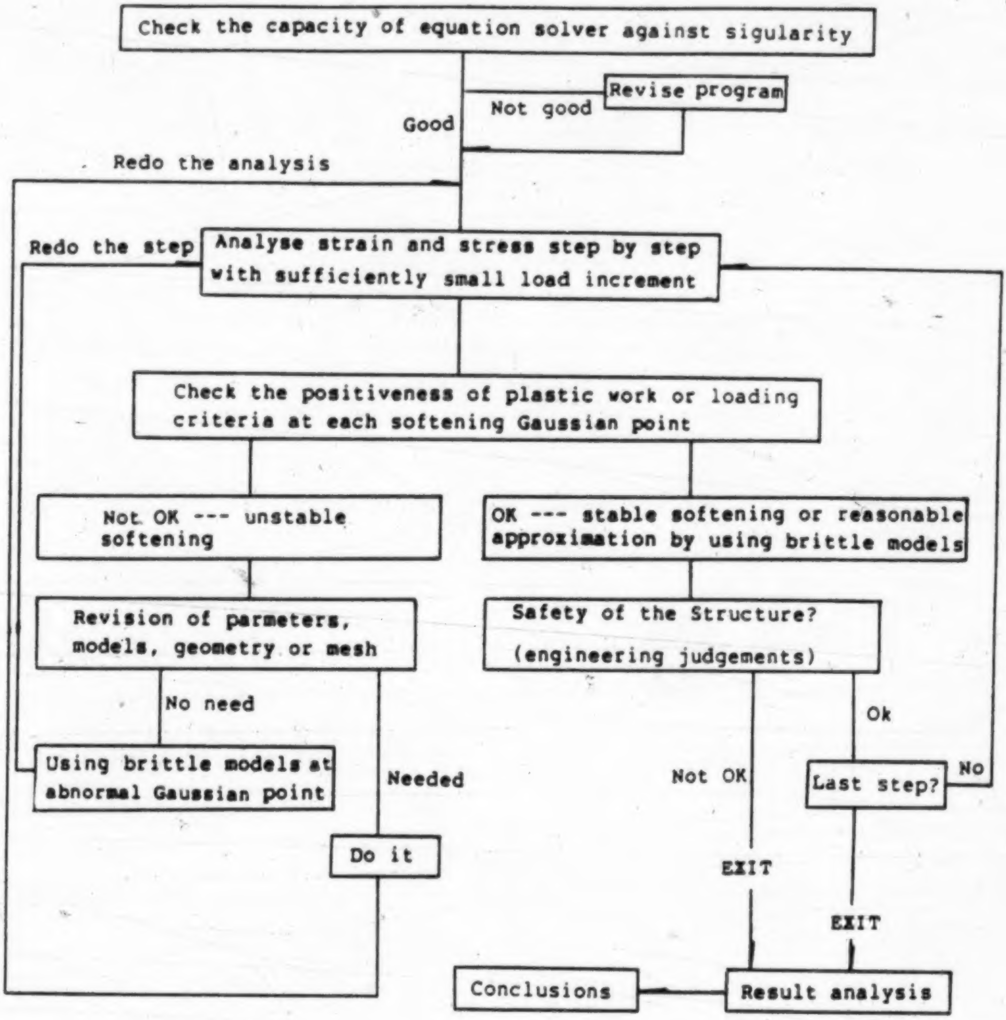
Check the capacity of equation solver against sigularity
Good
Not good
Revise program
Redo the analysis
Redo the step
Analyse strain and stress step by step with sufficiently small load increment
Check the positiveness of plastic work or loading criteria at each softening Gaussian point
Not OK --- unstable softening
OK --- stable softening or reasonable approximation by using brittle models
Revision of parmeters, models, geometry or mesh
Safety of the Structure? (engineering judgements)
No need
Using brittle models at abnormal Gaussian point
Needed
Do it
Not OK
Ok
Last step?
No
EXIT
EXIT
Conclusions
Result analysis

Figure D.2: Programming flow chart for unstable strain softening

E. APPENDIX - INCREMENTAL THEORIES CONCERNING MATERIAL STABILITY

In light of the study on the solution bevavior of finite element analyses, the general incremental theory concerning strain softening is reviewed and studied to deepen our understanding.

E.1 Basic Assumptions

First, let us review the proof of the existence of the minimum potential energy and uniqueness of the solution in the incremental theory. We should specially mention one assumption and one condition behind the complex derivation and deduction.

The assumption of linear stress strain path enables linearization in nonlinear finite element analyses. It provides an arbitrarily small distance along the strain-stress path in each incremental step. The assumption of an arbitrarily small distance can be made if and only if the response can be simplified as a quasi-static process. Otherwise, all the developed theories on the potential energy or uniqueness of solution are not applicable. Dynamic theories are needed to describe such a process until the object becomes stable at the new equilibrium position.

This assumption also is a sufficient condition for the existence of the minimum potential energy for Drucker's stable materials. The stable condition of a material may be expressed as an inequality derived from Drucker's postulate in the form:

$$\int_{(1)}^{(2)}(\sigma_{ij} - \sigma_{ij}^{(1)})d\epsilon_{ij} \geq 0 \ . \tag{E.1}$$

This inequality (Martin,1975) implies that, along any strain-stress path from state(1) to state(2), the above integration is non-negative. The equal sign may spoil the uniqueness of displacements if the travelled distance along the path is not zero. However, the solution is, at least, defined in certain solution subspaces. We will not repeat this note when we mention the uniqueness of solution. In the incremental theory, the distance between the two integration limits should be an arbitrarily small quantity. In the first order approximation, we have

$$\int_{(1)}^{(2)}(\sigma_{ij} -\sigma_{ij}^{(1)})d\epsilon_{ij} = \frac{1}{2}<\Delta\sigma_{ij}>\{\Delta\epsilon_{ij}\} \ . \tag{E.2}$$

Under the assumption of linear paths, it is an exact expression. Therefore, Martin's condition is equivalent to that in terms of perturbation energy.

It is easy to prove that Drucker's postulate or Martin's inequality is both necessary and sufficient condition for a stable solution, if any kind of incremental loads are allowed to act on the body under consideration. Its sufficiency is well known, and it must be necessary, otherwise, we can always apply a certain form of incremental loads on the unstable material to destory the quasi-static state.

The behavior of strain softening materials violates Martin's inequality. But, we may have true solution in the arbitrarily close vicinity of the original equilibrium position. This arouses our interest to seek narrower sufficient condition, or further, the necessary and sufficient condition for true incremental solutions.

E.2 Quasi-static State

In order to raise a narrower condition, let us consider the condition that the process can be assumed as quasi-static. As mentioned before, at least, it is a necessary condition. In a purely mechanical system, it means that a new equilibrium position should be gradually reached within an arbitrarily small distance along the strain-stress path for any point of the body, if external incremental loads are arbitrarily small and applied or released so slowly that time effect can be negelected. Therefore, physically, it is easy to understand that it is also sufficient for a normal solution.

Take the observed data in construction of an earth dam as an example. If the dam remains stable, a quasi-static process is indicated by a displacement-height curve without minus stiffness and no local collapse found from sudden increases of observed displacements in any portion of the dam, although local strain softening of materials may takes place here and there. Certainly, a stable solution can be obtained for such a quasi-static process.

Another example is a sample test for a strain softening material. A quasi-static state is indicated by the stable increase of the controlled boundary displacements, which corresponds with an extremely slow release of the external load. With stable incremental displacements as boundary condition, a true solution can also be obtained.

Although the quasi-static condition is both necessary and sufficient, but it is too general and too conceptual in use. To be more specific, this concept is closely related with the basic dynamic equations. For a point in the body, the incremental equilibrium equation in direction i takes the form:

$$\Delta\sigma_{ji,j} + \Delta F_i = \rho\frac{\partial^2\Delta u_i}{\partial T^2} , \tag{E.3}$$

where tensor expressions are used. The comma in subscripts means the partial derivative with respect to the direction indicated by the subscript following it. T is for real time, ρ is the density and ΔF_i is the incremental body force.

When displacement increments are taken as unknown, the above equation becomes

$$\frac{1}{2}C_{jikl}(\Delta u_{k,lj}+\Delta u_{l,kj}) + \Delta F_i = \rho\frac{\partial^2\Delta u_i}{\partial T^2} , \tag{E.4}$$

in which C_{jikl} is the constitutive tensor and ΔF_i should be arbitrarily small in the incremental theory. From the dynamic theory, we know that the above equation can be transformed into independent equations in the eigenvector directions of C_{jikl}. With all the eigenvalues being positive, the solution can be expressed in a harmonic (if $C_{jikl}$is elastic) or pseudo-harmonic type (if C_{jikl} is for hardening), and the amplitude will be arbitrarily small if the incremental force is arbitrarily small. Therefore, a quasi-static condition can be assumed. If the C_{jikl} is half positive definite, the solution will be finite even infinite in the direction corresponding to the zero eigenvalue.

When strain softening has developed in a certain region of a body, under further loading, C_{jikl} is indefinite with minus eigenvalues, the basic motion corresponding to a minus eigenvalue is in the form of hyperbolic cosine functions; i.e.

$$\Delta u_i = [A(\frac{e^{-PT}+e^{PT}}{2}) + B]_i \; . \tag{E.5}$$

in which P are real number defined by C_{jikl} and density ρ, A and B is defined by initial conditions. No solution in the incremental sense can be obtained. But, damping forces will change the governing equation into stable types at last.

When displacement increments are known, the quasi-static state can be assumed at a point if and only if the forced motion is harmonic or pseudo-harmonic. This requires that the whole structure can be assumed to be quasi-static.

In statics, generally, we cannot determine the unstable softening before the calculation, but we always neglect the dynamic term. This is the reason why we may obtain absurd solutions for strain softening materials.

E.3 The Loading Criteria

From now on, where it is convenient we use conventional expressions in terms of velocity, e.g.
$u_i = u_i^t + \dot{u}dt$, $du = \dot{u}dt$ and so on with $dt > 0$, and we suppose that $dt = 1$. Here, t is not for real time, but for the convenience of derivation.

Now let us check the physical meaning of the loading criteria in terms of energy expressions. For any part of the body, when the incremental external loads extremely slowly applied or released, the work ΔW^{ext} done by external loads is equal to the amount of increase of the elastic energy ΔE^E plus the plastic work ΔW^P which is always positive in consuming the energy. i.e.

$$\Delta W^{ext} = \Delta E^E + \Delta W^P \ . \tag{E.6}$$

Suppose a body is at the equilibrium state(0), then goes to state(1) in the next incremental step,

$$\Delta W^{ext} = \int_\Omega \int_{(0)}^{(1)} F_i d\dot{u}_i dv + \int_{ST} \int_{(0)}^{(1)} T_i d\dot{u}_i ds \ , \tag{E.7}$$

in which, F_i is body forces and T_i is surface loads, and we omit the term for prescribed displacements since it can be incorporated into the term for surface loads. The first order approximation of ΔW^{ext} is

$$\Delta W^{ext} = \int_{\Omega} (F_i \dot{u}_i + \frac{1}{2}\dot{F}_i \dot{u}_i) dV + \int_{ST} (T_i \dot{u}_i + \frac{1}{2}\dot{T}_i \dot{u}_i) ds \ . \qquad (E.8)$$

By using the principle of virtual work, we have

$$\Delta W^{ext} = \int_{\Omega} (\sigma_{ij}\dot{\epsilon}_{ij} + \frac{1}{2}\dot{\sigma}_{ij}\dot{\epsilon}_{ij}) d\Omega \ . \qquad (E.9a)$$

The first order approximation of the elastic energy increment is

$$\Delta E^{E} = \int_{\Omega} (\sigma_{ij}\dot{\epsilon}^{E}_{ij} + \frac{1}{2}\dot{\sigma}_{ij}\dot{\epsilon}^{E}_{ij}) d\Omega \ . \qquad (E.9b)$$

The first order approximation of the plastic work is

$$\Delta W^{P} = \int_{\Omega} (\sigma_{ij}\dot{\epsilon}^{P}_{ij} + \frac{1}{2}\dot{\sigma}_{ij}\dot{\epsilon}^{P}_{ij}) d\Omega \ . \qquad (E.9c)$$

With the assumed linear relationship, the above equations give the exact values. It is easy to see that the energy conservation will always be kept in the mathematical form.

If we review the concepts of loading criteria (Table 2.1 and eqn. 2.13 to 2.15) and compare with the above energy expressions. In Fig. E.1, we can find that the sign of ΔW^{ext}, is defined by $l_1=<\frac{\partial F}{\partial \sigma}>\{d\sigma\}$, since the contribution of terms such as $\dot{\sigma}_{ij}\dot{\epsilon}_{ij}$ can be neglected in determining signs. Image

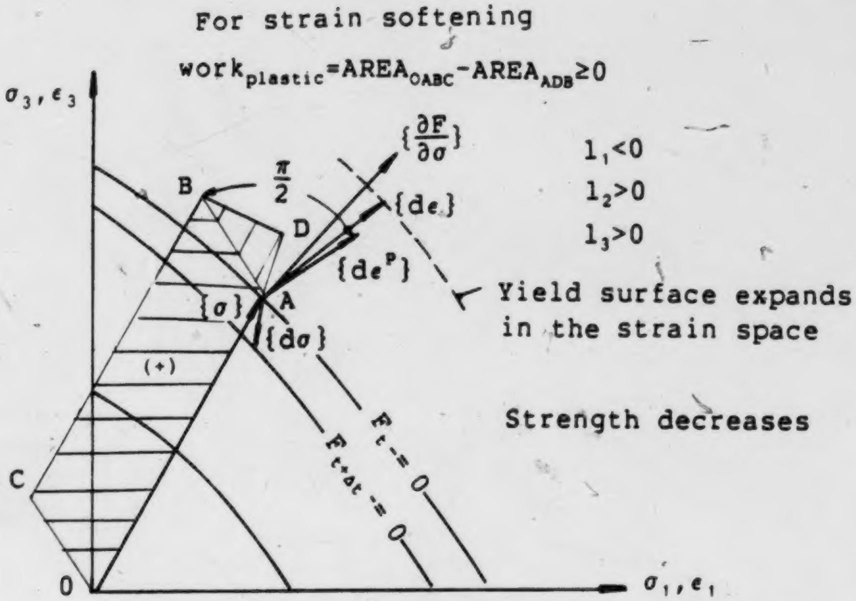
For strain softening
$work_{plastic} = AREA_{OABC} - AREA_{ADB} \geq 0$
σ_3, ϵ_3
$\{\frac{\partial F}{\partial \sigma}\}$
$l_1<0$
$l_2>0$
$l_3>0$
B
$\frac{\pi}{2}$
D
$\{d\epsilon\}$
$\{d\epsilon^p\}$
$\{\sigma\}$
A
$\{d\sigma\}$
Yield surface expands in the strain space
(+)
Strength decreases
$F_t = 0$
$F_{t+\Delta t} = 0$
C
0
σ_1, ϵ_1

a. Permissible incremental strain and stress

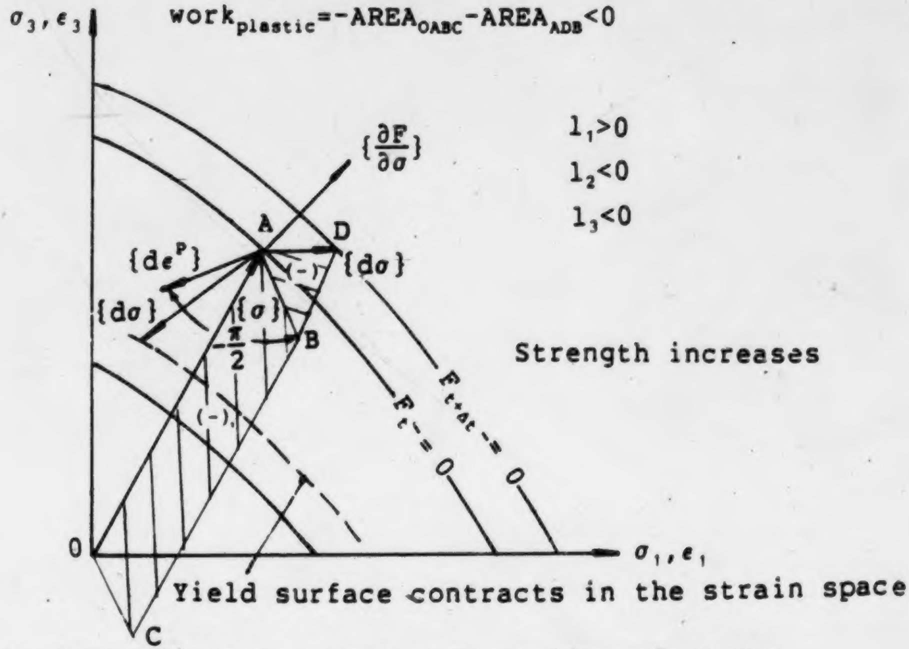
σ_3, ϵ_3
$work_{plastic} = -AREA_{OABC} - AREA_{ADB} < 0$
$\{\frac{\partial F}{\partial \sigma}\}$
$l_1>0$
$l_2<0$
$l_3<0$
A
D
$\{d\epsilon^p\}$
(-)
$\{d\sigma\}$
$\{d\sigma\}$
$\{\sigma\}$
$\frac{\pi}{2}$
B
Strength increases
(-)
$F_{t+\Delta t} = 0$
$F_t = 0$
0
σ_1, ϵ_1
Yield surface contracts in the strain space
C

b. Impermissible incremental strain and stress

Figure E.1: Criteria for permissible solutions

that the yield surface is also expressed in the strain surface (Fig. E.1) and note that this surface should be expands during loading, it can be found that the sign of ΔW^p is determined by $l_3=<\frac{\partial f}{\partial \sigma}>\{d\epsilon^p\}$. Since only two of l_1, l_2 and l_3 are independent (see details in the explanation of Table 2.1), the loading criteria stipulate a correct mode of engergy conversion of strain softening in agreement with the following facts:

1. External forces do positive work,
2. Elastic energy decreases,
3. plastic work is positive, or frictional forces do positive work.

In a process in compliance with the loading criteria, all the release elastic energy is consumed in situ, because the energy conservation is satisfied in any infinitesimal element. This differentiate the stable and unstable softening (brittle failure) in statics. It is easy to check no conservation in situ for brittle models.

Obviously, the loading criteria are necessary conditions for the true solution. Otherwise, the plastic work will becomes negative and this is absurd.

No violation of the loading criteria is also a sufficient condition. This is because all aspects of the true solution have been guaranted by the adopted incremental theory except the correct energy conversion mode. The loading criteria just guarantee the correct energy conversion. Physically, the process in compliance with the loading criteria reproduces a picture we observed from field investigation and laboratory tests. Based on the latter, the constitutive relationship has been formulated.

E.4 The Principle of Potential Energy and the Uniqueness of Solution

As we know, for stable materials, the existence of the minimum potential energy can be proved by using Martin's inequality along any strain-stress path for the extremes. A linear path is such a path. It can also be strictly proved that the maximum will be reached if Martin's inequality is violated, i.e.

$$\int_{(1)}^{(2)} (\sigma_{ij} - \sigma_{ij}^{(1)}) d\epsilon_{ij} \leq 0 \ . \qquad (E.10)$$

Fig. E.2, in fact, provides an example for one dimensional situation. For the proof of general situations, the only thing we need to do is to use "less than" sign in Martin's inequality and to follow the conventional proof for stable materials. Because all the inequalities derived in the original proof change signs from "greater than" to "less than", we will obtain the conclusion of the maximum. The proof for stable materials can be found in advanced text books (e.g. Wang, 1982).

When a body consists of both stable and unstable materials (Fig. E.3), the extremes may not exist for the whole body. However, by using the principle of virtual work,

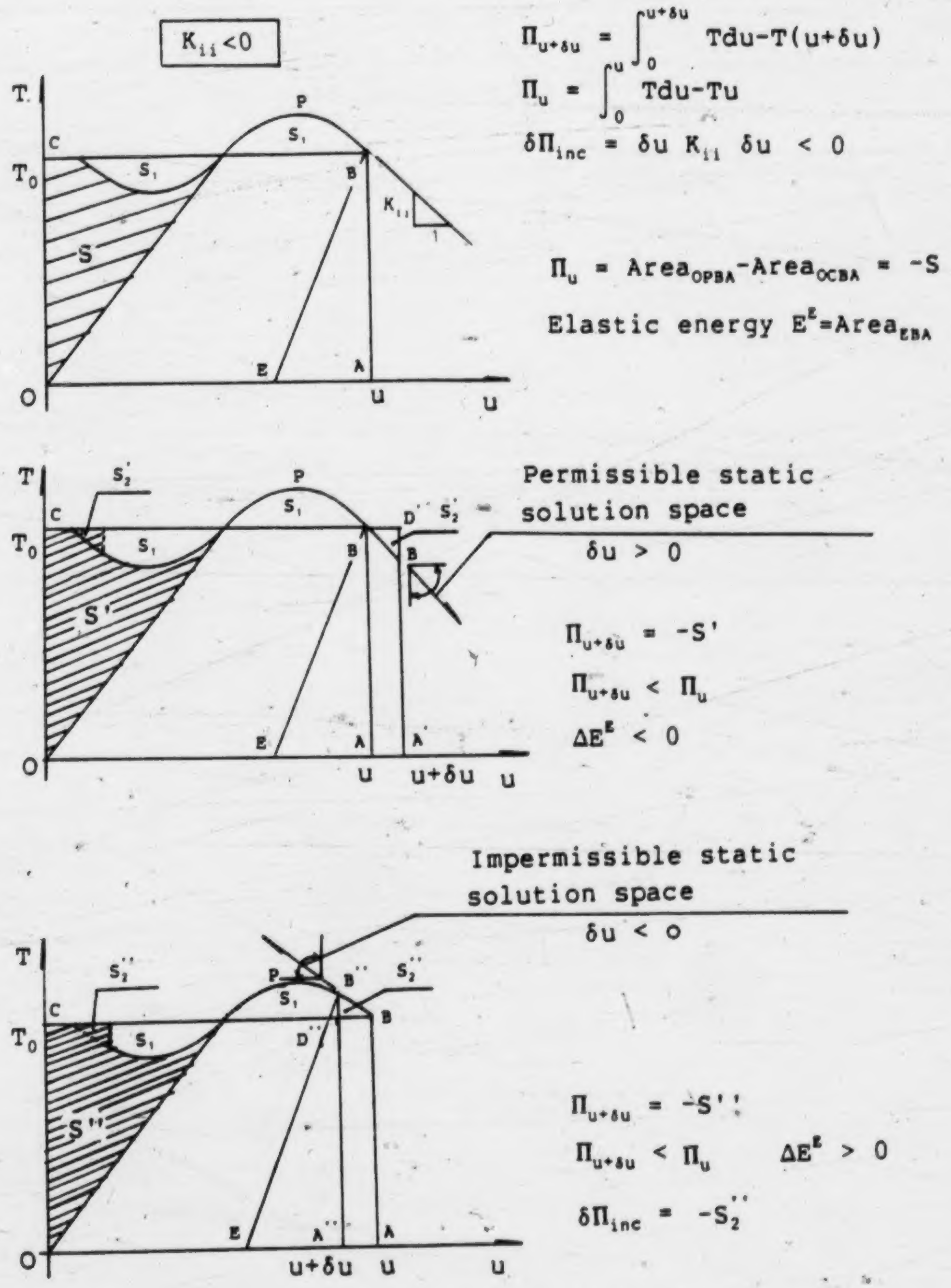
$K_{ii}<0$
T
P
C
S_1
S_1
T_0
B
K_{ii}
1
S
E
A
O
u
u
T
S_2'
P
S_1
C
D'
S_2'
T_0
S_1
B
B
S'
E
A
A'
O
u
u+δu
u
T
S_2''
P
B''
S_2''
S_1
C
B
T_0
S_1
D''
S''
E
A''
A
O
u+δu
u
u

$$\Pi_{u+\delta u} = \int_0^{u+\delta u} T du - T(u+\delta u)$$

$$\Pi_u = \int_0^u T du - Tu$$

$$\delta\Pi_{inc} = \delta u \; K_{ii} \; \delta u \; < 0$$

$$\Pi_u = \text{Area}_{OPBA} - \text{Area}_{OCBA} = -S$$

Elastic energy $E^E = \text{Area}_{EBA}$

Permissible static solution space

$\delta u > 0$

$$\Pi_{u+\delta u} = -S'$$

$$\Pi_{u+\delta u} < \Pi_u$$

$$\Delta E^E < 0$$

Impermissible static solution space

$\delta u < 0$

$$\Pi_{u+\delta u} = -S''$$

$$\Pi_{u+\delta u} < \Pi_u \qquad \Delta E^E > 0$$

$$\delta\Pi_{inc} = -S_2''$$

Figure E.2: The maxiumum potential energy

the global equilibrium equations can still be established, but the solution needs to be checked.

As to the uniqueness of solution, the proof should be started from a natural state (i.e. a zero state) for the first incremental step. Then, the existence of uniqueness should be assumed at the end of the last incremental step. When the relationship between $\dot{\sigma}_{ij}$ and $\dot{\epsilon}_{ij}$ is not unique (imcompressible or perfect elastoplastic material), the uniqueness is refered only to $\dot{\sigma}_{ij}$.

If strain softening totally governs in a region, i.e. inequality E.10 is satisfied everywhere, the uniqueness of solution can be easily proved, no matter the solution is permissible or not. Two main points in following the procedure of a conventional proof for stable materials are:

1. by using the principle of virtual work, it can be obtained that

$$\int_{\Omega} (\dot{\sigma}_{ij}^{(2)} - \dot{\sigma}_{ij}^{(1)})(\dot{\epsilon}_{ij}^{(2)} - \dot{\epsilon}_{ij}^{(1)})d\Omega = 0 \ , \tag{E.11}$$

   in which (1) and (2) denote two set of complete solutions. Here, to use the principle of virtual work only requires a stress field in equilibrium and a displacement field being kinematically possible. Therefore, impermissible static solution can be included.

2. by using inequality E.10, we can have

For strain softening

$$\int_{\Delta\Omega_i^{sof}} (\sigma_{ij}\dot{\epsilon}_{ij} + \frac{1}{2}\dot{\sigma}_{ij}\dot{\epsilon}_{ij})d\Omega > 0 \quad \text{(external work)}$$

$$\int_{\Delta\Omega_i^{sof}} (\sigma_{ij}\dot{\epsilon}^{E}_{ij} + \frac{1}{2}\dot{\sigma}_{ij}\dot{\epsilon}^{E}_{ij})d\Omega < 0 \quad \text{(elastic energy increment)}$$

$$\int_{\Delta\Omega_i^{sof}} (\sigma_{ij}\dot{\epsilon}^{P}_{ij} + \frac{1}{2}\dot{\sigma}_{ij}\dot{\epsilon}^{P}_{ij})d\Omega > 0 \quad \text{(plastic work)}$$

$$\int_{\Delta\Omega_i}\left[\int_{(1)}^{(2)} (\sigma_{ij} - \sigma^{(1)}_{ij})d\epsilon_{ij}\right]d\Omega \geq 0 \quad \text{(macro stable)}$$

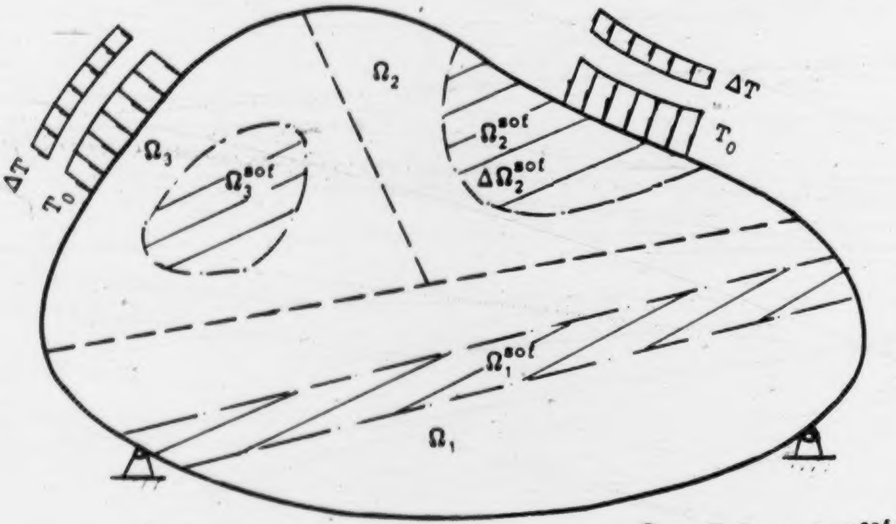
Ω_2
ΔT
T_0
Ω_2^{sof}
$\Delta\Omega_2^{sof}$
ΔT
T_0
Ω_3
Ω_3^{sof}
Ω_1^{sof}
Ω_1

$\Omega = \Sigma\,\Omega_i + \Sigma\,\Omega_i^{sof}$

Ω_i — stable material

Ω_i^{sof} — unstable material

Figure E.3: Strain softening in a body

$$(\dot{\sigma}_{ij}^{(2)} - \dot{\sigma}_{ij}^{(1)})(\dot{\epsilon}_{ij}^{(2)} - \dot{\epsilon}_{ij}^{(1)}) \le 0 \ . \qquad \text{(E.12)}$$

This is also because all the inequalities in the original proof change signs. Here, the derivation requires incremental linear strain-stress paths. Certainly, it can include impermissible solutions. Since eqn E.11 applies for any infinitesimal region, equal sign should be taken in condition E.12. Therefore, the proof is obvious.

In Fig. E.3, for all the subregion Ω_i or Ω_i^{sof}, the uniqueness of solution exists if they are considered separately. A natural train of thought is that the uniqueness of solution may exist at least under certain conditions. No strict proof will be given below. However, it can be understood like this:

1. Suppose there exist two sets of complete solutions, $\dot{u}_i^{(1)}$ and $\dot{u}_i^{(2)}$ with same loads and same boundry conditions.
2. Image that state (2) is reached from state (1), i.e. along the strain-stress path (2)-(1). The additional strain-stress path is corresponding to zero body force, zero external load and zero displacement boundary conditions on the outside boundary.
3. If the $\dot{u}_i^{(2)-(1)}$ on the joint boundary is zero, the uniqueness can be proved. Since zero stress state is a solution for each subregion with zero displacement or load boundary conditions. Thus, $\dot{\sigma}^{(2)}-\dot{\sigma}^{(1)}$ will be zero due to the uniqueness of solution in each

subregion.

4. If $\dot{u}_i^{(2)-(1)}$ is not equal zero, the total potential energy of all subregions will change due to new deformation. It generally impossible since no external work can be provided by zero boundary conditions and zero body forces. One exceptation is that the summation of the incremental potential energy of all subregions is zero. Only for this exception, there is no uniqueness of solution.

In finite element analyses, no uniqueness of solution corresponds to a zero energy mode of the global stiffness matrix with respect to certain non-zero displacement vectors. By using techniques against singularity, acceptable solution can be obtained for engineering judgement.

In conclusion, theoretical background is reviewed and strengthened for unstable materials. In practice, we may suppose that there exist a true solution, then, we can use the principle of virtual work to formulate the governing equations. After solving by introducing the boundary conditions, we check the solutions by the loading criteria. If the criteria are kept, we have true solutions. If not, they should be discarded. As a remedy, we may statically obtain approximate solutions for the final equilibrium positions (e.q. using brittle models).

F. APPENDIX - THE AITKEN ACCELERATION METHOD AND SPARSE QUASI-NEWTON LS & LDU UPDATES

For simplicity, in the following introduction, bolded letters are used to denote a matrix or a vector.

F.1 The Newton-Raphson Iteration Method

The Newton-Raphson iteration scheme is used most frequently to solve a system of nonlinear equations:

$$\mathbf{f}(\mathbf{u}^*) = 0 \ . \tag{F.1}$$

In nonlinear finite element analyses of this research, $\mathbf{u}^*$ is unknown displacements and

$$\mathbf{f}(\mathbf{u}^*) = {}^{t+\Delta t}\mathbf{R}(\mathbf{u}^*) - {}^{t+\Delta t}\mathbf{F}(\mathbf{u}^*) \ , \tag{F.2}$$

in which

t is internal time to indicate the beginning of certain loading step,

t+Δt is for the end of the loading step,

R is the vector of external nodal forces, which is independent of of $\mathbf{u}^*$ under the small strain and deformation assumptions,

F is the vector of equivalent nodal forces corresponding to internal stresses in all elements.

By expanding eqn. F.1 to Taylor's series of the first oder, the (i-1)th approximation during of iterations can be expressed as

$$\mathbf{f}(\mathbf{u}^*) = \mathbf{f}({}^{t+\Delta t}\mathbf{u}^{(i-1)}) + (\frac{\partial \mathbf{f}}{\partial \mathbf{u}})(\mathbf{u}^* - {}^{t+\Delta t}\mathbf{u}^{(i-1)}) \ . \tag{F.3}$$

Substituting eqn. F.2 into the above equation and using eqn. F.1, and note that **R** is independent of **u**, we obtain

$${}^{t+\Delta t}\mathbf{R}^{(i-1)} - {}^{t+\Delta t}\mathbf{F}^{(i-1)} + [-\frac{\partial \mathbf{F}}{\partial \mathbf{u}}](\mathbf{u}^* - {}^{t+\Delta t}(\mathbf{u})^{(i-1)}) = 0 \ . \tag{F.4}$$

Then, we define

$$\Delta\mathbf{u}^{(i)} = \mathbf{u}^* - {}^{t+\Delta t}\mathbf{u}^{(i-1)}, \tag{F.5}$$

and recognize that

$$\frac{\partial \mathbf{F}}{\partial \mathbf{u}} = {}^{t+\Delta t}\mathbf{K}^{(i-1)}, \tag{F.6}$$

where ${}^{t+\Delta t}\mathbf{K}^{(i-1)}$ is the tangential stiffness matrix at the itereation i-1.

And so, by approximation we have the N-R iteration scheme:

$${}^{t+\Delta t}\mathbf{K}^{(i-1)}\Delta\mathbf{u}^{(i)} = {}^{t+\Delta t}\mathbf{R} - {}^{t+\Delta t}\mathbf{F}^{(i-1)} \ , \tag{F.7}$$

$${}^{t+\Delta t}\mathbf{u}^{(i)} = {}^{t+\Delta t}\mathbf{u}^{(i-1)} + \Delta\mathbf{u}^{(i)}. \tag{F.8}$$

In the modified N-R method, the factorized stiffness matrix is stored and unchanged once it assembled.

F.2 The Aitken Acceleration Method

In the Aitken acceleration method, a diagonal relaxion matrix α is used for the displacement incremental vector to speed up the convergence of eqn. F.7, but the factorized stiffness matrix remains unchanged as in the modified N-R method. From the second iteration, the scheme takes the form of

$$ {}^{t+\Delta t}\mathbf{K}^{(1)}\Delta\mathbf{u}^{(i)} = {}^{t+\Delta t}\mathbf{R} - {}^{t+\Delta t}\mathbf{F}^{(i-1)} , \tag{F.9} $$

$$ {}^{t+\Delta t}\mathbf{u}^{(i)} = {}^{t+\Delta t}\mathbf{u}^{(i-1)} + \alpha\Delta\mathbf{u}^{(i)}. \tag{F.10} $$

In the original version of the Aitken method, the relaxion factor, i.e. each diagonal element of matrix α is calculated as

$$ \alpha_{ii}^{(i-1)} = \frac{\Delta u_i^{(i-1)}}{\Delta u_i^{(i-1)} - \Delta u_i^{(i)}} , \tag{F.11} $$

by using successive values of the corresponding element of the displacement vector.

Obviously, if $\Delta u_i^{(i-1)} - \Delta u_i^{(i)}$ in Eqn. F.11 is very small or zero, the estimated secant stiffess will be very sharp or even cause singularity. In an improved method developed by Boyle and Jennings (1973), a scalar factor is adopted for all degrees of freedom to avoid sinqularity, i.e. all the diagonal elements α_{ii} in matrix α are the same. The scalar factor α_{ii} is determined by three successive iterations and the expressions are:

$$\alpha_{ii}^{(i)} = \frac{[\mathbf{u}^{(i-2)} - \mathbf{u}^{(i-1)}]^T[\mathbf{u}^{(i-1)} - \mathbf{u}^{(i)}]}{[\mathbf{u}^{(i-2)} - \mathbf{u}^{(i-1)}]^T[\mathbf{u}^{(i-2)} - 2\mathbf{u}^{(i-1)} + \mathbf{u}^{(i)}]} \qquad (F.12)$$

for a symmetric stifness matrix **K**;

$$\alpha_{ii}^{(i)} = \frac{[\mathbf{u}^{(i-2)} - 2\mathbf{u}^{(i-1)} + \mathbf{u}^{(i)}]^T[\mathbf{u}^{(i-1)} - \mathbf{u}^{(i)}]}{[\mathbf{u}^{(i-2)} - 2\mathbf{u}^{(i-1)} + \mathbf{u}^{(i)}]^T[\mathbf{u}^{(i-2)} - 2\mathbf{u}^{(i-1)} + \mathbf{u}^{(i)}]} \qquad (F.13)$$

for a non-symmetric matrix.

F.3 Sparse Quasi-Newton LS & LDU Updates

F.3.1 General update formulation

In successive iterations to solve eqn. F.1. By using eqn. F.6, we have the approximate expression

$$\mathbf{f}^{(i-1)} = \mathbf{f}(\mathbf{u}^{(i)} - \Delta\mathbf{u}^{(i-1)}) = \mathbf{f}^{(i)} - \mathbf{K}^{(i)}\Delta\mathbf{u}^{(i-1)} , \qquad (F.14)$$

and so

$$\mathbf{f}^{(i)} - \mathbf{f}^{(i-1)} = \mathbf{K}^{(i)}(\mathbf{u}^{(i)} - \mathbf{u}^{(i-1)}) . \qquad (F.15)$$

The above equation is called the Quasi-Newton update. It tries to find an approximate $K^{(i)}$ for the next iteration and so the repeated reformations can be saved.

Let

$$K^{(i)} = K^{(i-1)} + \Delta K^{(i-1)} \quad , \tag{F.16}$$

and

$$f^{(i)} - f^{(i-1)} = Y^{(i-1)} \quad , \tag{F.17}$$

then,

$$Y^{(i-1)} = (K^{(i-1)} + \Delta K^{(i-1)})\Delta u^{(i-1)} \quad , \tag{F.18}$$

or

$$\Delta K^{(i-1)}\Delta u^{(i-1)} = p^{(i-1)} \quad , \tag{F.19}$$

in which

$$p^{(i-1)} = Y^{(i-1)} - K^{(i-1)}\, \Delta u^{(i-1)} \quad . \tag{F.20}$$

By assuming $f^{(i)}=0$ approximately,

$$K^{(i-1)}\, \Delta u^{(i-1)} = -f^{(i-1)} \quad . \tag{F.21}$$

From eqn. F.17 and F.20,

$$\mathbf{p}^{(i-1)} = \mathbf{f}^{(i)} . \tag{F.22}$$

Therefore, eqn. F.19 now becomes

$$\Delta\mathbf{K}^{(i-1)}\Delta\mathbf{u}^{(i-1)} = \mathbf{f}^{(i)} , \tag{F.23}$$

where $\mathbf{f}^{(i)}$ can be calculated by

$$\mathbf{f}^{(i)}(\mathbf{u}^{(i)}) = \mathbf{f}^{(i)}(\mathbf{u}^{(i-1)} + \Delta\mathbf{u}^{(i)}) , \tag{F.24}$$

after (i-1)th iteration. Now, for a problem with the total number of degrees of freedom equal to N, the task is to find all the elements of matrix $\Delta\mathbf{K}^{(i-1)}$ with a total number of N^2 (F.23). However, we have only N equations. Conventionally, the Frobenius norm solution is adopted for matrix $\Delta\mathbf{K}^{(i-1)}$. Then, matrix $\mathbf{K}^{(i)}$ can be obtained from eqn. F.16, and so the (i)th iteration can go on.

In summary, the Quasi-Newton update scheme can be expressed as

$$\begin{aligned}
&\mathbf{K}^{(i-1)}\ \Delta\mathbf{u}^{(i-1)} = \mathbf{R} - \mathbf{F}^{i-1} , \\
&\mathbf{u}^{(i)} = \mathbf{u}^{(i-1)} + \Delta\mathbf{u}^{(i)}, \\
&\mathbf{f}^{(i)} = \mathbf{R} - \mathbf{F}(\mathbf{u}^{(i)}), \qquad \text{if } \mathbf{f}^{(i)} < \text{Tolerance, stop, or} \\
&\Delta\mathbf{K}^{(i-1)}\Delta\mathbf{u}^{(i-1)} = \mathbf{f}^{(i)} , \\
&\mathbf{K}^{(i)} = \mathbf{K}^{(i-1)} + \Delta\mathbf{K}^{(i-1)}, \quad \text{then go to next iteration.}
\end{aligned} \tag{F.25}$$

In order to reduce calculation time, the updates should be carried out on the factorized global stiffness matrix and keep the sparsity unchanged. The DM and TZ methods have been developed to meet the above requirements. For simplicity, in the following introduction, we omit the superscripts for iteration times.

F.3.2 The DM method

The DM method was developed by Dennis and Marwil (1982). It is suitable for **LS** fatorization of matrix **K**, i.e. in (i-1)th iteration, in eqn. F.21

$$\mathbf{K}\Delta\mathbf{u} = \mathbf{LS}\Delta\mathbf{u} = -\mathbf{f} , \qquad (F.26)$$

where **L** is a lower triangular matrix, **S** is an upper triangular matrix, and in solving eqn. F.26, let

$$\mathbf{Lv} = -\mathbf{f} , \qquad (F.27)$$

and

$$\mathbf{S}\Delta\mathbf{u} = \mathbf{v} , \qquad (F.28)$$

then, both **Δu** and **v** are needed for the further update. Now, we can have a new **f** in (i)th iteration, and let $\mathbf{K}+\Delta\mathbf{K}=\mathbf{L}(\mathbf{S}+\Delta\mathbf{S})$, i.e. $\Delta\mathbf{K}=\mathbf{L}\Delta\mathbf{S}$. Thus, eqn. F.23 becomes

$$\mathbf{L}\Delta\mathbf{S}\Delta\mathbf{u} = \mathbf{f} \quad , \tag{F.29}$$

and let

$$\Delta\mathbf{S}\Delta\mathbf{u} = \mathbf{z} \quad , \tag{F.30}$$

then

$$\mathbf{z} = \mathbf{L}^{-1}\mathbf{f} \quad . \tag{F.31}$$

It is convenient to use the notation

$$\mathbf{e}_i^T = <0\ 0\ 0\ \ldots\ 1\ \ldots\ 0\ 0\ 0>$$

in which, only the ith element is unit and all others are zero. Now, the ith row of $\Delta\mathbf{S}$ can expressed as $\mathbf{e}_i^T\Delta\mathbf{S}$, and its Frobenius norm solution is

$$\mathbf{e}_i^T\ \Delta\mathbf{S} = z_i\Delta\mathbf{u}^{iT}/(\Delta\mathbf{u}^{iT}\ \Delta\mathbf{u}^i) \quad , \tag{F.32}$$

in which z_i is the ith element of vector $\mathbf{z}$ solved from eqn. F.31, and $\Delta\mathbf{u}^i$ is first solved from eqn. F.28, then transformed according to the sparsity of matrix $\mathbf{S}$, i.e. the jth element Δu_j^i of vector $\Delta\mathbf{u}^i$ is set to be zero if the element S_{ij} of matrix $\mathbf{S}$ is zero. Here, S_{ij} is located at ith row and jth column. Thus, $\Delta\mathbf{S}$ can be obtained. The iteration procedure is the same as eqn. F.25, but $\mathbf{K}^{(i-1)}$ and $\mathbf{K}^{(i)}$ are replaced by $\mathbf{LS}$ and $\mathbf{L}(\mathbf{S}+\Delta\mathbf{S})$.

F.3.3 The TZ method

The TZ method was developed by Tewarson and Zhang (1987), which is suitable for **LDU** factorization, i.e. **K=LDU**. Here, **L** is a lower triangular matrix , **D** is a diagonal matrix and **U** is an upper triangular matrix. In the TZ method, **L**, **D** and **U** are all updated. If **L** is updated first, we call it TZ_L; if **U** is updated first, we call it TZ_U and if **L** and **U** are updated alternatively, we call it TZ_{LU}. Notation $\hat{}$ denotes to update once and $\hat{\hat{}}$ denotes to update twice.

In TZ_L, **LDU** is updated in the manner:

$$\mathbf{LDU} \text{ ------- } \hat{\mathbf{L}}\hat{\mathbf{D}}\mathbf{U} \text{ ------- } \hat{\mathbf{L}}\hat{\hat{\mathbf{D}}}\hat{\mathbf{U}}$$

The procedure is similar to eqn. F.25, and the particular iteration procedure for TZ_L is as follows.
Solve equations

$$(\mathbf{LDU})\Delta\mathbf{u} = \Delta\mathbf{Q} = -\mathbf{f} \ . \qquad (F.33)$$

Let

$$(\mathbf{DU})\Delta\mathbf{u} = \mathbf{v}, \quad \mathbf{Lv} = \Delta\mathbf{Q} \ , \qquad (F.34)$$

$$\mathbf{U}\Delta\mathbf{u} = \mathbf{w}, \quad \mathbf{Dw} = \mathbf{v} \ . \qquad (F.35)$$

Then, solve **v**, **w** and **Δu** and so

$$u = u + \Delta u \ . \qquad (F.36)$$

Check the new unbalance term:

$$f = f(u) \ . \qquad (F.1)$$

If the solution is not convergent, update **LDU** and repeat the solution from eqn. F.33 to F.36 until convergence.

In updating **LD** to $\hat{\mathbf{L}}\hat{\mathbf{D}}$, evaluate

$$g_i = w^{iT} w / (\bar{w}^{iT} \ \bar{w}^i) \ , \qquad (F.37)$$

$$r_i = 1/(\bar{w}^{iT} \ \bar{w}^i) \ , \qquad (F.38)$$

where, w^i is a vector by zeroing the elements of w (eqn. F.35) according to the sparsity of ith row of matrix **L**. And, $\bar{w}^i$ is a vector by setting the jth element of w to zero accoding to the sparsity of the ith row of matrix **L** only if $i>j$, but setting it to zero according to the ith row of matrix **U** if $i<j$.

After g_i and r_i are obtained, update **D** and **L** to $\hat{\mathbf{D}}$ and $\hat{\mathbf{L}}$ by using the expressions:

$$\hat{d}_j = d_j + r_i f_j w_j^j \ , \qquad (F.39)$$

$$\hat{l}_{ij} = l_{ij} + (r_i f_i - l_{ij} r_j f_j) w_j^i \ / \ \hat{d}_j \ . \qquad (F.40)$$

In order to update $\hat{\mathbf{D}}$ and $\hat{\mathbf{L}}$ further to $\hat{\hat{\mathbf{D}}}$ and $\hat{\mathbf{U}}$, determine vector **f'** with its element

$$f'_i = f_i - g_i f_i \ . \qquad \text{(F.41)}$$

Solve the vector **z** from the following equations

$$\mathbf{L}\mathbf{z} = \mathbf{f}' \ . \qquad \text{(F.42)}$$

Calculate

$$r'_i = \mathbf{\Delta u}^{iT}\mathbf{\Delta u}^i \ , \qquad \text{(F.43)}$$

in which, $\mathbf{\Delta u}^i$ should be treated according to the sparsity of the matrix **U**.

Finnally update $\hat{\mathbf{D}}$ and **L** to $\hat{\hat{\mathbf{D}}}$ and $\hat{\mathbf{U}}$ by using the the following expressions:

$$\hat{\hat{d}} = \hat{d}_i + r'_i z_i \Delta u^i_i \ , \qquad \text{(F.44)}$$

$$\hat{u}_{ij} = u_{ij} + r'_i z_i (\Delta u^j_i - \Delta u^i_i + U_{ij}) \ / \ \hat{\hat{d}}_i \ . \qquad \text{(F.45)}$$

In the TZ_U method, **D** to **U** are updated first. Let $\hat{\mathbf{D}}\hat{\mathbf{U}}=\mathbf{DU}+\mathbf{\Delta U}$, then $\mathbf{\Delta K}=\mathbf{L\Delta U}$. By using the basic equations, we can have

$$\Delta U \Delta u = L^{-1} f = z \ , \qquad (F.46)$$

in which, f is found from the (i-1)th iteration.
To leave room for the further update of L, we solve the equations

$$\Delta U \Delta u = G f = \bar{z} \ , \qquad (F.47)$$

in which G is a diagonal matrix with its element

$$g_i = \Delta u^{iT} \Delta u^i \ / (\Delta \bar{u}^{iT} \ \Delta \bar{u}^i) \ , \qquad (F.48)$$

where Δu_i is obtained from Δu according to the sparsity of matrix U, while $\Delta \bar{u}_i$ is obtained from Δu according to the sparsity both of matrix L and U (similar to $\Delta \bar{w}_i$ in eqn. F.38). Solving eqn. F.47 as in the TZ_L method, we have

$$\hat{d}_i = d_i + r_i z_i \Delta u^i_i \ , \qquad (F.49)$$

$$\hat{U}_{ij} = U_{ij} + r_i z_i (\Delta u^i_j - r_i z_i \Delta u^i_i U_{ij}) / \ \hat{d}_i \ , \qquad (F.50)$$

in which

$$r_i = (\Delta \bar{u}^{iT} \ \Delta \bar{u}^i)^{-1} \ . \qquad (F.51)$$

To update L and $\hat{D}$ further to $\hat{L}$ and $\hat{\hat{D}}$, let

$$\hat{v} = \hat{D}^{-1}(v + \bar{z}) \ , \tag{F.52}$$

$$\hat{f} = f - L\bar{z} \ . \tag{F.53}$$

Here f is the new unbalance term after obtaining Δu and vector $\bar{z}$ is equal to GZ (eqn. F.47). Then, the Frobenius solution of ΔL can be obtained from the equations below

$$\Delta L\hat{v} = \hat{f} \ . \tag{F.54}$$

The specific expressions for $\hat{\hat{D}}$ and $\hat{L}$ are

$$\hat{\hat{d}}_i = \hat{d}_i + r_i'\hat{f}_i\hat{v}_i^i \ , \tag{F.55}$$

$$\hat{l}_{ij} = l_{ij} + (r_i'\hat{f}_i - l_{ij}r_j'\hat{f}_j)\hat{v}_j^i \ / \ \hat{\hat{d}}_j, \quad i<j \ , \tag{F.56}$$

in which

$$r_i' = (\hat{v}^{iT}\ \hat{v}^i)^{-1} \ . \tag{F.57}$$

In short, the procedures of method TZ_U are

1. solve eqn. F.34 to F.36 for Δu and v,
2. evaluate g_i and r_i by using eqn. F.48 and F.51,
3. update D and U to $\hat{D}$ and $\hat{U}$ by using eqn. F.49 and F.50,

4. determine $\bar{z}$ from eqn. F.47 and $\hat{f}$ and $\hat{v}$ from eqn. F.52 to F.54,
5. update $\hat{D}$ and L to $\hat{\hat{D}}$ and $\hat{L}$ by using eqn. F.55 to F.57.

As mentioned before, TZ_{LU} method can be easily formulated by using methods TZ_L and TZ_U alternately.

G. APPENDIX - LIMIT EQUILIBRIUM ANALYSES

In the "REPORT", a multiple-wedge method is used and the results have been compared with those obtained from the Morgenstern-Price method. Here, Sarma's method is used. By experience, Sarma's method is also a general method which has been proved to be effective.

The division of slices is illustrated in Fig. G.1, in which 11 vertical slices are used and the piezometric head is estimated from the "REPORT".

Eight groups of results obtained by the Sarma method will be described. For each group, a short note or comment is given.

1. Comparison for different methods

Table G.1 Comparison between different methods

Case	Strength				Factor of safety SF					
	Core & Boot		Yellow Clay		Multiple wedge		Sarma		Morgenstern & Price	
	C' kpa	φ'	C' kpa	φ'	SF	δ°	SF	δ°	SF	δ°
a	0	19	0	20	1.243	8.9	1.21	10	1.267	12.0
b	51	0	0	20	1.243	8.8	1.22	10	1.293	11.1
c	0	19	0	15.0	1.000	8.8	0.99	10	1.012	12.0
d	51	0	0	14.81	1.000	8.6	1.00	10	1.034	10.8

(1) Case a & b : "critical state" of soils.
(2) Case c & d : limit equilibrium state.

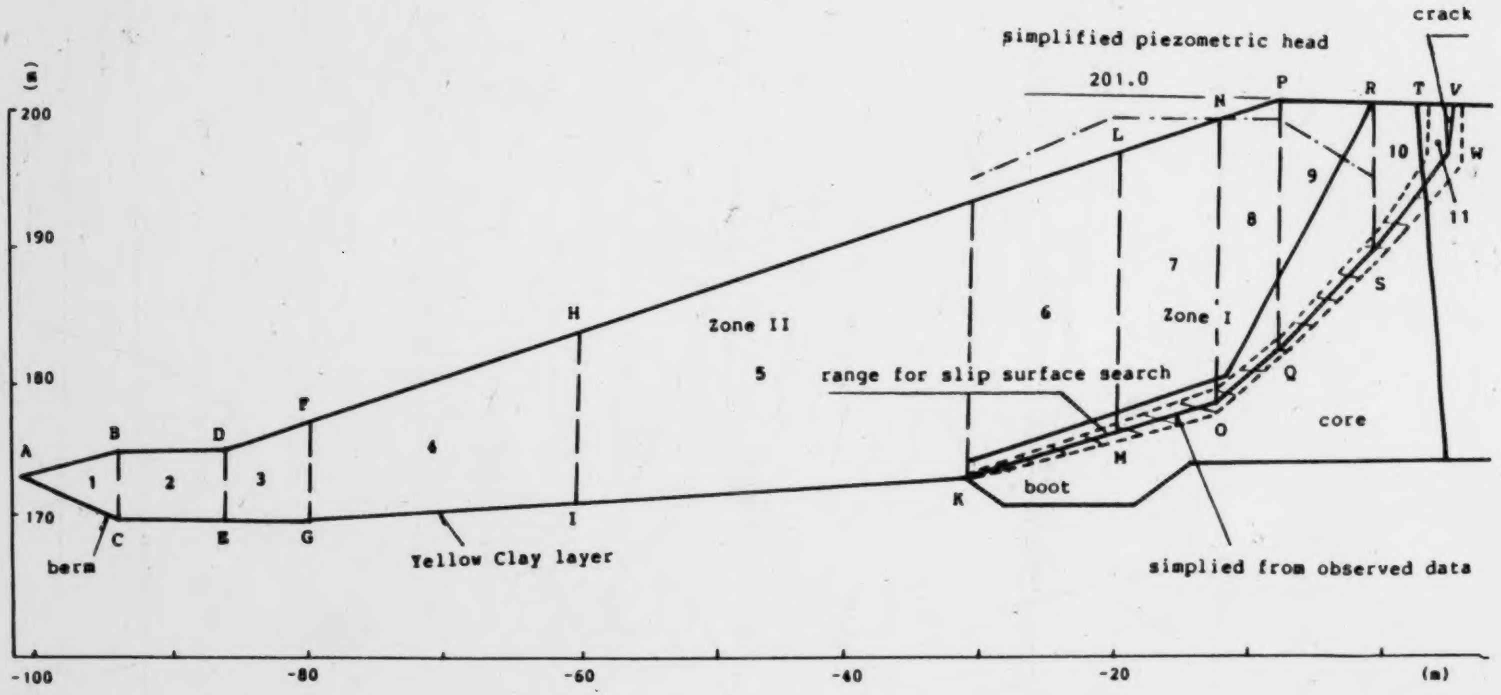
crack
simplified piezometric head
201.0
(m)
200
190
180
170
-100
-80
-60
-40
-20
(m)
A
B
C
D
E
F
G
H
I
K
L
M
N
O
P
Q
R
S
T
V
W
1
2
3
4
5
6
7
8
9
10
11
Zone II
Zone I
range for slip surface search
core
boot
berm
Yellow Clay layer
simplied from observed data

Figure G.1: Limit equilibrium analyses by Sarmar's method

In Table G.1, results obtained from the multiple-wedge, Sarma's and Morgenstern-price methods are listed.

The parameters which are not listed in the table are:

Strength at toe: $C' = 0$, $\phi' = 30^\circ$,

Unit weight, 18.5 for Core ,

21.3 for Zone I & II fill .

The above table shows that all the methods are effective. Our results are close to those from multiple-wedge method. It is not strange because both of the two methods are multiple-wedge methods. The difference may mainly come from reproducing the geometry by simple measurements on the available figures, minor difference among the adopted unit weights, and different number of slices as well as different values of angles of thrust line δ.

The slip surface in Fig. G.1 is simplified from the observed data. Therefore, it is not the critical one obtained by searching the slip surface. Errors of factors of safety (SF) are less than 2% within the searching range.

2. Influence of unit weight

The same unit weight of 18.5 kN/M^3 for the core are used throughout the "REPORT", but different unit weights from 20.5-22 kN/M^3 are suggested or used in the "REPORT" for Zone I & II fills. Table G.2 shows the influence of the unit weight of Zone II on safety factors (SF). The case in Table G.2 corresponds with case c in Table G.1.

From the Table G.2, we can see that reduction of the unit weight by 0.5 kN/M^3 will reduce SF by about 1%. This is because normal pressures will be reduced on the Yellow Clay layer.

Table G.2 Influence of unit weight of Zone II

γ (kN/M)$_3$	22.0	21.5	21.0	20.5
SF	1.009	0.999	0.988	0.980

3. Influence of the peak friction angle of the Yellow Clay

With zero cohesion, the friction angle ϕ' of the Yellow Clay was varied in the "REPORT" from $\phi'=20^\circ$ (corresponding to the "critical state" of the material) to $\phi'=15^\circ$ (corresponding to very large shear strain development). Table G.3 shows that 1° decrease leads to 4-5% reduction of safety factors. The influence is very large.

Table G.3 Influence of ϕ' in the Yellow Clay

ϕ'	20°	19°	18°	17°	16°	15°
SF	1.21	1.16	1.12	1.07	1.03	1.01

4. Influence of the undrained shear strength

Table G.4 shows the influence of the average C_u upon factors of safety. Various average values of C_u for the core are suggested or mentioned in the "REPORT", ranging from 65 kpa to 35 kpa. Every 5 kpa reduction leads to 3% reduction of SF. Because an average C_u is difficult to determine, the error may be not small.

Table G.4 Influence of average C_u

Cu average	65	60	55	50	45	40	35
SF	1.10	1.07	1.03	1.00	0.97	0.94	0.90

5. Operational undrained strengths in the core and boot

Corresponding to different cases in Table G.5 (next page), operational undrained strengths have been re-estimated in the "REPORT" as compared with effective stress analyses. Similar calculations by means of Sarma's method are also done with the results listed in the same table. The differences between the two group results mainly come from the uplift pressure calculation. Higher pressures in the boot are used in the "REPORT".

From this table, we can see that the average strength might be around 43 kpa near the failure, corresponding to case D with SF = 1.01 to 1.04.

6. Material parameters used in finite element analyses

Two sets of different material models and parameters have been used in our calculation and in the "REPORT". Because brittle behaviors and strain-softening models have been adopted in our calculation and in the "REPORT" respectively, it is difficult to study the influences of all parameters. In Table G.6, factors of safety calculated from two sets of peak strengths are compared.

Two factors of safety obtained from peak strengths are nearly the same. It is because cohesions is a little bit larger for the Yellow Clay layer and Zone II fill while ϕ' is a little bit smaller in our calculation. Our predicted

Table G.5 Operational undrained shear strengths

Case	Effective Stress Analyses						Total Stress Analyses				
	Core & Boot		Yellow Clay		Factor of Safety		Operational Cu (kpa) (estimated)			Factor of Safety	
	C' kpa	ϕ'	C' kpa	ϕ'	REPORT	Ours	Core	Boot	Average	REPORT	Ours
A	15	21	10	20	1.409	1.43	46	80	62	1.409	1.43
B	0	21	0	20	1.217	1.24	33	65	48	1.217	1.23
C	6	20	5	17.5	1.116	1.12	31	62	45	1.118	1.12
D	0	19	0	16	1.012	1.03	29	59	43	1.012	1.04

A: Intact strength.
B: 'Critical state' C' = 0.
C: With pre-existing shears.
D: Large strain plus progressive failure.

failure height in trial finite element analyses is only at EL. 198.0m, three meters below the top. This is because we use brittle model for the Yellow Clay and strain-softening model for the core, while a strain-softening model is adopted for the Yellow Clay and a perfectly plastic model is for the core in the "REPORT". Here, we can see the importance of the correct simulation of post peak behavior.

Table G.6 Comparison of different peak strengths

Material	Core & Boot			Yellow Clay			Zone I & II			Factor of safety
Parameter	γ kN/M^3	Cu kpa	ϕ °	γ kN/M^3	C' kpa	ϕ' °	γ kN/M^3	C' kpa	ϕ' °	
"REPORT"	18.5	50	0	20	0	20	22	10	25	1.25
Ours	18.5	51	0	18	6	18	21	13.5	24	1.24

Note: Pre-shear and construction defects have been considered in determining peak strengths.

7. Effective and total stress analyses at EL. 198.0m

In our trial analyses, the dam fails at EL. 198.0m. Factors of safety are calculated at this elevation for two cases. The parameters in case c and d (Table G.1) are used. From observed data, we know that the piezometric heads are at least 5m-6m lower on average at EL. 198.0m than those at EL. 201.0m. Decrease of uplift forces due to the change of elevation is taken into account in effective stress analyses. Only decrease of the elevation is taken into account in total stress analyses.

In the above calculations, the same slip surface is adopted. Although the most critical slip surfaces are not same for different elevations, the deviation of one slip surface from the other is not large and the relative error of SF between the two surfaces is less than 0.5%.

Table G.7 Factor of safety at EL. 198.0m

Case	Effective stress analysis			Total stress analysis	
	case c see Table G.1	Piez. Head unchanged	Piez. Head decreased by 5.5 m	Case d see Table G.1	Cu unchanged
EL.	201.0	198.0	198.0	201.0	198.0
SF	0.99	1.07	1.165	1.000	1.120

Table G.7 shows that the influence of pore presure changes upon safety factors amounts to about 10% i.e. 1.165-1.07, which cannot be neglected. From EL. 198.0m to EL. 201.0m, the change of safety factors in the effective analysis is 4% to 5% larger than the change in the total stress analysis. It is simply because total analyses do not reflect the influence of pore pressure changes.

8. Upper and lower bounds of factors of safety

The upper and lower bounds of safety factors for crest level at EL. 201.0m can be found by using peak and residual strengths. In Table G.8, the results by means of the Sarma's method are compared with the results taken from the "REPORT". In the table, the condition "peak, with shears" means that reductions of the strengths due to pre-shears in the Yellow Clay and rutting shears in the core have been taken into account.

The difference between our and other people's results are mainly caused by the assumption on pore pressures. The pore pressures used in the "REPORT" are a little bit greater than ours. They used pore pressure ratios, r_u=0.42 for the core and r_u=0.53 for the boots. Ours are based directly on the observed data along the slip surface.

Table G.8 Upper and lower bounds of factors of safety

Condition	Core		Yellow Clay		SF	
	C'	φ'	C'	φ'	REPORT	OURS
Peak intact	15	20	10	20	1.41	1.46
Peak with shears	6	20	6	18	1.21	1.23
Residual	0	13	0	12		0.73

A brief discussion is given below.

Suppose that F=1.0 at EL. 201.0 m,

The total reduction of SF due to pre-shears and progressive failure will be

$$\frac{1.41-1.0}{1.41} = 29\% \qquad \text{(in REPORT)} ,$$

$$\frac{1.46-1.0}{1.41} = 31\% \qquad \text{(ours)} .$$

The reduction due to pregressive failure will be

$$\frac{1.21-1.0}{1.41} = 14.8\% \qquad \text{(in REPORT)} ,$$

$$\frac{1.23-1.0}{1.46} = 14.8\% \qquad \text{(ours)} .$$

Suppose that we can predict the reduction of the strength due to material defects before the design

The reduction of SF will be

$$\frac{1.21-1.0}{1.21} = 17.4\% \qquad \text{(in REPORT)} ,$$

$$\frac{1.23-1.0}{1.23} = 18.7\% \qquad \text{(ours)} .$$

If we use residual strengths, the underestimation of SF will be

$$\frac{1.0-0.73}{1.0} = 27\% \qquad \text{(ours)} .$$

In short, the role of progressive failure is very important for the case history of the Carsington Dam failure.